Optics measurements and corrections for colliders and other storage rings

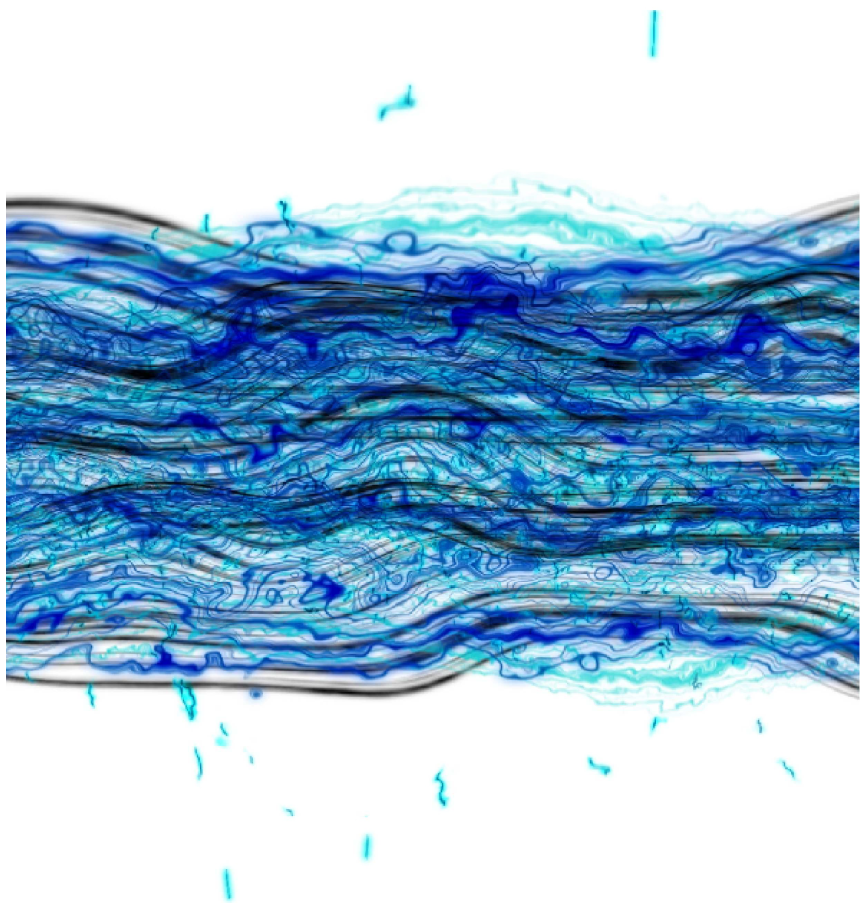

Glenn Vanbavinckhove

Optics measurements and corrections for colliders and other storage rings

Optics measurements and corrections for colliders and other storage rings

Universiteit van Amsterdam
Science Park 904
1098 XH Amsterdam
homepage: http://www.uva.nl/

This work was supported by the National Institute for Subatomic Physics (NIKHEF), which is subsidized by the Netherlands Organization for Scientific Research (NWO).

ISBN: 978-94-907-3205-9

Optics measurements and corrections for colliders and other storage rings

Academisch Proefschrift

ter verkrijging van de graad van doctor aan de
Universiteit van Amsterdam
op gezag van de Rector Magnificus
Prof. dr. D.C. van den Boom
ten overstaan van een door het college voor
promoties ingestelde commissie, in het openbaar
te verdedigen in de Agnietenkapel
op woensdag 16 januari 2012, te 12.00 uur

door

Glenn Vanbavinckhove

geboren te Oostende, België.

Promotor:	Prof. dr. J. J. Engelen
Co-promotor:	Prof. dr. L. R. Evans
Overige leden:	Prof. dr. S. C. M. Bentvelsen
	Prof. dr. J. F. J. van den Brand
	Prof. dr. ir. P. J. de Jong
	Prof. dr. P. M. Kooijman
	Prof. dr. P. Kruit
	Prof. dr. F. L. Linde
	Dr. R. Tomás Garcia

Faculteit der Natuurwetenschappen, Wiskunde en Informatica

Contents

Introduction

The research field for this thesis is accelerator physics. Accelerator physics is a branch of applied science which covers a large variety of different topics ranging from electromagnetism to material science. The sub-category in accelerator physics which studies the properties of particle beams under the influence of electromagnetic fields is called beam physics.

The topic for this thesis is beam optics[1]. The study of beam optics has been conducted since the beginning of the 20$^{\text{th}}$ century. The continuous interest in this field is motivated by the fact that the boundaries of physics are constantly being pushed and thus better technology is required to cope with new developments.

There are several reasons for the detailed study of beam optics. In the case of colliders, it is because the detailed measurement and corrections of the optics functions determine the luminosity. Large deviations from the design model limit the physical aperture and may lead to potentially dangerous situations where the accelerator gets damaged.

CERN

CERN, originally standing for "Conseil Européen pour la Recherche Nucléaire", is the European laboratory for particle physics. The laboratory was founded in 1954, partly as an effort to revive and reunite European science after the Second World War. Today CERN has 20 member states, and serves as an international particle accelerator laboratory. The main role of the laboratory is to provide large scale experimental infrastructure for high-energy particle physics. More specifically, engineers and physicists at CERN design, construct, operate and maintain particle accelerators and detectors and the infrastructure (such as IT) needed to run this accelerator complex. CERN's accelerator complex, shown in figure 1, is a succession of particle accelerators that can reach increasingly higher energies. Each accelerator boosts the speed of a beam of particles, before injecting it into the next one in the sequence. The Large Hadron Collider (LHC) is CERN's flagship accelerator. As its name implies, the LHC accelerates Hadrons (protons and ions) and it is the most powerful machine in the world today, with an ultimate energy of 7 TeV per proton beam.

Hadron versus lepton accelerators

Studies conducted for different machines using different particle species are presented in this thesis. Particles can be classified into two categories. The first category is called hadrons. Hadrons are composed of quarks (an elementary particle) which are held together by the strong force. An example of a hadron is a proton. The second classification is leptons. Leptons are fundamental, point-like particles like the electron.

Both species are used in accelerators around the world, in particular protons and electrons (and their anti-protons). Hadron colliders are being used as 'discovery machines' because of their high-energy. Lepton machines are being used as 'precision machines' because of the point-like nature of the beam particles.

[1] The term optics is taken as an analogy with the study of light transport with lenses

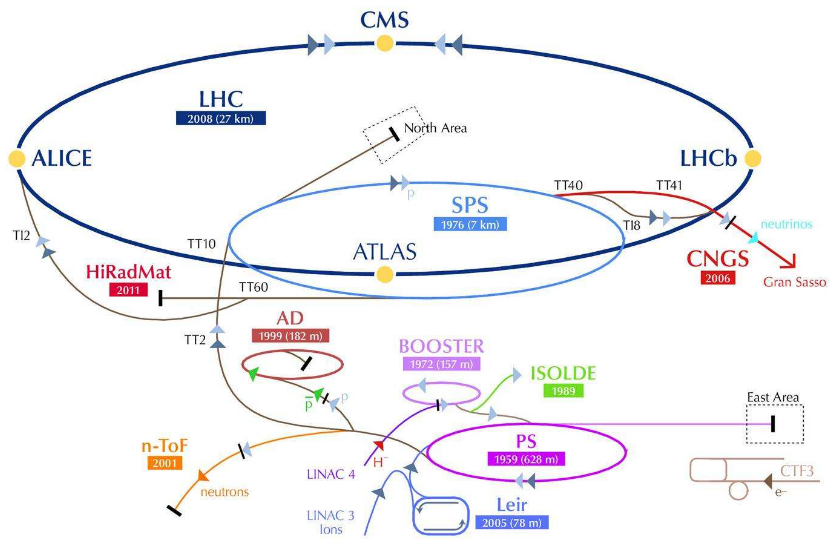

Figure 1: CERN accelerator complex

Outline of the thesis

This study started in November 2008 at the BE-ABP-LCU section at CERN. The first year of this study was dedicated to the further development of the optics measurement and correction algorithms and the implementation of a new technique which allowed the identification of local error sources. Experiments were conducted in the CERN SPS to test the algorithms that were developed. This allowed us to evaluate the performance of the measurement and correction algorithms and improve them when necessary.

Due to the unfortunate incident on 19 September 2008, the operation of the LHC was halted for one year. On the 20$^{\text{th}}$ of September 2009, operations resumed and the LHC was circulating beams again. First LHC measurements for this thesis were conducted at 450 GeV on the 23$^{\text{rd}}$ of November 2009. From then on the energy increased to an intermediate energy of 3.5 TeV. As a precaution it was decided to operate the LHC at energies lower than 7 TeV between 2009-2012 (for the 2012 physics run an energy of 4 TeV is used). It is planned to increase the energy to 7 TeV in 2014.

During the course of this thesis two collaborations with external institutes were started. The first collaboration was carried out with the synchrotron SOLEIL in Saint-Aubin, France. This collaboration was aimed at non-linearity measurements in electron machines. The second collaboration was with the Relativistic Heavy Ion Collider in Brookhaven, NY, USA. After the successful implementation of the newly developed technique to identify local error sources at CERN, it was decided to implement this technique at RHIC in November 2010.

Chapter 1 highlights and discusses the beam dynamics which is used throughout this thesis. The discussion is kept short and references are provided for further reading. The first section contains the motivation for the optics correction. Different instruments and techniques were used to conduct the measurements and apply the corrections. This is explained in detail in chapter 2. Chapter 3 discusses the results of the measurements and corrections for CERN's SPS. These tests were performed as a preparation for the LHC. The main part of the thesis is the presentation of the results of the LHC. An introduction to the optics of the LHC is given in chapter 4. In this chapter some simulations of the optics is also discussed. The LHC optics commissioning from 2009 until 2011 is discussed in chapter 5. The most important results are presented. Special optics studies for the LHC are discussed in chapter 6. The techniques used for the LHC were implemented in the Relativistic Heavy Ion collider (RHIC) at BNL. The first results and suggested improvements are discussed in chapter 7. The algorithms that were developed for the LHC, a hadron collider, have been extended to the damping ring of CLIC, a lepton machine. The simulations are discussed in chapter 8. The first tests were conducted in SOLEIL, this is discussed in section 8.4.1. The Graphical User Interface that has been used intensively during the commissioning of the LHC is discussed in chapter 9

Chapter 1

Beam dynamics

In this chapter the accelerator beam dynamics which is used throughout this thesis is introduced. The discussion is kept short and references are included for further reading. Most of the material was taken from [1] and [2]. The fundamental equations of charged particle beam optics is discussed in section 1.1. Section 1.2 discusses the matrix formalism to describe beam line transport. Section 1.3 discusses the luminosity. Perturbations and their corresponding mitigations play an important role in the operation of every accelerator, this is discussed in section 1.4. Finally, the resonance driving terms which are used to measure coupling and higher order resonances are discussed in section 1.6.

1.1 Fundamentals of charged particle beam optics

The Lorentz force for a particle carrying a single basic unit of electrical charge can be written as:

$$\mathbf{F} = e\mathbf{E} + e[\mathbf{v} \times \mathbf{B}]. \tag{1.1}$$

The Lorentz force has two components, due to the electrical field $\mathbf{E}$ and the magnetic field $\mathbf{B}$. When the speed of the particle is close to the speed of light($v \approx c$) the magnetic field needed is much smaller than the electrical field to have the same force. So the $\mathbf{E}$ will be ignored.

The acceleration due to the Lorentz force follows from equating it to the centrifugal force:

$$m\gamma v^2 \boldsymbol{\kappa} = e[\mathbf{v} \times \mathbf{B}], \tag{1.2}$$

$\boldsymbol{\kappa} = (\kappa_x, \kappa_y, 0)$ is defined as the local curvature of the trajectory in the 'transverse' (to the $\mathbf{v}$, $\mathbf{B}$ plane) directions,

$$\kappa_{x,y} = \frac{1}{\rho_{x,y}}, \tag{1.3}$$

$\rho_{x,y}$ is defined as the local bending radius of the trajectory. The transverse speeds are much smaller than the longitudinal speed ($p_{x,y} \ll p_z$). With these assumptions, equation (1.2) can be rewritten as:

$$\frac{1}{\rho}[\mathrm{m}^{-1}] = |\frac{e}{p}B| = |\frac{ec}{\beta E}B|. \tag{1.4}$$

Equation (1.4) can be written in more practical units:

$$\frac{1}{\rho}[\mathrm{m}^{-1}] = 0.2998\frac{|B[T]|}{\beta E[GeV]}. \tag{1.5}$$

Note that in equation (2.4), β and γ are the Lorentz' relativistic parameters and not the Courant-Snyder parameters (which are introduced in section 1.2.1). The relativistic parameters are defined as follows:

$$\begin{aligned} \beta &= \frac{v}{c}, \\ \gamma &= \frac{1}{\sqrt{1-\beta^2}}, \end{aligned} \tag{1.6}$$

where v is the velocity of the particle and c the speed of light.

1.2 Matrix formalism in Linear Beam Dynamics

In Appendix A the equation of motion is derived up to the 2^{nd} order. The most commonly used coordinate system in accelerator physics is the Frenet-Serret coordinate system [2]. This system is convenient as it follows the particles with respect to the reference path. The following approximations are introduced:

- Higher order terms are ignored.
- It is assumed that the particle has the design energy.

With the above approximations, the equation of motion is reduced to Hill's equation:

$$z'' + K(s)z = 0, \tag{1.7}$$

s is the position of the particle along the reference path, z stands for the horizontal or vertical position and *K(s)* is an arbitrary function resembling the focusing parameter along a beam line. The solutions of this differential equation where *K(s)* remains constant are:

$$K > 0: \quad C(s) = \cos(\sqrt{K}s),\ S(s) = \tfrac{1}{\sqrt{K}}\sin(\sqrt{K}s), \tag{1.8}$$

$K < 0:$

$$C(s) = \cosh(\sqrt{|K|}s),\ S(s) = \tfrac{1}{\sqrt{|K|}}\sinh(\sqrt{|K|}s), \tag{1.9}$$

these linearly independent solutions satisfy the following initial conditions:

$$\begin{aligned} C(0) = 1,\ C'(0) = \left.\frac{dC}{ds}\right|_{s=0} = 0, \\ S(0) = 0,\ S'(0) = \left.\frac{dS}{ds}\right|_{s=0} = 1. \end{aligned} \tag{1.10}$$

Any arbitrary solution z(s) can be expressed as a linear combination of these two principal solutions:

$$\begin{aligned} z(s) = C(s)z_0 + S(s)z'_0, \\ z'(s) = C'(s)z_0 + S'(s)z'_0, \end{aligned} \tag{1.11}$$

where z stands for either x or y. Equation (1.11) can be written down in a matrix. The motion is separated in both planes since coupling is not considered for the moment. Both planes can be combined into a 4×4 matrix describing the transformation of all four coordinates:

$$\begin{bmatrix} x(s) \\ x'(s) \\ y(s) \\ y'(s) \end{bmatrix} = \begin{bmatrix} C_x(s) & S_x(s) & 0 & 0 \\ C'_x(s) & S'_x(s) & 0 & 0 \\ 0 & 0 & C_y(s) & S_y(s) \\ 0 & 0 & C'_y(s) & S'_y(s) \end{bmatrix} \begin{bmatrix} x_0 \\ x'_0 \\ y_0 \\ y'_0 \end{bmatrix}. \tag{1.12}$$

In the next paragraphs the linear transformation matrices for a variety of beam line elements will be introduced.

Drift space

In the area where no magnetic elements are installed or in a weak bending magnet, the focusing parameter $K(s) = 0$, equation (1.12) can be expressed as:

$$\begin{bmatrix} z(s) \\ z'(s) \end{bmatrix} = \begin{bmatrix} 1 & s \\ 0 & 1 \end{bmatrix} \begin{bmatrix} z_0 \\ z'_0 \end{bmatrix}, \tag{1.13}$$

where z stands for the horizontal or vertical position.

Dipole

In the case of a pure sector dipole the transformation is expressed as:

$$\begin{bmatrix} z(s) \\ z'(s) \end{bmatrix} = \begin{bmatrix} \cos\theta & \rho\sin\theta \\ -\frac{1}{\rho}\sin\theta & \cos\theta \end{bmatrix} \begin{bmatrix} z_0 \\ z'_0 \end{bmatrix}, \tag{1.14}$$

where $\theta = \frac{s}{\rho}$ is the angle and ρ is the bending radius.

Quadrupole

For a pure quadrupole the field gradient or quadrupole strength $K(s)$ can be either positive, for focusing, or negative, for defocussing. For $K = |K|$ the transformation for a focusing quadrupole is expressed as:

$$\begin{bmatrix} z(s) \\ z'(s) \end{bmatrix} = \begin{bmatrix} \cos\sqrt{K}s & \frac{1}{\sqrt{K}}\sin\sqrt{K}s \\ -\sqrt{K}\sin\sqrt{K}s & \cos\sqrt{K}s \end{bmatrix} \begin{bmatrix} z_0 \\ z'_0 \end{bmatrix}, \tag{1.15}$$

and for the other plane with $K = -|K|$ the solution is:

$$\begin{bmatrix} z(s) \\ z'(s) \end{bmatrix} = \begin{bmatrix} \cosh\sqrt{|K|}s & \frac{1}{\sqrt{|K|}}\sinh\sqrt{|K|}s \\ \sqrt{|K|}\sinh\sqrt{|K|}s & \cosh\sqrt{|K|}s \end{bmatrix} \begin{bmatrix} z_0 \\ z'_0 \end{bmatrix}. \tag{1.16}$$

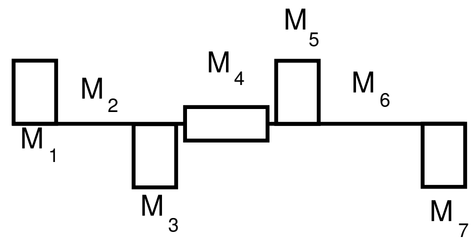

Figure 1.1: Example of a beam line with 7 elements.

Particle traveling through a beam line

With the transport of the particle through any beam line consisting of drift spaces, bending magnets or quadrupoles, it becomes rather straightforward to track the particle.

The transformation matrix for the whole beam line becomes the product of the individual matrices. For example for figure 1.1 the transformation matrix is expressed as:

$$M(s|s_0) = M_7 ... M_3 M_2 M_1. \tag{1.17}$$

The position and angle of the particle are then easily found by:

$$\begin{bmatrix} z(s) \\ z'(s) \end{bmatrix} = M(s|s_0) \begin{bmatrix} z_0 \\ z'_0 \end{bmatrix}. \tag{1.18}$$

In accelerator physics various nomenclature is used for defining a sequence of elements. A FODO cell is defined as a focusing quadrupole followed by drift space, defocussing quadrupole and a drift space. A FBDB cell, shown in figure 1.2 is the same as a FODO except that the drift space is replaced by a bending magnet.

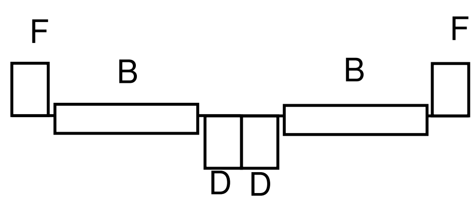

Figure 1.2: Graphical representation of a FBDB cell.

A triplet, shown in figure 1.3 is defined as three quadrupoles placed consecutively, where the quadrupole in the middle has the opposite polarity of the two on the outside.

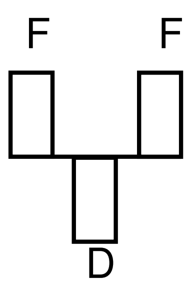

Figure 1.3: Graphical representation of a triplet cell.

1.2.1 Beam emittance

The area occupied by particles in phase-space is called the beam emittance ϵ, shown in figure 1.4. Until now only a single particle has been considered, but a real beam consists of many particles and it would be impractical to calculate the trajectory for every individual particle.

Each particle at any point along a beam line is represented by a point in six-dimensional phase space with coordinates $(x, p_x, y, p_y, \sigma, E)$ where $p_x \sim p_0 x'$ and $p_y \sim p_0 y'$ are the transverse momenta with $p_0 = \beta E_0$, σ is the coordinate along the trajectory, E_0 and E are respectively the ideal and real particle energies.

In the definition of the beam emittance it is assumed there is no coupling between the horizontal and vertical dimensions. However, the coupling can introduce emittance sharing between the two planes [3, 4, 5, 6].

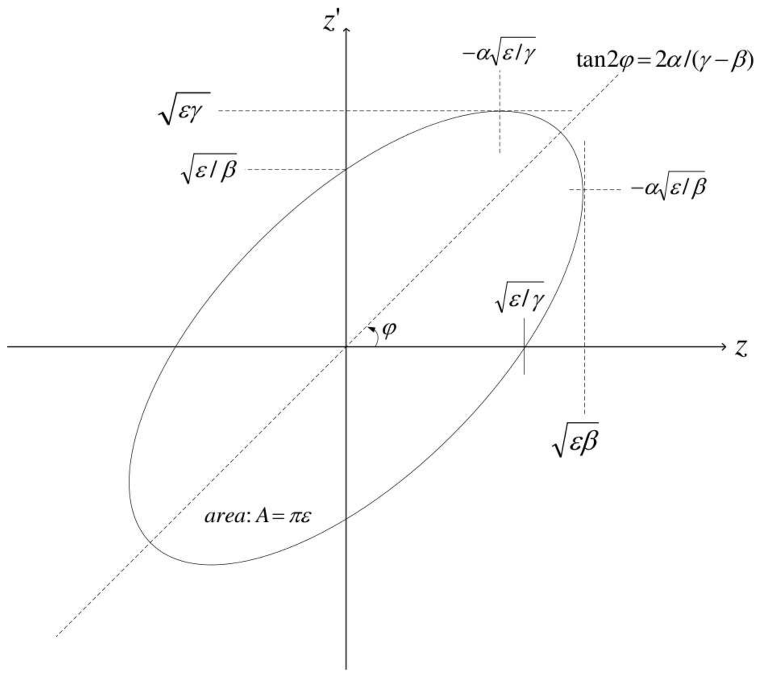

Figure 1.4: Phase space ellipse.

Liouville's theorem states that under the influence of conservative forces the particle density in the phase space stays constant. This theorem provides a powerful tool to describe a beam in phase space.

It is common to surround all particles of a beam in phase-space by an ellipse called the phase ellipse. The phase ellipse is described by:

$$\gamma z^2 + 2\alpha z z' + \beta z'^2 = \epsilon, \tag{1.19}$$

where α, β and γ are called the Courant-Snyder parameters [7]. β is the betatron amplitude function, α is defined as $-\frac{1}{2}\frac{\partial\beta}{\partial s}$ and $\gamma = \frac{1+\alpha^2}{\beta}$.

Every particle trajectory can be described by:

$$z(s) = a\sqrt{\beta}\cos\phi + b\sqrt{\beta}\sin\phi, \tag{1.20}$$

$$z'(s) = a\left(\frac{1}{2\sqrt{\beta}}\beta'\cos\phi - \frac{\sin\phi}{\sqrt{\beta}}\right) + b\left(\frac{1}{2\sqrt{\beta}}\beta'\sin\phi + \frac{\cos\phi}{\sqrt{\beta}}\right), \tag{1.21}$$

where ϕ is defined as the betatron phase. The amplitude factors a and b can be found by setting s=0:

$$\begin{aligned} \phi = 0, \quad \beta = \beta_0, \quad z(0) = z_0, \\ \alpha = \alpha_0, \quad z'(0) = z'_0, \end{aligned} \tag{1.22}$$

from these boundary conditions the amplitude factors become:

$$\begin{aligned} a &= \frac{1}{\sqrt{\beta_0}} z_0, \\ b &= \frac{\alpha_0}{\sqrt{\beta_0}} z_0 + \sqrt{\beta_0} z'_0. \end{aligned} \tag{1.23}$$

Inserting equations (1.23) into equation (1.20) the transfer matrix from s_0 to s_1 in any beam line becomes:

$$\begin{bmatrix} z(s_1) \\ z'(s_1) \end{bmatrix} = \begin{bmatrix} \sqrt{\frac{\beta_1}{\beta_0}}(\cos\phi + \alpha_0\sin\phi) & \sqrt{\beta_1\beta_0}\sin\phi \\ -\frac{1+\alpha_0\alpha_1}{\sqrt{\beta_1\beta_0}}\sin\phi + \frac{\alpha_0-\alpha_1}{\sqrt{\beta_1\beta_0}}\cos\phi & \frac{\beta_0}{\beta_1}(\cos\phi - \alpha_1\sin\phi) \end{bmatrix} \begin{bmatrix} z(s_0) \\ z'(s_0) \end{bmatrix}. \tag{1.24}$$

For illustration, the evolution of the Courant-Snyder parameters in a drift space is given by:

$$\beta(z) = \beta_0 - 2\alpha_0 z + \gamma_0 z^2, \tag{1.25}$$
$$\alpha(z) = \alpha_0 - \gamma_0 z, \tag{1.26}$$
$$\gamma(z) = \gamma_0. \tag{1.27}$$

The initial values are taken at the beginning of the drift space. The location of the betatron waist (z^*) is defined where $\alpha(s) = 0$, shown in figure 1.5. Equation (1.25) can be expressed as ($z_0 = 0$):

$$\beta(z - z^*) = \beta^* + \frac{(z - z^*)^2}{\beta^*}, \tag{1.28}$$

where $z^* = \alpha_0 \beta^*$ and β^* is the β-function at the waist. β_{IP} is defined as the value of the β-function at the interaction point.

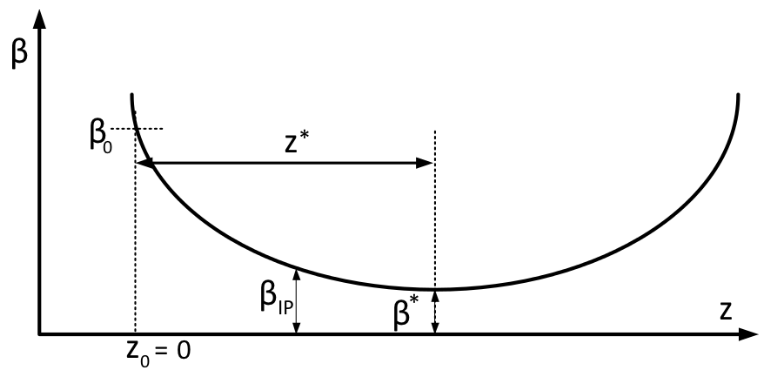

Figure 1.5: Graphical representation of the β-function in a drift space.

1.2.2 Periodic systems

In particle beam dynamics the equation of motion in periodic lattices (such as circular accelerators) is similar to Hill's equation:

$$z'' + K(s)z = 0, \tag{1.29}$$

where K(s) is periodic with the period L:

$$K(s) = K(s + L). \tag{1.30}$$

The solutions of Hill's equation have been formulated in Floquet's theorem [2]. The betatron phase advance for one full turn is:

$$\phi = \int_s^{s+L} \frac{ds}{\beta(s)}. \tag{1.31}$$

The number of betatron oscillations is called the tune (Q), which is the betatron phase advance divided by 2π:

$$Q = \frac{1}{2\pi} \int_s^{s+L} \frac{ds}{\beta(s)}. \tag{1.32}$$

1.3 Luminosity

The luminosity (assuming Gaussian beams) is defined as:

$$L = \frac{R}{4\pi} N_b \frac{N_1 N_2}{\sigma_x \sigma_y} \omega_{fr}, \tag{1.33}$$

where N_1 and N_2 are the intensities of beam 1 and beam 2, respectively. N_b is the number of bunches, R is the reduction factor (due to the crossing angle, bunch length, etc.), ω_{fr} is the revolution frequency and σ_x, σ_y are the beam sizes at the interaction point for the horizontal and vertical plane, respectively.

Introducing the β^* for the two beams separately and assuming equal emittances ($\epsilon_{x1} = \epsilon_{x2}$ and $\epsilon_{y1} = \epsilon_{y2}$), equation (1.33) can be written as:

$$L = \frac{R}{2\pi} N_b \frac{N_1 N_2}{\sqrt{(\beta^*_{x1} + \beta^*_{x2})(\beta^*_{y1} + \beta^*_{y2})\epsilon_x \epsilon_y}} \omega_{fr}, \tag{1.34}$$

where it is obvious that when the β^*'s deviate from the model the luminosity will be affected.

1.4 Perturbations

Perturbations can either be caused by transverse or longitudinal misalignments of magnets with respect to the ideal path or imperfections in the magnetic field. These errors in the magnetic field can be caused by higher order multipole fields. In this section perturbations due to a dipole and quadrupole field are discussed. Perturbations which are experienced by off-momentum particles such as dispersion and chromaticity are also discussed in detail.

1.4.1 Dipole field perturbations

The dipole perturbation terms cause a shift in the beam path or closed orbit without affecting the focusing properties of the beam line. A dipole field error at point s_k deflects the beam by an angle θ. $M(s_m|s_k)$ is the transformation matrix of the beam line between the point s_k , where the kick occurs, and the point s_m, where the beam position is observed. The displacement of the beam center line can be written as:

$$\Delta z = M_{12}\theta. \tag{1.35}$$

Due to the linearity of the equation of motion, the effect of many kicks caused by dipole errors can be calculated by the summation of individual beam center displacements at the observation point s_m for each kick. The orbit response arising from a dipole field error is given by the product of the Green function and the kick angle. The Green function (used to solve inhomogeneous differential equations) for Hill's equation is:

$$G(s, s_k) = \frac{\sqrt{\beta(s)\beta_k}}{2\sin(\pi Q)} \cos[\pi Q - |\phi_s - \phi_k|], \tag{1.36}$$

$$z(s) = \frac{\sqrt{\beta(s)}}{2\sin\pi Q} \sum_k \sqrt{\beta_k}\theta_k \cos[\pi Q - |\phi_s - \phi_k|], \tag{1.37}$$

the summation is over individual dipole error kicks k with deflection angle θ_k. From equation (1.37) it is obvious that when the tune is equal to an integer the orbit becomes infinity, i.e. it becomes unstable. This behavior is called the integer resonance.

1.4.2 Quadrupole field perturbations

Gradient field errors have a first-order effect on the β-function, betatron phase and tune. The transfer matrix of an infinitesimal localized perturbing quadrupole error (k) is [2]:

$$m(s_1) = \begin{bmatrix} 1 & 0 \\ -k(s_1)ds_1 & 1 \end{bmatrix}. \tag{1.38}$$

The perturbed one-turn transfer matrix $\mathbf{M}(s_1) = \mathbf{M}_0(s_1)m(s_1)$. The phase advance of the perturbed machine can be obtained from the trace of $\mathbf{M}$:

$$\begin{aligned} \Delta\phi &\approx \frac{1}{2}\beta(s_1)k(s_1)ds_1, \\ \Delta Q &\approx \frac{1}{4\pi}\beta(s_1)k(s_1)ds_1. \end{aligned} \tag{1.39}$$

For a distributed gradient error, the tune shift is:

$$\Delta Q = \frac{1}{4\pi} \oint \beta(s_1)k(s_1)ds_1. \tag{1.40}$$

The beta-beat is expressed as:

$$\frac{\Delta\beta(s)}{\beta(s)} = -\frac{1}{2\sin(2\pi Q)}\int_s^{s+C} k(s_1)\beta(s_1)\cos[2(Q_0\pi + |\phi - \phi_1)|]ds_1. \tag{1.41}$$

From equation (1.41) it is obvious that when the tune equals a half integer the beta-beat becomes infinity, i.e, the particle motion becomes unstable. This behavior is called the half integer-resonance.

1.4.3 Dispersion function

One of the most important perturbations is derived from the fact that the particle beams are not quite monochromatic but have a finite spread of energies around the nominal energy E. The variation in the deflection caused by such a chromatic error Δp in bending magnets is the lowest order of perturbation given by the term $\frac{\delta}{\rho_0}$, where $\delta = \frac{\Delta p}{p_0} << 1$. All quadratic and higher powers of δ are ignored. The Green function method is used to solve the equation including the perturbation:

$$z'' + K(s)z = k_{0z}(s)\delta. \tag{1.42}$$

The perturbation due to the dispersion is:

$$D(s) = \frac{\sqrt{\beta(s)}}{2\sin\pi Q}\sum_k \sqrt{\beta_k}\theta_k\cos[\pi Q - |\phi_s - \phi_k|]. \tag{1.43}$$

With the solution of equation (1.43) the 2x2 matrix can be expanded to a 3x3 matrix, which will now include the first order dispersion:

$$\begin{bmatrix} u(s) \\ u'(s) \\ \delta \end{bmatrix} = \begin{bmatrix} C_x(s) & S_x(s) & D_u(s) \\ C'_x(s) & S'_x(s) & D'_u(s) \\ 0 & 0 & 1 \end{bmatrix} \begin{bmatrix} u_0 \\ u'_0 \\ \delta \end{bmatrix}. \tag{1.44}$$

1.4.4 Chromatic effects

Bending as well as focusing is affected if the particle momentum deviates from the ideal momentum. The dependence of the focusing strength on the momentum is called chromatic perturbation. Higher energy particles are focused less than ideal energy particles and lower energy particles are overfocused. The variation of tunes with energy is called the chromaticity and is defined as:

$$Q' = \frac{\Delta Q}{\frac{\Delta p}{p_0}}. \tag{1.45}$$

The chromaticity is derived from second and higher order perturbations in (x, y, δ). The relevant equations of motion, including only the quadrupole and sextupole terms:

$$\begin{aligned} x'' + kx = & \quad kx\delta - \tfrac{1}{2}m(x^2 + y^2), \\ y'' - kx = & \quad -ky\delta + mxy, \end{aligned} \tag{1.46}$$

introducing $x = x_\beta + D_x\delta$, the horizontal position and $y = y_\beta$, the vertical position. m is the strength of the sextupole. It is assumed that there is no vertical dispersion ($D_y = 0$). Ignoring also the non-chromatic terms of second order:

$$\begin{aligned} x''_\beta + kx_\beta = & \quad (k - mD_x)x_\beta\delta, \\ y''_\beta - ky_\beta = & \quad -(k - mD_x)y_\beta\delta. \end{aligned} \tag{1.47}$$

The perturbation terms are linear in the betatron amplitude. These errors will result in a phase shift:

$$\begin{aligned} \Delta\phi_x = & \quad -\tfrac{1}{2}\delta\oint \beta_x(k - mD_x)ds, \\ \Delta\phi_y = & \quad \tfrac{1}{2}\delta\oint \beta_y(k - mD_x)ds. \end{aligned} \tag{1.48}$$

Using the definition of the chromaticity:

$$\begin{aligned} Q'_x = & \quad -\tfrac{1}{4\pi}\oint \beta_x(k - mD_x)ds, \\ Q'_y = & \quad \tfrac{1}{4\pi}\oint \beta_y(k - mD_x)ds. \end{aligned} \tag{1.49}$$

When the sextupole strengths are put to zero the natural chromaticities are achieved:

$$\begin{aligned} Q'_{x0} &= -\tfrac{1}{4\pi}\oint \beta_x k ds, \\ Q'_{y0} &= \tfrac{1}{4\pi}\oint \beta_y k ds. \end{aligned} \tag{1.50}$$

The natural chromaticities are always negative, which is to be expected since focusing is less effective for higher energy particles ($\delta > 0$).

1.4.5 Coupling

Random and systematic skew-quadrupole errors in the main dipole and quadrupole magnets and orbit errors in the arc sextupole magnets give rise to coupling between the transverse planes.

Matrix approach

Equation (1.24) shows the transfer matrix in a beam line, considering one-turn and for both planes the one-turn matrix can be written:

$$T = \begin{bmatrix} M_1 & 0 \\ 0 & M_2 \end{bmatrix} = \begin{bmatrix} (\cos\phi_1 + \alpha_1 \sin\phi_1) & \beta_1 \sin\phi_1 & 0 & 0 \\ -\gamma\sin\phi_1 + \cos\phi_1 & (cos\phi_1 - \alpha_1\sin\phi_1) & 0 & 0 \\ 0 & 0 & (\cos\phi_2 + \alpha_2\sin\phi_2) & \beta_2\sin\phi_2 \\ 0 & 0 & -\gamma\sin\phi_2 + \cos\phi_2 & (cos\phi_2 - \alpha_2\sin\phi_2) \end{bmatrix}. \tag{1.51}$$

When introducing coupling the one-turn map is rewritten to [8]:

$$T = \begin{bmatrix} M_1 & N_1 \\ N_2 & M_2 \end{bmatrix}, \tag{1.52}$$

if N_1 and N_2 equal 0 the x and y plane will be decoupled. For the case the motion is coupled a similarity matrix transformation can be found to relate to the normal modes form. This method is following Edwards and Teng [9], [10]. The normalized motion in the horizontal and vertical planes is written as:

$$\begin{bmatrix} \hat{x} \\ \hat{p_x} \\ \hat{y} \\ \hat{p_y} \end{bmatrix} = \begin{bmatrix} \gamma & 0 & \bar{C}_{11} & \bar{C}_{12} \\ 0 & \gamma & \bar{C}_{21} & \bar{C}_{22} \\ -\bar{C}_{22} & \bar{C}_{12} & \gamma & 0 \\ \bar{C}_{21} & -\bar{C}_{11} & 0 & \gamma \end{bmatrix} \begin{bmatrix} A_x\cos\phi_x \\ A_x\sin\phi_x \\ A_y\cos\phi_y \\ A_y\sin\phi_y \end{bmatrix}, \tag{1.53}$$

where C and γ are the coupling parameters. Note that this γ denotes neither the Twiss nor the relativistic parameter.

There is a second method to describe coupling which uses the approach of G. Ripken [11]. In this approach four β-modes are introduced ($\beta_{11}, \beta_{12}, \beta_{21}, \beta_{22}$). The mode β_{11} is the horizontal and β_{12} is the vertical mode in the horizontal plane. The same is valid for the vertical plane. This means that when the coupling is zero the modes β_{12} and β_{22} are zero. The two methods are related to each other as follows [12]:

$$\begin{aligned} \beta_x &= \frac{\beta_{11}}{1-u}, \alpha_x = \frac{\alpha_{11}}{1-u}, \\ \beta_y &= \frac{\beta_{21}}{1-u}, \alpha_y = \frac{\alpha_{21}}{1-u}, \end{aligned} \tag{1.54}$$

where $\sin\phi = \pm\sqrt{u}$ is the rotation of the x-y plane. When $\phi = 0$ there is no coupling and $\beta_x = \beta_{11}$ and $\beta_y = \beta_{21}$.

Tune split and coupling coefficient

Two observables which are often used during operations are the tune split and coupling coefficient [13]. The two eigentunes $Q_{1,2}$ under the influence of coupling are written as:

$$\begin{aligned} Q_1 &= Q_x - \frac{\Delta}{2} + \frac{1}{2}\sqrt{\Delta^2 + (C^-)^2}, \\ Q_2 &= Q_y + \frac{\Delta}{2} - \frac{1}{2}\sqrt{\Delta^2 + (C^-)^2}, \end{aligned} \tag{1.55}$$

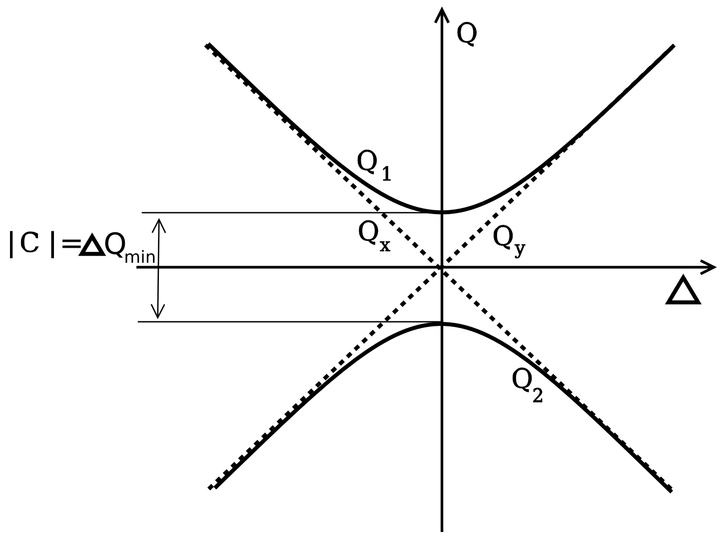

Figure 1.6: Illustration of the effect of coupling on tune measurements.

Q_x and Q_y are the free tunes without any coupling. Δ is the uncoupled fractional tune split ($\Delta = Q_x - Q_y - p$), where p is the integer tune split.

The coupling coefficients are approximately related to the skew quadrupoles in the ring as:

$$C^{\binom{+}{-}} = |C^{\binom{+}{-}}| e^{i\psi^{\binom{+}{-}}} = \sum_l k_l \sqrt{\beta_x^l \beta_y^l}\, e^{i(\Delta\phi_x^{sl} \pm \Delta\phi_y^{sl})}, \tag{1.56}$$

$|C^{\binom{+}{-}}|$ and $\psi^{\binom{+}{-}}$ are respectively the coupling coefficients amplitude and phases, k_l is the integrated strength of the skew quadrupole at location l. β_x^l and β_y^l are the beta functions at the location of the skew quadrupole. $\Delta\phi_x^{sl}$ and $\Delta\phi_y^{sl}$ are the phase advances between the skew quadrupoles and the observation point.

The tune split ΔQ is expressed by:

$$|\Delta Q| = |Q_1 - Q_2 - p| = \sqrt{\Delta^2 + |C^-|^2}. \tag{1.57}$$

1.5 Momentum compaction factor

The synchronization of particle motion in a synchrotron depends heavily on the total path length. The first order deviation of the total path length for an off-momentum particle from the reference path is given by:

$$\Delta C = \oint \frac{x}{\rho} ds = \left[\oint \frac{D(s)}{\rho} ds \right] \delta. \tag{1.58}$$

The momentum compaction factor is defined as the relative increase in closed-orbit length C for an off-momentum particle.

$$\alpha_c = \frac{1}{C}\frac{d\Delta C}{d\delta} = \frac{1}{C}\oint \frac{D(s)ds}{\rho} \approx \frac{1}{C}\sum_i \langle D \rangle_i \theta_i, \tag{1.59}$$

where $\langle D \rangle_i$ and θ_i are the average dispersion function and the bending angle of the i^{th} dipole.

The relative difference of the off-momentum and on-momentum revolution period is:

$$\frac{\Delta T}{T_0} = \frac{\Delta C}{C} - \frac{\Delta v}{v} = (\alpha_c - \frac{1}{\gamma^2})\frac{\Delta p}{p_0} = \eta\delta, \tag{1.60}$$

or equivalently, $\Delta f / f_0 = -\eta\delta$, where f is the revolution frequency and $T_0 = \frac{1}{f_0}$ is the revolution period of a synchronous particle.

The phase-slip factor η is:

$$\eta = \alpha_c - \frac{1}{\gamma^2} = \frac{1}{\gamma_t^2} - \frac{1}{\gamma^2}, \tag{1.61}$$

here $\gamma_t \equiv \sqrt{\frac{1}{\alpha_c}}$ is called the γ-transition or simply γ_t, and $\gamma_t mc^2$ is the transition energy. For FODO cell lattices, $\gamma_t \approx Q_x$. Below the transition, with $\gamma < \gamma_t$ and $\eta < 0$, a higher momentum particle will have a revolution period shorter than that of a synchronous particle. Above the transition energy, with $\gamma > \gamma_t$, the converse is true.

1.6 Non-linear beam dynamics

In this section the concept of the resonance driving terms will be introduced. The derivation of the resonance driving terms up to the first order is given in appendix C. The evolution of the linearly normalized horizontal variable is given by:

$$\begin{aligned} h_x^-(N) &= \sqrt{2I_x}e^{i(2\pi\upsilon_x N+\psi_{x,0})} \\ &\quad -2i\sum_{jklm} j f_{jklm}(2I_x)^{\frac{j+k-1}{2}}(2I_y)^{\frac{l+m}{2}}e^{i[(1-j+k)(2\pi\upsilon_x N+\phi_{x0})+(m-l)(2\pi\upsilon_y N+\phi_{y0})]}, \end{aligned} \tag{1.62}$$

and the vertical horizontal variable by:

$$\begin{aligned} h_y^-(N) &= \sqrt{2I_y}e^{i(2\pi\upsilon_y N+\psi_{y,0})} \\ &\quad -2i\sum_{jklm} l f_{jklm}(2I_x)^{\frac{j+k}{2}}(2I_y)^{\frac{l+m-1}{2}}e^{i[(k-j)(2\pi\upsilon_x N+\phi_{x0})+(1-l+m)(2\pi\upsilon_y N+\phi_{y0})]}, \end{aligned} \tag{1.63}$$

$\mathbf{h}$=$(h_x^+, h_x^-, h_y^+, h_y^-)$ is called the resonance base. N the number of turns. I and ϕ the action-angle variables and f_{jklm} is the resonance driving term. The terms $jklm$ are related to the potential $(x^u y^v)$, where $j+k=u$ and $l+m=v$.

The first term on the right hand side of equations (1.62) and (1.63) is the main betatron tune line. The position in the spectrum gives the fractional part of the tune. The second term gives the non-linear terms as well as the coupling and is related to the resonance driving terms f_{jklm}. The relation between the amplitude and phase of the measured higher order resonance line in the spectrum and the resonance driving term f_{jklm} is given by:

$$\begin{aligned} H(1-j+k, m-l) &= j\,|f_{jklm}|\,(2I_x)^{\frac{j+k-1}{2}}(2I_y)^{\frac{l+m}{2}}, \\ \phi_{jklm} &= \psi_{jklm} + (1-j+k)\psi^x_{jklm} + (m-l)\psi^y_{jklm} - \frac{\pi}{2}, \end{aligned} \tag{1.64}$$

$$\begin{aligned} V(k-j, 1-l+m) &= l\,|f_{jklm}|\,(2I_x)^{\frac{j+k}{2}}(2I_y)^{\frac{l+m-1}{2}}, \\ \phi_{jklm} &= \psi_{jklm} + (k-j)\psi^x_{jklm} + (1-l+m)\psi^y_{jklm} - \frac{\pi}{2}, \end{aligned} \tag{1.65}$$

$$(j-k)Q_x + (l-m)Q_y = p\,\epsilon\,N, \tag{1.66}$$

where the horizontal line in the spectrum is given by $H(1-j+k, m-l)$ and the vertical line $V(k-j, 1-l+m)$. In case of decoherence there is a reduction factor of the spectral line due to the amplitude detuning [14]. The decoherence factor corresponding to the horizontal spectral line (m, n) is:

$$\left| m + n\frac{\upsilon'_{yx}}{\upsilon'_{xx}} \right|, \tag{1.67}$$

where m and n are the indexes for the resonance $mQ_x + nQ_y = p$.

Tables 1.1 to 1.4 give an overview of the resonance driving terms for the different potential terms. With $a_{jklm}e^{i\phi^a_{jklm}}$ being the amplitude and phase of the spectral line.

An example of the spectrum of one of the BPMs in the LHC is shown in figure 1.7. The main betatron and secondary lines up to the normal sextupole are labeled.

Normal quadrupole (potential term x^2, y^2)						
n	jklm	resonance	horizontal line	vertical line	$\|a_{jklm}\|$	ϕ^a_{jklm}
2	1100	(2,0)	(1,0)		$\sqrt{2I_x}$	$\psi_{x,0}$
2	0011	(0,2)		(0,1)	$\sqrt{2I_y}$	$\psi_{y,0}$

Table 1.1: Resonance driving term and the spectrum for the normal quadrupole.

Skew quadrupole (potential term xy)						
n	jklm	resonance	horizontal line	vertical line	$\|a_{jklm}\|$	ϕ^a_{jklm}
2	0110	(1,-1)		(1,0)	$2\|f_{0110}\|\sqrt{2I_x}$	$\phi_{0110}+\psi_{x,0}-\frac{\pi}{2}$
2	1001	(0,2)	(0,1)		$2\|f_{1001}\|\sqrt{2I_y}$	$\phi_{1001}+\psi_{y,0}-\frac{\pi}{2}$
2	1010	(0,2)	(0,-1)	(-1,0)	H:$2\|f_{1010}\|\sqrt{2I_y}$ V:$2\|f_{1010}\|\sqrt{2I_x}$	$\phi_{1010}-\psi_{y,0}-\frac{\pi}{2}$ $\phi_{1010}-\psi_{x,0}-\frac{\pi}{2}$

Table 1.2: Resonance driving term and the spectrum for the skew quadrupole.

Normal sextupole (potential term x^3)						
n	jklm	resonance	horizontal line	vertical line	$\|a_{jklm}\|$	ϕ^a_{jklm}
3	1200	(1,0)	(2,0)		$2\|f_{1200}\|2I_x$	$\phi_{1200}+2\psi_{x,0}-\frac{\pi}{2}$
3	2100	(1,0)	(0,0)		$4\|f_{2100}\|2I_x$	$\phi_{2100}-\frac{\pi}{2}$
3	3000	(3,0)	(-2,0)		$6\|f_{3000}\|2I_x$	$\phi_{3000}-2\psi_{x,0}-\frac{\pi}{2}$

Table 1.3: Resonance driving term and the spectrum for the normal sextupole term 1.

Normal sextupole (potential term xy^2)						
n	jklm	resonance	horizontal line	vertical line	$\|a_{jklm}\|$	ϕ^a_{jklm}
3	0111	(1,0)		(1,1)	$2\|f_{0111}\|\sqrt{2I_x}$	$\phi_{0111}+\psi_{x,0}+\psi_{y,0}-\frac{\pi}{2}$
3	0120	(1,-2)		(1,-1)	$2\|f_{0120}\|\sqrt{2I_y}$	$\phi_{0120}+\psi_{x,0}-\psi_{y,0}-\frac{\pi}{2}$
3	1002	(1,-2)	(0,2)		$2\|f_{1002}\|\sqrt{2I_y}$	$\phi_{1002}+2\psi_{y,0}-\frac{\pi}{2}$
2	1011	(0,0)	(-1,1)	(-1,0)	H:$2\|f_{1011}\|\sqrt{2I_y}$ V:$2\|f_{1011}\|\sqrt{2I_x 2I_y}$	$\phi_{1011}-\frac{\pi}{2}$ $\phi_{1011}-\psi_{x,0}+\psi_{y,0}-\frac{\pi}{2}$
2	1020	(0,-2)	(-1,-1)	(-1,0)	H:$2\|f_{1020}\|\sqrt{2I_y}$ V:$4\|f_{1020}\|\sqrt{2I_x 2I_y}$	$\phi_{1020}-2\psi_{y,0}-\frac{\pi}{2}$ $\phi_{1020}-\psi_{x,0}-\psi_{y,0}-\frac{\pi}{2}$

Table 1.4: Resonance driving term and the spectrum for the normal sextupole term 2.

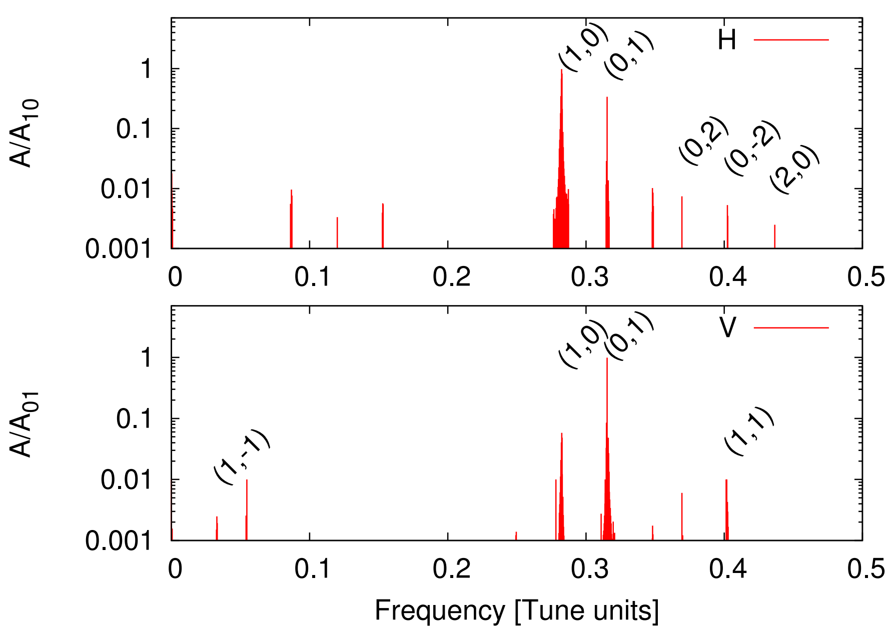

Figure 1.7: The normalized spectrum for BPM8L1B2 for the horizontal plane (top) and vertical plane (bottom). The main betatron and secondary lines up to the normal sextupole are labeled.

1.6.1 Coupling terms

A general introduction to the resonance driving terms has been given. A complete description of the implementation for the coupling can be found in [15]. The coupling generated by skew quadrupole sources is:

$$f_{\binom{1001}{1010}}(s) = -\frac{1}{4(1 - e^{2\pi i(Q_x \mp Q_y)})} \sum_l k_l \sqrt{\beta_x^l \beta_y^l} e^{i(\Delta\phi_x^{sl} \mp \Delta\phi_y^{sl})}, \tag{1.68}$$

where k_l is the strength of the skew quadrupole at location l. β_x^l and β_y^l are the beta functions at the location of the skew quadrupole. $\Delta\phi_x^{sl}$ and $\Delta\phi_y^{sl}$ are the phase advances between the skew quadrupoles and the observation point.

Relating resonance driving term and coupling

In section 1.4.5 the coupling was introduced. In equation (1.53) the matrix solution was shown for coupling using a "symplectic rotation". In this section the relation between the coupling resonance driving term and the $|C|$ is given. For a more detailed explanation see [10].

$$\begin{aligned} \left|\bar{C}\right| &= 1 - \frac{1}{1+4(|f_{1001}|^2 - |f_{1010}|^2)}, \\ \gamma^2 &= \frac{1}{1+4(|f_{1001}|^2 - |f_{1010}|^2)}. \end{aligned} \tag{1.69}$$

For the closest tune approach, the relation to the resonance driving terms is:

$$\Delta Q_{min} = \frac{2\gamma(\cos 2\pi Q_x - \cos 2\pi Q_y)}{\pi(\sin 2\pi Q_x + \sin 2\pi Q_y}, \tag{1.70}$$

$$\times \left(\frac{4\sqrt{|f_{1001}|^2 - |f_{1010}|^2}}{1+4|f_{1001}|^2 - |f_{1010}|^2} \right). \tag{1.71}$$

Chapter 2

Optics measurement techniques

In this chapter the different algorithms, techniques and instrumentations used for the optics measurements and corrections are discussed. Section 2.1 introduces the most important beam instrumentation used during the conducted measurements. Several measurement techniques which are used in the LHC are described and discussed. Section 2.2 discusses and compares the free, driven oscillations and K-modulation techniques. Section 2.3 discusses the data analysis tools and compares their results. Section 2.4 discusses how the optics functions are measured. Section 2.5 discusses the different correction methods. Finally, a brief discussion of other methods used to measure and/or correct the linear optics is presented in section 2.6.

2.1 Beam instrumentation

It would be impossible to conduct the measurements without proper beam instrumentation. In this section the most important beam instrumentation for the measurement is introduced.

Beam Position Monitor

The Beam Position Monitors (BPMs) are the eyes of any accelerator. They are usually composed of two or four conductor plates. When the BPM is composed of 2 plates, it is called a single plane BPM. When it is composed of four plates it is called double plane BPM. With single plane BPM the position of the beam can only be measured in one direction. The beam position is obtained by measuring the voltage on the plates.

The voltage is proportional to the rate of variation of the magnetic flux associated with the beam current. In general, the beam position is:

$$z \sim \frac{w}{2}\frac{U_+ - U_-}{U_+ + U_-} = \frac{w}{2}\frac{\Delta}{\epsilon}, \tag{2.1}$$

where U_+ and U_- are either the current or the voltage signals from the right or up and left or down plates. $\Delta = U_+ - U_-$ is called the difference signal, $\epsilon = U_+ + U_-$ is called the sum signal and $\frac{w}{2}$ is the effective width of the beam position monitors. Equation (2.1) may require nonlinear calibration. This is especially important for light sources, where the responses have a cubic response, due to the shape of the beam pipe. This means that the measured signal is equal to:

$$z_{obs} = Az_{real} + Bz_{real}^3, \tag{2.2}$$

z is the position either in the horizontal or in the vertical plane, A and B are constants. Measurements of the normalized difference signal with proper calibration provide information about the beam transverse coordinates.

For the optics measurements the BPMs are vital instruments.

Beam Loss Monitors

The loss of only a fraction (10^{-8}) of the beam can have a severe impact on the operation. For the LHC, over 3000 ionization chambers, called Beam Loss Monitors (BLMs) [16], are installed to abort the beam if the loss rates exceed the quench levels.

For the optics measurements, the BLMs were used in the LHC as an observational tool to determine how large a kick could be applied.

Measuring the beam current

The beam current is one of the basic quantities of the beam. The measurements of the beam current are mostly done by the beam current transformers (BCT). The principle is based on the effect of the beam electro-magnetic fields, in a transformer where the number of windings for the beam is 1.

The BCT is used together with the BLMs for the measurements to see if any losses appear when exciting betatron oscillations.

Synchrotron light monitor

The synchrotron light telescopes [17] measure the profiles of the beam particles (electrons, protons and ions). For the LHC it was also used to verify that the abort gap is clear. For the LHC, at collision energy each telescope will image visible light from a superconducting dipole used to widen beam separation at the RF cavities. This source must be supplemented by a 2-period superconducting undulator 1 m from the dipole.

The two LHC synchrotron-light telescopes will measure the transverse beam profiles. The abort-gap monitor will verify that the 3-μs gap contains an acceptably small number of particles, since a partial kick during the rise of the abort kicker may drive them into a magnet and cause a quench.

For the optics measurements the synchrotron light monitors are used to keep track of the beam profile and beam size. It is used to see if the kicks increase the emittance.

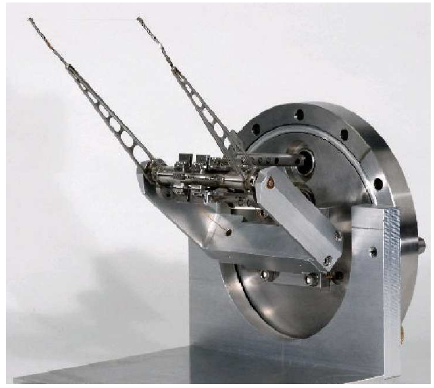

Figure 2.1: Example of a wirescanner.

Wire scanners

The wire scanners, an example as shown in figure 2.1, are used to measure the beam emittance, through an indirect measurement.

The wire scanners pass an electrical wire through the beam and measure the current induced by the beam. The beam profile (σ) is deduced from a fit of the measured current in the wire. The emittance is calculated by (assuming $D_{x,y} = 0$):

$$\epsilon = \frac{\sigma^2}{\beta}, \tag{2.3}$$

the β is taken either from the model or from the propagated value using the segment-by-segment technique. During operations it is common to describe emittance independent of the beam energy, called the normalized emittance [2] (ϵ_N)

$$\epsilon_N = \beta\gamma\epsilon, \tag{2.4}$$

where β and γ are the relativistic parameters, defined in equation (1.6).

For the optics measurements it is important to know the beam emittance. When the beam emittance is too large, the betatron oscillations could cause losses, limiting their amplitude.

Collimators

Collimators are protection devices installed in the LHC and other accelerators around the world. They protect the accelerator against beam losses. For the LHC two insertions (IR3 and IR7) are dedicated to collimation and are equipped with about 54 movable, two-sided collimators.

The collimators play a vital role in the protection of the LHC. For the optics measurements, a too tight collimator settings decreases the kick amplitude, and therefore the measurement resolution. For this reason during most measurements the collimators are put in their parking positions (open) since the beam intensity is safe.

Tune measurements

Several methods can be applied for measuring the tune. This can be done by applying a kick and looking at the transverse spectrum. The second system which is used is the base band tune (BBQ) [18], [19] which allows to continuously measure the tune by measuring the residual beam oscillations.

The tune measurements are used during the optics measurements to identify the main betatron tunes. These tunes are used as input for the analysis of SUSSIX and the multiturn application.

2.2 Measurement instruments

Different instruments are available to introduce transverse oscillations. An alternative method, called K-modulation, used to measure β^* will be introduced.

2.2.1 Q-kicker/Aperture kicker

The tune and aperture kicker is used to introduce transverse oscillations. The only difference between the tune and aperture is the strength of the magnet. The name tune kicker comes from the fact that when operating with the kicker's low strength, the data could be used to measure the tune. When operating with higher strength, the kicker is used to measure the available dynamic aperture. This kicker has to be strong enough to kick the beam until losses are observed, which indicate the aperture. The tune and aperture kicker have three disadvantages. One is the available strength at higher energies. For instance for the LHC, which has an energy between 450 GeV of 7 TeV. When the energy is above injection, 450 GeV the tune/aperture kicker strength is not sufficient anymore to introduce transverse oscillations.

The second disadvantage of using the tune/aperture kicker is decoherence. If the particles all have the same betatron tune, the observed centroid motion is harmonic. However, if the beam contains a spread of tunes, the motion will decohere as the individual betatron phases of the particles disperse. The phase space distribution of the beam spreads from a localized bunch to an annulus which occupies all betatron phases, and the observed centroid of the beam will show a decaying oscillation. The two main sources for decoherence are [20]:

- The transverse nonlinearity due to magnetic field aberrations.
- The energy spread of the beam which is coupled to betatron tune through the chromaticity.

The envelope of the turn-by-turn motion $a_z(N)$ is calculated to study the effect of the decoherence on the transverse oscillations. Where z is either the horizontal or vertical plane.

$$a_z(N) = ZA(N), \tag{2.5}$$

where $A(N)$ and Z are defined respectively as the decoherence factor and kick amplitude:

$$Z = \beta\Delta z'/\sigma_z, \tag{2.6}$$

β being the β-function, $\Delta z'$ is the kick angle and σ_z the beam size.

The decoherence factor caused by the chromaticity is given by:

$$\begin{aligned} \alpha &= 2\sigma_s Q' Q_s^{-1} \sin(\pi Q_s N), \\ A(N) &= e^{-\alpha^2/2}, \end{aligned} \tag{2.7}$$

where σ_s is the rms relative energy spread, Q_s is the synchrotron tune and Q' the chromaticity.

The decoherence due to transverse nonlinearity follows a Gaussian pattern when $Z \gg 1$, and then changes to a $1/N^2$ power law when $Z \ll 1$. The decoherence factor becomes:

$$\begin{aligned} A(N) &\approx e^{-(Q_g N)^2/2} \quad (Z \gg 1), \\ A(N) &\approx \frac{1}{1+(\frac{Q_g}{Z}N)^2} \quad (Z \ll 1), \end{aligned} \tag{2.8}$$

where Q_g is called the characteristic tune and is defined as $4\pi\frac{\partial Q_z}{\partial \epsilon_z}$, where $\frac{\partial Q_z}{\partial \epsilon_z}$ is the derivative of the tune with the emittance.

From equations (2.7) and (2.8) it is obvious that is rather easy to distinguish the two effects. The decoherence due to chromaticity haves an oscillating behavior through the kick, indicating high chromaticity. The decoherence due to amplitude detuning will damp the oscillation. Correcting these effects is important as the measurement resolution depends on the number of turns that can be analyzed.

2.2.2 AC-dipole

The disadvantages from the decoherence are overcome with the AC-dipole [21]. The effect of the AC-dipole has been studied in great detail. The amplitude of the driven coherent oscillation at location (assuming a linear machine) is written as [22, 23, 24, 25]:

$$z_m(s) = \frac{B_a L}{4\pi(B\rho)\Delta Q}\sqrt{\beta(s)\beta_a}, \tag{2.9}$$

where B_aL is the integrated AC-dipole field strength, $B\rho$ is the magnetic rigidity, $\beta(s)$ and β_a are the β-function at location s and the ac-dipole, respectively. ΔQ is the difference between the driven and free tune ($\Delta Q = Q_{free} - Q_{driven}$). In equation (2.9) it is shown that when the driving tune is equal to the free tune the oscillation diverges (resonance occurs when $Q_{driven} = Q_{free}$). The driven oscillations differ to the free oscillations proportionally to the ΔQ. This affects the reconstructed optics parameters. There are two approaches to calculate the optics parameters from the driven oscillations.

- By introducing a quadrupole error at the location of the AC-dipole in the model which represents the driven oscillation [26].
- By the use of equations in [27], [28] and [29].

Both approaches have been used in this thesis giving equal results.

Figure 2.2 shows the effect of changing the $\Delta Q = Q_{driven} - Q_{free}$ on the β-beat. When ΔQ becomes larger, i.e driving the AC-dipole tune further away from the free tune, the effect on the β-beat becomes larger.

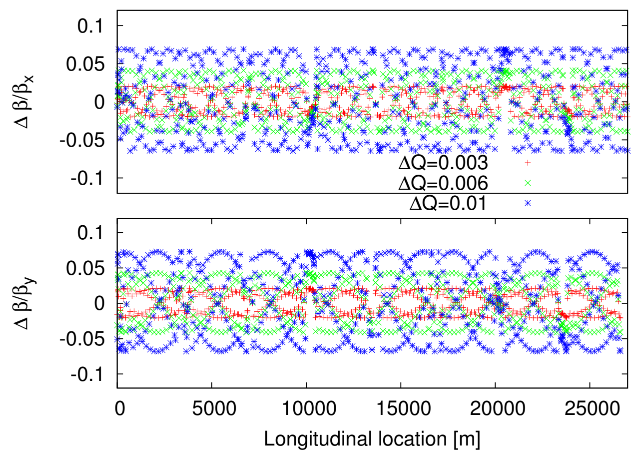

Figure 2.2: Effect of the AC-dipole on the β-beat is shown for different $\Delta = Q_{driven} - Q_{free}$.

2.2.3 K-modulation

K-modulation is the only technique that does not require special beam instrumentation, except the tune measurement. The only requirement is that the quadrupoles are independently powered at the location where the β has to be measured. The idea of the K-modulation is that a small trim is introduced in one of the quadrupoles. This trim has an effect on the tune which can then be measured, in the LHC this is done with a BBQ system, and from there the β at that location can be deduced.

For a distributed gradient error, the tune shift is:

$$\Delta Q = \frac{1}{4\pi} \oint \beta(s_1)k(s_1)ds_1. \tag{2.10}$$

In the case of a single quadrupole error equation 2.10 can be simplified to:

$$\Delta Q = \frac{1}{4\pi}\bar{\beta}\Delta kL. \tag{2.11}$$

After re-arranging equation 2.11 the average β function at that quadrupole is given by:

$$\bar{\beta} = \frac{4\pi\Delta Q}{\Delta kL}. \tag{2.12}$$

The two parameters that determine the accuracy of the measurement are the trim in the quadrupole and the tune uncertainty. These two parameters determine the accuracy of the measurement in the following ways:

- The accuracy of the trim depends on how the trim (Δk) is transfered to the current level.

- The largest uncertainty comes from the measurement of the tune in the BBQ system.

A third effect which could affect the accuracy of the measurement is the coupling, if the coupling is too large the tune shift will not be measured correctly when tunes are brought closer.

Figure 2.3 shows one of the measurements done for the β^* of the LHC. The quadrupoles that were trimmed are the inner triplet magnets (explained in chapter 4), which has as a consequence that both beams were affected.

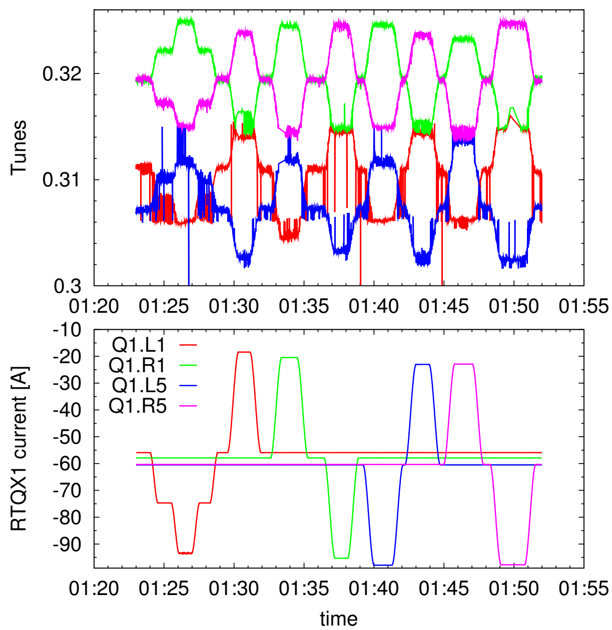

Figure 2.3: Example of a K-modulation that was carried out for the measurement of the β^* at the LHC. The top plot shows the measured tunes and bottom the trims applied in the inner triplet magnets for IR1 and IR5.

2.2.4 Comparison between the different methods

Table2.1 shows an overview of the different measurement techniques

Method	Invasive	Advantages	Disadvantages
Tune/Aperture kicker	Yes	-Easy to operate -No cancellation needed	-Not strong enough at higher energies -Emittance growth -Decoherence
AC-dipole	Yes/No	-AC-dipole can be used for higher energies. -No decoherence.	-Driven oscillation -Potentially dangerous
K-modulation	No	- Could be done with higher intensity	-Slow

Table 2.1: Comparison between the different measurement techniques.

2.3 Analysis techniques

Two analysis techniques are used to calculate the phase and amplitude of the main betatron tune line. Each technique has advantages and disadvantages. These two techniques are introduced below. A detailed comparison between the two methods is presented.

2.3.1 Interpolated FT

An interpolated Fourier Transform (FT) such as a modified version of SUSSIX [30] is used to identify the amplitude and phases of each main betatron tune line and higher resonance lines. A Fourier analysis uses a time series x(1), x(2),...,x(N) of N orbit measurements for consecutive turns as input. This time series is expanded as a linear combination of N functions:

$$x(n) = \sum_{j=1}^{N} \phi(Q_j) e^{2\pi i Q_j n}. \tag{2.13}$$

The expansion can be done efficiently with a FFT algorithm. The frequency corresponding to the largest value of ϕ is taken as the approximate tune. The error due to the discrete frequency steps is equal to:

$$|\Delta Q| \leq \frac{1}{2N}. \tag{2.14}$$

So, for example if the needed resolution is 0.001, about 500 turns would be needed.

The interpolated FT is an improvement to the normal FFT. Interpolating the shape of the Fourier spectrum around the main peak significantly improves the resolution. Thereby the same resolution can be achieved by processing data for a much smaller number of turns.

The basic idea of an interpolated FT is that the shape of the Fourier spectrum is known, and equal to that of a pure sinusoidal oscillation with tune Q_{Fint}

$$|\phi(Q_j)| = |\frac{\sin N\pi(Q_{Fint} - Q_j)}{N \sin \pi(Q_{Fint} - Q_j)}|. \tag{2.15}$$

So the formula for the interpolated tune Q_{Fint} reads:

$$Q_{Fint} = \frac{k}{N} + \frac{1}{\pi} \arctan\left(\frac{|\phi(Q_{k+1})| \sin(\frac{\pi}{N})}{N \sin \pi(Q_{fint} - Q_j)}\right), \tag{2.16}$$

where $|\phi(Q_k)|$ is the peak of the Fourier spectrum, and $|\phi(Q_{k+1})|$ its highest neighbor. So, instead of using only the peak value of the FFT, one interpolates between the two highest points. For large N the error is given by:

$$|\Delta Q| \leq \frac{C_{Fint}}{N^2}. \tag{2.17}$$

So, for example if a resolution is needed of 0.001, about 31 turns are enough (noise not taken into account). Where C_{Fint} is a numerical constant. The resolution improves quadratically with the number of turns. For N $\gg$ 1, equation 2.16 may be approximated by a simpler form:

$$Q_{Fint} \approx \frac{k}{N} + \frac{1}{\pi} \arctan\left(\frac{|\phi(Q_{k+1})|}{|\phi(Q_k)| + |\phi(Q_{k+1})|}\right). \tag{2.18}$$

The interpolated FFT is used in SUSSIX. A modified version of SUSSIX developed in [14] was used intensively during the measurements. The output of the code is post-processed to identify the main betatron and higher order tune lines.

Figure 2.4 shows the error of phase, β and the horizontal and vertical tune with respect to the number of turns. From the figure it is obvious that the improvement is achieved by analyzing more turns, especially for numbers of turns below 1000. For this reason data is always acquired for the maximum number of turns possible during measurements.

2.3.2 Singular Value Decomposition

Singular Value Decomposition (SVD) is widely used in signal processing and statistics. It is used here for three applications. The first one is to filter bad BPMs [32], the second one is to identify the main components of the BPM signals [33]. The third one is to invert the response matrix for correction. Similar application were SVD is used is called Model Independent Analysis (MIA) [34].

A SVD is defined mathematically for a $m \times n$ matrix as:

$$M = U\Sigma V^*, \tag{2.19}$$

in this definition U is an $m \times n$ matrix. Σ is an $n \times n$ diagonal matrix containing non-negative real numbers, which are the singular values. V^* is $n \times n$ matrix, defined as the conjugate transposed of V.

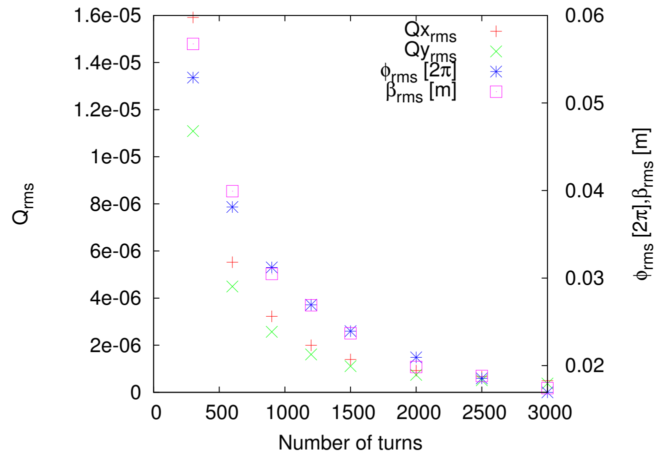

Figure 2.4: rms error for β, phase and the horizontal and vertical tunes with respect to the number of turns.

SVD for the measurement of the linear optics

The data from m BPMs recording T turns can be represented in a matrix form [33], where "+" and "-" represent the orthogonal vectors representing a betatron mode (cos, sin). $\Sigma_{m\times m} = [\sigma^+, \sigma^-, ...], V_{m\times m} = [\upsilon^+, \upsilon^-, ...]$ and $U_{t\times m} = [u^+, u^-, ...]$, are the corresponding non-negative singular values, the eigenvectors representing the spatial variation of betatron function, and the temporal eigenvectors representing the time evolution of the betatron mode respectively.

The Turn-by-Turn data in the m^{th} BPM can be expressed as:

$$b_t^m = \sqrt{2J_t\beta_m}\cos(\phi_t + \phi_m). \tag{2.20}$$

The BPM matrix is normalized by the number of turns $B = \frac{b_t^m}{T}$, the covariance matrix is given by:

$$C_B^{mn} = \frac{1}{T}\sum_{t=1}^{T} b_t^m b_t^n, \tag{2.21}$$

$$\sum_{t=1}^{T}\frac{1}{T}\sqrt{\beta_m\beta_n}[\cos(\psi_m - \psi_n) + \cos(2\phi_t + \psi_m + \psi_n)], \tag{2.22}$$

$$< J > \sqrt{\beta_m\beta_n}\cos(\psi_m - \psi_n). \tag{2.23}$$

The eigenvalues and eigenvectors can be found by solving:

$$C_B\upsilon = \lambda\upsilon. \tag{2.24}$$

Where $\upsilon = \sqrt{2J\beta_m}\cos(\phi_0 + \psi_m)$. From the m^{th} component of the secular equation the condition is that:

$$\sum_{n=1}^{M}\beta_n\sin(\phi_0 + \psi_n) = 0. \tag{2.25}$$

With two solutions:

$$\phi_0 = -\frac{1}{2}\tan^{-1}\left(\frac{\sum_n \beta_n \sin 2\psi_n}{\sum_n \beta_n \sin 2\psi_n}\right), \tag{2.26}$$

and $\phi_0 + \frac{\pi}{2}$, corresponding to the two eigenvalues

$$\lambda_\pm = \frac{1}{2} < J > \left[\sum_{n=1}^{M}\beta_n \pm \sum_{n=1}^{M}\beta_n\cos 2(\phi_0 + \psi_n)\right]. \tag{2.27}$$

The normal spatial eigenvectors are given by:

$$\upsilon_+ = \frac{1}{\lambda_+}\left[\sqrt{<J>\beta_m}\cos(\phi_0+\psi_m)\right], \quad (2.28)$$
$$\upsilon_- = \frac{1}{\lambda_-}\left[\sqrt{<J>\beta_m}\cos(\phi_0+\psi_m)\right], \quad (2.29)$$
$$(2.30)$$

and the corresponding normalized temporal vectors are given by:

$$u_+ = \sqrt{\frac{2J_t}{T<J>}}\cos(\phi_t-\phi_0), \quad (2.31)$$
$$u_- = -\sqrt{\frac{2J_t}{T<J>}}\sin(\phi_t-\phi_0). \quad (2.32)$$
$$(2.33)$$

The ψ and β can be derived from the betatron vectors:

$$\psi = \tan^{-1}\left(\frac{\sigma_-\upsilon_-}{\sigma_+\upsilon_+}\right), \quad (2.34)$$
$$\beta = <J>^{-1}(\sigma_+^2\upsilon_+^2+\sigma_-^2\upsilon_-^2). \quad (2.35)$$

2.4 Optics calculation

In this section the main functions for the calculation of the different optics functions will be discussed.

2.4.1 β from phase and amplitude

Two methods are used to calculate the β-function. The first method calculates the β through the phase advance, using the three BPM method [35]. The second method uses the amplitude of the main betatron oscillation.

The β from phase

The β function using the three BPM method uses the phase advance between three consecutive BPMs. Figure 2.5 shows a graphical representation for the phases of the 3-BPM method.

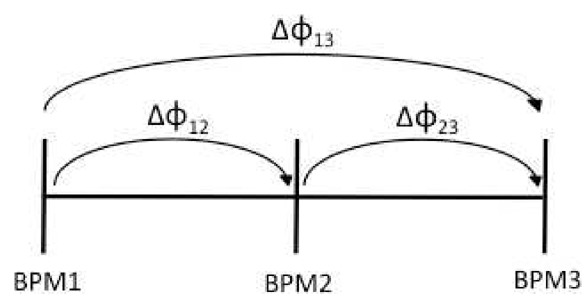

Figure 2.5: Graphical illustration of phases for the 3 BPM method

β_1, β_2 and β_3 can then be calculated as:

$$\beta_1 = \frac{\cot\phi_{12}-\cot\phi_{13}}{\frac{m_{11}}{m_{12}}-\frac{o_{11}}{o_{12}}}, \quad (2.36)$$
$$\beta_2 = \frac{\cot\phi_{12}+\cot\phi_{23}}{\frac{m_{22}}{m_{12}}+\frac{n_{11}}{n_{12}}}, \quad (2.37)$$
$$\beta_3 = \frac{\cot\phi_{23}-\cot\phi_{13}}{\frac{n_{22}}{n_{12}}-\frac{o_{22}}{o_{12}}}, \quad (2.38)$$

where m_{ij} is the matrix element from the transfer matrix (see equation 1.24) between BPM 1 and 2, n_{ij} between BPM 2 and 3 and finally o_{ij} between BPM 1 and 3. The matrix elements are taken from the model. ϕ_{ij} is the phase advance between BPM j and BPM i. The error on the β comes from the error on the phase and the phase advance between the two BPMs. The error becomes as follows:

$$\delta\beta_1 = \frac{\sqrt{(\csc^2(\phi_{12})\delta\phi_{12})^2 + (\csc^2(\phi_{13})\delta\phi_{13})^2}}{\left|\frac{m_{11}}{m_{12}} - \frac{o_{11}}{o_{12}}\right|}, \tag{2.39}$$

$$\delta\beta_2 = \frac{\sqrt{(\csc^2(\phi_{12})\delta\phi_{12})^2 + (\csc^2(\phi_{23})\delta\phi_{23})^2}}{\left|\frac{m_{22}}{m_{12}} + \frac{n_{11}}{n_{12}}\right|}, \tag{2.40}$$

$$\delta\beta_3 = \frac{\sqrt{(\csc^2(\phi_{23})\delta\phi_{23}))^2 + (\csc^2(\phi_{13})\delta\phi_{13})^2}}{\left|\frac{n_{22}}{n_{12}} - \frac{o_{22}}{o_{12}}\right|}. \tag{2.41}$$

With $\delta\phi_{ij}$ is the error on the phase advance between BPM j and BPM i. When the phase advance between the BPMs is close to 0, 90° or 180° the error on the β-function is diverging. In case of 90°, $\delta\beta_2$ is diverging because of the matrix elements in the denominator.

The β from amplitude

The orbit due to the betatron oscillation can be written as:

$$x_\beta(s) = \sqrt{2J\beta(s)}\cos(\phi(s) + \phi_0). \tag{2.42}$$

Where 2J is related to ϵ and is called the action. The amplitude of the main betatron signal is:

$$A(s) = \sqrt{2J\beta(s)}. \tag{2.43}$$

The beta from amplitude is easily calculated from the amplitude (A(s)) and the action (J):

$$\beta(s) = \frac{A(s)^2}{2J}. \tag{2.44}$$

The action is calculated using the β from the model and averaging it all around the ring:

$$2J = \left\langle \frac{A(s)^2}{\beta(s)_m} \right\rangle. \tag{2.45}$$

Comparison between the two methods Both methods use the model to calculate the β value at the BPM. In case of large β-beat the two methods start deviating. In [36] and [37] the effect on the β when the tunes were changed to the half integer resonance was investigated. A small quadrupolar error near the half integer resonance has a large effect on the β-beat. During the simulations it was discovered that the β from amplitude was less exact than the β from phase. An algorithm was developed to compensate for this effect [36].

2.4.2 Dispersion measurements

The dispersion is measured by taking the average orbit of the turn-by-turn data. The change in the orbit is caused by changing the radial steering, resulting in a change of the reference orbit:

$$z_D = D_z\frac{\Delta p}{p} \tag{2.46}$$

The horizontal and vertical dispersions are calculated as follows:

$$D_z = \frac{\Delta z_D}{\frac{\Delta p}{p}} \tag{2.47}$$

Where Δz_D is the orbit shift for an RF frequency trim (δ). Figure 2.6 shows an example of one of the horizontal BPMs for the LHC after applying a frequency trim.

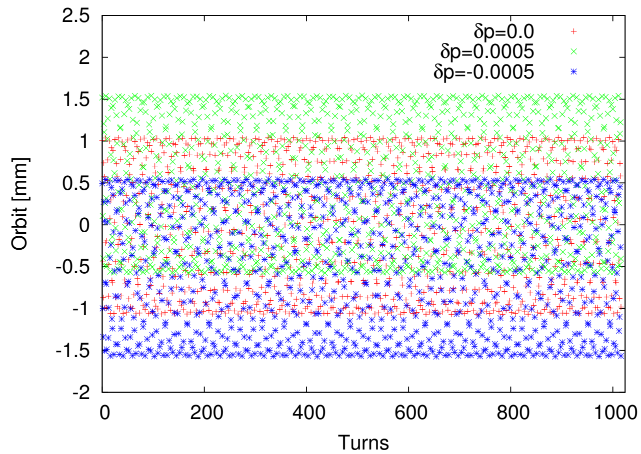

Figure 2.6: Turn-by-turn data showing the orbit change for different frequency trims.

The quantity $\frac{D_x}{\sqrt{\beta}}$ (normalized horizontal dispersion) appears to be very robust as it can be measured independently of the BPM calibration [38]. The horizontal dispersion (D_x) is measured by radial steering and the $\sqrt{\beta}$ is calculated from the amplitude of the Fourier analysis of the turn-by-turn data. This ensures that both observables are proportional to the BPM calibration. Therefore when looking at $\frac{D_x}{\sqrt{\beta}}$, the measurement is independent of the calibration of the BPMs.

Chromaticity

Another variable that can be determined while the dispersion measurement is conducted is the chromaticity. The tune change that is observed can be used for determining the chromaticity. Figure 2.7 shows a simulation of the tune change when a RF frequency trim is applied.

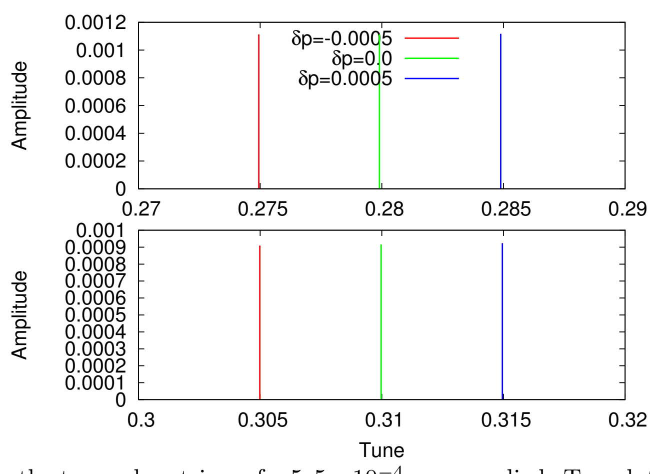

Figure 2.7: Change in the tune when trims of $-5, 5 \times 10^{-4}$ were applied. Top plot shows the horizontal plane, bottom plot the vertical plane.

The chromaticity can be found by fitting the tune versus δ. The slope is the chromaticity. In this simulation the ΔQ is 0.005 and with a momentum trim of 0.0005, the chromaticity is about 10. There is no tune spread around the main peak, as only a single particle was tracked.

2.4.3 Coupling

Local coupling measurements are described using the difference (f_{1001}) and sum (f_{1010}) resonance, introduced in section 1.6. The resonance driving terms are measured by identifying the corresponding amplitude and phase in the frequency domain ($a_{jklm}e^{i\phi^a_{jklm}}$ and $b_{jklm}e^{i\phi^b_{jklm}}$, respectively the resonance lines in the horizontal and vertical plane). The difference (f_{1001}) and sum (f_{1010}) resonance are then found at a BPM:

$$|f_{1001}| = \frac{1}{2}\sqrt{\frac{b_{1001}a_{1001}}{b_{1000}a_{1000}}}, \tag{2.48}$$

$$\phi_{1001} = \phi^a_{1001} - \psi_x + \frac{\pi}{2}, \tag{2.49}$$

$$|f_{1010}| = \frac{1}{2}\sqrt{\frac{b_{1010}a_{1010}}{b_{1000}a_{1000}}}, \tag{2.50}$$

$$\phi_{1010} = \phi^a_{1010} + \psi_x + \frac{\pi}{2}, \tag{2.51}$$

with $f_{jklm} = |f_{jklm}|\, e^{i\phi_{jklm}}$ and the terms $jklm$ are related to the potential $(x^u y^v)$, where $j+k=u$ and $l+m=v$. For a complete description of the implementation of the difference and sum resonance see ref. [15].

2.4.4 Chromatic functions

The dependence of the linear functions on energy is called the chromatic aberrations. The chromatic function for the β-function can be found by the Montague functions [39]

$$a_z = \frac{\Delta\beta_z}{\delta}\frac{1}{\beta_z}, \tag{2.52}$$

$$b_z = \frac{\Delta\alpha}{\delta} - \frac{\alpha_z}{\beta z}\frac{\Delta\beta_z}{\delta}, \tag{2.53}$$

the slopes $\frac{\Delta\beta_z}{\delta}$ and $\frac{\Delta\alpha}{\delta}$ are calculated by a linear fit. The chromatic β functions are defined as:

$$W_z = \sqrt{a_z^2 + b_z^2}, \tag{2.54}$$

$$\psi_z = \arctan\left(\frac{a_z}{b_z}\right). \tag{2.55}$$

2.4.5 Pseudo double monitors

Dual plane BPMs are needed to measure the coupling. The Pseudo double monitors are numerically constructed by shifting a vertical plane monitor towards the location of the nearest horizontal BPMs. This is realized by shifting the phase of the real spectrum lines in accordance with the vertical phase advance between the horizontal and vertical monitors, since the lines in the complex spectrum correspond to the sum and difference resonance. The assumption is made that the sections are free of non-linear sources.

2.5 Corrections methods

During the commissioning of the LHC two techniques were used to correct the linear optics. The first technique is the global correction, which is used to fit the parameters all around the ring. This is discussed in subsection 2.5.1. The second technique is called the segment-by-segment technique [40], [41] which was developed to identify and correct local optics errors. This new technique is discussed in great detail in subsection 2.5.2.

2.5.1 Global correction technique

Global correction techniques [42] were developed for the correction of phase, β, horizontal normalized dispersion and the coupling and vertical dispersion. The correction is computed using a response matrix using the ideal model. The perturbation of the optic functions at m BPMs due to the change in strength of n correctors is formulated into an $m \times n$ response matrix ($\mathbf{R}$).

$$\mathbf{R}\Delta\vec{k} = \Delta\vec{v}. \tag{2.56}$$

The measured and model optic function ($\vec{v}$) at m BPMs can be expressed into a vector:

$$\Delta\vec{k} = [\Delta v_1, \Delta v_2, \Delta v_3 ... \Delta v_m]\,. \tag{2.57}$$

Using the least square algorithm for the correction, to minimize the quadratic residual v at all BPMs:

$$\left|\left|\mathbf{R}\Delta\vec{k} - \Delta\vec{v}\right|\right|^2 = min. \tag{2.58}$$

The correction can be found by an SVD inversion.

Correction using normal quadrupoles

In the case of correction using normal quadrupoles, the **R**-matrix relates the phase-beating, beta-beating, normalized horizontal dispersion and tunes to the strength of all quadrupoles circuits.

$$\left(\Delta\vec{\phi}_x, \Delta\vec{\phi}_y, \frac{\Delta\vec{\beta}_x}{\beta_x}, \frac{\Delta\vec{\beta}_y}{\beta_x}, \Delta\frac{\vec{D}_x}{\sqrt{\beta}}, \Delta Q_x, \Delta Q_y\right) = \mathbf{R}\Delta\vec{k}. \tag{2.59}$$

The required strength is computed from the measurement error:

$$\Delta\vec{k} = -\mathbf{R}^{-1}\left(w_1\Delta\vec{\phi}_x, w_2\Delta\vec{\phi}_y, w_3\frac{\Delta\vec{\beta}_x}{\beta_x}, w_4\frac{\Delta\vec{\beta}_y}{\beta_y}, w_5\Delta\frac{\vec{D}_x}{\sqrt{\beta}}, w_6\Delta Q_x, w_6\Delta Q_y\right), \tag{2.60}$$

w_i stands for the weights that can be applied to correct the individual optical functions.

Correction using skew quadrupoles

In the case of correction using skew quadrupoles, the **R**-matrix relates the difference and sum resonance and the vertical dispersion to the strength of all skew quadrupoles circuits.

The required strength is computed from the measurement error:

$$\Delta\vec{k}_s = -\mathbf{R}^{-1}\left(w_1\Delta Re\{\vec{f}_{1001}\}, w_2\Delta Im\{\vec{f}_{1001}\}, w_3\Delta Re\{\vec{f}_{1010}\}, w_4\Delta Im\{\vec{f}_{1010}\}, w_5\Delta\vec{D}_y\right), \tag{2.61}$$

w_i stands for the weights that can be applied to correct the individual optical functions.

2.5.2 Local correction technique

The global correction technique has its limitations when it comes to identifying strong local sources. When using the global correction algorithm, a global fit is made around the ring. This created the need for the development of a new technique to ease the identification of strong local sources. This technique is called the segment-by-segment technique [40], [41]. It was developed initially for the LHC, and later was implemented for RHIC as well (see ch. 7).

The concept of the local correction is shown in figure 2.8 . The idea of the segment is to take a part of the accelerator and treat it as a beam line. The initial conditions of the beam line are the measured optics parameters.

The code that is developed has to fulfill the following functionalities:

- Identification local error sources.
- Calculation of effective corrections.
- Calculation of optics functions at elements such as wire scanners and collimators.

During the thesis several definitions will be used to explain the results from the segment-by-segment technique:

- Propagated model: model where the initial conditions are the measured optics functions.
- Fitted model: the propagated model is fitted to the measurements using local correctors.

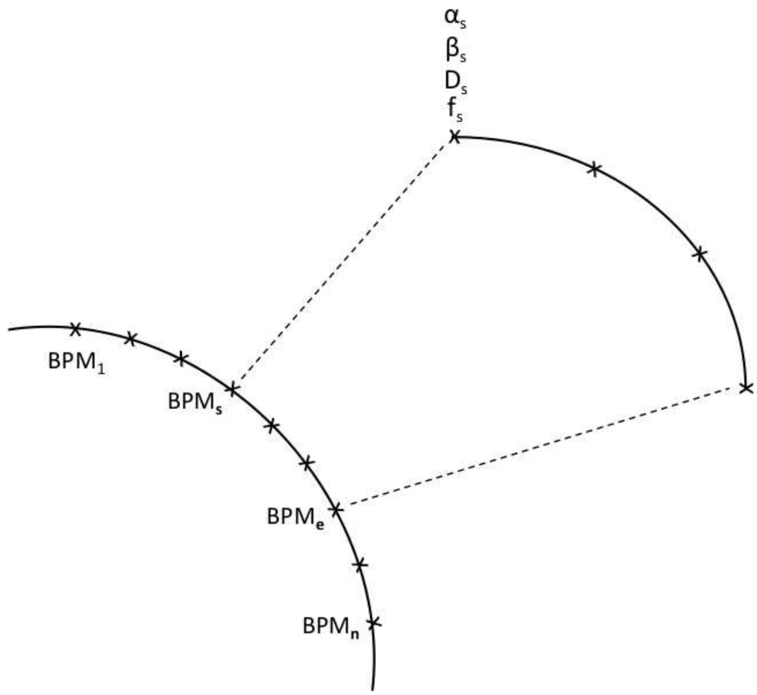

Figure 2.8: Graphical illustration of the segment-by-segment technique.

$$\begin{bmatrix} \beta_x \\ \alpha_x \\ \gamma_x \\ D_x \\ D'_x \\ \beta_y \\ \alpha_y \\ \gamma_y \\ D_y \\ D'_y \\ Re\{f_{1001}\} \\ Im\{f_{1001}\} \\ Re\{f_{1010}\} \\ Im\{f_{1010}\} \end{bmatrix}_i = \mathbf{M}_{MADX} \begin{bmatrix} \beta_x \\ \alpha_x \\ \gamma_x \\ D_x \\ D'_x \\ \beta_y \\ \alpha_y \\ \gamma_y \\ D_y \\ D'_y \\ Re\{f_{1001}\} \\ Im\{f_{1001}\} \\ Re\{f_{1010}\} \\ Im\{f_{1010}\} \end{bmatrix}_{start}, \tag{2.62}$$

the left hand side of equation (2.62) contains the optics values at the BPMs or elements in the segment line, where $\mathbf{M}_{MADX}$ is the transport matrix from the ideal model. The ideal model of the beam line uses the measured optical parameters as the initial conditions. By comparing the propogated model with the measured optical parameters in the beam line local deviations could be observed. Figure 2.9 shows an example using the β-beat as an observable. In this example an error of 0.1% was applied in the triplet left from IP1. The plot on the left shows that after 23500 m the measured β-beat (red) makes a local jump. In the right plot the fitted model (black) is shown and it can be seen that it is in good agreement with the measured β-beat (red). Other observables as Phase and $D_{x,y}$ were used. The observable which was used for the phase is the total phase advance. The total phase advance is defined as:

$$\Delta\phi_{error} = \Delta\phi_{mod} - \Delta\phi_{propagation}, \tag{2.63}$$

the phase advance here is not the BPM-to-BPM phase advance ($\Delta\phi = \phi_{i+1} - \phi_i$), but the phase advance between the i^{th} and the starting BPM ($\Delta\phi = \phi_i - \phi_0$). The total phase advance is then given by the difference between the measurement and the propagated model phase advance. When the phase advance between the model and the propagation are the same, no errors are present, and the observable $\Delta\phi_{error}$ will be zero along the beam line. If an error is present, $\Delta\phi_{error}$ will start deviating from zero after the location of the error.

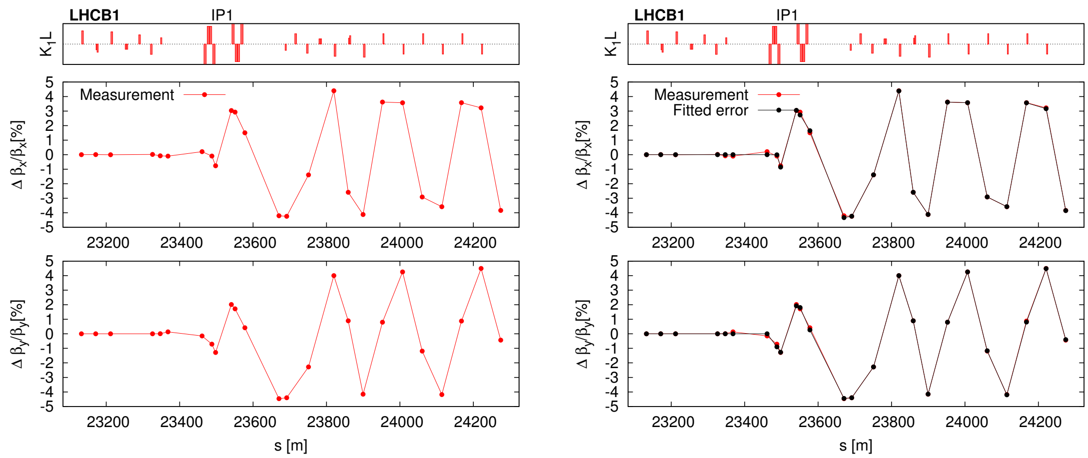

Figure 2.9: The left plot shows the β-beat when the error is not yet identified. The right plot shows the β-beat when the error is corrected. The top plots show the location and strength of the quadrupoles, the middle plot the horizontal β-beat and the bottom plot the vertical β-beat.

Figure 2.10 shows an example were an error of 0.1% was applied in the triplet left from IP1, using the total phase advance as an observable.

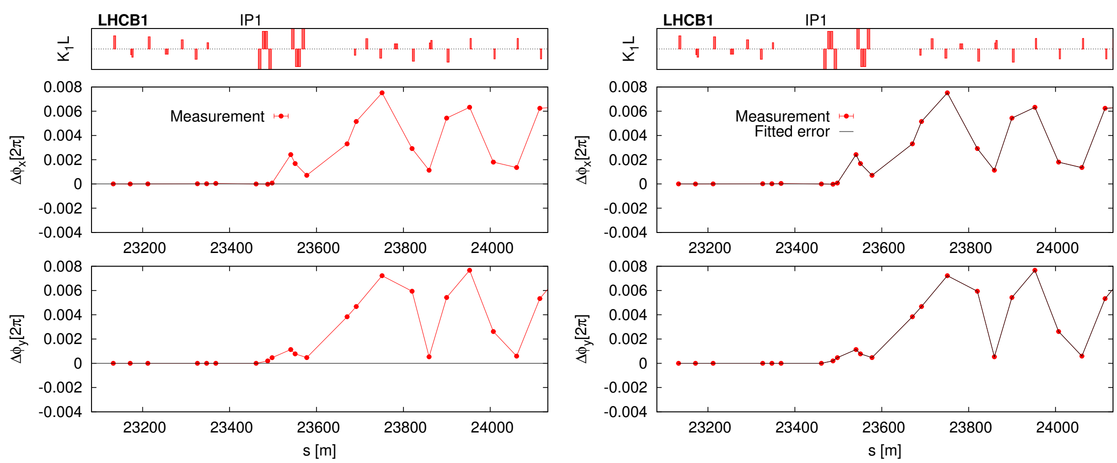

Figure 2.10: The left plot shows the observed error (red) and the right plot shows the same error (red) with fitted error correction (black). The top plots show the location and strength of the quadrupole, the middle plot the horizontal total phase advance and the bottom plot the vertical total phase advance.

The segment-by-segment technique was extended to include more optical functions. For the chromatic functions the observable could be implemented directly in MADX. As the resonance driving terms are not a direct observable in MADX, a matching script had to be implemented. The f_{1001} and f_{1010} are calculated from the R-matrix in MADX [43]. Figure 2.11 shows an example where an error was applied in the triplet left from IP1 using a strength of 0.0006 [m^{-2}].

2.6 Different techniques to measure and/or correct the linear optics

A short comparison between some other common techniques that are often used in accelerators will be made. Two techniques that are commonly used for the measurement and/or correction:

- COD: Closed Orbit Distortion [44].
- LOCO: Linear optics from closed orbits [45].

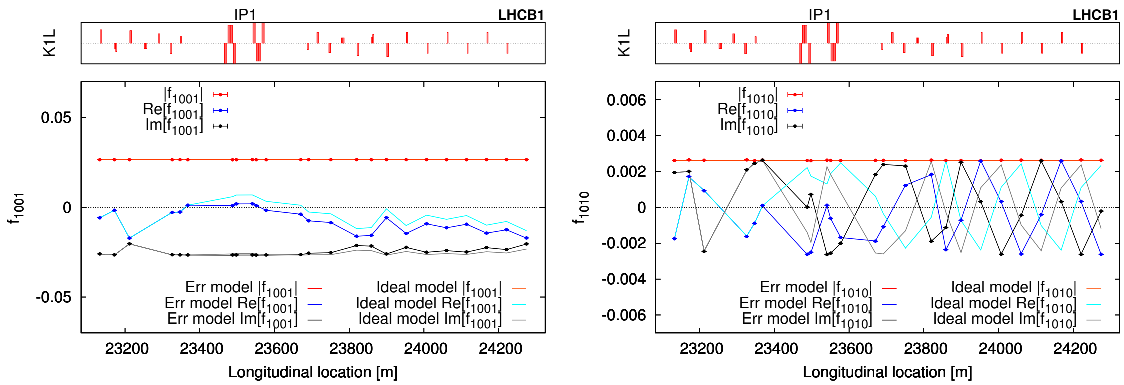

Figure 2.11: The left plot shows the difference resonance and the right plot the sum resonance where an error has been introduced (dots) and a fitted correction has been found (error model).

LOCO

Linear optics from closed orbits is a technique that is mainly used in light sources. It has been applied in the LHC as well [45]. The concept of LOCO is that the orbit correctors are used to measure the linear optics. A small kick is applied at every orbit corrector. The kicks from the correctors is done corrector by corrector. Orbit data is acquired for every kick:

$$y_{co}(s) = \frac{\sqrt{\beta(s)}}{2\sin\pi Q}\int_s^{s+C}\sqrt{\beta(s_i)}\frac{\Delta B(s_i)}{B\rho}\cos(\pi Q + |\phi(s) - \phi(s_i)|)ds_i. \tag{2.64}$$

If the kick that has been applied and the orbit change is known, the linear optics functions can be deduced rather easily. The correction is then found by minimizing:

$$R_{ij}^{diff} = \frac{R_{ij}^{meas} - R_{ij}^{model}}{\sigma_i}, \tag{2.65}$$

σ_i is the noise on the i^{th} monitor. This problem can be solved by using a SVD. The major disadvantage of the LOCO is that it is very time consuming for large storage rings.

2.7 Simulation codes

During the course of our studies two different accelerator codes were used to model the different accelerators presented in this thesis. These two sets of codes are not the only codes available. For a complete overview please refer to [46]. The motivation for using the two codes is that traditionally CERN has been using and maintaining MADX.

The first code which was used intensively is MADX (Methodical Accelerator Design) [47]. The source code of MADX is written in C,C++, Fortran90 and Fortran77. The second code which was used was the Polymorphic Tracking Code [48]. There is a conceptual difference between PTC and MADX [49]. PTC allows a symplectic integration through all accelerator elements giving the user full control over the precision (number of steps and integration type) and exactness (full or extended Hamiltonian) of the results. The degree of exactness is determined by the user and the speed of his computer. In MADX only normal quadrupolar and sextupolar errors can be assigned to bending magnets. Both codes are in perfect agreement when introducing such errors, but in PTC all other components can also be assigned to thick elements.

MADX was mainly used to model the different accelerators in the form of Twiss tables, which contains the optics functions. PTC on the other hand was used for tracking. The tracking with PTC is thick lens tracking in contrast to MAD which is thin lens tracking. The motivation to use thick lens tracking is that the accuracy increases significantly.

Chapter 3

SPS measurements as a test bed for the LHC

The nominal and the low γ_t SPS optics are presented. The SPS has been playing an important role as a test bed for the LHC, as the lattices are very similar. Before the LHC was switched on in 2008, several experiments were conducted in the SPS to test the developed measurement and correction algorithms. The motivation for measuring the low γ_t optics was the exploration of the developed algorithms, more specifically the algorithm that is used to calculate the β-function from phase, at different working points. Section 3.1 gives a description of the SPS. In section 3.2 the results of the measurements and corrections for the nominal optics are discussed. Section 3.3 is devoted to the discussion of the measurements for the low γ_t optics. Concluding remarks are drawn at the end of this chapter.

3.1 Description of the SPS

The SPS has 1317 normal conducting magnets in a circumference of 6.9 km. The particle beams (protons or ions) are delivered to the SPS from the PS [50] at an energy of 26 GeV. The SPS consists of 108 FODO cells. In 84 cells each of the drift is replaced by a dipole. For nominal optics the phase advance per cell is almost $\pi/2$, resulting in tunes close to 27. For low γ_t optics the phase advance per cell is reduced to around 67 degrees, this moves the tunes approximately down to 20. An overview of the main parameters is listed in table 3.1. A more detailed description can be found in [51]. For both optics the measurements were conducted at injection energy.

Parameter	nominal optics	low γ_t optics
Injection energy	26 GeV/c	26 GeV/c
Extraction energy	450 GeV/c	450 GeV/c
Horizontal tune	26.13	20.13
Vertical tune	26.18	20.18
Transition energy	22.8	18
Maximal β-functions $\beta_{x,y}$	105 m	105 m
Minimal β-functions $\beta_{x,y}$	20 m	30 m
Maximal dispersion D_x	4.77 m	8 m

Table 3.1: Main parameters of the SPS. For the nominal and low γ_t optics.

3.1.1 Magnets and beam instrumentation

The relevant magnets in the SPS for the experiments are listed in table 3.2. The SPS has limitations with respect to the available correction schemes. The amount of available normal and skew quadrupoles to correct the linear optics is limited. Only three normal quadrupole families and one skew quadrupole circuit are available. Therefore an alternative correction scheme was developed using orbit bumps at the sextupoles. Sextupoles in combination with horizontal orbit correctors are used to correct the beta-beat and horizontal dispersion. Vertical orbit correctors are used to correct coupling and vertical dispersion. In this correction scheme there are almost as many observables as sextupoles.

Name	Description	number installed	β_x [m]	β_y [m]
MDH	Horizontal orbit corrector	106	$\sim$101	$\sim$21
MDV	Vertical orbit corrector	106	$\sim$21	$\sim$101
QF1	Focusing quadrupole	54	$\sim$103	$\sim$21
QF2	Focusing quadrupole	70	$\sim$103	$\sim$21
QD	Defocussing quadrupole	108	$\sim$21	$\sim$103
LQSA	Skew quadrupole	6	$\sim$22	$\sim$97
LSF	Lattice sextupoles focusing	54	$\sim$100	$\sim$22
LSD	Lattice sextupoles defocussing	54	$\sim$22	$\sim$100

Table 3.2: An overview of the relevant magnets for the conducted experiments.

The beam instrumentation which was used during the measurements is listed in table 3.3. Beam position monitors are installed close to the quadrupoles. The installed BPMs are single plane, meaning only one plane can be measured with each BPM. This imposes a limitation on the optics measurements which require information from both planes. This led to the development of a technique called pseudo-double plane BPMs. The Multi Orbit Position System (MOPOS) [52] is used to collect the signal from the BPMs. Approximately 1000 turns are acquired using the multi-turn acquisition code [31].

Name	Description	number installed	β_x [m]	β_y [m]
MKQH	Horizontal kicker	1	$\sim$64	$\sim$37
MKQV	Vertical kicker	1	$\sim$34	$\sim$70
BPMH	Horizontal BPM	103	$\sim$103	$\sim$20
BPMV	Vertical BPM	95	$\sim$20	$\sim$103
BWS.51995	Wire scanner (emittance measurement)	1	$\sim$83	$\sim$27

Table 3.3: An overview of the relevant beam instrumentation and kickers for the conducted experiments.

3.1.2 Low γ_t optics

An alternative optics scheme was developed to cope with the instabilities in the SPS [53]. The main intensity limitation for single bunch has been identified as transverse mode coupling instability (TMCI) at injection [54]. In the longitudinal plane, indications for loss of Landau damping [55] were observed with LHC bunch trains of nominal intensity with small injected emittance. These instability thresholds scale proportionally to the slippage factor, when assuming constant longitudinal bunch parameters. The reduction of the γ_t (section 1.5) has been studied in [56] and more recently in [57]. The reduction of γ_t is achieved by changing the dispersion function $D_x(s)$, increasing the slippage factor. Several solutions were considered [58]. A promising solution by decreasing the tunes has been presented in [57]. The phase advance per cell was changed from $\frac{\pi}{2}$ to $\frac{3\pi}{16}$. This change in the phase advance allowed to measure the β-function using the 3-BPM phase method, as this method cannot be applied to a phase advance equal to $\frac{\pi}{2}$.

Figure 3.1 shows the horizontal and vertical β-function and horizontal dispersion function for the nominal optics (left), and the low γ_t optics (right). Only 1/6 of the circumference is shown, meaning that the SPS has a sixfold symmetry. For the dispersion, the 4 oscillations observed for the nominal optics are reduced to 3 oscillations for the low γ_t optics. The maximal β-function does not change. The minimal β function is increased approximately from 20 to 30 m. For the low γ_t optics the maximum dispersion is increased from 5 to 8 m, this resulted in a decrease of the γ_t from 22.8 to 18.

3.2 Results for the nominal optics

The lattice of the SPS is very similar to the lattice of the LHC. This was the direct motivation to implement and test the developed tools and algorithms in the SPS. In the following paragraphs

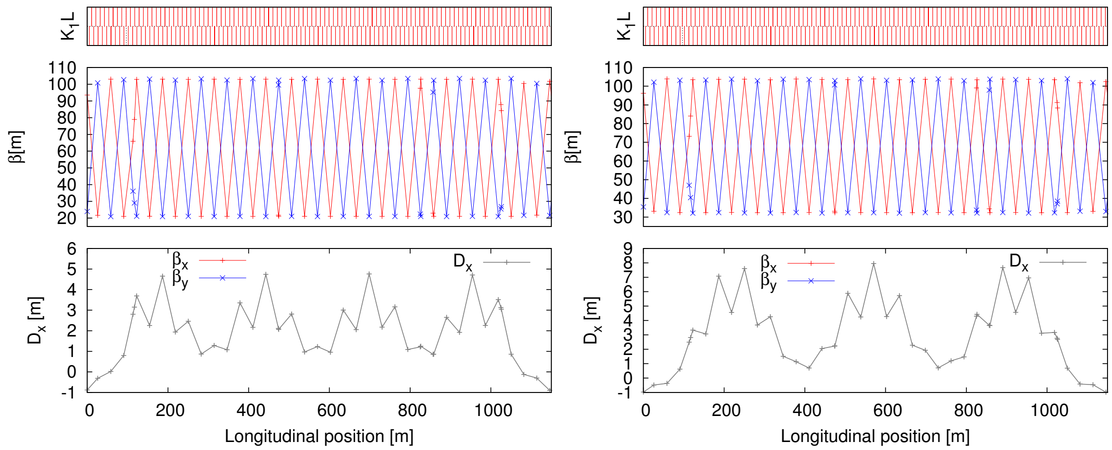

Figure 3.1: Horizontal and vertical $\beta-$function (middle) and horizontal dispersion function (bottom) are shown for the nominal optics (left) and the low γ_t optics (right). Only 1/6 of the circumference is shown.

results for the different measurements and corrections conducted in the SPS for the nominal optics will be presented. In the first paragraph the measurement and correction of the phase and normalized horizontal dispersion will be discussed. The following paragraph will discuss the measurement and correction of coupling and vertical dispersion.

3.2.1 Optics corrections in the SPS using horizontal orbit bumps

Figure 3.2 shows the horizontal (left), and vertical (right) $\phi-$beat. The normalized horizontal dispersion is shown in figure 3.3. Before (red), and after (blue) corrections were implemented. The measurement in the vertical plane was of bad quality and was therefore disregarded in the correction process. The horizontal data on the other hand shows good results. Only 75% of the calculated correction was applied. This resulted in a reduction of the horizontal rms $\phi-$beat from 3.58° to 1.78°. The normalized horizontal dispersion deviation was unaffected by the correction, remaining at an rms of 0.02 $\mathrm{m}^{\frac{1}{2}}$. This result shows that the phase advance can be corrected without deteriorating the horizontal dispersion.

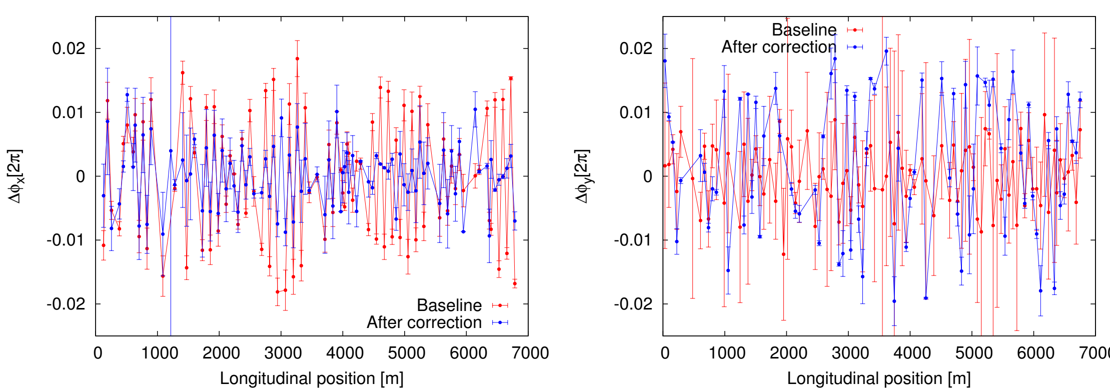

Figure 3.2: Horizontal, left and vertical, right $\phi-$beat. Before (red) and after (blue) corrections were applied.

Horizontal orbit bumps at sextupoles are used to correct the phase advance and the horizontal dispersion. The phase is a robust and model independent observable. Measuring the β-function close to 90° phase advance using the 3-BPM method [35] increases the systematic and random error bar.

In section 3.4 this will be discussed in more detail. Figure 3.4 shows the simulated closed orbit (top), for the applied corrector strength (bottom). The correction is calculated using a response matrix. The largest excursion on the orbit is expected to be ~ 3.5 mm, and the highest applied corrector strength is approximately 30 μrad. The weight for the correction was placed both on the phases and the dispersion.

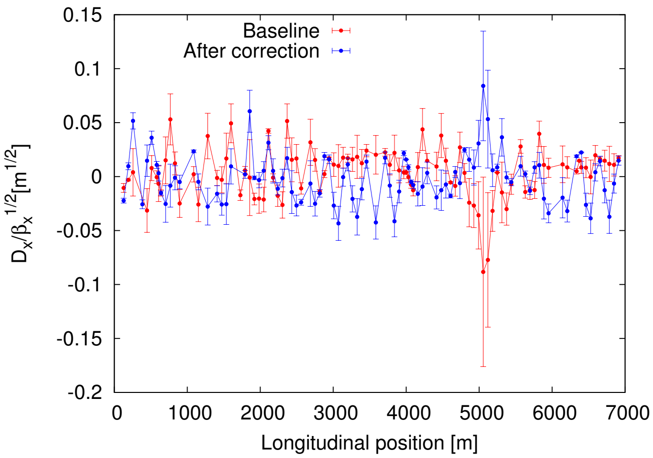

Figure 3.3: The normalized horizontal dispersion. Before, red and after, blue corrections were applied.

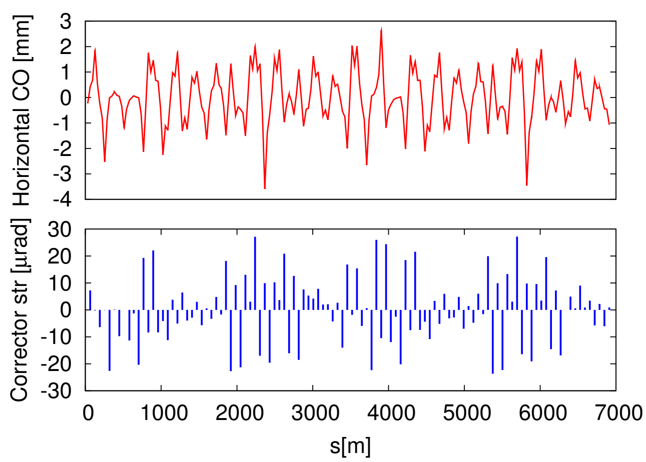

Figure 3.4: Figure showing the simulated closed orbit, top for the applied corrector strength, bottom.

3.2.2 Optics corrections in the SPS using vertical orbit bumps

In normal conditions SPS has equal integer transverse tunes, see table 3.1. This implies that $\phi_x \approx \phi_y$ all around the ring, considerably simplifying the coupling correction. In order to get closer to the LHC the SPS integer tunes are split by one, this allows to see the f_{1001} modulation in the SPS as in the LHC. This is achieved by moving the integer part of the vertical tune from 26 to 27. Vertical orbit bumps are used to correct the coupling and vertical dispersion. The coupling is measured by identifying the secondary tune line in the BPM and calculating the corresponding resonance driving terms.

Figure 3.5 shows the simulated closed orbit (top), for the applied corrector strength (bottom). The correction is calculated using a response matrix. The largest excursion on the orbit is expected to be about 3.0 mm and the highest applied corrector strength is approximately 35 μrad. The weight for the correction was placed on the difference resonance and vertical dispersion, but not on the sum resonance. As the difference resonance is the leading resonance in the SPS.

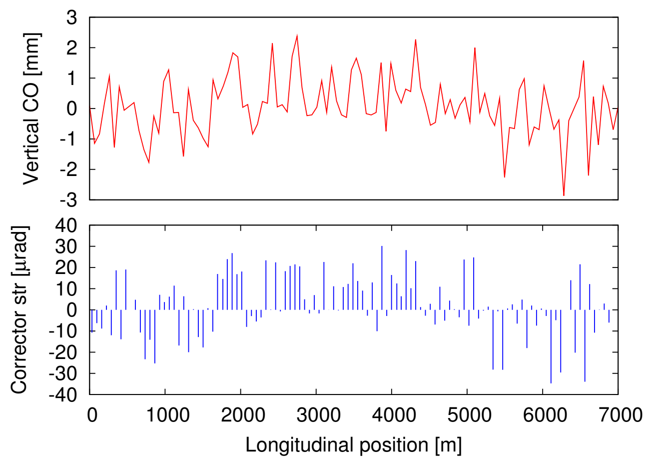

Figure 3.5: Figure showing the simulated closed orbit, top for the applied corrector strength, bottom.

In figure 3.6 the difference resonance f_{1001} (left), and the sum resonance, f_{1010}, (right) are plotted before and after corrections. From top to bottom: the absolute value, the real and the imaginary part are shown. In figure 3.7 the vertical dispersion is plotted. The correction was calculated by simultaneously applying weight on the difference resonance and the vertical dispersion, but disregarding the sum resonance.

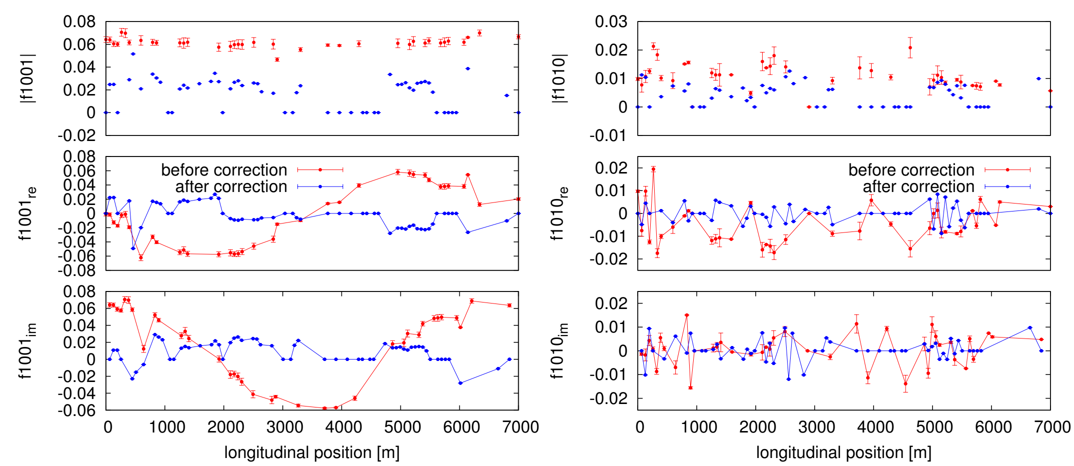

Figure 3.6: Difference resonance, left and sum resonance, right. Before, red and after, blue corrections were applied.

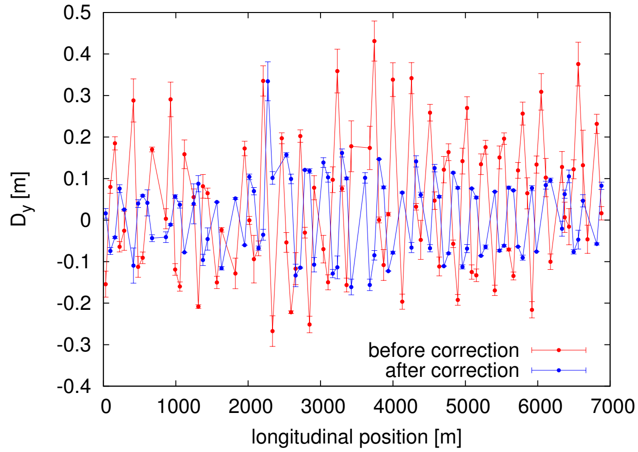

Figure 3.7: Vertical dispersion before (red) and after corrections (blue).

Both the difference resonance and vertical dispersion has been corrected with a factor two. The rms for the vertical dispersion is reduced from 0.187 m to 0.095 m. The rms for the difference resonance (f_{1001}) was reduced from 0.061 to 0.028. Zero weight was placed on the sum resonance, but it was still corrected from a rms of 0.024 to 0.022. The simultaneous correction of the coupling and the vertical dispersion was for the first time successfully applied in the SPS.

3.3 Measurements for the low γ_t optics

The motivation for this experiment was the exploration of the developed algorithms, more specifically the algorithm that is used to calculate the β-function from phase, at different working points. A decrease of the error and an improvement of the precision on the β-function was expected, as the phase advance between the BPMs was reduced from 90° to 67°.

In figure 3.8 the ϕ-beat (left) and the β-beat (right) are shown for the low γ_t optics. The observed β-beat is around 20% for both planes without any corrections.

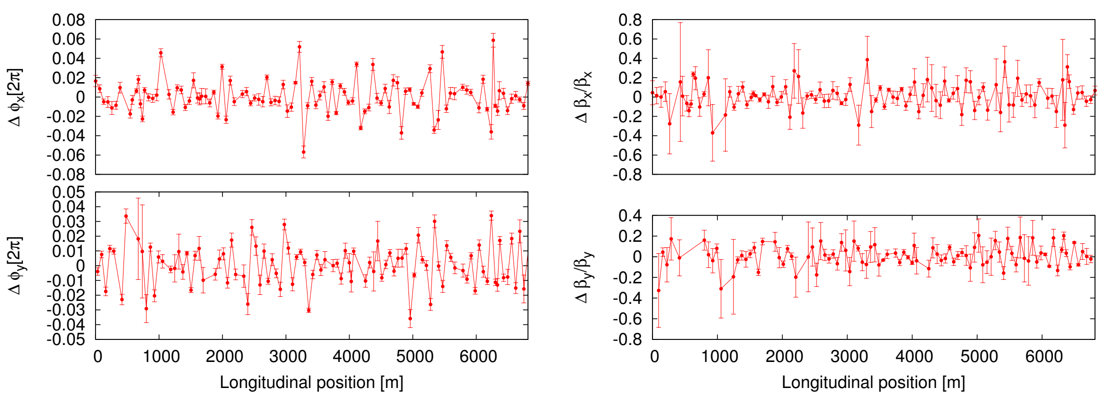

Figure 3.8: The ϕ-beat, left and the β-beat, right is shown for the low γ_t optics

Dispersion measurements were performed by applying a frequency trim, shifting the beam to a different orbit. Three different $\frac{\Delta p}{p}$ settings of $0.0, 1.24 \times 10^{-3}$ and 0.99×10^{-3} were applied. The normalized horizontal dispersion is shown on the left in figure 3.9. The top graph shows model and measurement, and the bottom graph the dispersion beat. This result shows a good agreement between model and measurement. The vertical dispersion is shown on the right of figure 3.9. The horizontal and vertical dispersion show a large error bar. Both dispersion beat measurements are within the error bars.

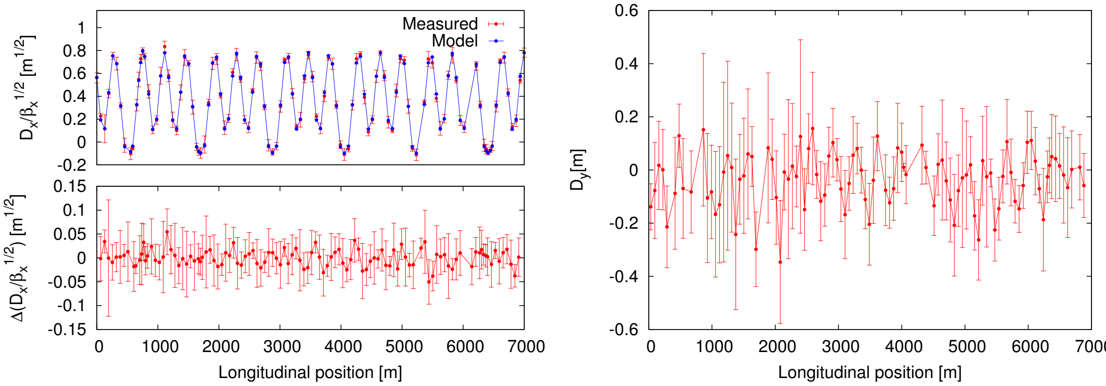

Figure 3.9: Horizontal normalized dispersion on the left and vertical dispersion on the right.

In figure 3.10 the difference resonance, f_{1001}, (left) and the sum resonance, f_{1010}, (right) are plotted before and after corrections. From top to bottom: the absolute value, the real and the imaginary part are shown. The measurement of f_{1010} for the low γ_t optics is a factor 3 lower than for the nominal optics. No abrupt jumps are observed, meaning that no strong local sources are present.

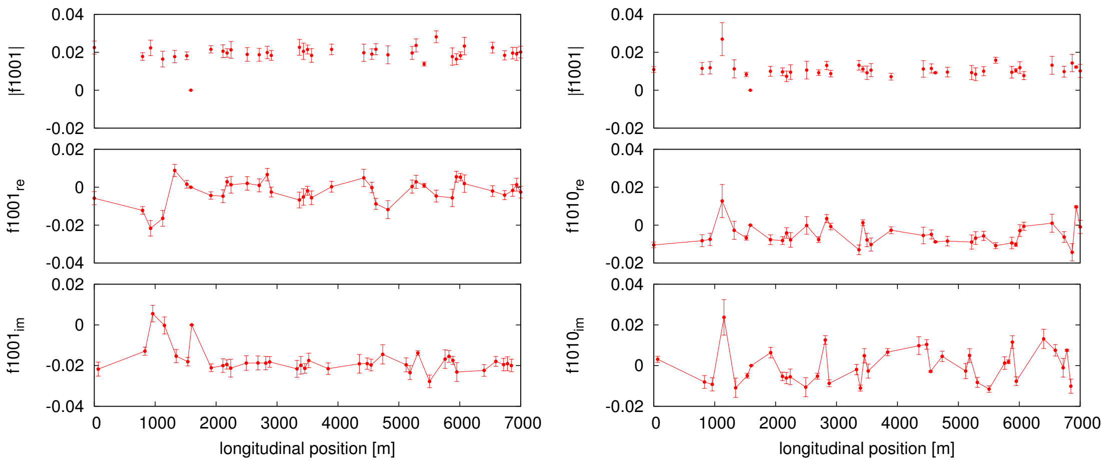

Figure 3.10: Difference resonance, left and sum resonance, right for the low γ_t optics.

3.4 Discussion

Measurements and corrections were conducted for linear optics parameters. Phase advance and horizontal dispersion were successfully corrected using horizontal orbit bumps at the sextupoles for the first time in the SPS. Coupling and vertical dispersion were successfully corrected for the first time using vertical orbit bumps at the sextupoles. For the measurement and correction of the coupling and vertical dispersion the SPS integer tunes were split by one. This was done to get closer to the LHC tunes and to see the f_{1001} modulation in the SPS as in the LHC. Table 3.4 shows rms values of optics parameters before and after corrections, for both the nominal and low γ_t optics.

Figure 3.11 shows a histogram of the phase measurement error (left) and the relative beta measurement error (right). Two cases are presented nominal optics (red) and low γ_t optics (blue). The histogram for the phase error indicates a slightly larger error distribution for the low γ_t optics. The analysis for both cases was done for a similar number of turns. In figure 3.12 the turn-by-turn data is shown for one of the BPMs. The BPM signal measured for the low γ_t optics has slightly more noise than the nominal optics, probably due to the BPM settings.

Measured parameter	before correction	after corrections	low γ_t optics
Horizontal phase-beat [°]	3.58	1.78	7.40
Vertical phase-beat [°]	1.74	5.23	9.20
Normalized horizontal dispersion [$\sqrt{m}$]	0.020	0.021	0.017
Vertical dispersion [m]	0.187	0.095	0.108
$\lvert f_{1001}\rvert$	0.061	0.028	0.020
$\lvert f_{1010}\rvert$	0.024	0.022	0.012

Table 3.4: rms values of the optics parameters before and after corrections were applied for the nominal optics and the low γ_t optics.

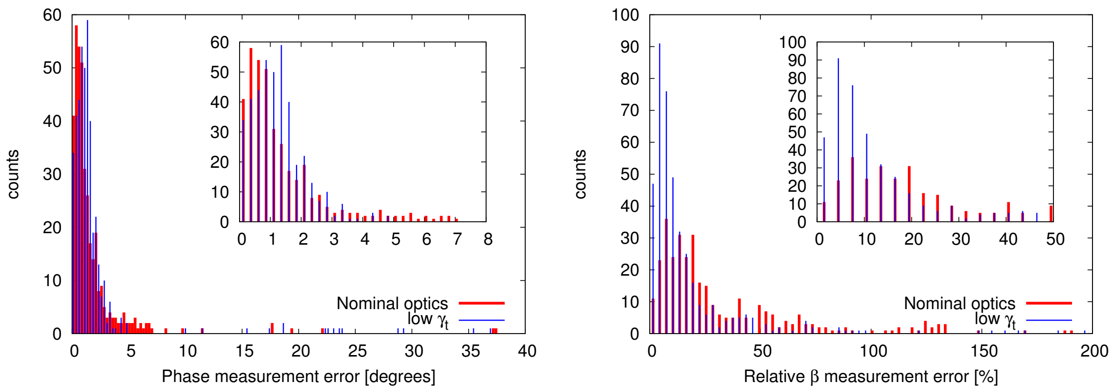

Figure 3.11: Phase measurement error, left and relative beta measurement, right. Two cases are plotted. Red being the nominal optics and blue the low γ_t optics.

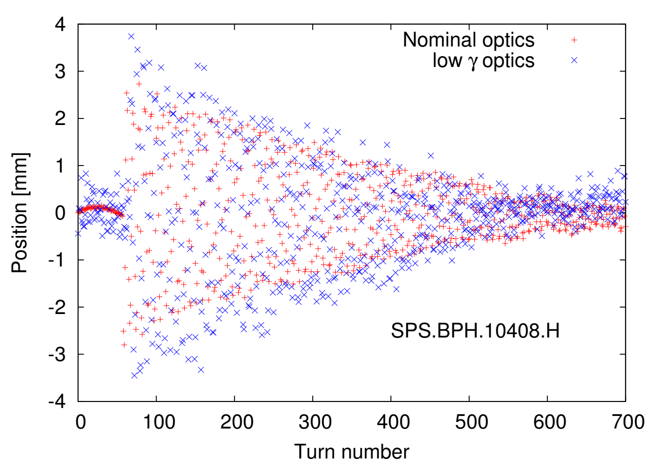

Figure 3.12: Turn-by-turn data for nominal optics, red and low γ_t optics, blue

An improvement was observed for the β measurement when using the low γ_t optics. Figure 3.11 shows the error distribution for the statistical error on the phase (left) and the relative beta error (right). The histogram on the phase error shows an increase in the measurement error for the low γ_t optics with respect to the nominal optics. This is because the measurement for the low γ_t optics was more noisy than for the nominal optics. Nevertheless a significant improvement is still observed for the relative error on the β for the low γ_t optics. This shows the importance of the phase advance between BPMs on the β measurement.

Chapter 4

An introduction to the optics of the LHC

With its circumference of 27 km, 1232 superconducting dipoles, 392 superconducting quadrupoles and many other cutting-edge technologies, the large hadron collider, a very complex machine, is nothing short of an engineering marvel. The parameters and equipment that play an important role in the optics measurements will be discussed in section 4.1. In this section the main beam parameters of the LHC, the various IRs located around the machine, and the arcs will be discussed in detail. Some important concepts such as ramp, squeeze and crossing angles will be introduced.

Section 4.2 discusses the simulations conducted to get a better insight into the performance of the measurement and corrections techniques. Basic simulations were conducted to investigate the measurement error on the β-function. Coupling simulations were conducted to investigate what the effect of losing some of the skew quadrupoles was. During the commissioning, requests to measure the β^* and waist came from the experiments. The limitations of these algorithms are discussed in detail. Lastly, simulations for the chromatic functions were conducted to test the algorithms and the results were compared with the model.

4.1 Optics of the LHC

The LHC is constructed in the former LEP tunnel [59]. In figure 4.1 a schematic plot of the LHC is shown. Beam 1 is injected in the clock-wise direction at IR2 and beam 2 is injected counter clock-wise in IR8. The LHC consists of 8 arcs and 8 long straight sections. Four out of eight long straight sections house the experiments.

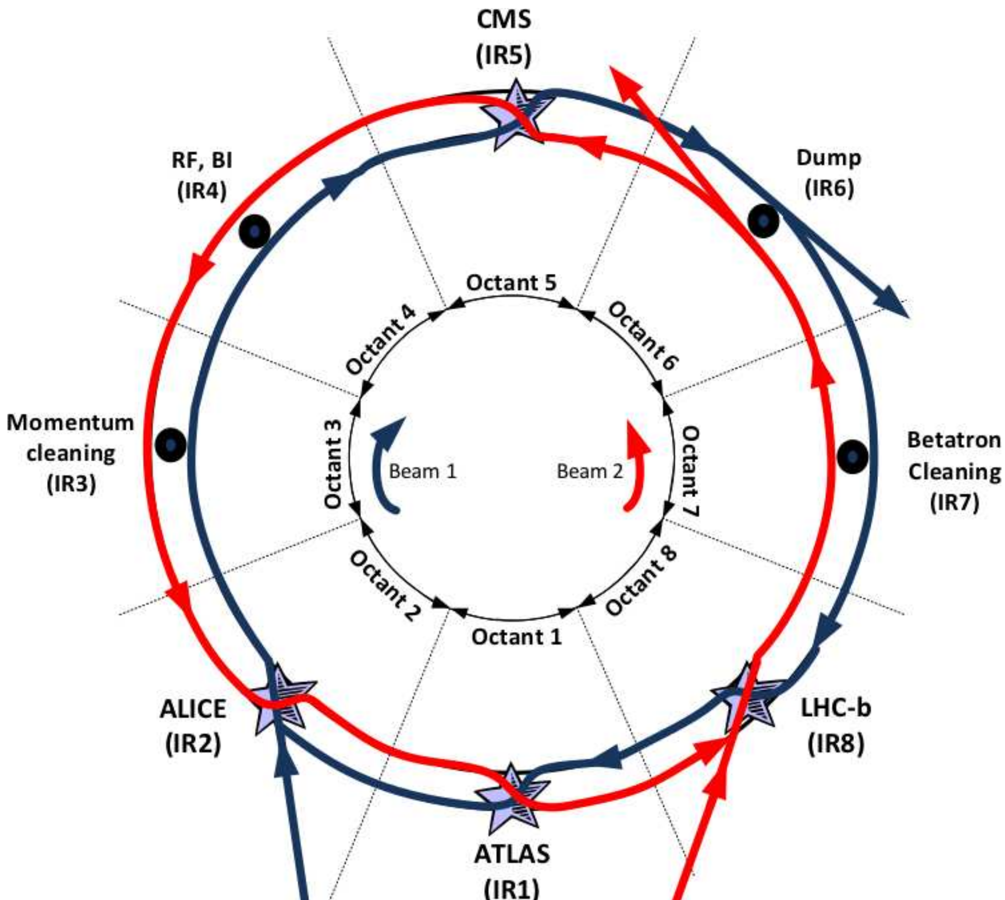

Figure 4.1: Schematic layout of the LHC

The main beam parameters for the LHC are listed in table 4.1 [60]. The intermediate energy of 3.5 TeV was a safety measure as a precaution after the incident in 2008 [61]. The incident happened because of a failure of the interconnection between two magnets of the 13 kA dipole circuit. Additional measurements revealed other connections not complying with the specifications. A quench at the 7-13 kA level in such a connection can lead to a fast and unprotected thermal run-away and hence opening of the circuit. This was the motivation to operate the LHC at a current of 6 kA, corresponding to an energy of 3.5 TeV, until the consolidation of the new splices in the shutdown in 2013-2014.

[1] The base line machine operation assumes that the longitudinal emittance is deliberately blown up at the middle of the ramp in order to reduce the intra beam scattering growth rates.

[2] The emittance at injection energy refers to the emittance delivered to the LHC by the SPS without any increase due to injection errors and optics mis-match. The RMS beam sizes at injection assume the nominal emittance value quoted for top energy (including emittance blowup due to injection oscillations and mismatch).

[3] Dimensions are given for Gaussian distributions. The real beam will not follow a Gaussian distribution but more realistic distributions do not allow analytic estimates for the IBS growth rates.

[4] The RMS beam sizes in IP1 and IP5 assume a β-function of 0.55 m.

[5] The RMS beam sizes in IP1 and IP5 assume a β-function of 1 m.

[6] The RMS beam sizes in IP2 and IP8 assume a β-function of 10 m.

[7] The RMS beam sizes in IP2 and IP8 assume a β-function of 3 m.

Parameter	**Injection**	**Design energy**	**Intermediate energy**
Proton energy [GeV]	450	7000	3500
Relativistic gamma (γ)	479.6	7461	3731
Number of particles per bunch	1.15 10^{11}	1.15 10^{11}	1.15 10^{11}
Number of bunches	2808	2808	2808
Longitudinal emittance (4σ) [eVs]	1.0	2.5[1]	1.4[1]
Transverse normalized emittance [μm rad]	3.5[2]	3.75	3.75
Circulating beam current [A]	0.582	0.582	0.582
Stored energy per beam [MJ]	23.3	62	28
RMS bunch length[3] [cm]	11.24	7.55	$\sim$9
RMS beam size at the IP1 and IP5 μm	375.2	16.7[4]	31.70[5]
RMS beam size at the IP2 μm	279.6	70.9[6]	100.2[6]
RMS beam size at the IP8 μm	279.6	38.83[7]	54.91[7]
Tunes horizontal/vertical	64.28/59.31	64.31/59.32	64.31/59.32
Peak luminosity in IP1 and IP5 [$cm^{-2}sec^{-1}$]	-	1,5 x 10^{33}	1,0 x 10^{34}
Peak luminosity per bunch crossing in IP1 and IP5	-	5.34 x 10^{29}	3,56 x 10^{30}

Table 4.1: Main beam parameters

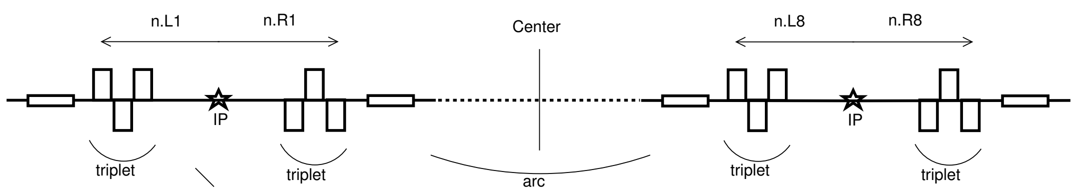

Figure 4.2: An illustration of the naming convention for the magnets in the LHC. n is the n^{th} magnet of the sub-group with respect to the center of that specific IP.

4.1.1 Long straight sections

In this paragraph the different long straight sections are discussed. The discussion is limited to the aspects of interest for the optics. Detailed description of the layout of the interaction regions can be found in [60]. A short overview of the straight sections is listed in table 4.2.

Straight section	Description
IR1	ATLAS experiment
IR2	ALICE experiment
IR3	Momentum collimation system
IR4	RF, feed-back systems, LHC beam instrumentation
IR5	CMS experiment
IR6	Beam abort system for B_1 and B_2
IR7	Betatron collimation system
IR8	LHCb experiment

Table 4.2: Description of the different straight sections and their purpose in the LHC.

The naming of the magnets in the LHC is straightforward. Every sub-group of magnets (dipole, quadrupole, skew-quadrupole, ...) has his own sequence. The sequence starts at the interaction point, see figure 4.2 for a description and continues until the middle of the ARC. In the figure, n is the n^{th} magnet of that sub-group with respect to the center of that IP.

Long straight section point 1 and 5

Point 1 and 5 house the high luminosity experiments at IR1, for the experiment ATLAS [62] and IR5, for the experiment CMS [63]. These two experiments are identical in terms of optics, except for the crossing-angle scheme: the crossing angle in IR1 is in the vertical plane and in IR5 in the horizontal plane. The small β-function values at the IP are generated by using a triplet quadrupole assembly ('inner triplets'), detailed information about the matching constraints can be found in [64].

Figure 4.3 shows a schematic layout of IR1 at injection energy with no crossing angle for beam 1. The interaction region contains the following structures:

- A 31 m long superconducting low-β single bore triplet assembly (operated at a temperature of 1.9 K). The triplet quadrupoles are powered by two nested power converters. An additional trim power converter is installed for the Q_1 quadrupole.
- A pair of separation/recombination dipoles separated by about 88 m. The D1 3.4 m long conventional warm magnet dipole next to the triplet is a single bore. The 9.45 m long superconducting dipole magnet is a double bore (operated at a temperature of 4.5 K).
- Four matching quadrupole magnets. Q_4 is a wide-aperture magnet (operated at a temperature of 4.5 K). Q_5 to Q_7 are normal-aperture quadrupole magnets (operated at a temperature of 1.9 K)
- Q_4 to Q_{10} are individually powered magnets (operated at a temperature of 1.9 K).
- Two independent skew quadrupoles are installed at the triplet assembly.

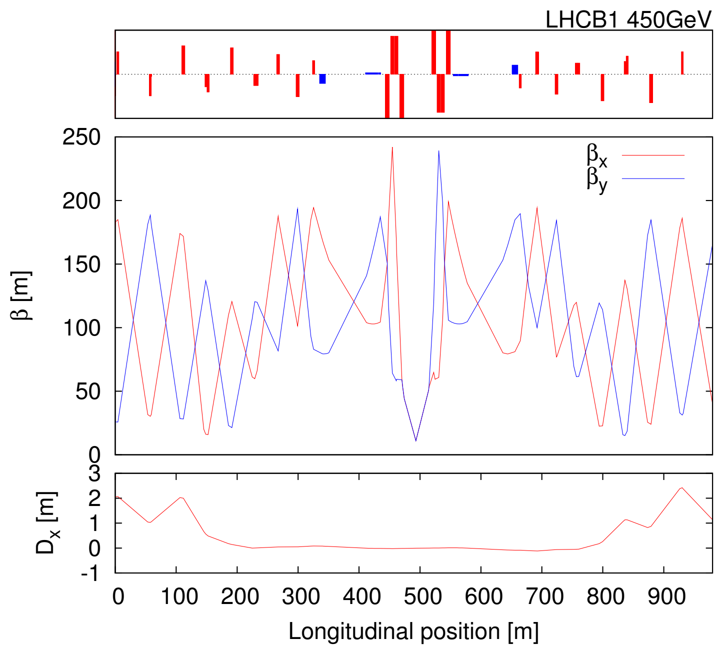

Figure 4.3: IR1, IR5 layout is shown at injection energy for beam 1. Top shows layout of the interaction region. Quadrupole magnets in red and dipoles in blue. In the middle the horizontal, red and vertical, blue β-function is shown. The bottom plot shows the horizontal dispersion. No crossing angle was applied.

Long straight section point 2

Long straight section at point 2 houses IR2, for the experiment ALICE [65], which is a detector for heavy ion collisions and houses the injection elements for beam 1. As a consequence IR2 must satisfy a large range of optics constraints. A complete overview of the IR2 optics layout can be found in [66]. The aperture in the interaction region was designed such that it can accommodate both beams in the common part of the LHC with a minimum separation of 10σ.

Figure 4.4 shows the schematic layout of IR2 at injection energy for beam 1 with no crossing angle. The interaction region consists of the following structures:

- A 31 m long superconducting single bore triplet assembly (operated at a temperature of 1.9 K). The triplet quadrupoles are powered in series, one trim circuit is installed that allows independent steering.

- A pair of 9.45 m long separation/recombination superconducting dipoles separated at about 66 m (operated at a temperature of 1.9 K).
- Four matching quadrupole magnets. Q_4 and Q_5 are wide-aperture magnets (operated at a temperature of 4.5 K). Q_6 and Q_7 are quadrupole magnets (operated at a temperature of 1.9 K)
- The injection septum MSI is located between Q_6 and Q_5 on the left-side of IR2. The injection septum kicks the injected beam in the horizontal plane towards the closed orbit of the circulating beam.
- The injection kicker MKI is located between Q_5 and Q_4 on the left-side of IR2. The injection kicker kicks the injected beam in the vertical plane towards the closed orbit of the circulating beam.
- A large absorber (TDI [67])is placed 15 m upstream from dipole D1 to protect the cold elements in case of an injection failure.
- Two independent skew quadrupoles are installed at the triplet assembly.

Optics constraints were placed on the vertical phase advance between the MKI and TDI, it must be at a value of 90°. Furthermore the phase advance between the TDI and the two auxiliary collimators must be an integer multiple of $180° \pm 20°$. These constraints are necessary to guarantee an optimal protection should injection fail.

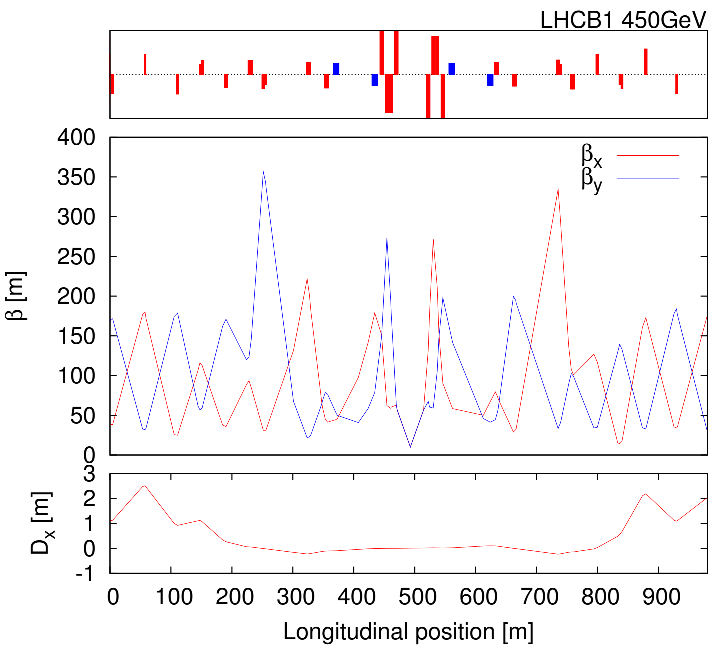

Figure 4.4: IR2 layout is shown at injection energy for beam 1. Top shows layout of the interaction region. Quadrupole magnets in red and dipoles in blue. Middle shows the horizontal and vertical β-function. The horizontal dispersion is shown at the bottom. No crossing angle was applied.

Long straight section 3

Long straight section at point 3 houses the momentum collimation system. This system was designed to absorb particles with a relative momentum offset higher than $\pm 10^{-3}$. Figure 4.5 shows the schematic layout of IR3 at injection energy for beam 1. This region contains the following structures:

- Q_6, made of superconducting MQTL modules.
- A dog-leg structure made of two sets of MBW warm single bore wide aperture dipole magnets was installed to generate dispersion.
- The warm dual-bore (MQW) magnets Q_4 and Q_5 left and right from the IP are powered in series.

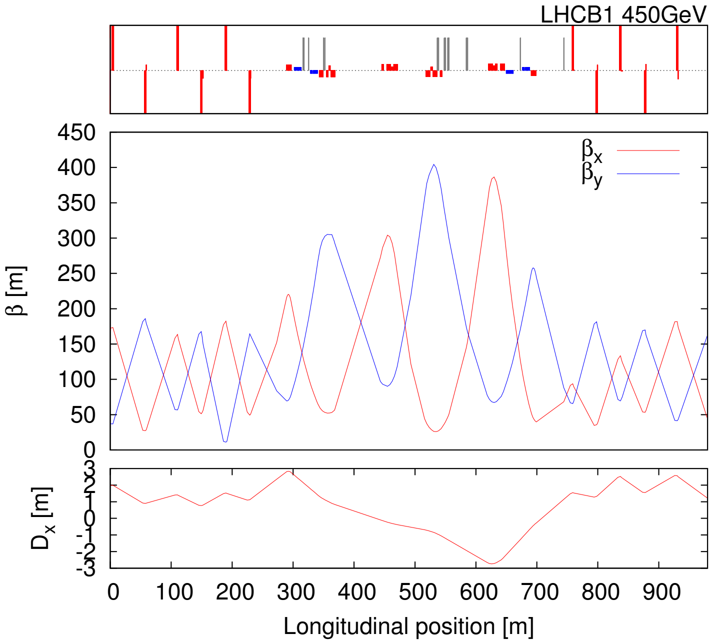

Figure 4.5: IR3 layout is shown at injection energy for beam 1. Top shows a layout of the interaction region. Quadrupole magnets in red and dipole in blue. The collimators are in gray. The Middle plot shows the horizontal and vertical β-function. The horizontal dispersion is shown at the bottom.

Long straight section 4

Long straight section at point 4, houses the RF and feed-back systems as well as some of the LHC Beam instrumentation [68]. Figure 4.6 shows the schematic layout of IR4 at injection energy for beam 1. This region consists of the following structures:

- Two independent RF systems for beam 1 and beam 2 are installed, this requires a larger beam separation in the long straight section of IR4.
- Increased beam separation is provided by two pairs of dipole magnets. In order to be able to provide sufficient space to house the RF.

Long straight section 6

Long straight section at point 6, houses the beam abort systems for beam 1 and beam 2. The beam extraction from the LHC is achieved by kicking the circulating beam horizontally into an iron septum magnet which deflects the beam in the vertical direction away from the machine components to absorbers in a separate tunnel [69]. Figure 4.7 shows the schematic layout of IR6 at injection energy for beam 1. This region consists of the following structures:

- Large drift space, such that the length of the kicker and septum are minimized.
- Extraction septum is protected by the TCDS absorber.
- The Q_4 quadrupole is protected by the TCDQ.

Long straight section 7

Long straight section at point 7 houses the betatron collimation system that absorbs particles where the β function differs – implying different phase advance – from the nominal setting. Larger β-function is generated such that particles would be absorbed in this region and not in the arcs. Figure 4.8 shows the schematic layout of IR7 at injection energy for beam 1. This region consists of the following structures:

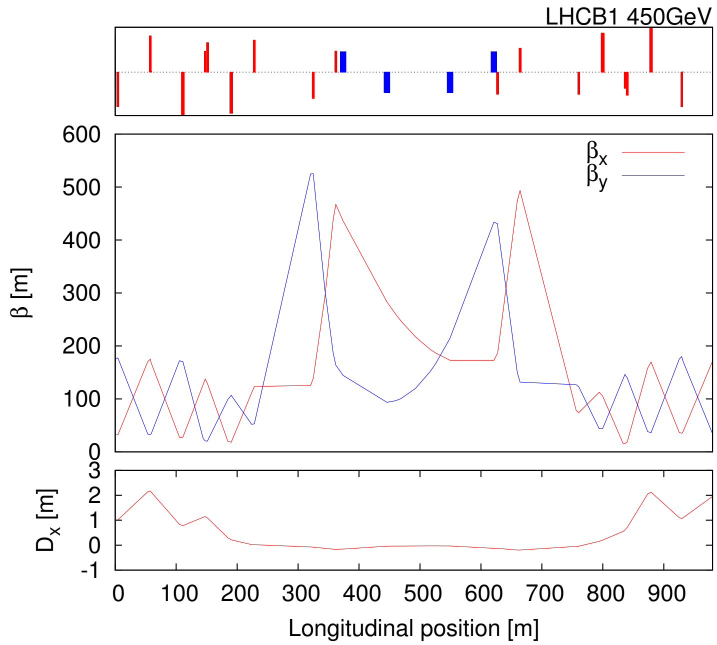

Figure 4.6: IR4 layout is shown at injection energy for beam 1. Top plot shows the layout of the interaction region. Quadrupole magnets in red and dipole in blue. In the middle plot the horizontal and vertical β-function. The horizontal dispersion is shown at the bottom.

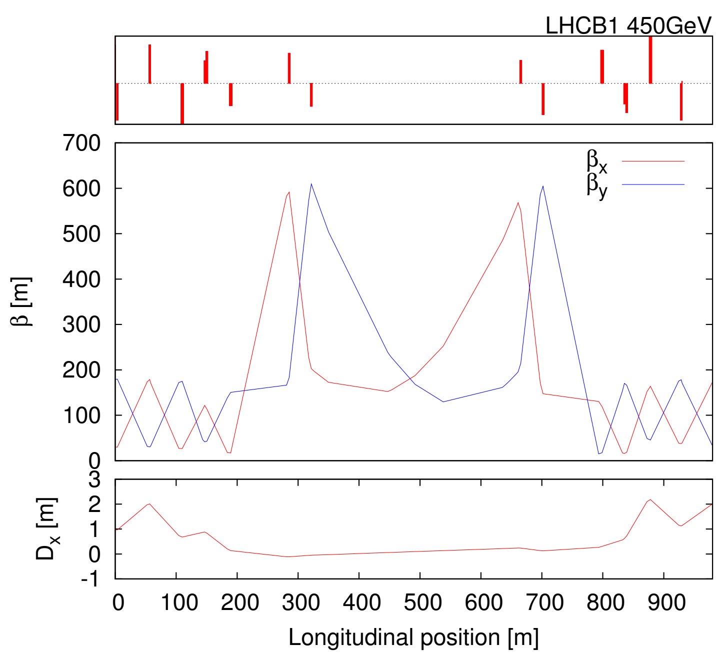

Figure 4.7: IR6 layout is shown at injection energy for beam 1. Top shows the layout of the interaction region. Quadrupole magnets in red and dipole in blue. The middle plot shows the horizontal and vertical β-function. The horizontal dispersion is shown at the bottom.

- Q_6, made out of superconducting MQTL modules.
- Dog-leg structure made out of two sets of MBW warm single bore wide aperture dipole magnets.
- The warm dual-bore (MQW) magnets Q_4 and Q_5 left and right from the IP are powered in series.

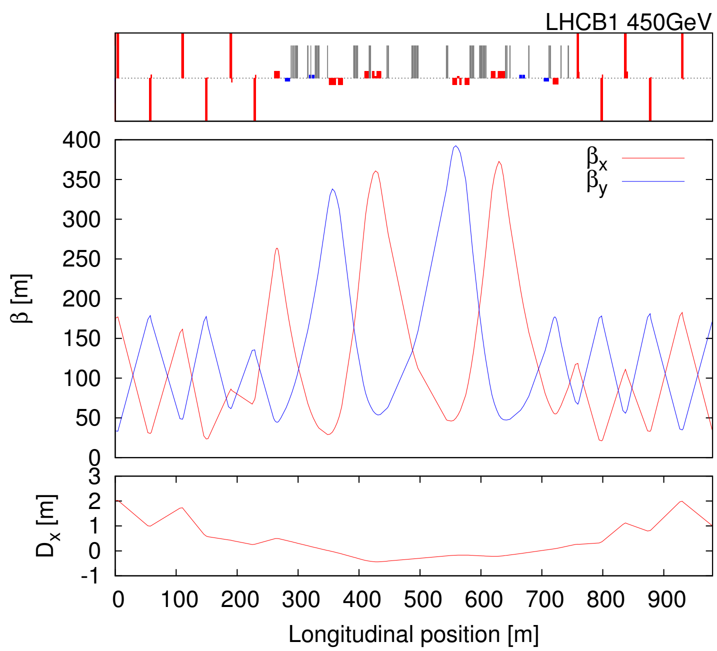

Figure 4.8: IR7 layout is shown at injection energy for beam 1. Top shows the layout of the interaction region. Quadrupole magnets in red and dipole in blue. Collimators are shown in gray. The middle shows the horizontal and vertical β-function. The horizontal dispersion at the bottom.

Long straight section 8

Long straight section 8 houses IR8, the LHCb [70] experiment – which investigates B-Physics – and the injection elements for beam 2. As with the other experiments the small β-function is generated using a triplet quadrupole assembly. The same vacuum chamber is shared by the two rings for the same low-β triplet magnets and the D_1 separation dipole magnet. Special constraints are imposed on the optics during injection for Beam 2. The matching constraints are discussed in [71]. Sufficient space had to be provided for the spectrometer, therefore IR8 is shifted by about 11.25 m towards IR7. Figure 4.9 shows a schematic layout of IR8 at injection energy with no crossing angle for beam 1. The interaction region consists of the following structures:

- A 31 m long superconducting low-β single bore triplet assembly (operated at a temperature of 1.9 K). The triplets quadrupoles are powered by two nested power converters. An additional trim power converter is installed for the Q_1 quadrupole. Other than for the other experiments the Q_1 magnet is located in the tunnel, instead of being supported by a cantilever inside the experimental cavern.
- Three warm dipole magnets are installed to compensate the deflection generated by the LHCb spectrometer magnet.
- A pair of separation/recombination dipoles separated by about 54 m. The D1 is a 9.45 m single bore long superconducting dipole magnet next to the triplet. The 9.45 m long superconducting dipole magnet is a double bore (operated at a temperature of 4.5 K).
- Four matching quadrupole magnets. Q_4 is a wide-aperture magnet (operated at a temperature of 4.5 K). Q_5 to Q_7 are normal-aperture quadrupole magnets (operated at a temperature of 1.9 K)

- Injection for beam 2 happens on the right side of IP8. The 21.8 long injection septum is located between Q_6 and Q_5. The 15 m long injection kicker is located between Q_5 and Q_4.

- Two independent skew quadrupoles are installed at the triplet assembly.

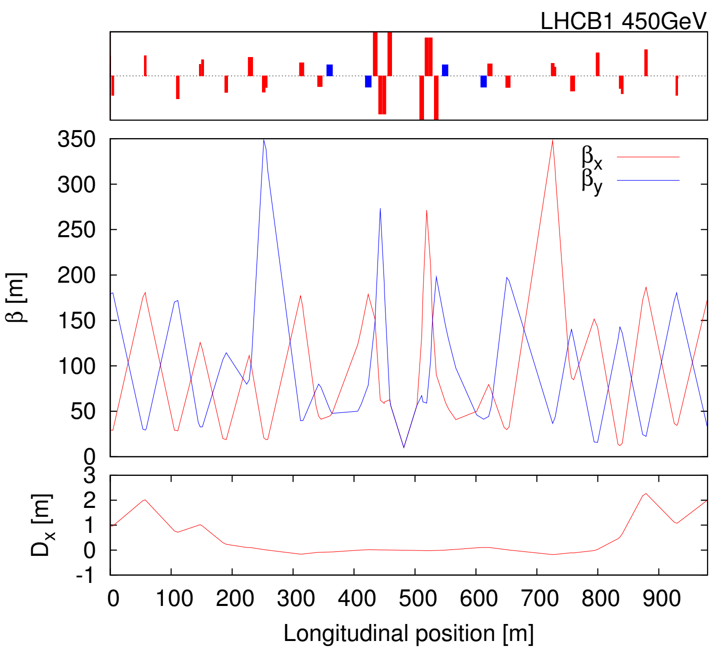

Figure 4.9: IR8 layout is shown at injection energy for beam 1. Top shows the layout of the interaction region. Quadrupole magnets in red and dipole in blue. The middle plot shows the horizontal and vertical β-function. The horizontal dispersion is shown at the bottom. No crossing angle was applied

4.1.2 Arc sections

One arc is constructed out of 23 FBDB cells. The horizontal and vertical phase advance per cell is approximately $90° \pm 2°$. There is a tune split of 2 units in the arcs. The layout of one of the arcs is shown in figure 4.10, a detailed description can be found in [60]. The maximum and minimum β is about 180 and 30 m in the horizontal and vertical plane respectively. The maximum and minimum dispersion is around 1 and 2 m respectively.

Several corrector circuits are installed in the arcs to cope with the different effects. The corrector magnets located in the arcs of the LHC can be split into two distinct categories:

- The lattice corrector magnets, attached on both sides of the main quadrupole magnets are installed, in the Short Straight Section (SSS) cryostat's.

- The spool-piece corrector magnets, which are thin non-linear windings attached directly on the extremities of the main dipoles.

The corrector circuits are separated per beam. Contrary to the main dipole circuits and the two families of lattice quadrupoles, the arc corrector magnets can be adjusted independently for the two beams. An overview of the different arc corrector magnets is summarized in table 4.3.

4.1.3 Tolerances

Tolerances for the optics are specified in [72]. For these simulations different criteria such as the control of the mechanical aperture or the preservation of the dynamic aperture were considered. Table 4.4 shows a summary of the tolerances.

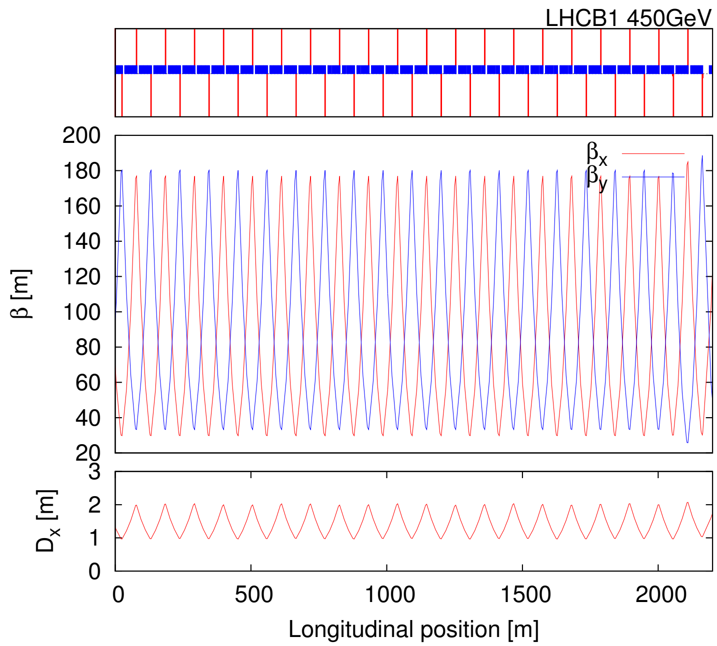

Figure 4.10: Layout of the arcs is shown at injection energy for beam 1. Top plot shows the layout for Quadrupole magnets (red) and dipole (blue). The middle plot shows the β-function for the horizontal (red) and vertical plane (blue). The bottom plot shows the horizontal dispersion.

Name	Description
MSCBH/V	Combined arc orbit corrector and chromaticity or lattice sextupoles. Installed at each focusing and defocussing quadrupole. Arc orbit correctors are powered independently. Sextupoles are divided into two families per beam.
MSS	Lattice skew sextupoles. In each ring and each sector of the machine, four focusing sextupoles are tilted by 90^o and are powered in series.
MQT	Tune-shift or tuning quadrupoles. Two families of 8 tuning quadrupoles per ring and per sector, QTF and QTD, equip the short -straight sections from quadrupole 14 and quadrupole 21 (left and right).
MQS	Arc skew quadrupole corrector magnets. In both of the rings, each sector of the machine is equipped with 2 pairs of skew quadrupoles at quadrupole 23 and 27.
MO	Landau damping or lattice octupoles. Each short section not equipped with MQT or MQS type magnets contains a lattice octupole MO, making a total of 168 MO type magnets per ring.
MCS	Sextupole spool-piece corrector magnets. Each bore of the main dipoles will carry a small sextupole corrector magnet at one end.
MCD/O	Octupole-decapole spool-piece corrector magnet. Every other dipole is equipped at the opposite end.

Table 4.3: Description of the different straight sections and their purpose in the LHC.

Beam observable	Criteria	Tolerance at injection optics	Tolerance at collision optics
Peak radial closed orbit [mm]	Mechanical aperture	4	3
Horizontal rms closed orbit [mm]	Feed down effect	0.4	0.4
Vertical rms closed orbit [mm]	Feed down effect	0.4	0.4
Peak horizontal β-beating [%]	Mechanical aperture	14	15
Peak vertical β-beating [%]	Mechanical aperture	16	19
rms horizontal β-beating [%]	Mechanical aperture	4.8	5.2
rms vertical β-beating [%]	Mechanical aperture	55	5.6
Parasitic horizontal dispersion $(\frac{\Delta D_x}{\sqrt{\beta_x}}_{rms})$ $[m^{\frac{1}{2}}]$	Mechanical aperture	1.30×10^{-2}	1.25×10^{-2}
Parasitic vertical dispersion $(\frac{\Delta D_y}{\sqrt{\beta_y}}_{rms})$ $[m^{\frac{1}{2}}]$	Mechanical aperture	1.20×10^{-2}	1.00×10^{-2}
Maximum momentum deviation $\frac{\Delta p}{p}$	Mechanical aperture	$\pm 1.5 \times 10^{-3}$ (injection energy) $\pm 0.86 \times 10^{-3}$ (top energy)	$\pm 0.86 \times 10^{-3}$

Table 4.4: Tolerances for the LHC optics.

4.1.4 Ramp

The ramp is the mechanism of the beam acceleration. It is called the ramp because of the shape the dipole current follows when the beam is accelerated. Figure 4.11 shows an example of one of the dipoles during the ramp. The acceleration is provided by eight superconducting cavities [73]. Eight superconducting cavities per beam are installed on the left side of IP4. Aside from accelerating the beam, the cavities ensure that the bunches stay bunched.

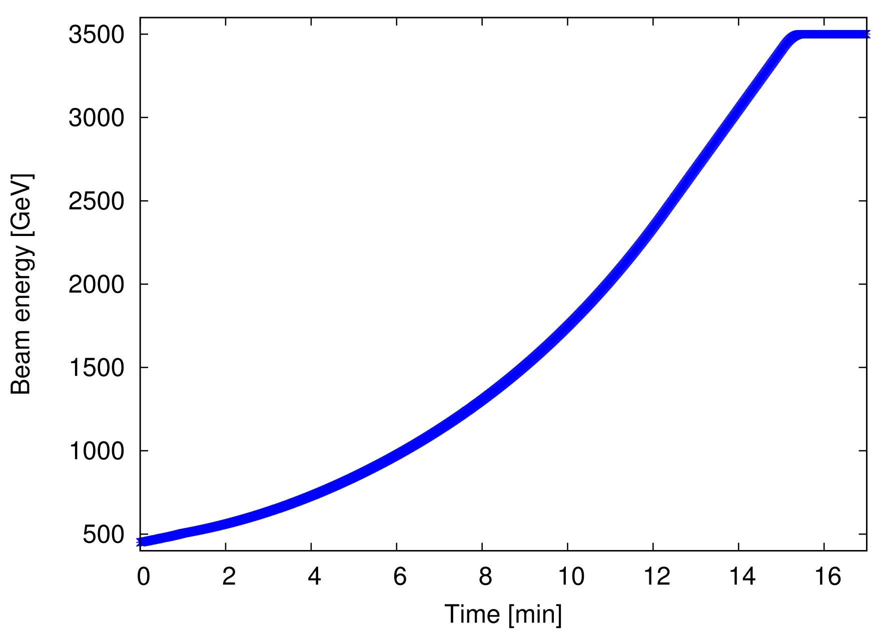

Figure 4.11: Illustration of the current in of the dipoles in the LHC during the ramp.

The beam is injected at an energy of 450 GeV, which is the extraction energy from the SPS. When the chromaticity and tunes are corrected, and (in the case of physics runs) the bunches are injected, the ramp is started. When the beam is accelerated the beam emittance is reduced, as the beam emittance is inversely proportional to the energy.

4.1.5 Squeeze

'Squeeze' is the mechanism of reducing the beam size at the interaction point. This is done by reducing the β^*, hence squeezing the beam. The squeeze for IR1 is used here as an example. Figure 4.12 shows the β-function through the squeeze. The β-function in the arcs remains constant and the β^* is matched using the quadrupoles in the insertion regions. To reach a β^* lower than the design 11 m, the β in the triplets has to be increased.

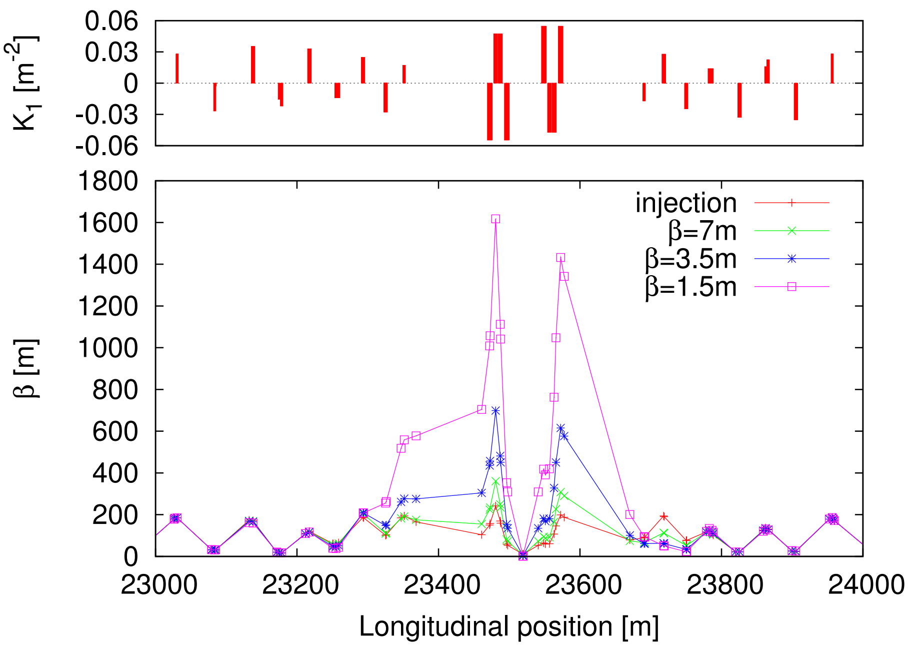

Figure 4.12: Horizontal β-function in the insertion region of IR1 for different β^* (bottom). The location of the quadrupoles, the strengths are for injection optics (top).

Between the injection optics and a β^* value of 1.5 m, the β in the triplets increases by a factor of approximately 8. The squeeze has a large impact on the currents in the insertion regions. Figure 4.13 shows the currents in the magnets in the insertion regions of IR1. The triplets are not shown as they stay constant. When squeezing down to a β^* value of 1.5 m, the maximum current change in the magnets is about 700 A with respect to the injection optics.

The motivation behind this effort is to reach a small spot size, in order to reach higher luminosity. The bottom plot of figure 4.13 shows the beam size with respect to the β^* (red). The blue plot shows the luminosity with respect to the maximum value at 1.5 m in percentage. At injection optics, the luminosity produced is 80% less than for a β^* value of 1.5 m

4.1.6 Crossing angles

During the optics measurements the crossing angles are zero and the bumps are not collapsed, i.e, during the measurements the beams are not colliding. The bumps and the crossing angle are introduced by using the orbit correctors around the IRs. The effect of collapsing the bumps is negligible. Simulations were conducted to investigate the effect of introducing the crossing angle. The crossing angle in IR5, IR8 is horizontal and in IR1, IR2 is vertical, the maximum orbit caused by the crossing angle is about 8 mm. Figure 4.14 shows the horizontal and vertical orbit together with the normalized horizontal and vertical dispersion beat.

The effect of the crossing angle in the horizontal dispersion is obvious, two large steps are observed around IP5 and IP8. The effect on the vertical dispersion is less, as the ideal machine does not have any vertical dispersion.

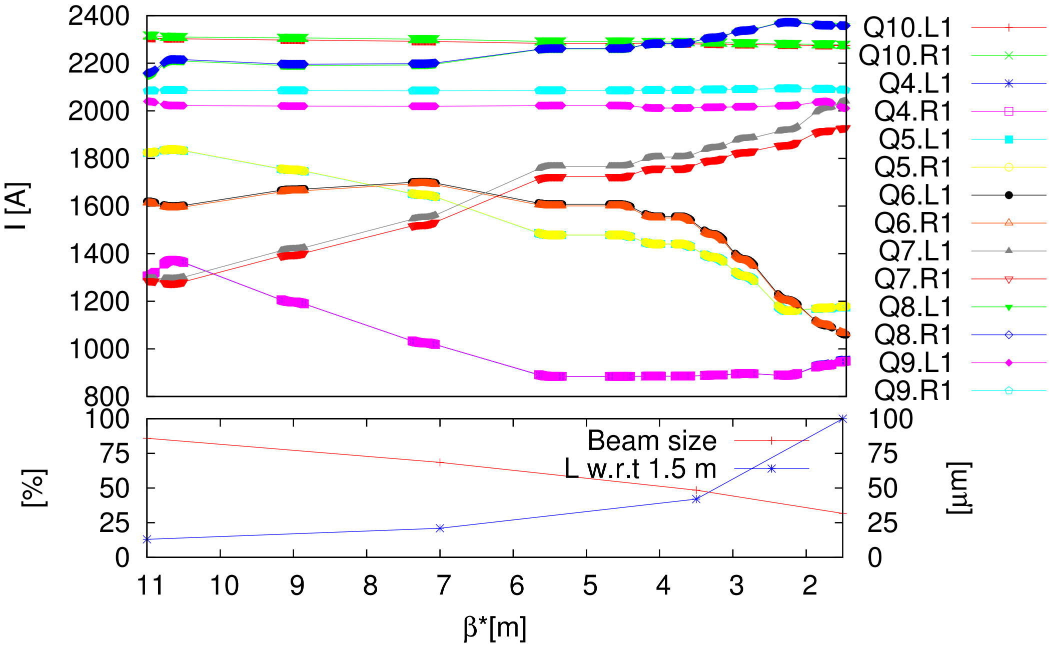

Figure 4.13: The current in the magnets in the insertion region IR1 with respect to β^* (top), luminosity and beam size with respect to the β^* in IR1.

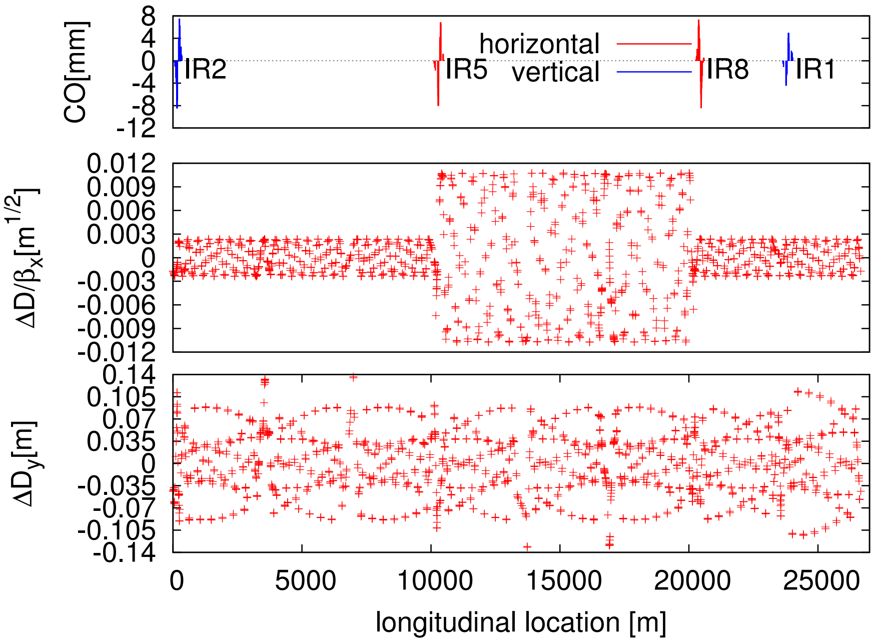

Figure 4.14: Horizontal normalized (middle) and vertical dispersion (bottom) beat for optics with and without crossing angle for beam 1. Top plot shows the horizontal and vertical orbit when introducing the crossing angle.

Figure 4.15 shows the β-beat generated by introducing the crossing angles. From the figure it can be observed that both in the horizontal and vertical plane, the β-beat is negligible. For IP8 a small leakage after the crossing angle was introduced is observed.

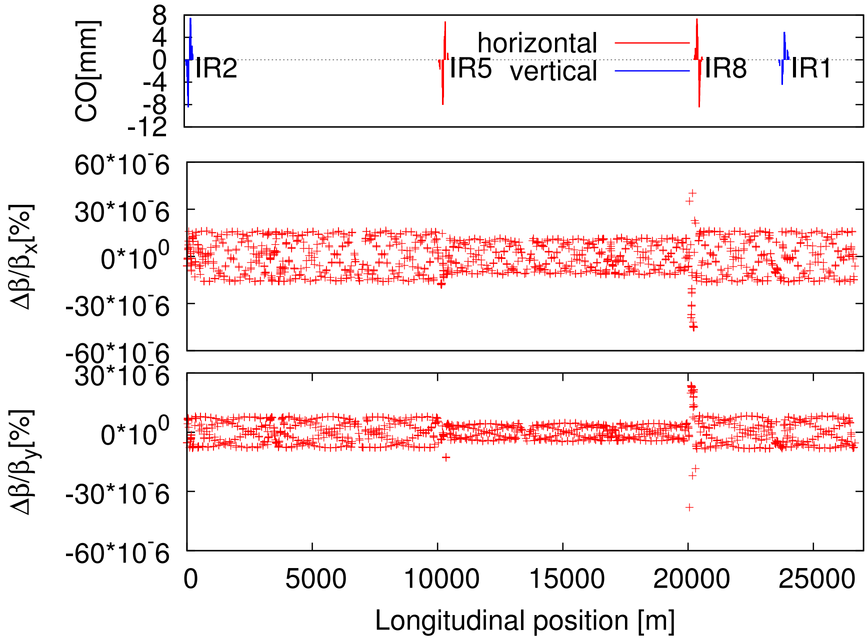

Figure 4.15: Horizontal (middle) and vertical β-beat (bottom) beat for optics with and without crossing angle for beam 1. Top plot shows the horizontal and vertical orbit when introducing the crossing angle.

4.2 Simulations for the LHC

Simulations play an important role in checking the performance of the LHC and to validate the algorithms developed. Subsection 4.2.1 will discuss the simulations performed to explore the measurement errors. After the unfortunate incident in 2008 (where several skew quadrupole correctors were damaged) coupling simulations were conducted to explore the coupling correction limitations, this is discussed in subsection 4.2.2. An algorithm was developed to easily derive the β^* and waist at the IPs. Simulations were conducted to explore the limitations of this algorithm. This is discussed in subsection 4.2.3. Chromatic β-functions play an important role when reaching lower β^*. This will be discussed in subsection 4.2.4, together with the limitations of the algorithms that were developed.

4.2.1 Simulations for measurements

Simulations were conducted to investigate the error on the β-functions from phase. Two cases were studied, the first one during injection and the second with squeezed beams where IP1, IP2, IP5 are at a β^* value of 1.5 m and IP8 is at 2 m. Noise of 150 μm is applied randomly to the turn-by-turn BPM data and a kick of about 1 mm in an arc focusing BPM is applied as well. In figure 4.16 the relative error on the β calculation (left), and on the right the relative error of the standard deviation are shown. The relative error is defined as error divided by the β at the location. From the figure it can be observed that the error from the 3-BPM method is larger than for the standard deviation. The error from the 3-BPM method is larger in the vertical plane than for the horizontal plane. The result of the right plot depends largely on the amplitude of the noise, larger noise will result in a larger error.

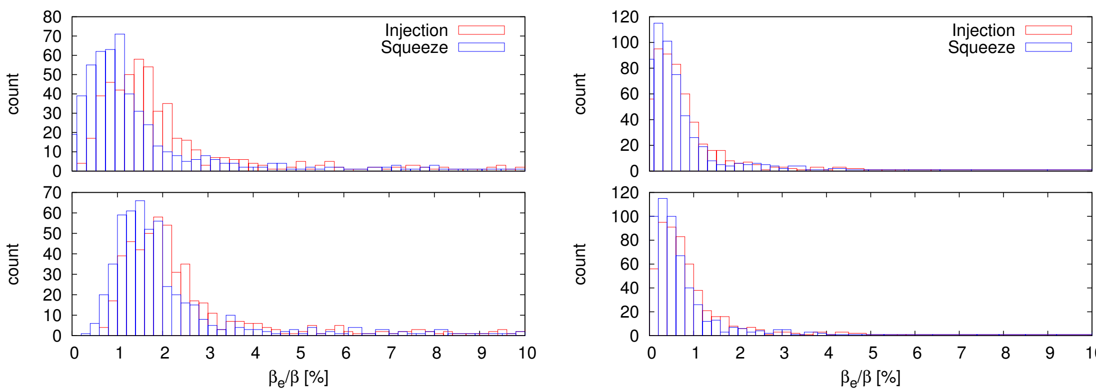

Figure 4.16: Simulation of the error on the β-functions from phase (left) and the standard deviation (right). Results for both the horizontal (top) and vertical (bottom) plane and the relative error are shown.

Figure 4.17 shows the β-beat between the simulations and the model for beam 1. Both the horizontal and vertical plane can be reconstructed with good agreement. The main part of the distribution is below 2%.

For both figures it is observed that the error for injection is slightly larger than for squeezed optics.

4.2.2 Coupling simulations for the LHC

After the 2008 incident, a few skew quadrupoles were damaged and subsequently removed from the tunnel. This could limit the correction of local coupling in the LHC. The damaged sector was sector 3-4. In the sector for beam 1 the skew quadrupole family kqs.r3b1 (2 magnets), kqs.l4b1 (2 magnets) and for beam 2 kqs.a34b2 (4 magnets) were removed. In order to increase the exibility in the coupling correction the use of vertical orbit bumps at the sextupoles was investigated. Moreover a simultaneous coupling and vertical dispersion can be implemented. Various studies [74], [75] addressing the optimal approach for the correction of the vertical dispersion and the sum and difference coupling resonances will be discussed here.

As the LHC is running on injection tunes of (59.28, 61.31) and collisions tunes of (59.31, 61.32), the difference coupling resonance ($Q_x - Q_y = N$) dominates. The effect of the sum resonance ($Q_x + Q_y = N$) is rather small.

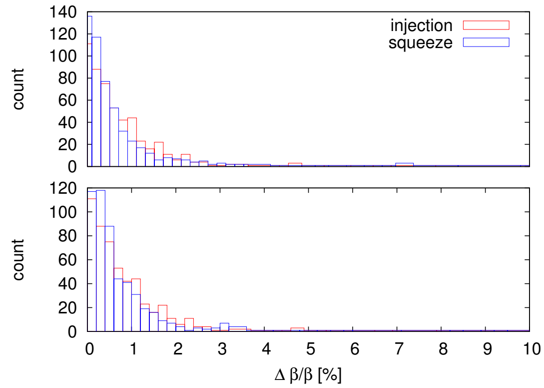

Figure 4.17: Simulation for the systematic error on the β calculation. The β-beat for both the horizontal (top) and vertical (bottom) plane is shown.

Simulations were conducted for both beams at injection [75]. Three cases were considered:

- Correction using skew quadrupole correctors, where weights were applied for the difference resonance.
- Correction using skew quadrupole correctors, where weights were applied for both the sum and difference resonance.
- Correction using vertical orbit bumps at the sextupoles, where weights were applied on both the difference resonance and the vertical dispersion.

The three cases were run for 100 seeds where transverse rotation to all quadrupoles was randomly applied distributed around the ring.

Skew quadrupoles

For the correction of the skew quadrupoles, no weight was placed on the vertical dispersion, as it would have been impossible to correct it. The reason for this is that in order to minimize the excitation of vertical dispersion the two skew quadrupole magnets of each pair are separated by a phase advance of $\mu_y = \pi$. Additionally, the two pairs are separated by a phase advance of $\mu_x + \mu_y = n\pi$ in order to minimize the β-beat generated by the skew quadrupole magnets[76].

Weights only on the difference resonance For the first simulation of the skew quadrupole correction, weights were only placed on the difference resonance. Figure 4.18 shows the difference and sum resonance. The difference resonance was significantly corrected for both beams. The correction for beam 1 was more effective than for beam 2. A possible explanation could be that the 4 missing magnets in sector 3-4 for beam 2 have a larger impact than the 4 missing magnets right from IR3 and left from IR4 for beam 1. As no weight was placed on the sum resonance, it was not corrected.

Figure 4.19 shows the vertical dispersion, which is generated after rotating randomly the quadrupoles. The generated vertical dispersion for beam 2 is larger than for beam 1. No weights were placed on the vertical dispersion and due to the π placement of the skew quadrupoles, it was impossible to correct the vertical dispersion.

Weights both on the sum and difference resonance For the second simulation for the skew quadrupole correction, weights were placed both on the difference and the sum resonance. Figure 4.20 shows the difference and sum resonance. The difference resonance was significantly corrected for both beams. The correction for beam 1 was more effective than for beam 2. Again, a possible explanation could be that the 4 missing magnets in sector 3-4 for beam 2 have a larger impact than the 4 missing magnets right from IR3 and left from IR4 for beam 1. This time the weight was also placed on the sum resonance, from the figure it is clear that it is possible to correct the sum resonance as well. The correction in beam 2 was less effective than for beam 1.

Figure 4.21 shows the vertical dispersion, which is generated after rotating the quadrupoles. The generated vertical dispersion for beam 2 is larger than for beam 1. No weights were placed on the

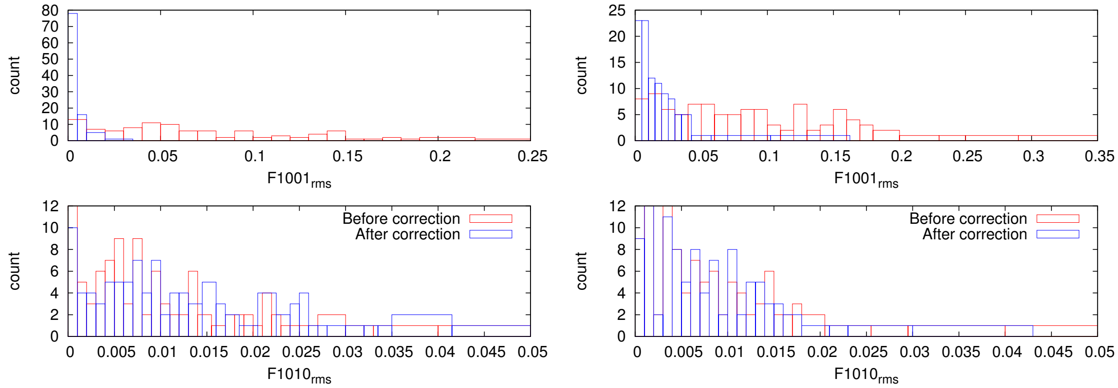

Figure 4.18: The difference (top) and sum (bottom) resonance for beam 1 (left) and beam 2 (right). Two cases are shown before (red) and after correction (blue). Results shown here where a weight was only placed on the difference resonance. Here the sum resonance is left uncorrected.

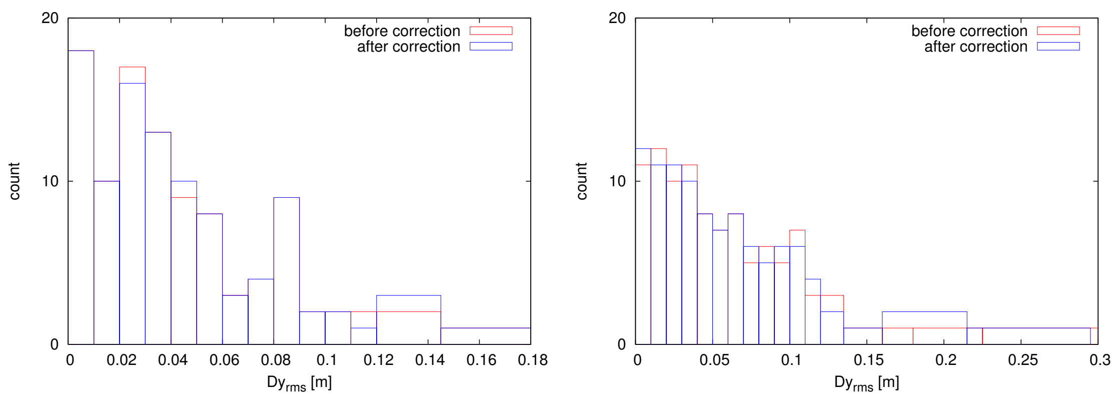

Figure 4.19: The vertical dispersion for beam 1 (left) and beam 2 (right). Two cases are shown before (red) and after correction (blue). Weight is placed on the difference resonance.

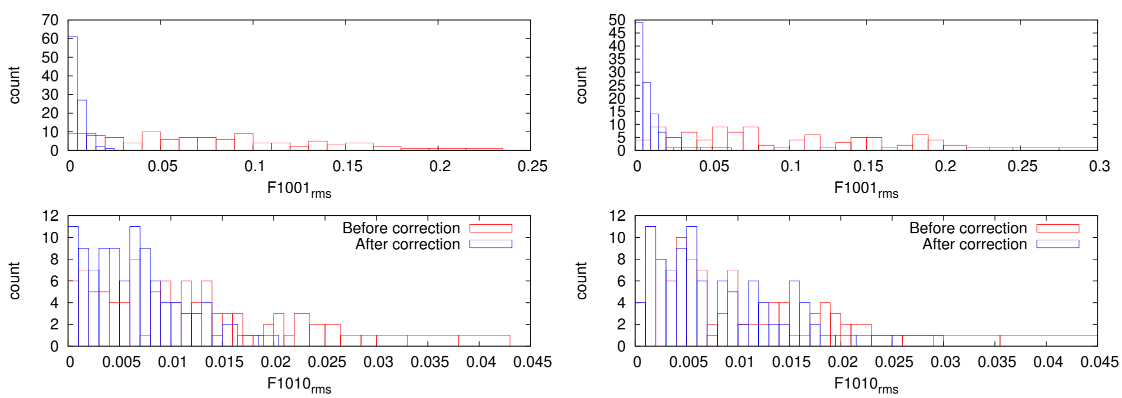

Figure 4.20: The difference (top) and sum (bottom) resonance for beam 1 (left) and beam 2 (right). Two cases are shown before (red) and after correction (blue). Weight is placed both on the difference and sum resonance.

vertical dispersion and due to the π-placement of the skew quadrupoles, it was impossible to correct the vertical dispersion.

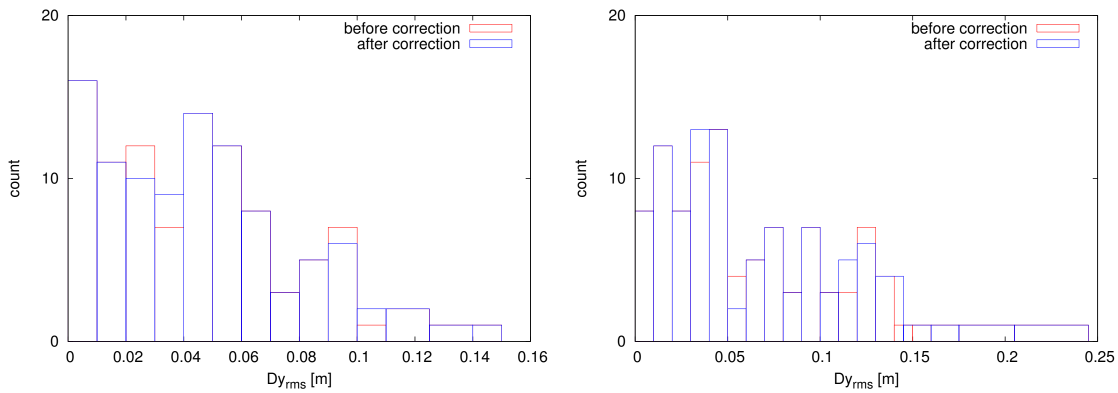

Figure 4.21: The vertical dispersion for beam 1 (left) and beam 2 (right). Two cases are shown before (red) and after correction (blue). Weight is placed both on the difference and sum resonance.

Strength in the skew quadrupoles In the previous paragraph it was shown that it is possible to correct both the difference and sum resonance. Figure 4.22 shows a comparison between the needed rms strength in the skew quadrupoles, for correction only on the difference resonance and correction on both the sum and difference resonance.

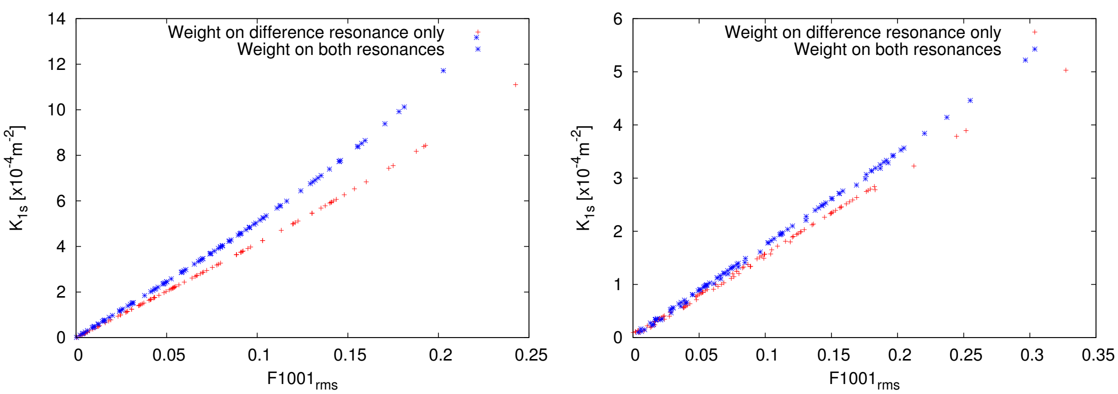

Figure 4.22: The rms corrector strength versus the f_{1001} for when weight was placed only on the difference resonance (red) and both on the difference and sum resonance (blue) for beam 1 (left) and beam 2 (right).

It is interesting to see that for beam 1 the needed corrector strength is higher than for beam 2. From the two plots in figure 4.22 it is clear that by applying weight on the difference and sum resonance the needed strength is significantly increased. As the contribution of the sum resonance to the coupling is an order of magnitude smaller, no weight should be put on the sum resonance.

Coupling correction using vertical orbit bumps at the sextupoles

An alternative correction scheme to correct the coupling was proposed. This scheme uses vertical orbit bumps at sextupoles. This correction scheme was already successfully applied in the SPS [74]. It could also be used in the case where the vertical dispersion would become an issue. This is because with the skew quadrupoles it is impossible to correct the vertical dispersion.

Figure 4.23 shows the orbit, difference and sum resonance. The difference resonance was significantly corrected for both beams significantly. As no weight was placed on the sum resonance, no correction was observed. Weights were only applied to the difference resonance and the vertical dispersion. The asymmetry in correction which was observed between the two beams when using skew quadrupoles as correctors is not observed anymore.

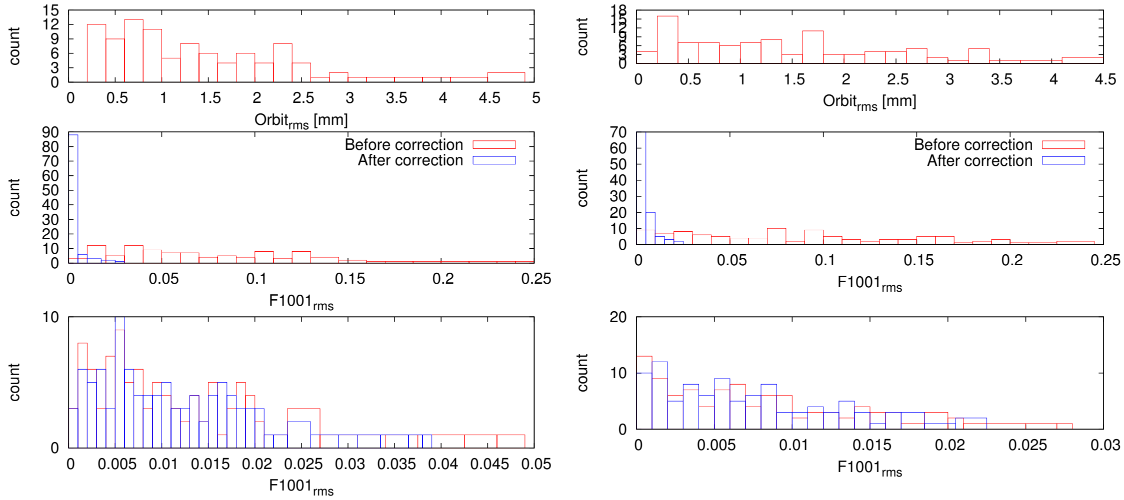

Figure 4.23: The orbit (top), difference (middle) and sum (bottom) resonance for beam 1 (left) and beam 2 (right). Two cases are shown before (red) and after correction (blue). Weight is placed both on the difference and the vertical dispersion.

Figure 4.24 shows the vertical dispersion, which is generated after rotating the quadrupoles. The generated vertical dispersion for beam 2 is larger than for beam 1. The vertical dispersion was significantly reduced for both beams.

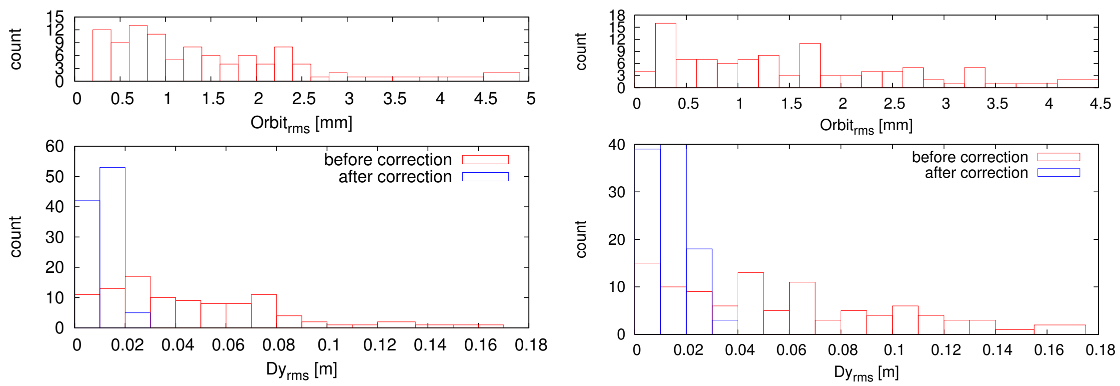

Figure 4.24: The orbit (top) and vertical dispersion (bottom) for beam 1 (left) and beam 2 (right). Two cases are shown before (red) and after correction (blue). Results shown here is for the case where weight was placed both on the difference and the vertical dispersion.

The rms vertical orbit which was needed to correct the coupling and the vertical dispersion is slightly larger for beam 2 than for beam 1. The peak orbit needed for the largest error is around 4.5 mm.

Needed correction strength for squeezed optics

All the simulations were conducted at injections. The effect of the errors on the squeezed optics was investigated. Figure 4.25 shows simulations conducted for corrections at injection and squeezed optics with all IPs at a β^* value of 2 m. The needed strength decreases when the optics is squeezed.

No problems were expected for squeezed optics. Therefore simulations were only conducted for injection optics.

Conclusion

When using skew quadrupoles there is a slight difference between beam 1 and beam 2. The needed strength for beam 2 is lower than for beam 1. A possible explanation is that the skew quadrupoles in

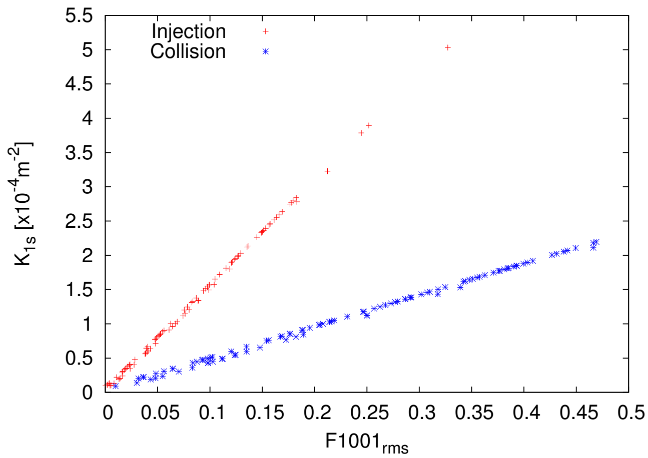

Figure 4.25: The rms corrector strength versus the f_{1001} for injection (red) and for squeezed optics (blue) with all IPs at a β^* value of 2 m.

sector 3-4 in beam 2 play a larger role than the skew quadrupoles right from IR3 and left from IR4 for beam 1.

When including the sum resonance in the correction a larger correction strength is needed. From the simulations, it is clear that the correction of the difference and sum resonance can be corrected separately.

Unfortunately, due to the specific placement of the skew quadrupoles it is impossible to correct the vertical dispersion using skew quadrupoles. Therefore the alternative correction scheme using vertical orbit bumps at the sextupoles could be used to correct the vertical dispersion and also the coupling.

4.2.3 Simulations for β^* and waist.

The motivation for conducting simulations for β^* and waist is twofold. A first study was conducted to estimate the systematic error. And a second study was conducted to estimate the effect of local errors in the triplets at the IPs. The motivation for the second simulation was that due to large error bars, the BPMs at the triplets are not always available. Simulations were conducted for a β^* value of 2 m and a β^* value of 3.5 m.

Introduction

In figure 4.26 an example for the principle of the segment-by-segment technique for propagation is shown. The black line shows the measured β-function. The red line represents normal propagation and the blue black propagation.

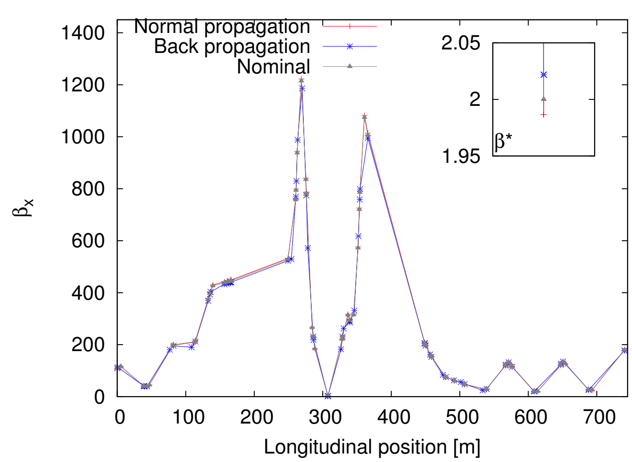

Figure 4.26: A graphical representation of the segment-by-segment technique principle.

The following nomenclature is used:

- IP = Name of the interaction point as defined in MADX.
- $\beta^{ip}[m]$ = Beta at the design IP.
- $\delta\beta^{ip}[m]$ = Error of the beta at the design IP.

Simulations

For the systematic error noise with a value of 150 μm was randomly applied to the BPMs, This is according to the specifications of the BPMs. During operation the BPMs 2-7 are normally used, and the BPMs which are close to the triplets. This was the direct motivation for the second simulation, which was conducted to investigate the effect of applying an error of 1% to the MQX magnets. This study would show how accurate the β^* and waist could be measured. Both studies were conducted for 100 seeds.

Simulations for all IPs at a β^* value of 2 m In figure 4.27 an estimate for the systematic error for both the β^* and waist is shown. The plot on the left shows a histogram for β^*, the plot on the right shows a histogram for the waist. The points represent the histogram for simulations. The solid lines are the Gaussian fit to the data. For a β^* value of 2 m the systematic error on β^* is $\sim 1\%$ and ~ 5 cm for the waist offset.

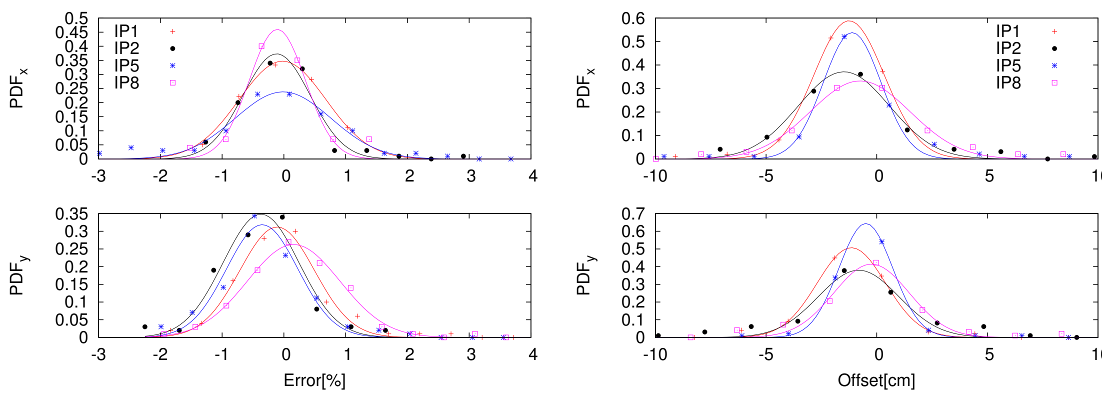

Figure 4.27: The left plot shows a histogram for β^*, the right plot shows a histogram for the waist. The solid lines are Gaussian fit to the data. For a β^* value of 2 m the systematic error on β^* is $\sim 1\%$ and $\sim 5cm$ for the waist offset.

In figure 4.28 an estimate for the error coming from a mismatch in the IR triplets is shown for β^* at 2 m. It can be observed that in the majority of the cases the β^* can be reproduced in a 5 % level. Except for for the vertical plane of IP5 where the β^* can be measured in a 10 % level.

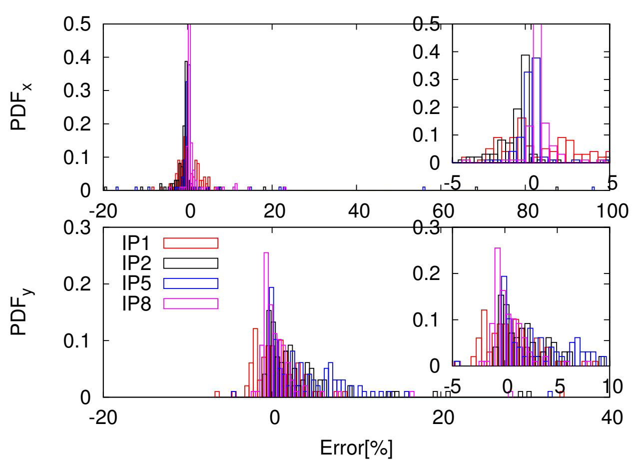

Figure 4.28: Plot showing histogram with the reproducibility of β^* at 2 m.

Simulations for all IPs at a β^* value of 3.5 m In figure 4.29 an estimate for the systematic error is shown for both the β^* and waist. The left plot shows a histogram for β^*, the right right plot shows a histogram for the waist. The solid lines are the Gaussian fit to the data. For $\beta^* = 2m$ the systematic error on β^* is $\sim 2\%$ and ~ 75 cm for the waist offset.

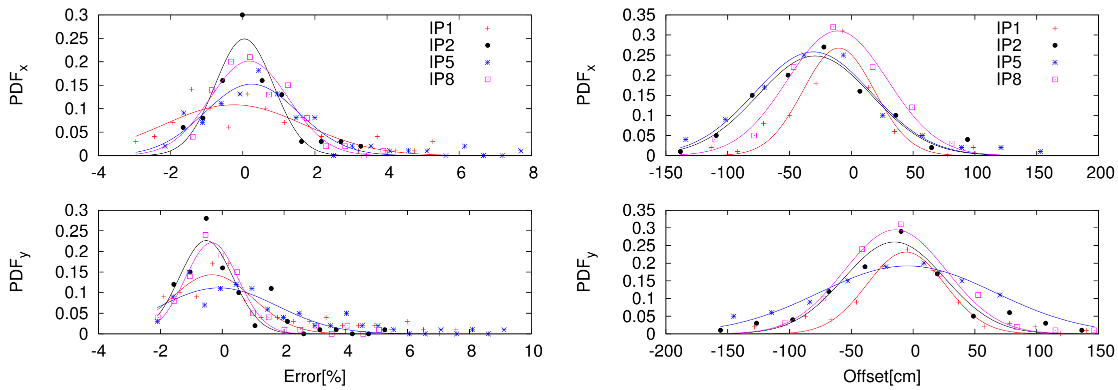

Figure 4.29: The left plot shows a histogram for β^*, the right plot shows a histogram for the waist. The solid lines are the Gaussian fit to the data. For β^* value of 2 m the systematic error on β^* is $\sim 2\%$ and ~ 75 cm for the waist offset.

In figure 4.30 an estimate for the error coming from a mismatch in the IR triplets for both the β^* and waist is shown.

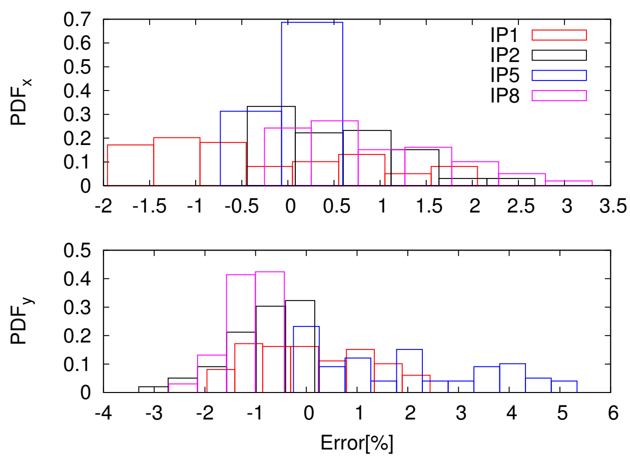

Figure 4.30: Histogram showing the reproducibility of β^* at 3.5 m. It can be observed that the β^* can be measured within a 1 % level. Except for the vertical plane of IP5.

Conclusions

When considering 1σ for the error estimates, see table 4.5, it becomes obvious that the result of calculating the waist from the propagation technique does not meet the required specifications of the experiments. This is more apparent for higher β^*. For this reason waist calculations are not presented, but alternative methods such as K-modulation should be used to determine the waist. The reproducibility of the β^* when local error in the triplets are applied is maximum 6%. The error applied was a magnitude bigger then the observed error in the IPs.

4.2.4 Simulations for chromatic functions.

When reaching lower β^* the control of the chromatic aberrations for the β-function is important to avoid aperture limitations. Algorithms were developed to measure these aberration. Dedicated

IP1				
Variable	$\mathbf{1}\sigma_x$	e_x[%]	$\mathbf{1}\sigma_y$	e_y[%]
β_{2m}	0.703	4.4	0.604	4.7
w_{2m}	1.594	4.5	1.544	4.1
$\beta_{3.5m}$	1.958	14.3	1.314	14.7
$w_{3.5m}$	28.804	11.0	31.512	6.9
IP2				
Variable	$\mathbf{1}\sigma_x$	e_x[%]	$\mathbf{1}\sigma_y$	e_y[%]
β_{2m}	0.768	9.1	0.869	10.8
w_{2m}	2.923	5.7	2.577	9.4
$\beta_{3.5m}$	1.143	12.7	1.224	16.8
$w_{3.5m}$	65.064	7.8	57.677	9.4
IP5				
Variable	$\mathbf{1}\sigma_x$	e_x[%]	$\mathbf{1}\sigma_y$	e_y[%]
β_{2m}	1.096	6.5	0.899	5.1
w_{2m}	1.842	4.5	1.723	4.3
$\beta_{3.5m}$	1.830	8.5	2.669	14.5
$w_{3.5m}$	66.768	6.2	100.906	6.7
IP8				
Variable	$\mathbf{1}\sigma_x$	e_x[%]	$\mathbf{1}\sigma_y$	e_y[%]
β_{2m}	0.643	13.5	1.060	2.6
w_{2m}	3.191	4.8	2.413	5.6
$\beta_{3.5m}$	1.536	10.2	1.212	5.9
$w_{3.5m}$	57.285	7.5	58.568	6.5

Table 4.5: Table showing 1σ for the error estimates and the error for both the horizontal and vertical plane. The two difference cases are presented, 2 and 3.5 m for IR1, IR2, IR5 and IR8.

simulations were conducted to test the implemented algorithms. The observable used is the Montague function [39].

The first simulation was conducted to find the possible limitations on the existing algorithms with respect to the δp range. A histogram of the relative measurement error is shown in Fig. 4.31. Two different simulations are shown. In red, a small frequency trim was applied, $\delta p = \pm 0.5 \times 10^{-3}$. For blue a medium radial frequency trims was applied, $\delta p = \pm 10^{-3}$. The error of the chromatic amplitude function increases when higher radial frequency trims are applied. This is because β is no longer linear for larger δp.

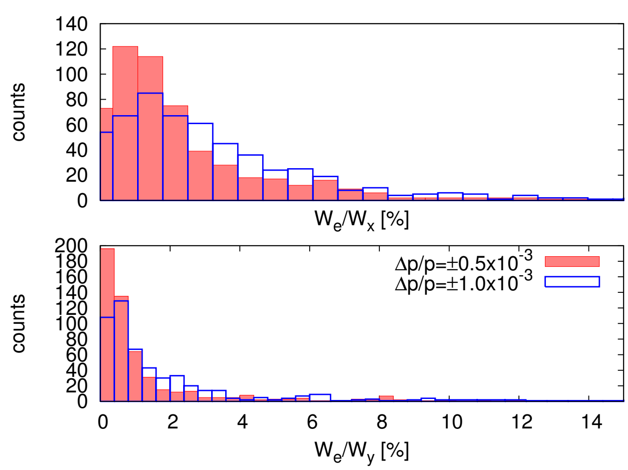

Figure 4.31: Histogram of the relative systematic measurement error is shown. For the horizontal plane (above) and vertical plane (below). Two different simulations are shown.

The second simulation was conducted to identify the systematic difference between the model and particle tracking. Two different models were used. One model was constructed using Twiss parameters at different δp settings (from here on defined as the external model). The other model was constructed using the chromatic function calculated in MAD-X (from here on defined as internal model). Figure 4.32 shows a histogram of the normalized difference between measurement and model, for both models. Small δp setting for external model (red), medium δp setting for the external (blue) and internal model (black) are shown. The small δp setting for the internal model is not shown, as the result is similar to the medium δp setting. A large discrepancy between the two models is observed, mainly in the vertical plane. This discrepancy is $\sim 5\%$ and 15%, respectively for the external and internal model. Tracking for different δp setting shows almost no influence in the vertical plane. However, in the horizontal plane, tracking for smaller δp shows larger error.

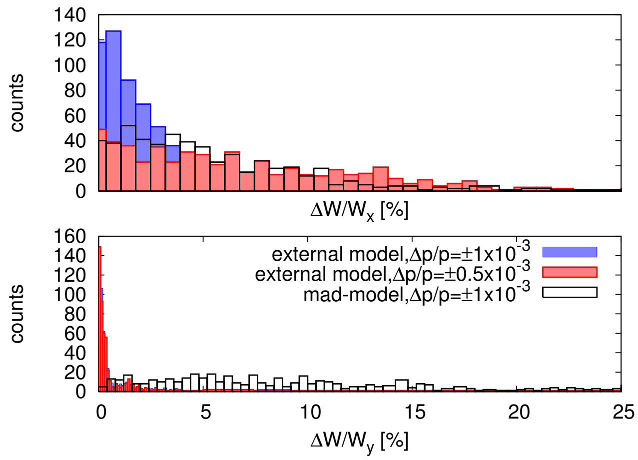

Figure 4.32: Histogram of the normalized difference between measurement and model, for small δp setting for external model (red) and model (pink) and for medium δp setting for external model (blue) and model (green). Large discrepancy between the two models is observed, mainly in the vertical plane.

The conclusion from the simulations is that δp settings in the range of $0.5 - 1 \times 10^{-3}$ should be applied. The external model is the preferred model. as a large discrepancy was observed between the internal model and tracking.

Chapter 5

LHC optics commissioning

The first two years of operation of the LHC were characterized by the exploration of this complex machine and its optics. The experiences derived from the first injection after the unfortunate incident in September 2008, from the second local corrections in the LHC at injection in March 2010, to the observations at the first ramp are described in section 5.1. One month after the first beam was injected in 2010, the high luminosity experiments, at IR1 and IR5, were squeezed to a β^* value of 2 m. The squeeze for IR8 and IR2 soon followed. The measurements and corrections at a β^* value of 2 m are discussed in section 5.2. In the second half of 2010 it was decided that the β^* settings should be changed to a value of 3.5 m, so that time could be saved in the commissioning of the crossing angles. The relaxed settings of a β^* value of 3.5 m are discussed in section 5.3. After a short technical stop from December 2010 to January 2011, the commissioning was resumed in February 2011. It was decided that the β^* for the high luminosity experiments could be further reduced to 1.5 m, and in August to a $beta^*$ value of 1 m. The β^* value of IP2 was kept at 10 m during the proton run of 2011. During the run of 2011 IP8 remained at a β^* value of 3 m. The commissioning of the proton run in 2011 is discussed in section 5.4. In October 2011 IP2 was commissioned with a β^* value of 1 m for the ions run. This is discussed in section 5.5. During dedicated machine development studies the first measurement of the f_{3000} resonance driving term was performed. This, together with the chromatic studies, is discussed in section 5.6. Performance of the beam position monitors and statistics on the error bars of the optics functions are discussed in section 5.8. Finally, section 5.8 gives an outlook on what to expect for the optics when the ultimate energy of 7 TeV will be reached.

5.1 Optics measurements at injection and during the energy ramp

The first measurements with circulating beam in the LHC were conducted in 2008 [40]. Injection oscillations for 90 turns were acquired for both beams. An initial $\beta-$beat of 40% and 100% in the horizontal and vertical plane respectively was observed for beam 2. Using the Segment-by-Segment technique, it was found that a cable swap between beam 1 and beam 2 magnets at IR3 were the direct cause for the large β-beat observed. After the shutdown and necessary repairs after the 2008 incident [77], beams were injected in the LHC again in November 2009. Since then several measurements at injection were conducted, these measurements are discussed in section 5.1.1. The measurements during the ramp and at flattop are discussed in section 5.1.2.

5.1.1 Injection measurements and corrections

An overview of the commissioning of the injection optics until May 2010 for beam 2 is shown in figure 5.1. The top plot shows the peak β-beat versus time and the bottom plot shows the rms orbit versus time. The horizontal plane is shown in red and the vertical plane in blue. The rms orbit has been reduced from initially 2 mm to 0.5 mm. A clear correlation between the rms orbit and the peak β-beat is observed since the orbit correction [78] assumes the ideal model.

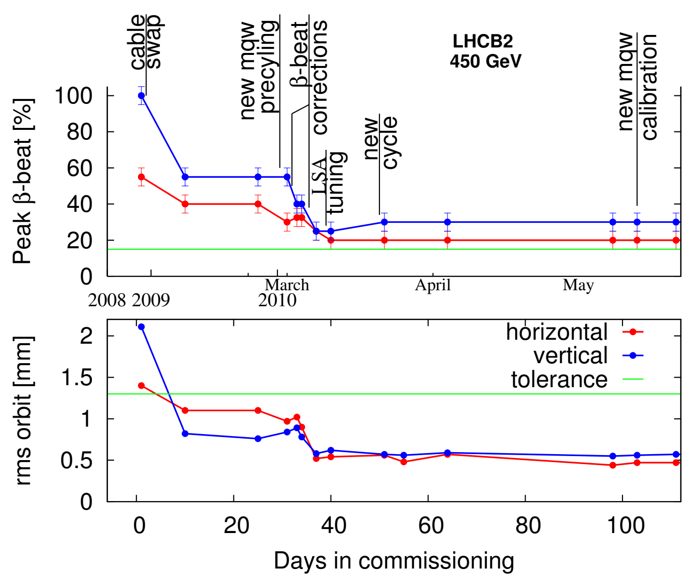

Figure 5.1: Overview of the commissioning of the injection optics until May 2010 for beam 2. Top plot shows the horizontal and vertical peak β-beat versus time. Bottom plot shows the horizontal and vertical rms orbit versus time. The tolerance for the β-beat and the orbit are shown in green.

In 2009 a β-beat of up to 60% was observed in the vertical plane of beam 2, this was not corrected at that time due to time limitations. Before the start-up in March 2010 a new precycle was introduced for the warm quadrupoles, MQW, this had no significant effect on the observed peak β-beat. The local β-beat corrections calculated using the segment-by-segment technique were implemented in March 2010, this successfully reduced the peak β-beat to a 20% level. In May 2010 new calibrations consistent with the β-beat corrections replaced the old corrections which maintained the good quality of the corrections. The 25% level for the peak β-beat was maintained for injection during 2010 and 2011, slightly above tolerances. Further corrections could improve the β-beating but the current level was considered to be acceptable for the existing aperture due to a lower than expected rms orbit. Before April 2010 the measurements at injection were conducted using either injection oscillations or the aperture kicker. From April 2010 on the AC-dipole was used.

β-beat measurements and corrections

β-beat measurements were conducted during 2009, 2010 and 2011. The steps in the correction process are discussed here. Figure 5.2 shows one of the first β-beat measurements in 2009. β-beat of up to

40% − 50%, well above the defined tolerances (shown by the blue horizontal lines), was observed for both beams.

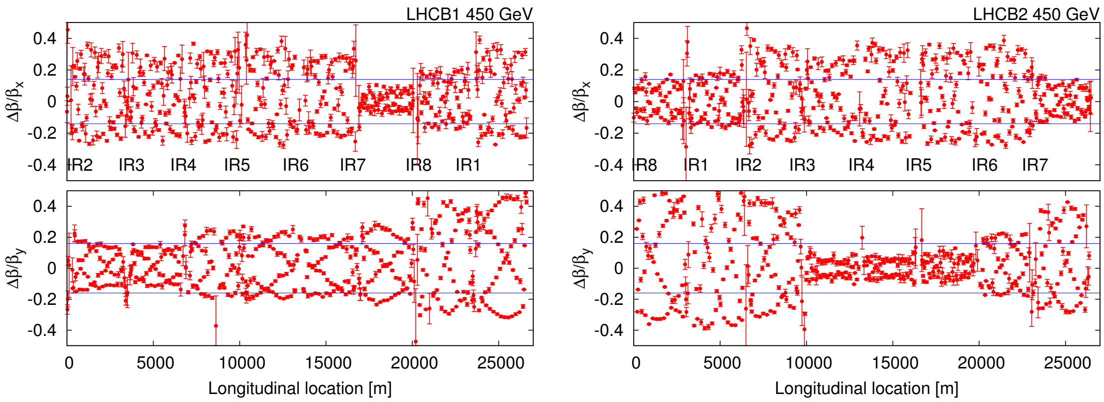

Figure 5.2: β-beat at injection for beam 1 (left) and beam 2 (right). The defined tolerances are shown by the blue horizontal lines.

Abrupt changes for the β-beat can be observed in IR1, IR2, IR7 and IR8 for beam 1. For beam 2, abrupt changes in IR2, IR3, IR6 and IR8 are observed. These abrupt changes show that strong local sources are present. With the help of the segment-by-segment technique, local corrections were calculated for IR2, IR3, IR7 and IR8. Figure 5.3 shows an example of a correction calculated for IR3 (only the vertical plane is shown), the phase error is shown. The phase error is defined as the difference between the measured phase advance and the model phase advance. The phase advance is taken with respect to the first BPM in a segment. The error has been reduced by a factor 6. The residual error is too small to be further corrected with the segment-by-segment technique.

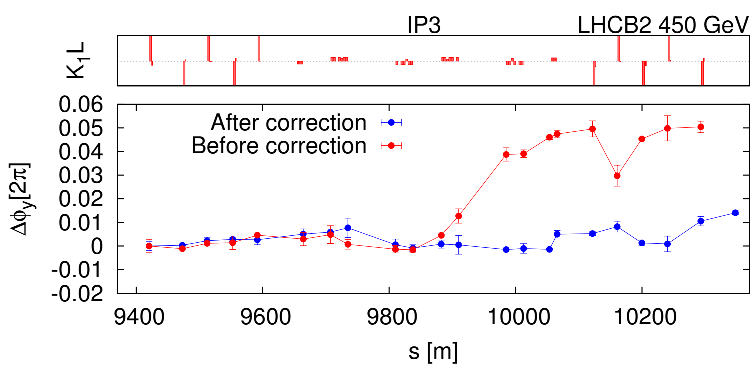

Figure 5.3: Illustration of a local correction at injection for IR3. Only the vertical plane is shown. The red line shows the phase error before correction and the blue one after correction.

The calculated corrections for IR2, IR3, IR7 and IR8 were identified as the leading sources [79] at injection. The $\beta-$beat before and after implementing the corrections is shown in figure 5.4.

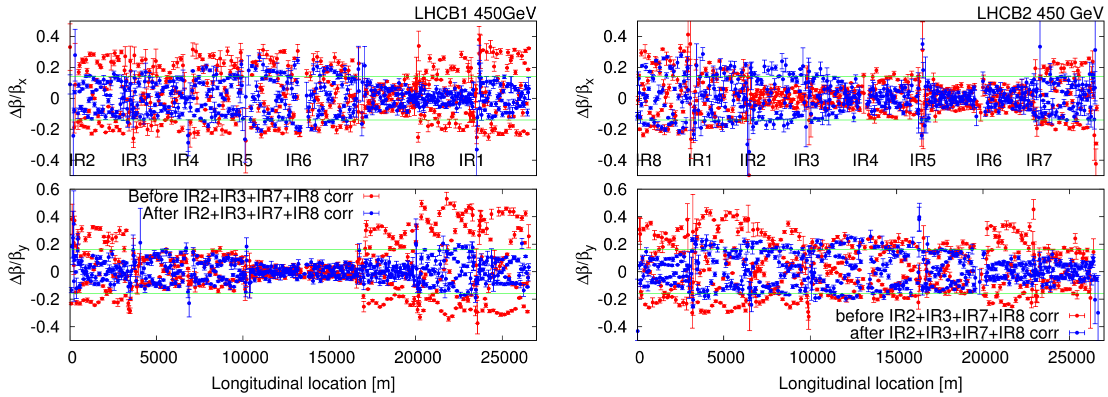

Figure 5.4: β-beat before (red) and after (blue) corrections. Beam 1 shown on the left and beam 2 on the right. Tolerances are shown by the green horizontal lines.

The abrupt changes that were initially observed in figure 5.2 are corrected, except for IR6. Correction in IR6 is a delicate process as the local phase advance has to be respected so that a safe extraction to the dump for both beams can be guaranteed. Trims applied to the magnets RQ4.L6.B1 and RQ4.R6.B2 cannot exceed 0.35% [80]. The peak β-beat has been corrected down to a $20\% - 30\%$ level. This is still above tolerances, but the peak β-beat has been reduced by about a factor of 2. This result was achieved by applying only local corrections. The current level of β-beat was considered to be acceptable for the existing aperture, due to a lower than expected rms orbit. The corrections applied for IR2, IR3, IR7 and IR8 are listed in table 5.1.

Magnet	**Initial** k_1 $[m^{-2}]$	**Final value** k_1 $[m^{-2}]$	$\vert$**Relative change**$\vert$ [%]
MQXB2.L2	-0.00950981581	-0.00955876581	0.51
MQXB2.R2	0.00950981581	0.00957177581	0.64
MQXB2.L8	-0.00950981581	-0.00955877581	0.51
MQXB2.R8	0.00950981581	0.00957177581	0.64
MQWA5.LR3	-0.001303924	-0.001325503	1.63
MQWA4.LR3	0.001241284	0.00120568417	2.8
MQWA5.LR7	-0.00133553657	-0.00135153657	1.18
MQWA4.LR7	0.00131382724	0.00133682724	1.72
MQWB5.L3	0.000972084	0.00106628597	9.6
MQWB4.L3	0.000688713	0.00079242757	15
MQWB4.R3	0.000688713	0.00080700072	17
MQWB5.R3	0.000972084	0.001070478	10
MQWB5.L7	-0.00003265771	0.00004934229	251.08
MQWB4.L7	0.00033168934	0.00021568934	53.78
MQWB4.R7	0.00033168934	0.00021568934	53.78
MQWB5.R7	-0.00003265771	0.00004934229	251.08

Table 5.1: Summary table showing the corrections applied to the quadrupole magnets at injection.

Warm quadrupoles in IR3 and IR7. In 2009 it was found that several errors were coming from the warm quadrupoles around IR3 and IR7, see table 5.1. IR3 and IR7 insertions are particularly constrained for optics correction since the main warm quadrupoles (MQWA) are powered in series on both sides and for both beams, while the trim quadrupoles (MQWB) are powered in series for both beams (but not for both sides). The size of the required relative corrections was at the 1% level for the MQWA quadrupoles and between 10% and 250% for the MQWB quadrupoles. The MQWB quadrupoles were trim magnets nominally set to a very low field. This explained the larger relative errors in the transfer function of these quadrupoles. These large corrections could only be understood by the fact that the magnetic precycle of the MQW magnets was still not identical to that used during the magnetic measurements [81].

New calibrations were implemented based on additional magnetic measurements. Figure 5.5 shows measurements of the beta-beat before the new calibrations (with corrections) and the new calibrations (without corrections).

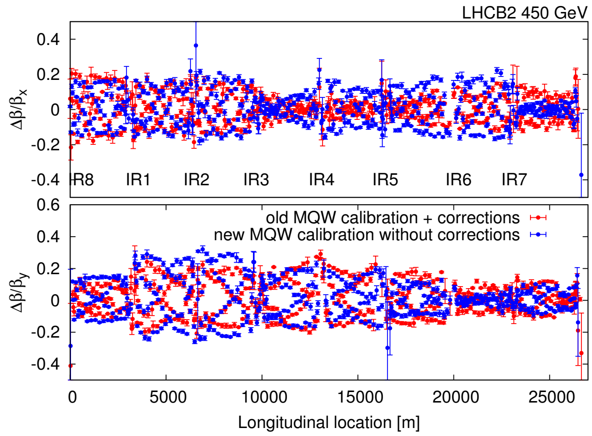

Figure 5.5: β-beat before (red) and after (blue) applying the new MQW calibrations.

Using the new calibrations as reference to estimate the error before and after the above corrections, see table 5.2. The errors were reduced by a factor of 2 to 2.5, except for MQWA4.LR3. Figure 5.5 still shows some residual error in IR3 and IR7. The conducted measurements and corrections were excellent, this showed that thanks to the segment-by-segment technique the magnet level could be reached. Part of this achievement was possible because of the lack of degeneracy between magnets strengths and BPMs.

Magnet	**Nominal gradient [T/m]**	**Estimated error before correction [%]**	**Estimated error after correction [%]**
MQWA5.LR3	1.957	1.1	-0.5
MQWA4.LR3	1.863	1.3	-1.5
MQWA5.LR7	2.005	1.0	-0.1
MQWA4.LR7	1.972	1.1	-0.6
MQWB5.L3	1.459	-11.1	-1.1
MQWB4.L3	1.034	-18.7	-2.5
MQWB4.R3	1.034	-16.6	1.5
MQWB5.R3	1.459	-11.2	-0.6
MQWB5.L7	0.049	-83.4	-8.5
MQWB4.L7	0.498	-32.6	1.9
MQWB4.R7	0.498	-44.1	-15.2
MQWB5.R7	0.049	-81.5	3.8

Table 5.2: The estimated error in the MQW magnets before and after the new calibrations.

b_2 correction at injection. The systematic quadrupolar component of the LHC dipoles has been determined from magnetic measurements [82] and [83]. A correction was prepared to correct the phase shift from the b_2 field errors in the dipoles [82], [83]. This quadrupolar error is corrected arc-by-arc using the MQT magnets to cancel the betatron phase shift. Figure 5.6 shows the total phase before and after implementing the corrections for beam 2. The sawtooth shape of the phase which can be observed before corrections is significantly reduced. This shape is a result of the phase deviating in the arcs, caused by the b_2 in dipoles.

Dispersion

Dispersion measurements are usually conducted for both beams in the same sessions as the β-beat measurements. Frequency trims corresponding to a $\frac{\delta p}{p}$ of ± 0.0015 were applied. Figure 5.7 shows the dispersion before and after applying local corrections in IR2, IR3, IR7 and IR8. The Vertical dispersion for both beams is similar, whereas the horizontal dispersion shows a small change from before to after the corrections.

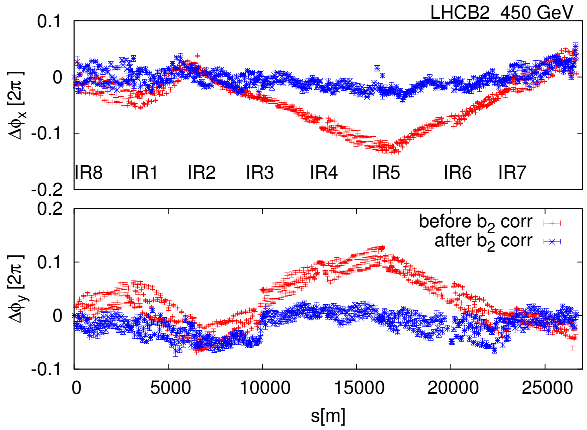

Figure 5.6: Effect of the b_2 corrections for beam 2. Before (red) and after (blue) dedicated b_2 corrections were applied.

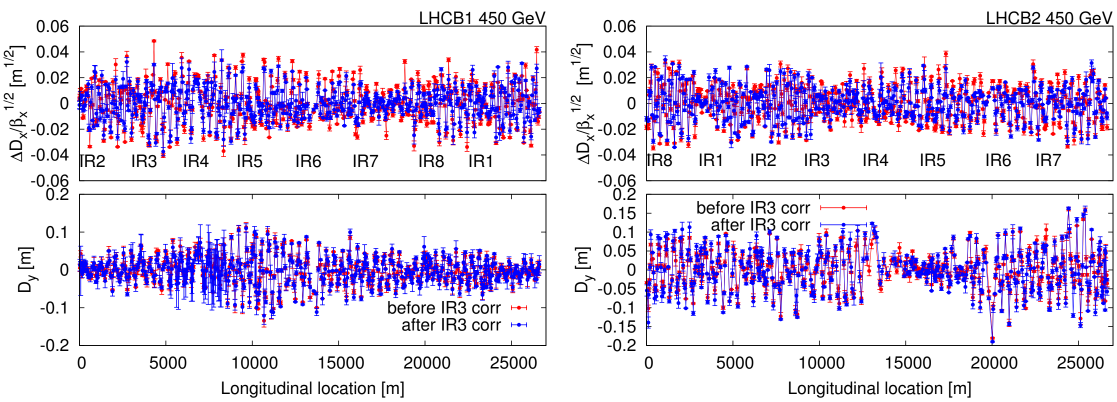

Figure 5.7: Normalized dispersion (top) and vertical dispersion (bottom) for beam 1 (left) and beam 2 (right), before and after IR3 corrections.

A peak vertical dispersion of 10 cm around IR5 is observed for beam 1. For beam 2 the peak is about 15 cm, but there are no big variations. The normalized dispersion beat is larger in beam 1 than in beam 2. The rms values for the normalized horizontal dispersion beat and vertical dispersion beat for both beams, before and after the corrections, are listed in table 5.3.

	Before IR3 correction		After IR3 correction	
	Beam 1	Beam 2	Beam 1	Beam 2
rms $\Delta\frac{D_x}{\sqrt{\beta_x}}$ [$\sqrt{m}$]	0.0156	0.0144	0.0125	0.0136
rms D_y [m]	0.0363	0.0487	0.0356	0.0543

Table 5.3: rms values for the normalized horizontal dispersion beat and vertical dispersion for both beams.

Before correction the rms value of the normalized horizontal dispersion is slightly above the tolerance of $0.013\sqrt{m}$ for both beams. After IR3 corrections the rms value is at about the tolerance. This shows that a small fraction of the observed normalized dispersion beat is coming from the IR3 quadrupoles. The vertical dispersion beat for beam 2 is larger than for beam 1. The vertical dispersion before and after correcting IR3 is comparable for both beams.

5.1.2 Measurements during the energy ramp and flat-top

Measurements were conducted during the energy ramp. The goal of these measurements was to investigate the change in the β-beat and coupling with respect to the energy.

β-beat

Figure 5.8 shows a measurement of the β-functions during the ramp. These measurements were conducted using the AC-dipole. Local corrections in IR2 and IR8 applied, for IR3 and IR7 the new calibrations were implemented. The corrections in IR2 and IR8 are decreasing gradually with energy and are zero at 700 GeV.

For both beams it is observed that during the first part of the ramp (up to 1 TeV) the reduction in the β-beat was the largest, and then remaining constant after 1 TeV. This is explained by the smaller effects of persistent current and remnant magnetization of the superconducting magnets and the lower remnant magnetization in the normal conducting magnets.

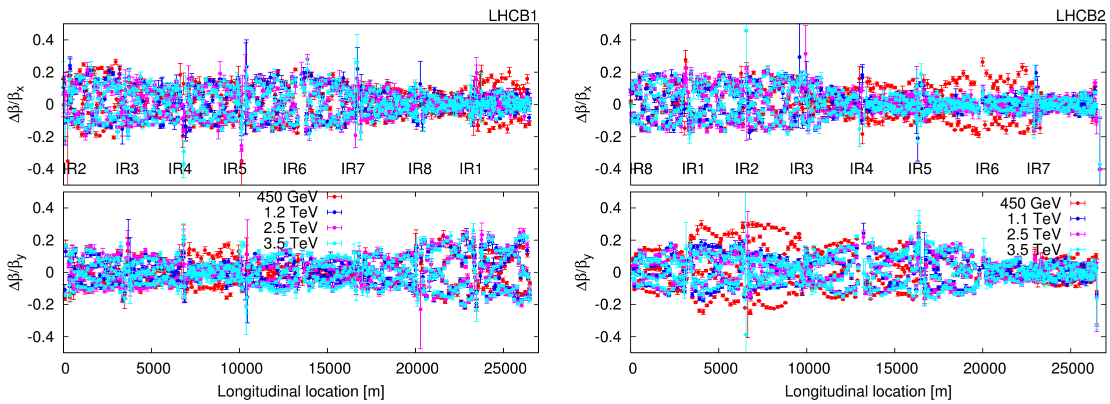

Figure 5.8: β-beat during the ramp for beam 1 (left) and beam 2 (right).

Figure 5.9 shows histograms of the difference in the β-beat between 450 GeV, 1.1 TeV and 2.5 TeV, 3.5 TeV. The left plot shows results for beam 1 and the right for beam 2. It is observed that the change in β-beat is largest at the beginning of the ramp. After about 1.2 TeV the change is within the measurement resolution. The change in the β-beat for beam 1 and beam 2 is similar.

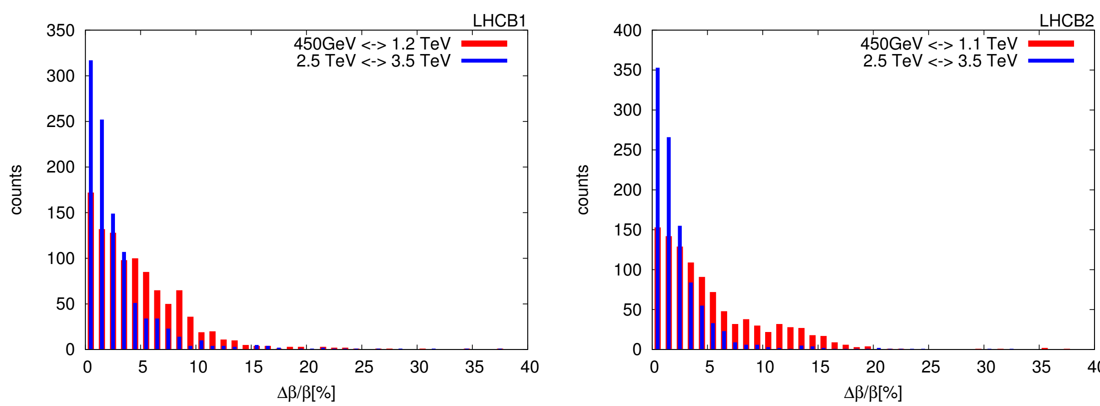

Figure 5.9: Difference in the β-beat between 450 GeV and 1.1 TeV (red) and between 2.5 TeV and 3.5 TeV (blue) for beam 1 (left) and beam 2 (right).

Coupling

Coupling, and the control of it, has an important impact during the ramp. Several measurements and corrections were conducted during the course of the commissioning. Usually the coupling is compensated on-line by using two orthogonal knobs constructed with arc skew quadrupoles to correct the real and imaginary parts of the difference coupling resonance. However, the on-line compensation is not able to detect and correct the local sources. Figure 5.10 shows the three coupling knobs implemented during the ramp. All knobs are implemented for beam 2, as for beam 1 no correction was needed.

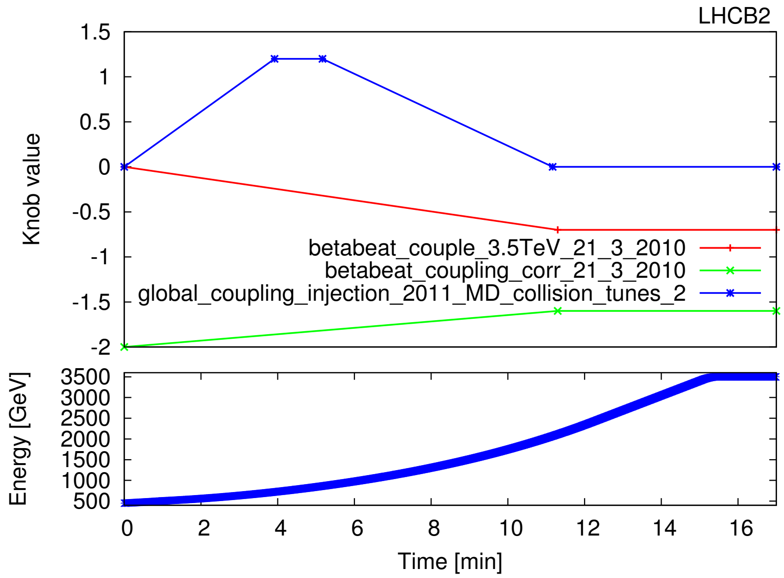

Figure 5.10: Coupling correction implemented during the ramp. Legend shows the name of the knob in the LSA system.

The knobs betabeat_couple_3.5TeV_21_3_2010 and betabeat_couple_corr_21_3_2010, were implemented in 2010 because the skew quadrupoles were reaching the maximum allowable current. The skew quadrupole families before and after applying the global correction using a response matrix are shown in figure 5.11. The strength needed in the skew quadrupole families is significantly reduced. Most notably for kqs.a78b2, which was reaching the maximum allowed current, the strength was reduced by a factor of 7.

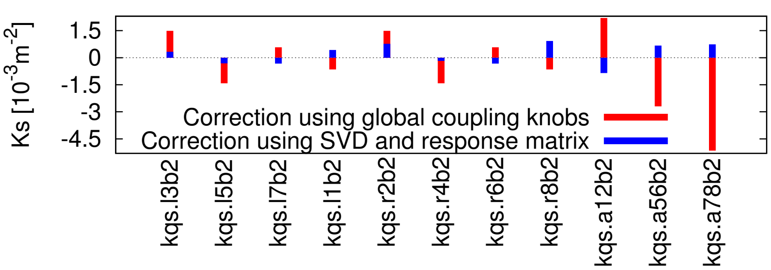

Figure 5.11: Skew corrector families for using the global orthogonal coupling knobs (red) and the response matrix using the SVD (blue).

During 2011 a growth in the coupling was observed during the energy ramp, see figure 5.12, right. It was decided to correct the growth of the coupling during the ramp. As during the collision tunes at injection machine development study [84] the tunes would be closer together, i.e a tune split of 0.01 instead of 0.03. This, together with a peak C^{-} of 0.01, could result in losing the beam during the ramp. A dedicated ramp was used to measure the coupling using the AC-dipole at several instances during the ramp, left plot in figure 5.12. A peak in the coupling is observed at about 900 GeV.

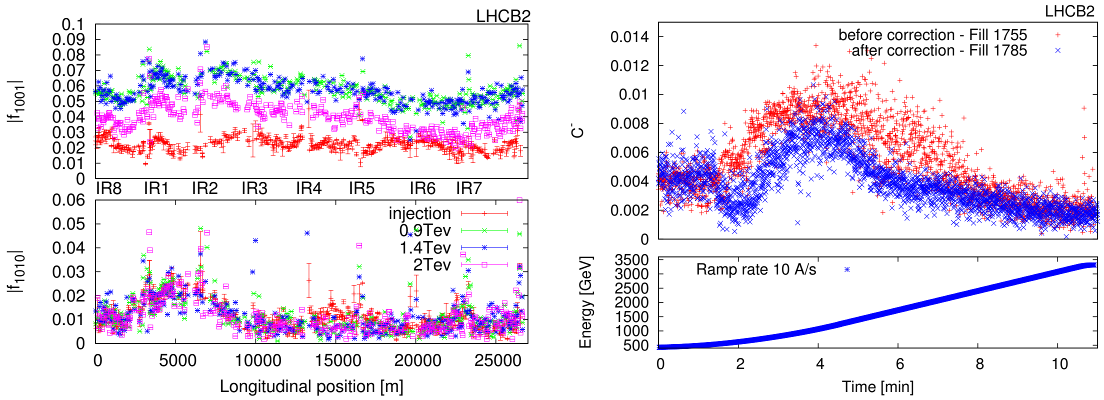

Figure 5.12: Coupling measurement f_{1001} (left) and c^- (right) between 450 GeV and 3.5 TeV.

Coupling correction was calculated for the different measurements. Figure 5.13 shows the coupling measurement at 900 GeV and the error reconstruction.
Coupling knob global_coupling_injection_2011_MD_collision_tunes_2 was implemented, shown in figure 5.10. The result before and after the corrections were implemented is shown in figure 5.12. The peak coupling has been reduced by about 20% to 30%.

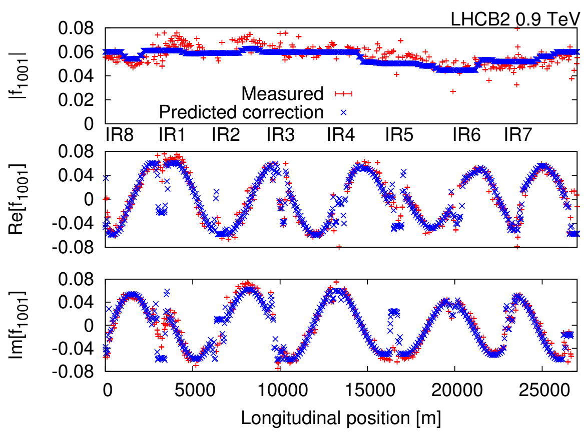

Figure 5.13: Measured coupling (red) and predicted error reconstruction for beam 2 at 900 GeV (blue).

5.2 Squeeze commissioning of all IRs down to β^* value of 2 m

In the beginning of 2010 the squeeze was commissioned with a β^* of 2 m at all IPs. In 2009 a partial squeeze of down to $\beta^* = 5$ m was carried out for IP5 [85]. In figure 5.14 an overview of the commissioning is shown . The measurement and corrections were conducted in 8 optics sessions within 23 days. The IRs were not squeezed simultaneously. The squeeze commissioning of IR1 and IR5 was done simultaneously, followed by IR8 and lastly IR2. The sequential squeezing of the IPs allowed for the investigation of the effect on the linear optics separately. The squeeze commissioning of β^* down to 2 m was the first time that all the IRs in the LHC were squeezed together.

Squeezing down IR1 and IR5 increased the β-beat to 40%. After applying a local correction in IR5 using the segment-by-segment technique the β-beat was reduced to the 25% level. Squeezing down IR8 increased the β-beat to a 45% level, after applying a local correction in that IR the β-beat was successfully reduced to 25%. Lastly, the squeeze of IR2 increased the β-beat with about 5%. After incorporating these corrections in the sequence of the LHC control system an increase in the β-beat of about 5% was observed.

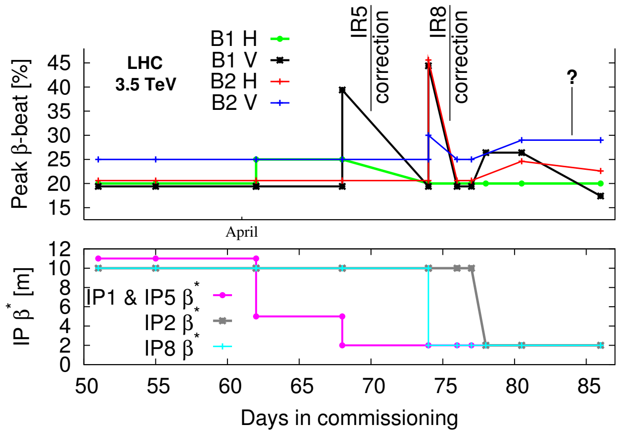

Figure 5.14: Overview of β^* squeeze commissioning down to 2 m.

5.2.1 β-beat measurements and corrections.

Figure 5.15 shows the β-beat for IP1 and IP5 at β^* value of 11 m (red) and a β^* value of 2 m (blue) for beam 1 (left) and beam 2 (right). A slight increase from about 20% to 40% is observed for beam 1 and from 20% to 30% for beam 2. The green lines indicate the tolerances.

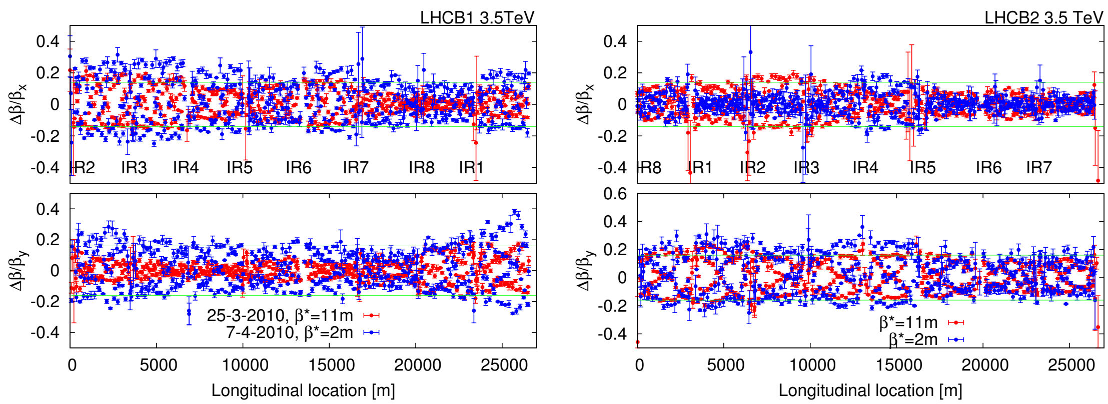

Figure 5.15: β-beat for IR1 and IR5 at flattop (red) and β^* at IR1,5 at 2 m (blue). Beam 1 is shown at the left and beam 2 on the right. The tolerances are indicated by the green lines.

For a β^* value of 2 m (blue) abrupt changes are visible in the horizontal plane of beam 1 at IR1 and IR5. For beam 2 only an abrupt change around IR5 in the vertical plane is observed. A suitable correction was calculated for IR5. Figure 5.16 shows a plot for the local correction of IR5 using the segment-by-segment technique. The use of the segment-by-segment technique allowed to locally identify and correct strong sources. The phase error, being the difference between the measured and model phase advance, was used as an observable. For IR1 no suitable correction was found using the triplets. The local IRS correction was distributed over the two MQXB2 magnets left and right from IR5, as the MQXB2 magnets of the triplet assembly are located at the common beam pipe. Consequently a suitable correction for the two beams had to be found.

Figure 5.17 shows the β-beat after the corrections in IR5 were implemented (red). The peak β-beat observed at 40%, shown in figure 5.15, is reduced to a 30% level. Subsequently IP8 was squeezed down to a β^* value of 2 m. Large increase in the β-beat of up to a peak β-beat of 50% was observed in both beams, figure 5.17 (blue). The largest increase is in the vertical plane for beam 1 and the horizontal plane for beam 2.

The β-beat arising from squeezing down IR8 is larger than the β-beat from squeezing down IP1 and IP5 together. Local corrections were calculated for IR8 using the segment-by-segment technique (shown in figure 5.18). The phase error in IR8 is about 1.5 times stronger than the phase error observed in IR5. After some investigation, it was concluded that the errors found in the two beams did not have the same sources and a suitable correction was found using two magnets which are not in the common beam pipe region, MQ5.R8B1 and MQ6.L8B2.

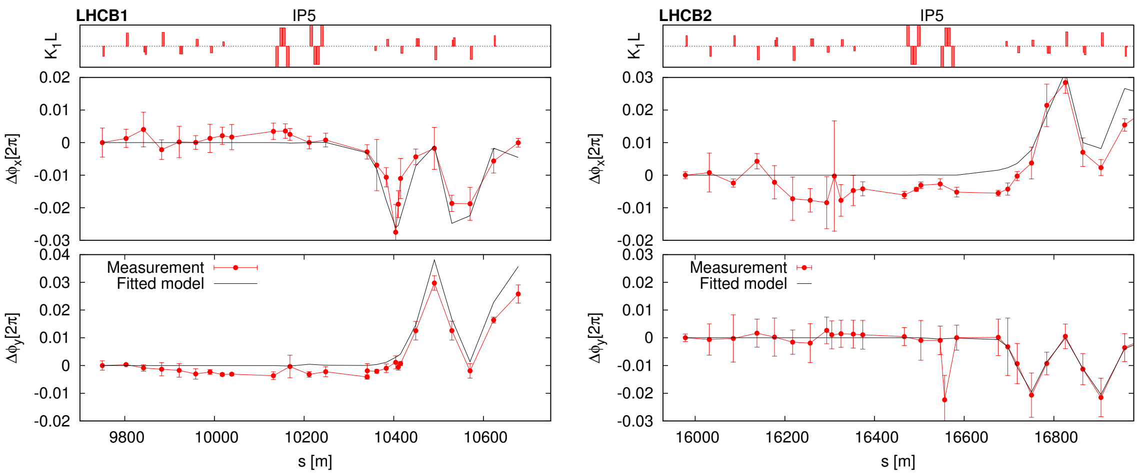

Figure 5.16: Local correction calculated for IR5 (this for IR1 and IR5 at a β^* value of 2 m). Beam 1 is shown on the left and beam 2 on the right. The red line shows the measured phase error and the black line shows the model phase error when a trim in the two MQXB2 magnets was applied.

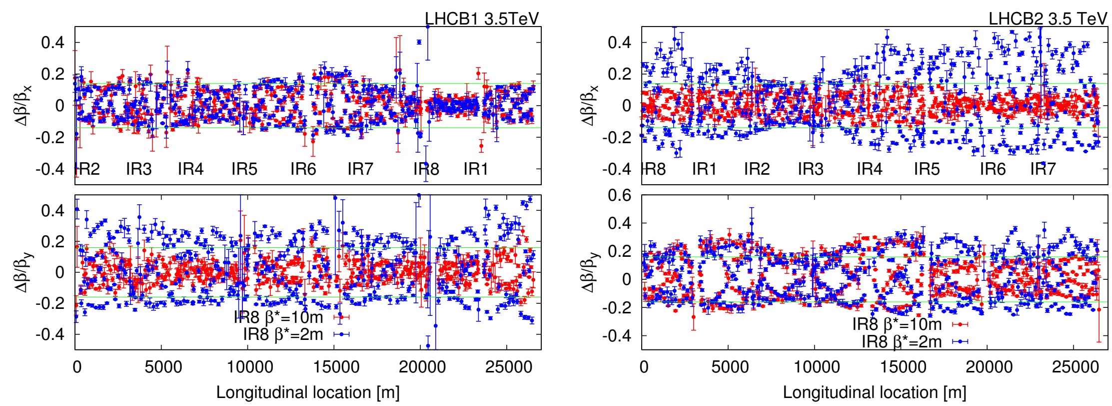

Figure 5.17: β-beat is shown for IP1 and IP5 at β^* value of 2 m, 10 m for IP8 in red and IP1, IP5 and IP8 at β^* value of 2 m in blue.

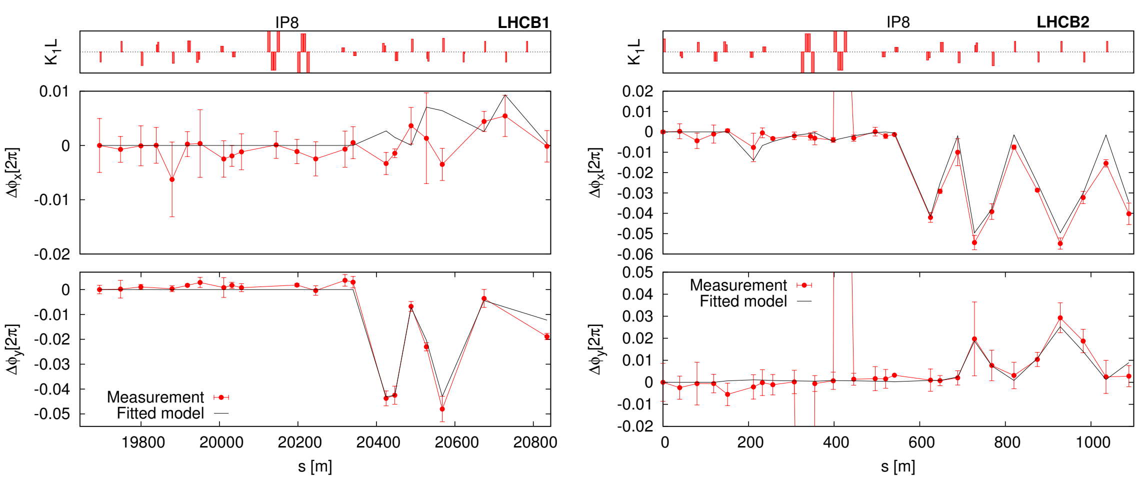

Figure 5.18: Local correction calculated for IR8, this for IP1, IP5 and IP8 at a β^* value of 2 m. Beam 1 is shown on the left and beam 2 on the right.

Lastly IR2 was squeezed to a β^* value of 2 m. A small increase of 5% was observed. No suitable correction was found for IR2 at that time. Figure 5.19 shows the β-beat for all IPs at β^* value of 2 m before and after applying corrections in IR5 and IR8. Without applying local corrections in IR5 and IR8 the peak β-beat observed is about 60% in the vertical plane of beam 1, well above the tolerance. After the local corrections were applied the peak β-beat was reduced to a 25% level. It was decided that commissioning could continue with a β-beat close to the tolerances.

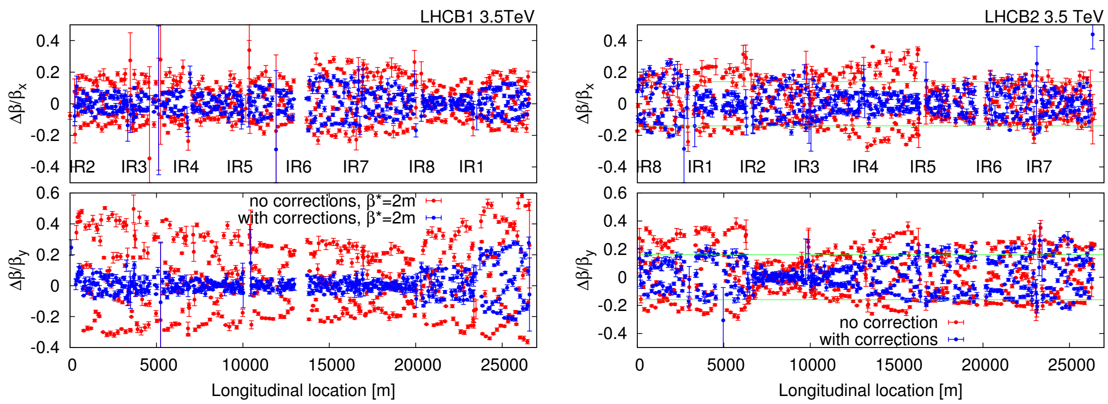

Figure 5.19: β-beat is shown for all IPs at $\beta^* = 2$ m before corrections (blue) and after corrections (red).

From figure 5.19 it is obvious that some local error sources were still present in IR1 and IR2. The corrections implemented for all IRs at a β^* value of 2 m are listed in table 5.4. Only two out of four IRs were corrected. The largest corrections applied were for IR8. A magnet change of up to 5% was needed to correct the β-beat to a sufficiently low level. As changes in the quadrupole strength introduce changes in the tunes, tune corrections were included in the implemented knobs. The tune compensation needed using the arc trim quadrupoles for both beams can be found in the last column. As the largest correction was applied for IR8, the largest tune compensation is needed for that correction.

Magnet	**Design** $K_1[\mathbf{m}^{-2}]$	**Maximum** $K_1[\mathbf{m}^{-2}]$	**Correction [%]**	**Tune compensation** $[\times 10^{-4}[\mathbf{m}^{-2}]]$
MQXB2.L5	-0.0087	0.018	-0.15%	kqtd.b1=-0.4811 kqtf.b1=-0.3900
MQXB2.R5	0.0087	0.018	0.12%	kqtd.b2=0.3689 kqtf.b2=0.4983
MQ5.R8B1	-0.0029	0.013	5%	kqtd.b1=0.8663 kqtf.b1=0.0187
MQ6.L8B2	0.0056	0.013	1.8%	kqtd.b2=0.1652 kqtf.b2=-1.05

Table 5.4: Local correction implemented for $\beta^* = 2$ m.

5.2.2 Coupling measurement and correction

Figure 5.20 shows the coupling for beam 1 (left) and beam 2 (right) when squeezing down IP1 and IR5 to β^* value of 2 m (blue) and at flattop (red). Only the difference resonance, f_{1001}, is shown, as this is the leading resonance for the coupling. Abrupt jumps are visible at IR1 and IR5 when the β^* was squeezed down to 2 m. The jump for IR5 is less visible for beam 2. The abrupt jumps are an indication that strong local coupling sources are present at the triplets.

The coupling in the transverse plane is generally compensated on-line [86]. This is done by using two orthogonal knobs constructed with arc skew quadrupoles to correct the real and imaginary parts of the difference coupling resonance. However, the on-line compensation is not able to detect and correct the local sources. A local coupling correction was calculated for IR1 and IR5. For the local coupling correction in IR1 and IR5 it was the first time that the segment-by-segment technique was used. Figure 5.21 shows coupling correction for IR1 and figure 5.22 for IR5, for beam 1 (left) and beam

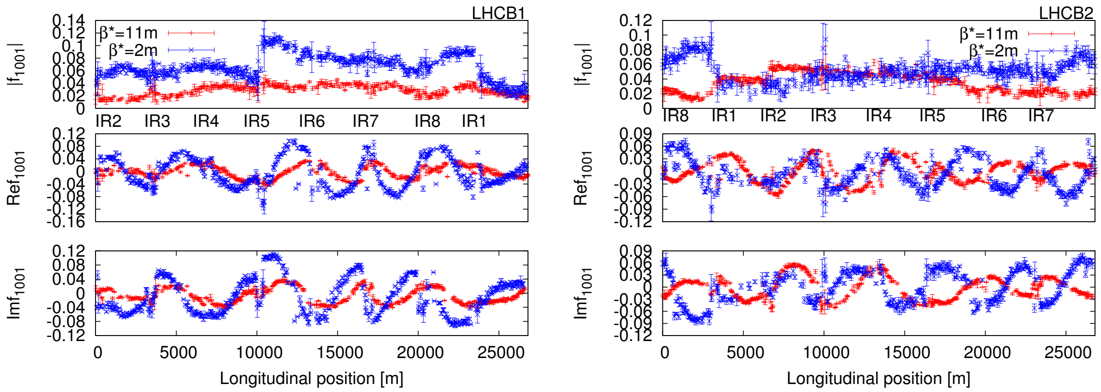

Figure 5.20: Difference coupling resonance for beam 1 (left) and beam 2 (right). Injection optics (IP1 and IP5 at a β^* value of 2 m) in blue and in red, IP1 and IP5 squeezed down to a β^* value of 2 m. The top plot shows the amplitude, middle plot the real part and bottom plot the imaginary part of f_{1001}.

2 (right). The dots show the measured coupling and the fitted model is represented by lines. Fitted model is applying the expected corrections into the model. In the absence of errors the observed f_{1001} is constant, when errors are added the amplitude shows abrupt jumps.

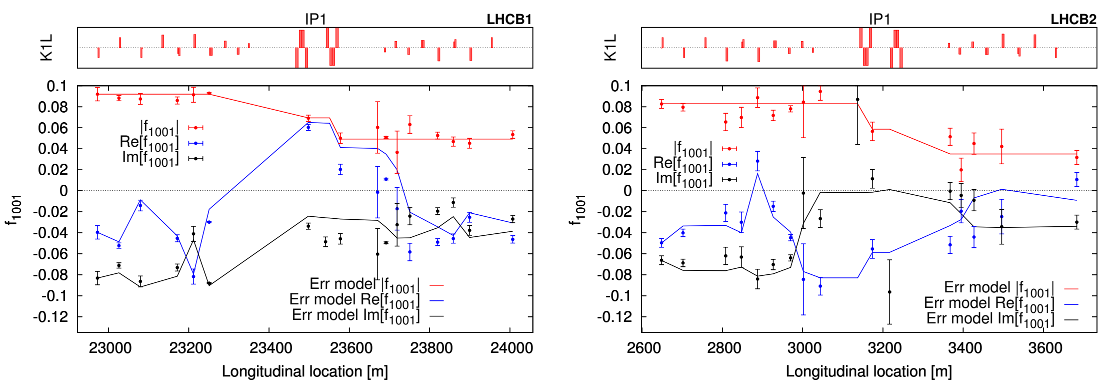

Figure 5.21: Local coupling correction for IR1 when β^* in IP1 and IP5 is squeezed down to 2 m. Beam 1 is shown on the left and beam 2 on the right. The dots show the measured coupling and the fitted model is represented by lines. Abrupt jumps are visible around 23500 m for beam 1 and around 3200 m for beam 2.

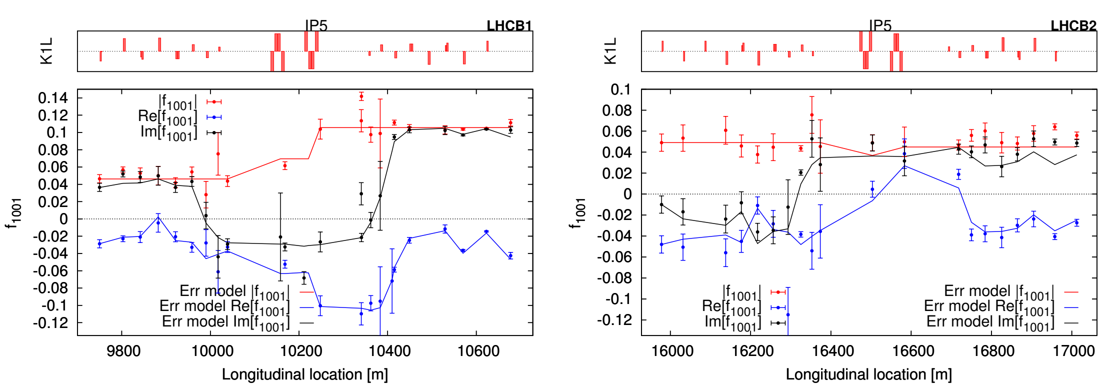

Figure 5.22: Local coupling correction for IR5 when β^* in IP1 and IP5 is squeezed down to 2 m. Beam 1 is shown on the left and beam 2 on the right. The dots show the measured coupling and the fitted model is represented by lines. Abrupt jumps are visible around 10200 m for beam 1 and around 16500 m for beam 2.

For both IR1 and IR5 the error arose from the tilts in the triplet quadrupoles. For these corrections two skew quadrupoles, RQSX3.L* and RQSX3.R*, at the triplets were used. The calculated strength was distributed over the two skew correctors left and right from the IP. Figure 5.23 shows the coupling before (red) and after (blue) the local corrections. After implementing the local correction the abrupt jumps of f_{1001} at IR1 and IR5 were corrected, yet the amplitude of f_{1001} was increased. This was due to the global coupling knob which was still compensating for previous errors. The global knobs needed to be re-optimized after the local correction.

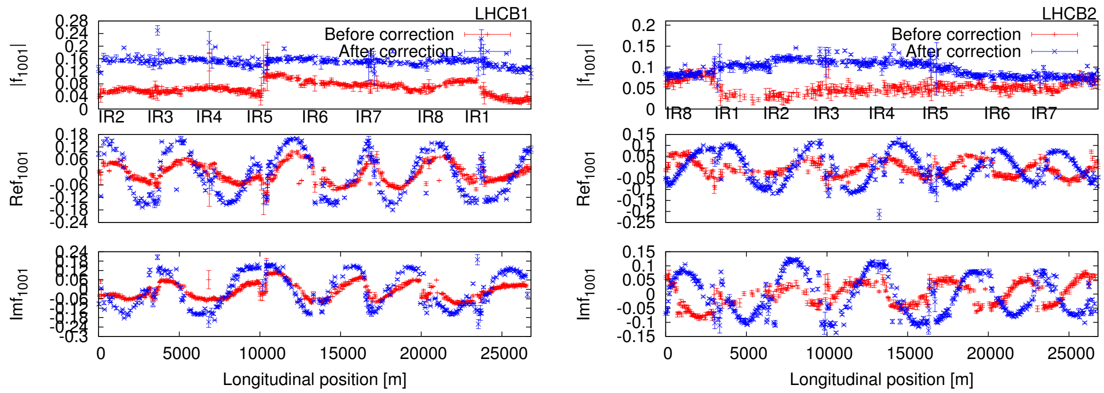

Figure 5.23: Difference resonance for beam 1 (left) and beam 2 (right). Before corrections (blue) and after corrections (red) for IR1 and IR5 squeezed down to a β^* value of 2 m.

Similar corrections were calculated for IR2 and IR8 where these IPs were squeezed down to a β^* value of 2 m. But they were not implemented during operations. An overview of the corrections used in the operations is listed in table 5.5 (as the full knobs were too strong, only 55% of the calculated strength was applied). This was due to the fact that the effect of the AC-dipole was not taken into account yet.

Magnet	Calculated correction K_{1s} $[m^{-2}]$
RQSX3.L1	6.0×10^{-4}
RQSX3.R1	6.0×10^{-4}
RQSX3.L5	6.0×10^{-4}
RQSX3.R5	8.0×10^{-4}

Table 5.5: Local coupling corrections implemented.

When implementing the corrections in table 5.5, the global coupling knobs had to be adjusted. Their settings before and after implementing the local coupling corrections are listed in table 5.6. The strength of the global coupling knobs was reduced by about a factor of 2 after the local coupling correction.

Knob value	Before correction	After correction
C^- imaginary part beam 1	-0.083	-0.04
C^- real part beam 1	0.02	0.0040
C^- imaginary part beam 2	0.0503	0.029
C^- real part beam 2	0.015	0.01

Table 5.6: Change of the global coupling knobs before and after implementing the local coupling corrections.

Figure 5.24 shows an illustration of the positive effect of identifying the local sources first and then applying coupling corrections with the global knob. The blue line shows the β^* value, the red line the current of one of the skew quadrupole families and the black line the current in the skew quadrupole right to IP5. It is observed that when the current increases in kqsx3.r5, meaning that the correction knob is applied, the current in the arc skew quadrupoles reduces significantly. Only 50 A correction in kqsx3.r5 was applied, but this correction resulted in a reduction of 100 A in the skew quadrupole family, kqs.a78b2.

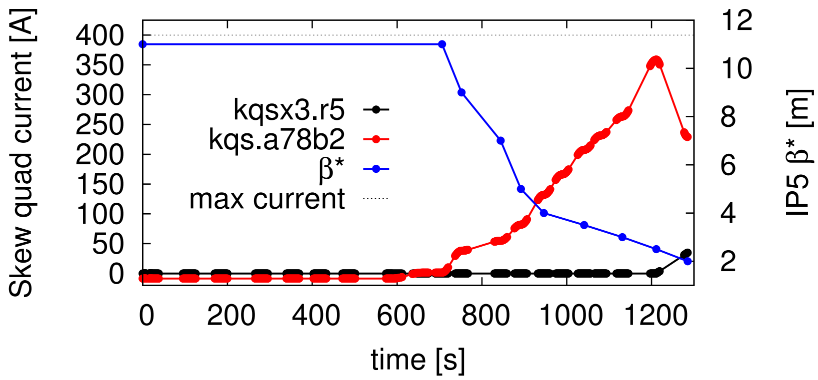

Figure 5.24: Illustration of the effect on the arc skew quads using a local coupling knob.

5.2.3 β^* for all IPs at β^* value of 2 m

The β^* measured using the segment-by-segment technique directly after the squeeze is listed in table 5.7. This measurement was done after the corrections were applied. The largest error on the β^* measurement is about 6%. The largest offsets of about 10% are observed in the vertical plane for IP1 and IP2 in beam 1 and IP8 for beam 2. An important asymmetry of about 15% between the vertical planes of IP2 for beam 1 and beam 2 is observed.

IP	Beam	β^*_x	error	β^*_y	error
IP1	1	2.02	0.01	1.78	0.05
IP2	1	2.02	0.06	1.80	0.01
IP5	1	2.10	0.02	2.02	0.04
IP8	1	2.11	0.10	1.92	0.01
IP1	2	2.00	0.04	2.05	0.03
IP2	2	2.03	0.04	2.13	0.10
IP5	2	1.95	0.12	2.11	0.05
IP8	2	2.21	0.03	1.85	0.01

Table 5.7: β^* measurements for all IPs at β^* value of 2 m right after the squeeze. This measurements is obtained after applying corrections.

5.3 Squeeze commissioning of all IRs down to β^* value of 3.5 m

After operating all IPs at a β^* value of 2 m it was decided in the second half of 2010 that the β^* should be increased to a more relaxed setting [87], [88]. The reason for this was that the commissioning of the crossing angles with additional aperture measurements would take too long at a β^* value of 2 m. At a β^* value of 3.5 m for IP1, IP2, IP5 and IP8 the limitations on the aperture were avoided. Operating at a relaxed settings of the β^* was the direct motivation to recommission the optics. Figure 5.25 shows an overview of the commissioning of all IPs at $\beta^* = 3.5$ m. In about 10 days and over 5 optics sessions, the optics was recommissioned. Local corrections were applied first, followed by a global correction for beam 2. The rise of β-beat observed at the end of the 10 days was due to the fact that several magnets were not driven in the LHC control system and due to the hysteresis effect.

5.3.1 β-beat correction

The local corrections for the β^* value of 3.5 m were based on the correction found for all IRs at the β^* value of 2 m, but they were more refined. Corrections were added in IR1, IR2 and IR6. A summary of the applied corrections is listed in table 5.8. For β^* value of 2 m only 4 correctors were used, whereas for the β^* value of 3.5 m the number of quadrupoles trimmed was increased to 12. For IR8 alone 4 correctors were used. The use of more correctors around IR8, such as the triplets, allowed a reduction of the correction strength needed. Several correction combinations are possible, and this

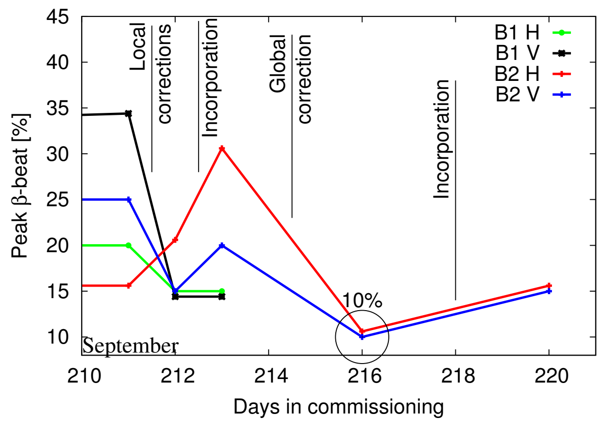

Figure 5.25: Overview of squeeze commissioning of all IPs at a β^* value of 3.5 m.

made it possible that large corrections in one single magnet were avoided. The largest calculated strength needed around IR8 for β^* value of 2 m was 5% (see table 5.4). For the β^* value of 3.5 m this was reduced by one order of magnitude to 0.5%. The largest change applied was for IR2 (2%).

Magnet	K name	Design $[\mathrm{m}^{-2}]$	Correction [%]
MQXB2.R1	ktqx2.r1	0.00871	0.09
MQM.5R2.B2	kq5.r2b2	0.00350	0.48
MQY.5L2.B2	kq5.l2b2	-0.00255	2.00
MQM.9R2.B1	kq9.r2b1	-0.00530	1.30
MQXB2.R5	ktqx2.r5	0.00871	-0.11
MQXB2.L5	ktqx2.l5	-0.00871	0.11
MQY.5L6.B2	kq5.l6b2	-0.00661	0.50
MQY.5L6.B1	kq5.l6b1	0.00644	0.60
MQM.6L8.B1	kq6.l8b1	-0.00535	0.50
MQY.4R8.B1	kq4.r8b1	0.00353	0.48
MQXB2.L8	ktqx2.l8	0.00882	0.26
MQXB2.R8	ktqx2.r8	-0.00882	-0.06

Table 5.8: Local correction implemented for $\beta^* = 3.5$ m.

Figure 5.26 shows the β-beat before (red) and after (blue) corrections. Beam 1 achieved a correction well within tolerances. For the horizontal plane of beam 2, on the other hand, the β-beat was increased from 15% to 25%. Yet it was verified that the targeted local errors were effectively corrected. The remaining uncorrected errors are responsible for the 25%.

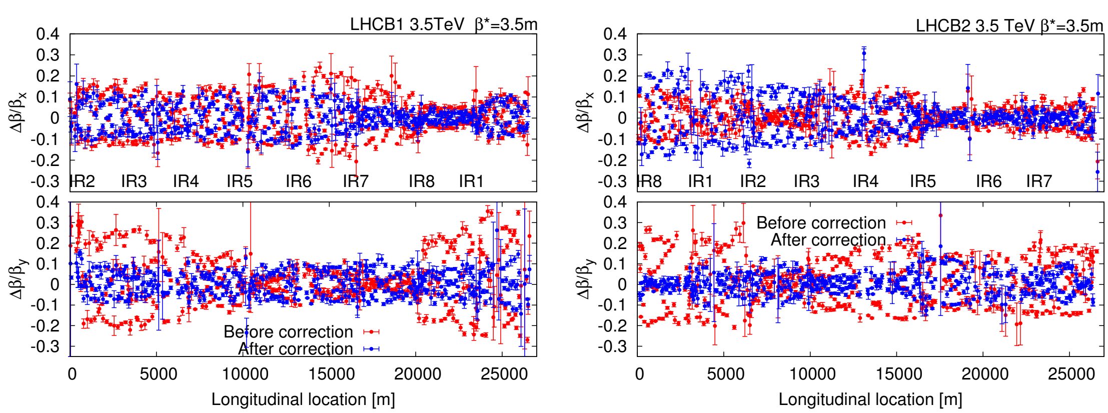

Figure 5.26: β-beat before (red) and after (blue) applying local corrections. Beam 1 is shown on the left and beam 2 on the right. This for all IPs at a β^* value of 3.5 m.

First global β-beat corrections in the LHC

As for beam 1 the β-beat was within tolerances a global correction was calculated only for beam 2. Therefore no common correctors could be used as this would affect beam 1. The left plot in figure 5.27 shows the β-beat before (red) and after (blue) global corrections were applied. The right plot in figure 5.27 shows the β-beat before (red) and after (blue) both local and global corrections were implemented. After the global corrections were implemented the peak β-beat was reduced from 30% to 10% for beam 2.

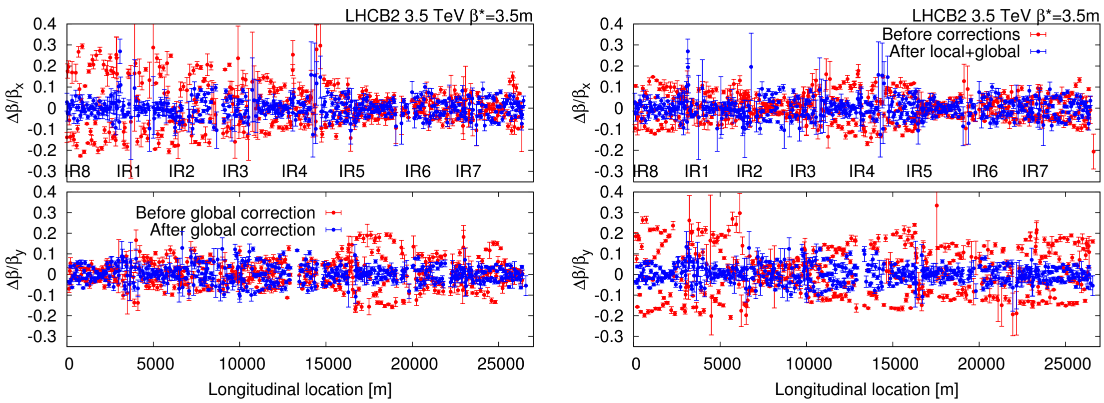

Figure 5.27: Left plot shows the $\beta-$beat before (red) and after (blue) applying global corrections for beam 2. The plot on the right shows the $\beta-$beat before (red) and after (blue) local and global corrections were implemented.

Applying the global correction to beam 2 showed that achieving a β-beat of 10% in the LHC was possible. This result was achieved by sequentially applying local corrections at the IR and global corrections around the ring.

Figure 5.28 shows the predicted correction for the β-beat (left) and the dispersion (right). The red plot shows the measurement and the blue one the predicted β-beat after correction. This correction was achieved by applying weight on the horizontal and vertical β-function and the dispersion.

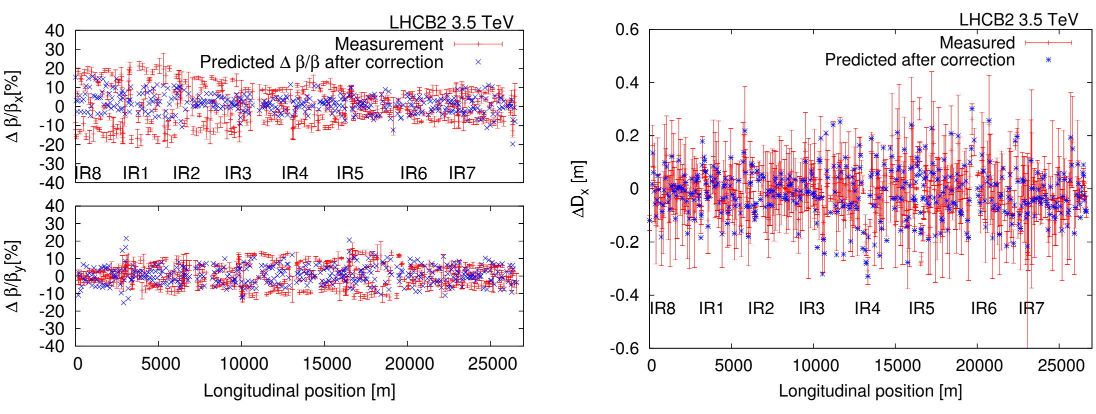

Figure 5.28: Predicted $\frac{\Delta\beta}{\beta}$ corrections for β-beat (left) and dispersion (right), this for all IPs at a β^* value of 3.5 m.

The correctors that were used for the global correction are shown in figure 5.29. A total of 145 correctors, distributed around the ring, were used to correct the beta-beat down to 10%. No quadrupoles were used in the arcs , only in the insertion regions (which are not common for both beams). The largest correctors are located around IR3, IR4 and IR6. The maximum strength implemented was about $5.5 \times 10^{-5}\mathrm{m}^{-2}$.

'Incorporation' versus 'trimmed'

'Trimming' a knob on-line is applying the calculated corrections at a certain step during the squeeze process. 'Incorporating' is including the knob in the controls system and running the complete sequence

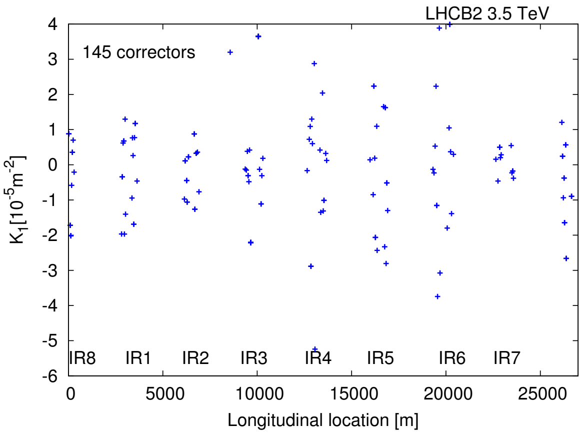

Figure 5.29: Quadrupole strength versus location around the ring for all IPs at a β^* value of 3.5 m.

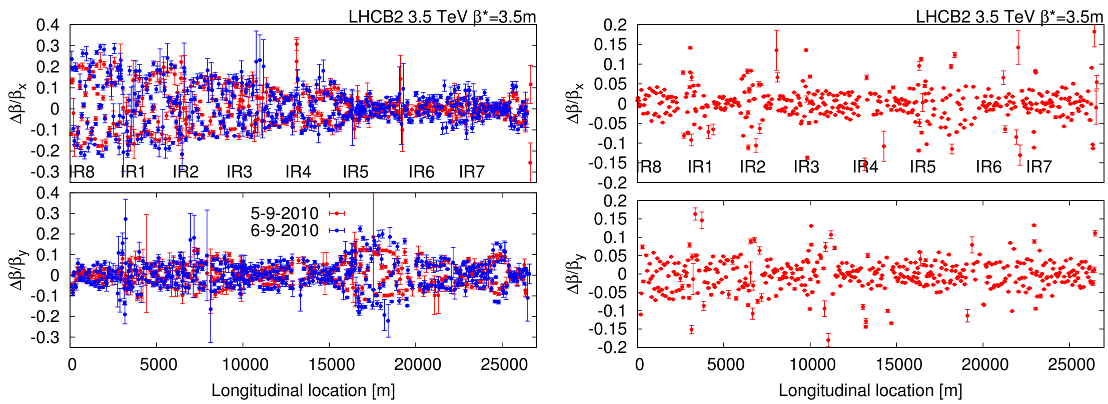

Figure 5.30: β-beat comparison between trimming and incorporating the knob with local corrections. The left plot showing the β-beat for trimming (red) and incorporating the knob (blue). The right plot shows the difference in the β-beat between trimming and incorporating the knob. This corresponds to a β^* value of 3.5 m in all IPs.

of steps for the squeeze. During the correction sessions for the β^* value of 2 m and 3.5 m differences were observed between trimming and incorporating the knob. An example of a difference observed for beam 2 (β^* value of 3.5 m) is shown in figure 5.30. The right plot in figure 5.30 shows the difference in the β-beat. A 5%-10% difference is observed. This was a problem that needed to be investigated.

Figure 5.31 shows some of the differences found in the quadrupole magnet currents. The vertical axis shows the difference in current before and after applying the trim. Two quadrupoles (Q5.L6B1 and Q5.L6B2) show a 10 A difference for trimming and incorporating. Q5.R2B2 shows a discrepancy due to the treatment of hysteresis.

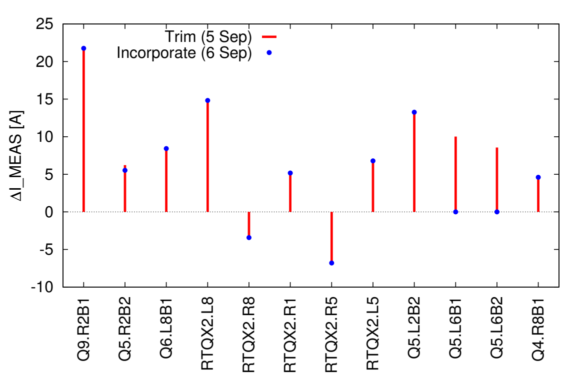

Figure 5.31: Difference in the quadrupoles currents between trimming and incorporating the knobs.

The difference becomes more relevant when looking at the global corrections, as around 145 correctors distributed around the ring were used. Figure 5.32 shows the β-beat, left for trimming and incorporating. The difference in the β-beat is shown on the right. A difference up to 15% is observed.

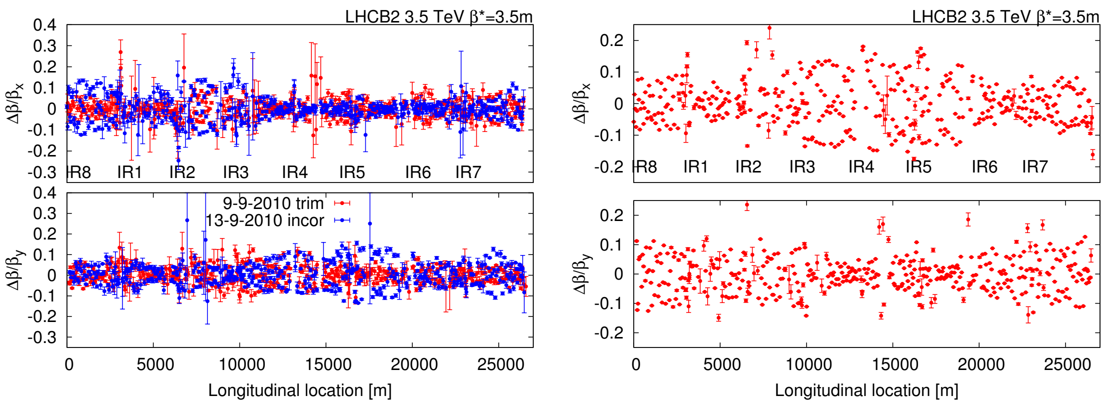

Figure 5.32: Difference in β-beat between trimming and incorporating the global correction at the β^* value of 3.5 m. The left plot shows the β-beat for trimming (red) and incorporating (blue) the knob. The right plot shows the difference in the β-beat between trimming and incorporating.

This discrepancy is explained by looking at the difference in the quadrupole currents. Figure 5.33 shows the difference in current between trimming and incorporating. From the figure it can be observed that the majority of the quadrupoles did not change, and some quads differ by 1 A. The small changes of 1 A are due to the treatment of hysteresis in the control system.

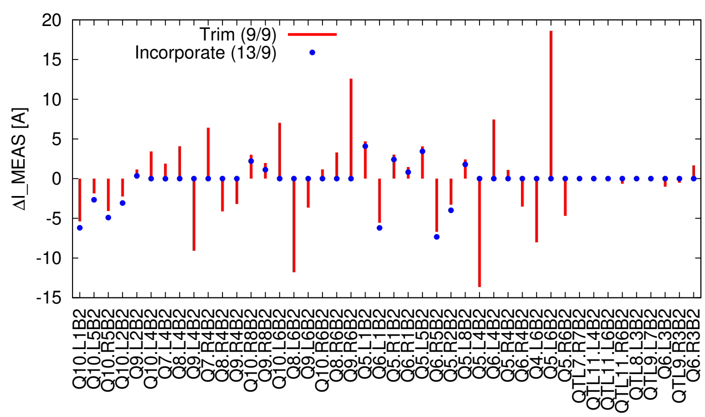

Figure 5.33: Difference in quadrupole currents for trimming and incorporating the knob.

After some investigation [89], [90] this problem was clarified as some magnets were not driven during the squeeze. The motivation for not driving some magnets was that these magnets were not used during the squeeze. So as a safety precaution it was decided not to include these magnets in the squeeze process. Small differences of about 1 A are also observed, this is explained by the controls system interpreting a change of hysteresis branch caused by the correction itself.

5.3.2 Coupling measurements

Coupling measurements were performed at $\beta^* = 3.5$ m. Figure 5.34 shows the coupling for beam 1 and figure 5.35 for beam 2. The figure on the left shows the difference resonance, and the one on the right the sum resonance. The initial coupling knobs for $\beta^* = 2$ m were re-calculated for $\beta^* = 3.5$ m, but due to time limitations they could not be included in the correction scheme.

For both beams jumps are observed in IR1, IR2, IR5, IR8. Both the difference and sum resonance show some jumps in these IPs. From the real and imaginary part of the sum resonance it is clear that

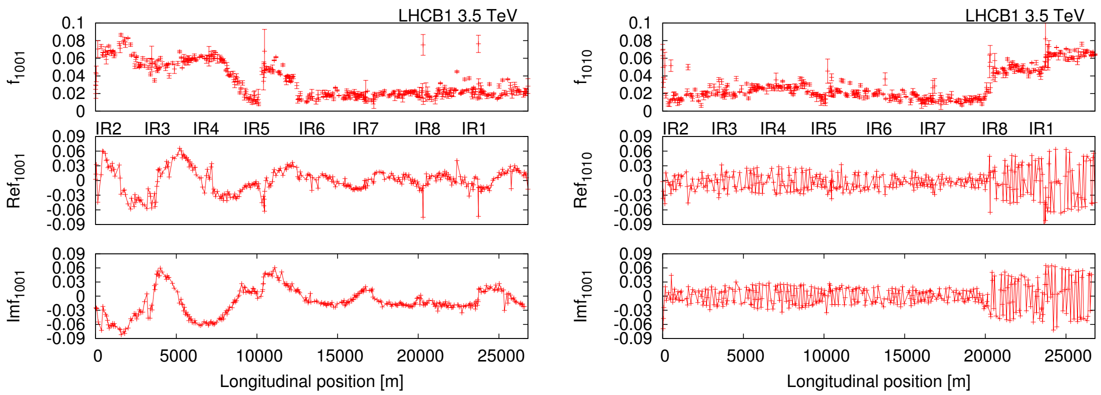

Figure 5.34: f_{1001} is shown on the left and f_{1010} on the right for beam 1, this for all IPs at a β^* value of 3.5.

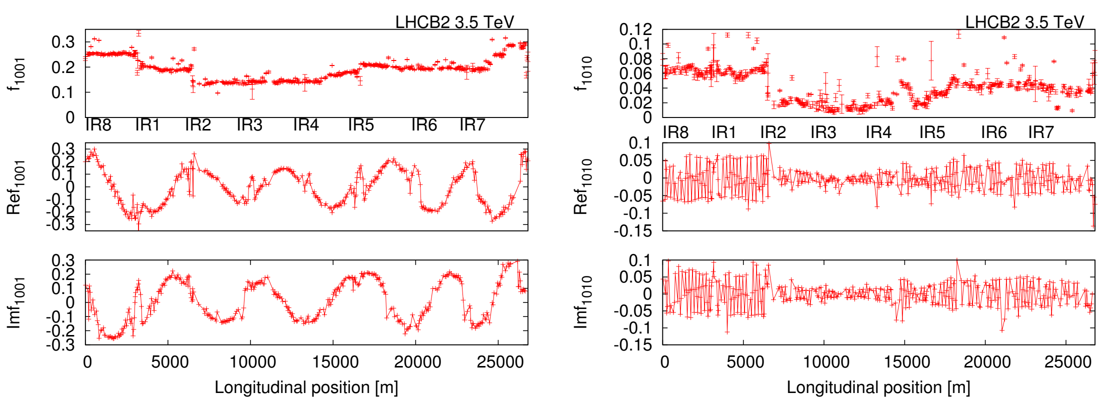

Figure 5.35: f_{1001} is shown on the left and f_{1010} on the right for beam 2, this for all IPs at a β^* value of 3.5.

the coupling corrections could be improved. The amplitude of the difference resonance is higher than the sum resonance. This was expected as the difference resonance is the leading coupling resonance.

5.3.3 Dispersion measurements

Dispersion measurements were performed for the first time with squeezed optics with all IPs at β^* value of 3.5 m. Frequency trims corresponding to a $\frac{\delta p}{p}$ of 3.4×10^{-4} and -4×10^{-4} were applied. When applying corrections with normal and skew quadrupoles it is important to check and make sure that the horizontal and vertical dispersion are not affected. Figure 5.36 shows the horizontal (left) and the vertical dispersion (right) for beam 1. The normalized horizontal dispersion before and after corrections are comparable. The vertical dispersion, however, shows a small increase.

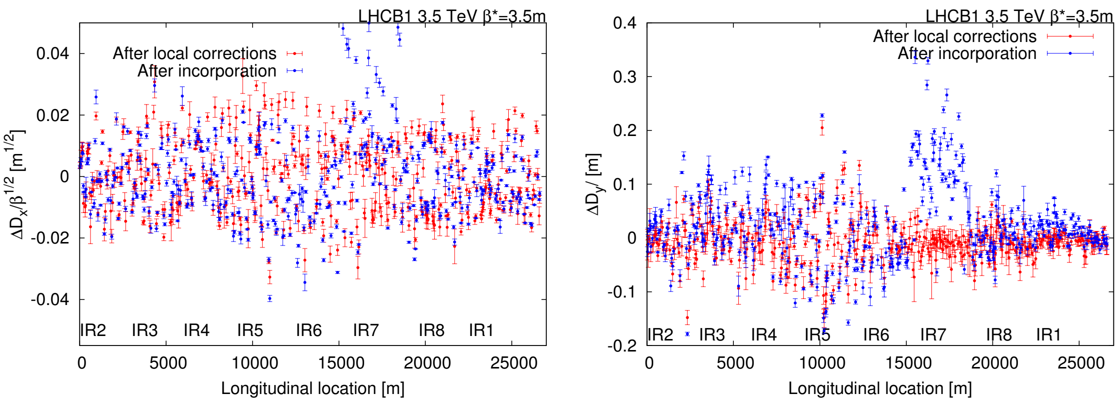

Figure 5.36: Normalized horizontal dispersion (left) and vertical dispersion (right) for beam 1, before (red) and after (blue) applying local and global corrections for all IPs with a β^* value of 3.5 m.

Figure 5.37 shows the horizontal (left) and the vertical (right) dispersion for beam 2. The dispersion before (red) and after (blue) corrections (local and global) were implemented. The normalized horizontal dispersion is comparable. The vertical dispersion, however, shows a small increase.

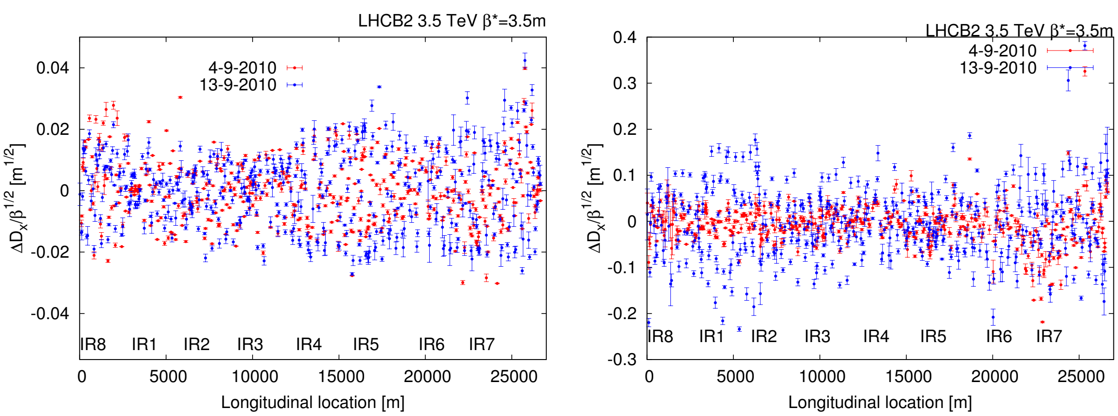

Figure 5.37: Normalized horizontal dispersion (left) and vertical dispersion (right) for beam 1, before (red) and after (blue) applying local and global corrections for all IPs with a β^* value of 3.5 m.

The rms values for the dispersion before and after corrections is listed in table 5.9. The rms value of normalized horizontal dispersion is below the tolerance of 0.0125.

For both the horizontal and vertical dispersion in beam 1 and beam 2, changes are observed between the two measurements. For beam 1 the measurement after the local corrections were implemented is shown in red and after incorporating the corrections in the squeeze process in blue . For beam 2 the measurement after the local corrections were implemented is shown in red and after incorporating and implementing the global corrections in blue. The changes could be explained by a change in the orbit, which introduces feed-down at the sextupoles, or the incorporation of the quadrupoles.

	Before corrections		After corrections	
	Beam 1	Beam 2	Beam 1	Beam 2
rms $\Delta\frac{D_x}{\beta_x}$ $[\frac{m}{\sqrt{\beta}}]$	0.0051	0.0037	0.0055	0.0055
rms D_y [m]	0.0367	0.0410	0.0448	0.0638

Table 5.9: rms values for the normalized horizontal dispersion beat and vertical dispersion for both beams before and after corrections.

5.3.4 β^* for all IPs at 3.5 m.

The β^*'s before and after the corrections were implemented are listed in table 5.10 and table 5.11 respectively. The largest error on the β^* measurement is about 6%. Before corrections were implemented an offset of up to 22% and large asymmetries between the two beams were observed. For instance for the vertical plane of IP2 and IP8, an asymmetry of respectively 34% and 17% was observed between the two beams. After the corrections the maximum offset observed is around 11%, comparable with the β-beat observed. The asymmetries that were observed for IP2 and IP8 are corrected down to 12% and 11% respectively .

IP	Beam	β^*_x	error	β^*_y	error
IP1	1	3.54	0.01	3.96	0.05
IP2	1	3.44	0.02	2.74	0.05
IP5	1	3.86	0.05	3.35	0.08
IP8	1	3.54	0.07	3.72	0.07
IP1	2	3.81	0.05	3.42	0.06
IP2	2	3.20	0.05	4.17	0.21
IP5	2	3.53	0.14	3.90	0.1
IP8	2	3.86	0.08	3.09	0.03

Table 5.10: β^* measurements at all IPs at a β^* value of 3.5 m before correction.

IP	Beam	β^*_x	error	β^*_y	error
IP1	1	3.59	0.06	3.90	0.57
IP2	1	3.37	0.21	3.24	0.04
IP5	1	3.82	0.06	3.73	0.17
IP8	1	3.65	0.15	3.73	0.07
IP1	2	3.42	0.05	3.58	0.17
IP2	2	3.89	0.06	3.66	0.13
IP5	2	3.50	0.12	3.64	0.08
IP8	2	3.57	0.06	3.33	0.09

Table 5.11: β^* measurements at all IPs at a β^* value of 3.5 m after correction.

5.4 Squeezing IR1 and IR5 below a β^* value of 2 m

In the beginning of 2011 it was decided that the β^* could be further decreased for the 2011 run [91]. Contrary to the 2010 run, not all IPs were squeezed to the same β^* value. Only the high luminosity experiments, IP1 and IP5, were squeezed to a β^* value of 1.5 m and later to a value of 1 m. IP2 and IP8 remained at a value of 10 m and 3 m respectively, during the proton run. IP2 was squeezed to a β^* value of 1 m for the ion run.

5.4.1 Overview

An overview of the squeeze commissioning for a β^* value of 1 m is shown in figure 5.38. The optics measurement and correction campaign in 2011 was completed in about 10 days, over 4 optics sessions. A peak β-beat of about 20% and 60% in the horizontal and vertical plane respectively for beam 1 was observed, as shown in figure 5.39. For beam 2 a peak β-beat of 30% and 25% for the horizontal and vertical plane respectively was observed, as shown in figure 5.40. The red dots show the measured β-beat before any corrections were applied. Large β-beat variations are observed for both beams, indicating that local error sources are present. After applying local corrections the observed local jumps were reduced significantly, shown by the green dots in figures 5.39 and 5.40. The peak β-beat for beam 1 was reduced to 20% and 15% for the horizontal and vertical plane respectively. For beam 2 the peak β-beat is reduced to 20% in both planes. Global corrections were applied separately for both beams. This was only possible because no common correctors were used. A β-beat of 10% is achieved for both planes in both beams, shown by the blue dots. Some out-layers above 10% are observed, most probably they are not physical.

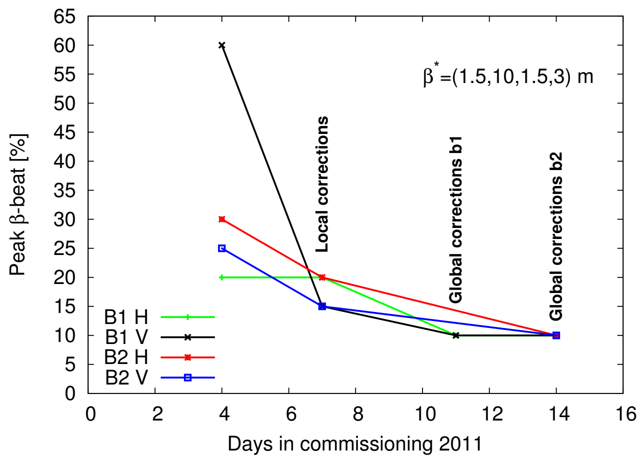

Figure 5.38: Overview of the applied corrections for the 2011 optics. On the horizontal axis 'days in commissioning' is represented and measured peak β-beat on the vertical axis.

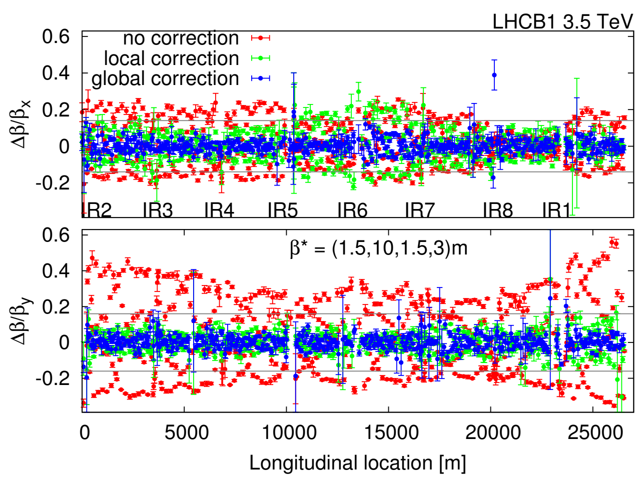

Figure 5.39: β-beat for beam 1 shown for the horizontal plane (above) and vertical plane (below). The three colors represent the β-beat measured at the different steps during the correction process. Measurements for the 'virgin machine' where no corrections were applied are shown in red. Measurements after applying local corrections are shown in green and measurements after both local and global corrections were applied are shown in blue. Tolerances are shown in black.

5.4.2 β-beat corrections

Corrections were applied for IP1 and IP5 at a β^* value of 1.5 m, 10 m for IP2 and 3 m for IP8. First local sources in the insertion regions were corrected using the Segment-by-Segment technique. After the strong local sources were corrected a global correction was calculated for both beams separately.

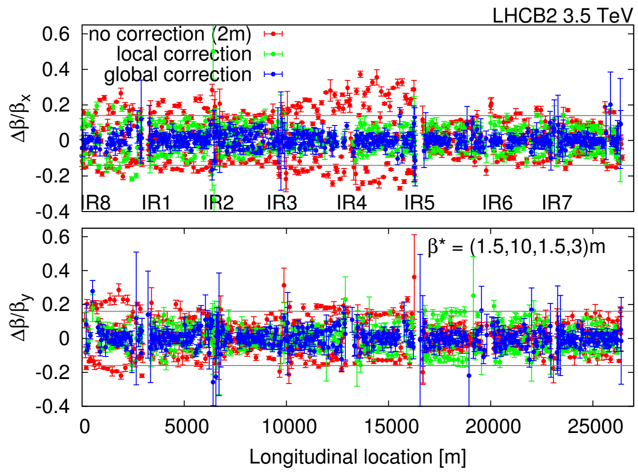

Figure 5.40: β-beat for beam 2 shown for the horizontal plane (above) and vertical plane (below). The three colors represent the β-beat measured at the different steps during the correction process. Measurements for the 'virgin machine' where no corrections were applied are shown in red. Measurements after applying local corrections are shown in green and measurements after both local and global corrections were applied are shown in blue. Tolerances are shown in black.

Local corrections

An illustration of a local correction in IR5 is shown in figure 5.41. Local corrections were calculated using the segment-by-segment technique. The local corrections for beam 2 were calculated at a β^* value of 2 m for IP1 and IP5. The reason for this was that beam 2 was lost due to a trip in skew quadrupole RQS.A78B2, driving the tune to 10^{th} order and 3^{th} order resonance, respectively in the horizontal and vertical plane. The local corrections for beam 1 and beam 2 were compared to several measurements below a β^* value of 4 m during the squeeze. The top plot shows the phase error in the horizontal plane and the bottom plot shows the vertical plane. The red line shows the measured error before local corrections were applied. The black line shows the fitted model, which is achieved by applying ktqx2.l5$= -1.0 \times 10^{-5}$ and ktqx2.r5$= -1.3 \times 10^{-5}$ to the local model to fit the measurements. The ktqx magnets, common for both beams, are trim quadrupoles nested in the triplets. The blue line shows the measured total phase error after applying the local correction in IR5. The error was reduced significantly. The implemented correction is not perfect, as the ktqx correctors are common for both beams. In this case a suitable correction for both beams had to be found. The triplet quadrupoles were identified as the leading error sources for the β-beat. The corrections were based on values found for the correction for all IRs at a β^* value of 3.5 m in 2010 [79]. Table 5.12 shows the local corrections for the triplets at IR1, IR5 and IR8. Two correctors (kq9.l1b1 and kq5.l6b2), one per beam, were additionally used to achieve a better correction. These two additional correctors represent the largest relative corrections.

Corrector	ΔK [10^{-5}m^{-2}]	Relative [%]
kq9.l1b1	3.8	-0.60
ktqx2.r1	-0.8	0.09
ktqx2.l5	1.0	0.11
ktqx2.r5	1.3	-0.15
kq5.l6b2	-4.6	0.70
ktqx2.l8	-2.3	0.26
ktqx2.r8	-0.5	-0.06

Table 5.12: Implemented local corrections are listed.

Global corrections

Global corrections for beam 1 and beam 2 were implemented separately. Only correctors acting on one beam were used. Figure 5.42 shows a distribution of the implemented correctors along beam 1 (top) and beam 2 (bottom). For beam 2 the distribution for both the calculated corrections in 2010 and

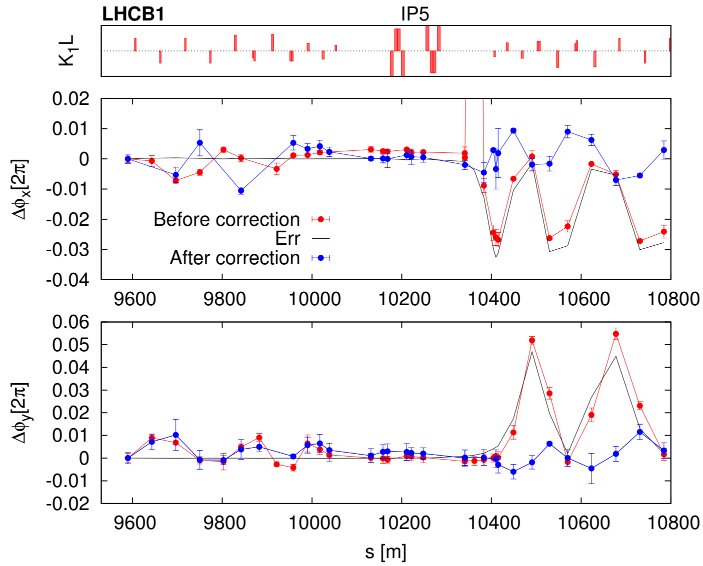

Figure 5.41: Illustration for local correction in IR5 using the segment-by-segment technique.

2011 are shown. No global correction was implemented for beam 1 during the correction campaign in 2010. A total of 95 and 112 correctors were used respectively for beam 1 and beam 2 to reduce the β-beat to a 10% level. The maximum strengths for both beams, 0.8 10^{-4}m^{-2}, are located around IR1. In 2011 112 correctors were used compared to 145 correctors in 2010 for beam 2, as less correctors were used a higher maximum strength was observed in 2011.

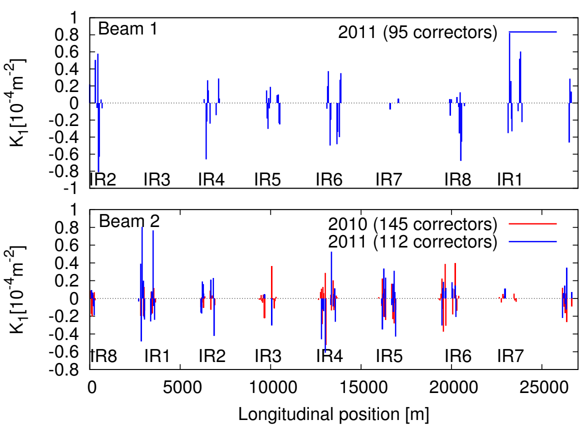

Figure 5.42: Distribution of correctors along the ring for beam 1 in 2011, shown in the top plot, and beam 2 in 2010 (red) and 2011 (blue), shown in the bottom plot. The correctors are trim quadrupoles, no common correctors were used. For beam 1 no global correction was applied in 2010. It can be observed that the largest corrector strengths applied are around IR1 for both beams.

5.4.3 Coupling measurements and correction

Coupling corrections were calculated for the triplets. The implemented corrections are listed in table 5.13. The largest correction implemented is for IR5. Figure 5.43 shows the difference and sum coupling resonances for beam 1 (left) and beam 2 (right) after the corrections. Before corrections (red) large jumps are observed at IR1, IR2, IR5 and IR8. After applying the local coupling corrections the jumps are reduced.

5.4.4 Dispersion measurement

Dispersion measurements were conducted for both beams after local and global correction were implemented. Figure 5.44 shows the normalized horizontal dispersion for beam 1 (left) and beam 2 (right).

Magnet	Calculated correction [m^{-2}]
kqsx3.l5	0.0007
kqsx3.r5	0.0007
kqsx3.l1	0.0005
kqsx3.r1	0.0005
kqsx3.l8	-0.0005
kqsx3.r8	-0.0005

Table 5.13: Local coupling corrections implemented.

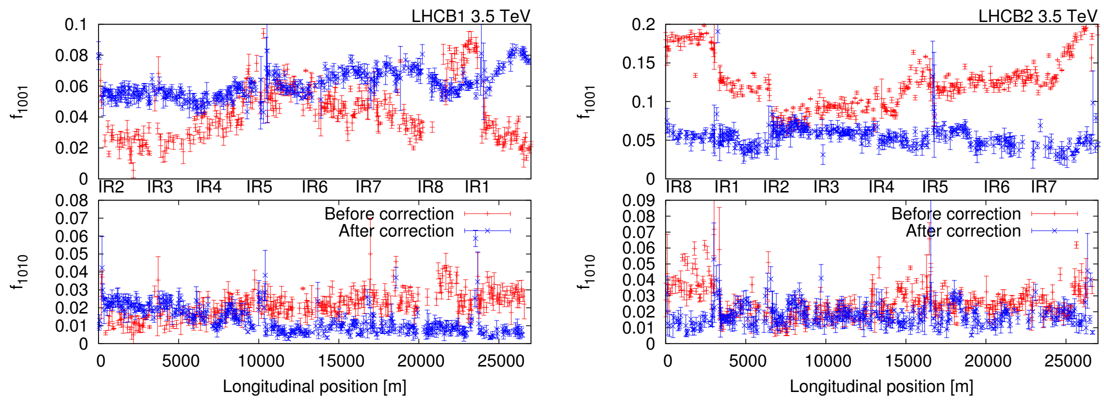

Figure 5.43: f_{1001} (top) and f_{1001} (bottom), before (red) and after (blue) correction for beam 1 (left) and beam 2 (right).

Figure 5.45 shows the vertical dispersion for beam 1 (left) and beam 2 (right). Large error bars were measured for the normalized horizontal dispersion of beam 2 and the vertical dispersion of beam 1 after local+global correction. The horizontal normalized dispersions for beam 1 and the vertical dispersions are comparable.

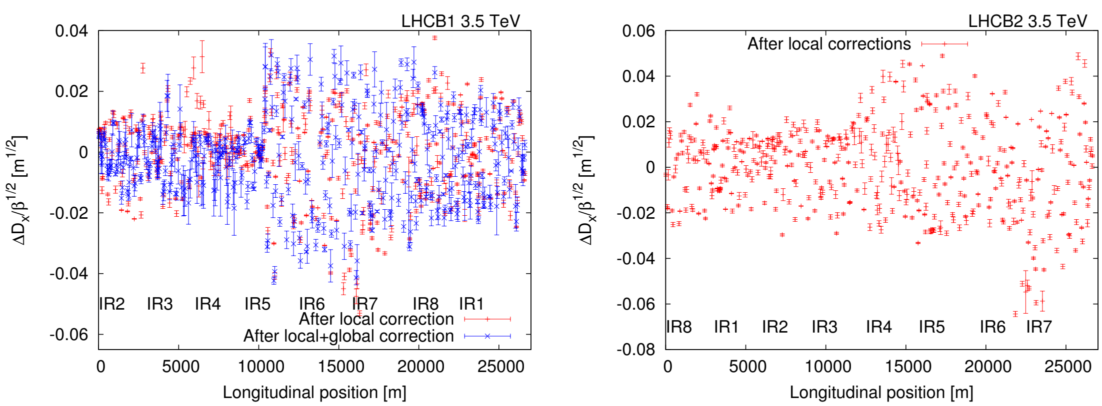

Figure 5.44: Normalized horizontal dispersion for beam 1 (left) and beam 2 (right). Measurements after local corrections are shown in red and after local + global corrections in blue. Only measurements after local corrections are shown for beam 2.

5.4.5 β^* measurements

β^* measurements were conducted for both beams after the local and local+global correction were implemented. The results are listed in table 5.14. After local corrections were applied asymmetries of up to 14% between the two beams were observed in the vertical plane of IP2 and IP5. After implementing the global correction the discrepancy in IP5 was corrected. The discrepancy in IP2 was reduced, but is still at the 10% level.

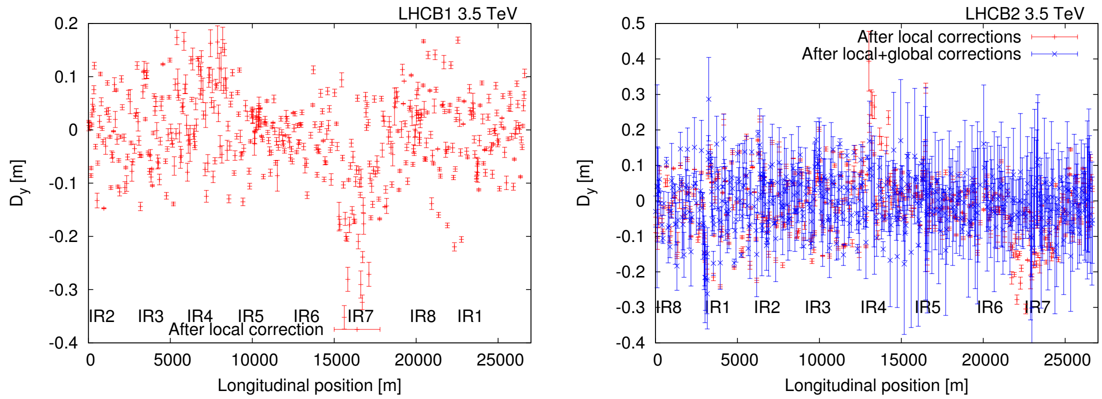

Figure 5.45: Vertical dispersion for beam 1 (left) and beam 2 (right). Measurement after local corrections are shown in red and after local + global corrections in blue. Only measurements after local corrections are shown for beam 1.

After local corrections					
IP	Beam	β_x^*	error	β_y^*	error
IP1	1	1.43	0.04	1.60	0.13
IP2	1	9.31	0.14	8.77	0.21
IP5	1	1.41	0.03	1.59	0.01
IP8	1	3.14	0.11	3.11	2.06
IP	Beam	β_x^*	error	β_y^*	error
IP1	2	1.55	0.10	1.54	0.05
IP2	2	10.15	0.14	10.28	0.03
IP5	2	1.53	0.05	1.38	0.04
IP8	2	3.18	0.11	3.15	0.14
After local and global corrections					
IP	Beam	β_x^*	error	β_y^*	error
IP1	1	1.53	0.02	1.59	0.14
IP2	1	9.82	0.34	9.67	0.67
IP5	1	1.52	0.02	1.51	0.08
IP8	1	2.97	0.06	3.08	0.04
IP	Beam	β_x^*	error	β_y^*	error
IP1	2	1.46	0.08	1.43	0.14
IP2	2	10.66	0.38	10.98	0.07
IP5	2	1.44	0.17	1.51	0.04
IP8	2	3.04	0.22	3.079	0.10

Table 5.14: β^* measurements listed for a design β^* value of 1.5 m in IP1 and IP5, 10 m in IP2 and 3 m in IP8. Measurements for the β^* both after local and local+global corrections were implemented are listed.

5.4.6 Pushing the boundaries, squeezing IP1 and IP5 down to a β^* value of 1 m.

New aperture measurements [92] showed that more aperture was available than initially thought. This allowed a further squeeze of the high luminosity experiments, IP1 and IP5, down to a β^* value of 1 m. For the optics commissioning of a β^* value of 1 m it was decided to keep the local and global corrections constant before squeezing. A minimal change was expected of keeping the global and local corrections constant during the squeeze [93] from a β^* value of 1.5 to 1 m, in IR1 and IR5.

β-beat comparison between a β^* value of 1.5 and 1 m

Figure 5.46 shows the β-beat for a β^* value of 1.5 m (red) and 1 m (blue), for IP1 and IP5, for beam 1 (left) and beam 2 (right). The increase in the β-beat was negligible for squeezing down to a β^* value of 1 m for IP1 and IP5.

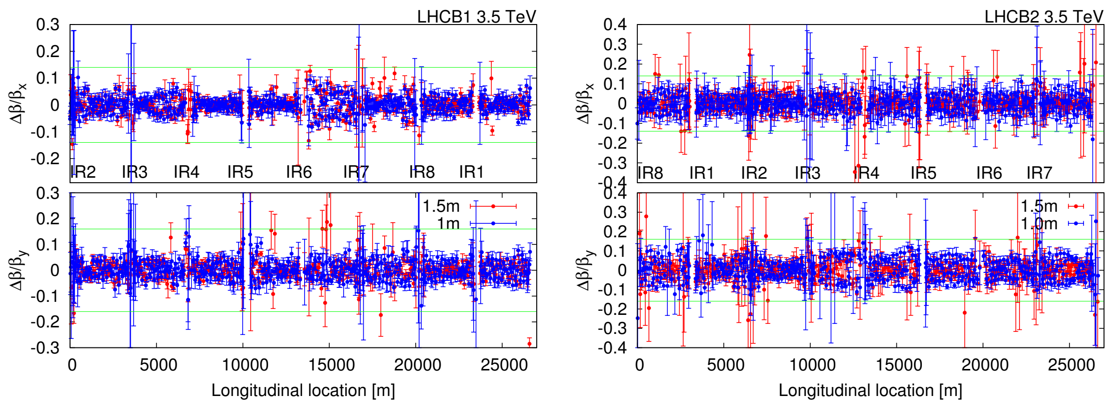

Figure 5.46: β-beat for β^* value of 1.5 m (red) and 1 m (blue). For beam 1 (left) and beam 2 (right). Tolerances are shown in green.

Figure 5.47 shows a histogram of the difference in the β-beat, for both planes and both beams, between the β^* values of 1.5 m and 1 m. The main part of the distribution is below 5%, which is about equal to the measurement resolution. Therefore it can be concluded that the local and global corrections remained valid for a β^* value of 1 m in IP1 and IP5.

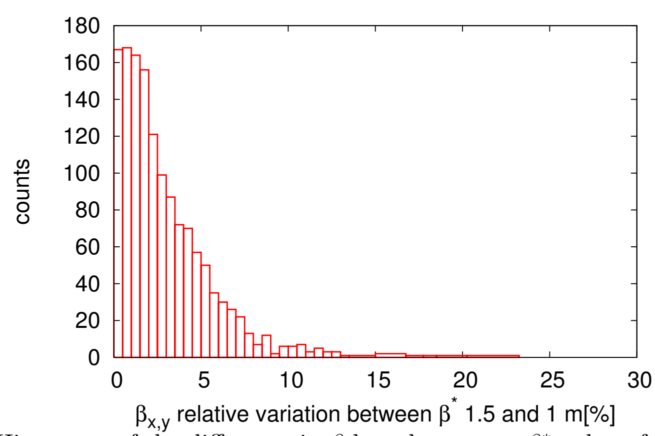

Figure 5.47: Histogram of the difference in β-beat between a β^* value of 1.5 m and 1 m.

Dispersion measurements

Dispersion measurements, shown in figure 5.48, were conducted for the β^* value of 1.5 m and the β^* value of 1 m in IP1 and IP5. Medium frequency trims in the order of ± 50 Hz, corresponding to a momentum offset of about $\mp 4 \times 10^{-4}$ was applied. Due to the large error bars in the measurement of the normalized horizontal dispersion in beam 2 and the vertical dispersion in beam 1 for the β^* value of 1.5 m (in IP1 and IP5) the data could not be presented. For the normalized horizontal dispersion in beam 1 and the vertical dispersion in beam 2 no large deviations for the β^* value of 1 m were observed as compared to 1.5 m.

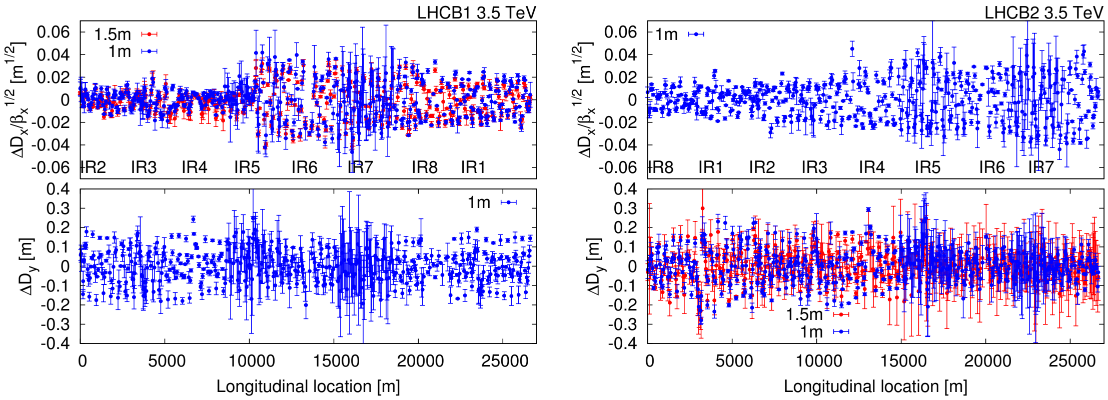

Figure 5.48: Normalized horizontal dispersion shown in the top plot and vertical dispersion in the bottom plot. Beam 1 is shown on the left and beam 2 on the right for β^* values of 1.5 m (blue) and 1 m (red).

β^* measurements

The results for the β^* measurements conducted are listed in table 5.15. The largest asymmetry between the two beams is about 6% in the vertical plane of IP2. The same asymmetry was observed for the β^* value of 1.5 m (see table 5.14). As the error bar for the vertical plane of IP2 beam 2 is large, no conclusion on possible improvement of IP2 can be drawn.

IP	Beam	β_x^*	error	β_y^*	error
IP1	1	0.97	0.03	1.04	0.17
IP2	1	9.72	0.08	9.93	0.04
IP5	1	0.99	0.03	0.95	0.11
IP8	1	3.10	0.41	2.77	0.25
IP	Beam	β_x^*	error	β_y^*	error
IP1	2	1.01	0.10	1.05	0.06
IP2	2	9.84	0.38	10.57	0.92
IP5	2	0.94	0.13	0.98	0.09
IP8	2	3.18	0.11	2.90	0.29

Table 5.15: β^* measurements for the design β^* of IP1 and IP5 at 1 m, 10 m in IP2 and 3 m at IP8

5.5 Squeezing down IR2 together with IR1 and IR5 to a β^* value of 1 m

The ALICE experiment, located at IR2, is the dedicated heavy ion experiment of the LHC. At the end of every run the LHC is switched from a proton machine to an ion machine [94]. IP2 was squeezed down to a β^* value of 1 m for ions, although the commissioning was done using protons. The motivation for using protons instead of ions was to ease the commissioning and a better measurement resolution was expected. Before the squeeze of IP2, the $\beta-$beat remained at 10%.

5.5.1 Measurement of the β-beat for IP2 from the β^* value of 10 m down to 1 m

The $\beta-$beat for the β^* value of 1 m for IP1 and IP5, 10 m for IP2 and 3 m for IP8 (red) and a β^* of 1 m for IP1, IP2, IP5 and 3 m for IP8 (blue) is shown in figure 5.49. A slight increase is observed for both beams. The horizontal plane is at a peak of 15% and the vertical plane at 25% for both beams. The error bars for beam 1 are slightly larger than for beam 2.

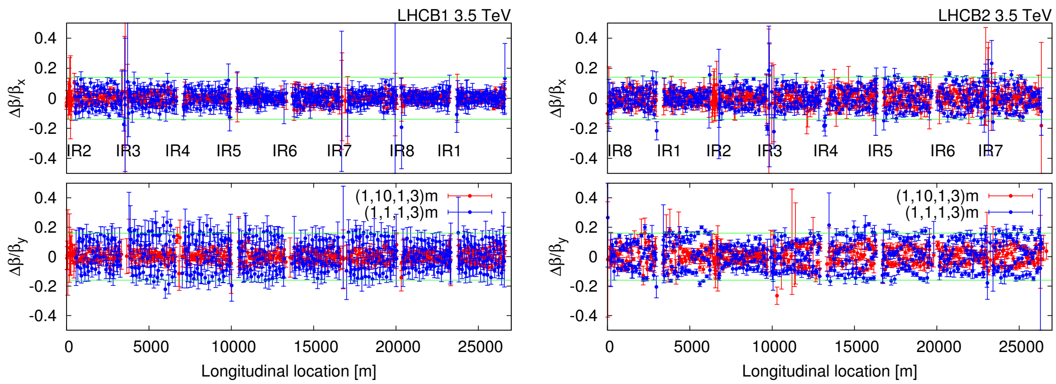

Figure 5.49: $\beta-$beat for beam 1 (left) and beam 2 (right). The red plot shows the $\beta-$beat for the β^* value of 1 m for IP1 and IP5, 10 m for IP2 and 3 m for IP8, and the blue plot for the β^* value of 1 m for IP1, IP2, IP5 and 3 m for IP8 . Tolerances are shown in green.

5.5.2 Correction at IP2 at a β^* value of 1 m

During the squeeze of IP2 down to the β^* value of 2 m in 2010 (see section 5.2.1), a small increase of the β-beat at the 5% level was observed. Therefore no large β-beat was expected by going down to 1 m β^* in IP2. The measurement confirmed a small increase of the β-beat of about $10 - 15\%$, bringing the $\frac{\Delta\beta}{\beta}$ slightly above the tolerances, as shown in figure 5.49. The motivation to correct this $\frac{\Delta\beta}{\beta}$ was to allow as much aperture as possible for the large external crossing angle. The large external crossing angle was needed to cancel the large angle induced by the ALICE spectrometer bump, and collisions were head-on [94], [95]. The correction was calculated separately for both beams. The predicted corrections for the β-beat (left) and horizontal dispersion (right) are shown in figure 5.50 for beam 1 and figure 5.51 for beam 2. The predicted change in the horizontal dispersion is larger for beam 1 than for beam 2, this is explained because weight was placed on the horizontal dispersion for beam 1. A small improvement was observed for the predicted correction of the horizontal dispersion in beam 2, even though no weight was placed on it. It was decided to not correct the horizontal dispersion for beam 2 as the needed quadrupole strengths would have been to large to correct both the phase and the horizontal dispersion.

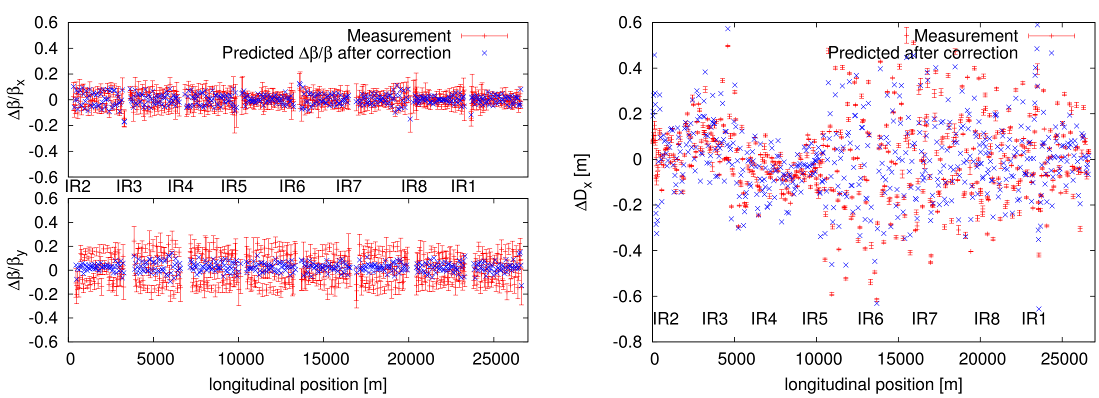

Figure 5.50: Predicted $\frac{\Delta\beta}{\beta}$ after correction for β-beat (left) and dispersion (right) for beam 1, this for a β^* value of 1 m for IP1, IP2, IP5 and 3 m for IP8 .

Only 20 quadrupoles in IR2 for both beams and no common correctors were used for this correction. The correctors used are shown in figure 5.52. As IR2 was squeezed separately the expected error sources were emerging from IR2. It was shown that by using only local correctors it is indeed possible to locally

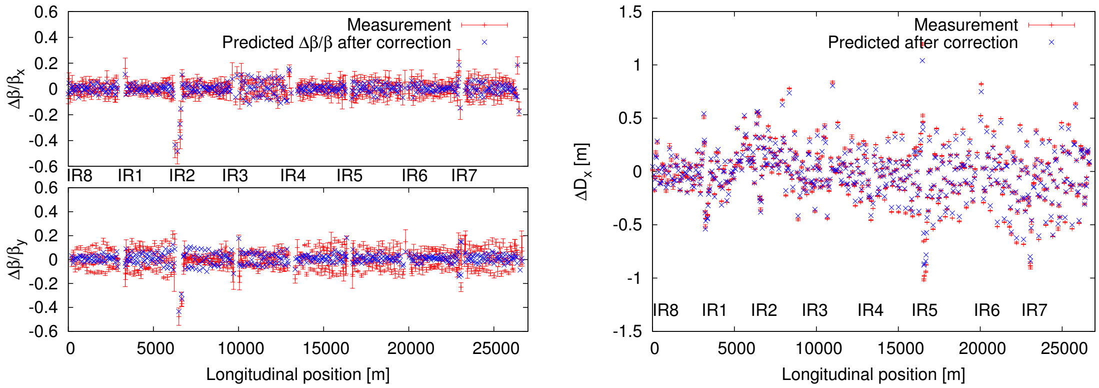

Figure 5.51: Predicted $\frac{\Delta\beta}{\beta}$ after correction for β-beat (left) and dispersion (right) for beam 1, this for a β^* value of 1 m for IP1, IP2, IP5 and 3 m for IP8 .

compensate for these errors. There is a difference of about a factor of 3 for the corrections between beam 1 and beam 2. The reason for this is that for beam 1, the correction is larger as the weight was placed on the dispersion, together with the horizontal and vertical phase. For beam 2 the weight was only placed on the phases. Due to time constraints no dispersion measurements were conducted after the corrections were implemented, so no conclusions on dispersion corrections can be drawn here.

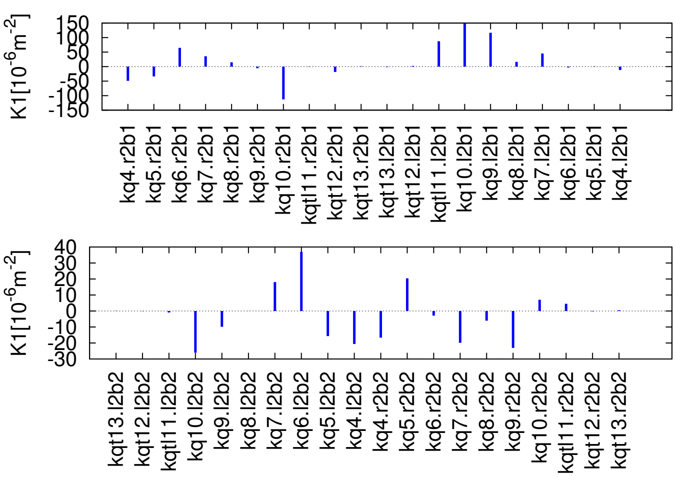

Figure 5.52: Correctors used for the global correction for beam 1 (top) and beam 2 (bottom).

5.5.3 Comparison of the $\beta-$beat before and after IR2 correction

The $\beta-$beat before and after the correction is shown in figure 5.53. Before the correction a beta-beat of around 15% and 20% was observed, after corrections this was reduced to 10% and 20%.

5.5.4 Coupling

Measurements were conducted for coupling before correction at the β^* value of 2 m and after correction for the β^* value of 1 m at IP2. Figure 5.54 shows measurements before (red) and after (blue) local corrections for IP2 were implemented. The result for beam 1 is shown on the left and for beam 2 on the right. The top plot shows the 'difference resonance' and the bottom plot the 'sum resonance'. The local corrections were calculated at IR2 for a β^* value of 2 m and did not change for a β^* value of 1 m. The corrections are listed in table 5.16. The corrections for IR2 are the largest corrections implemented during the commissioning, as IR2 has the strongest coupling source.

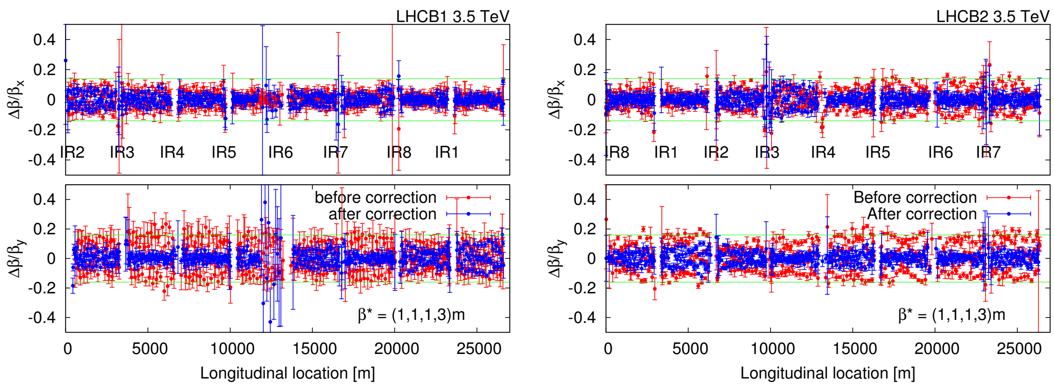

Figure 5.53: $\beta-$beat for beam 1 (left) and beam 2 (right) for the β^* value of 1 m for IP1, IP2, IP5 and 3 m for IP8, before (red) and after (blue) corrections at IP2. Tolerances are shown in green.

Magnet	**Calculated correction** $[m^{-2}]$
kqsx3.r2	-0.001
kqsx3.l2	-0.001

Table 5.16: Calculated corrections for IR2 at a β^* value of 2 m.

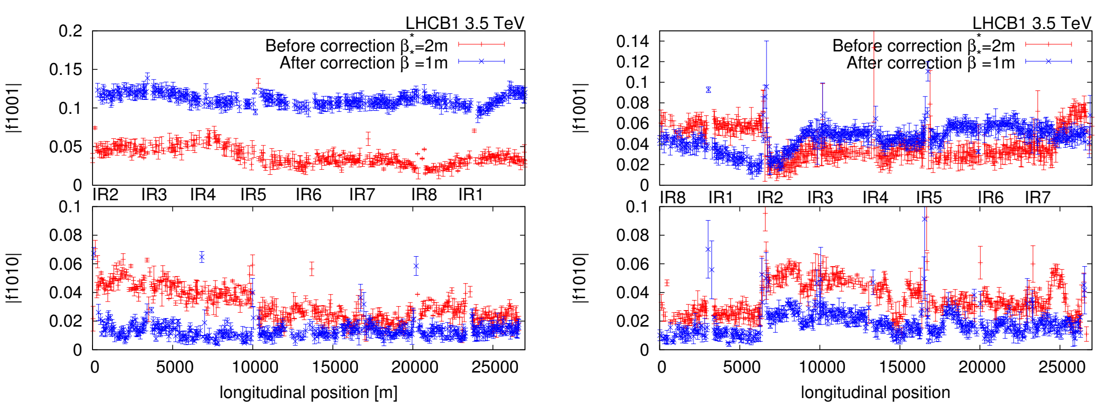

Figure 5.54: Difference (top) and sum resonance (bottom). For beam 1 (left) and beam 2 (right).

5.5.5 Dispersion

Dispersion measurements were conducted before and after the squeeze of IR2. The horizontal normalized dispersion is shown in figure 5.55 for beam 1 (left) and beam 2 (right). The red dots show measurements before squeezing IR2 and the blue dots after. For beam 1 the horizontal dispersion is decreased slightly and the bump around IR2 is not observable anymore. For beam 2, on the other hand, the horizontal normalized dispersion seems to have increased. The error bar for beam 1 is large between IR5 and IR8 for both the normalized horizontal and vertical dispersion, with IR2 squeezed. The same could be observed for beam 2 around IR5 and IR7 for IR2 unsqueezed.

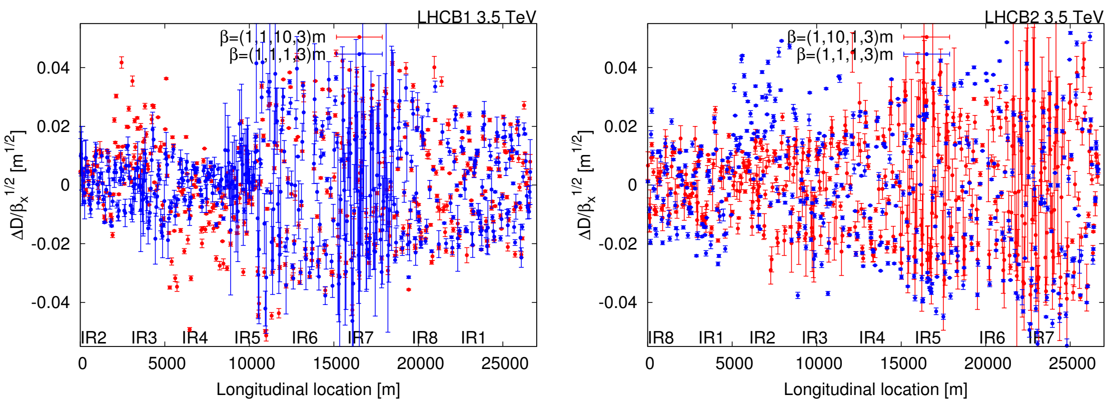

Figure 5.55: Horizontal dispersion for beam 1 (left) and beam 2 (right). Before squeezing IR2 (red) and after (blue).

The vertical dispersion is shown in figure 5.56 for beam 1 (left) and beam 2 (right). The red dots show the measurements before squeezing IP2 and the blue dots after.

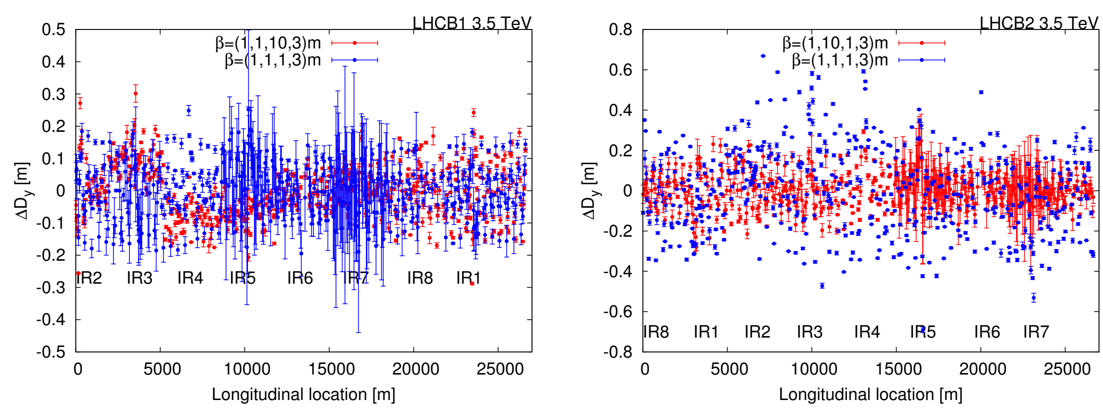

Figure 5.56: Vertical dispersion for beam 1 (left) and beam 2 (right). Before squeezing IR2 (red) and after (blue).

5.5.6 β^* measurements for IP2 at the β^* value of 1 m

β^* measurements were conducted before (see table 5.17) and after (see table 5.18) correcting IP2. Before corrections the largest asymmetry of about 11% between the two beams was observed in the horizontal plane of IP2. After correction this asymmetry was reduced to 4%. The predicted luminosity imbalance (IP1/IP5) between the high luminosity experiments was about 4% before corrections and -2% after corrections.

IP	Beam	β^*_x	error	β^*_y	error
IP1	1	1.05	0.05	0.93	0.03
IP2	1	1.0	0.05	1.03	0.01
IP5	1	0.99	0.02	1.07	0.19
IP8	1	2.96	0.29	2.86	0.13
IP1	2	0.96	0.05	1.06	0.08
IP2	2	1.11	0.12	1.11	0.16
IP5	2	1.01	0.14	1.10	0.03
IP8	2	3.08	0.15	2.73	0.21

Table 5.17: β^* measurements at design β^*=1 m for IP1,IP2,IP5 and 3 m for IP8 before correction.

IP	Beam	β^*_x	error	β^*_y	error
IP1	1	1.009	0.006	1.071	0.025
IP2	1	0.95	0.054	1.014	0.101
IP5	1	0.976	0.024	0.98	0.02
IP8	1	3.121	0.101	3.088	0.164
IP1	2	0.99	0.045	1.015	0.074
IP2	2	1.006	0.096	1.031	0.03
IP5	2	1.011	0.191	1.04	0.042
IP8	2	2.966	0.046	2.956	0.289

Table 5.18: β^* measurements at design β^*=1 m for IP1,IP2,IP5 and 3 m for IP8 after correction.

5.6 Non-linear and chromatic measurements

Non-linearities and chromatic measurements play an increasingly important role when β^* decreases. The higher order correctors affect the dynamic aperture when the β^* is squeezed below 1 m [79]. This was the direct motivation for conducting measurements for higher-order and chromatic functions. Paragraph 5.6.1 discusses the effect of the non-linear chromaticity correction on the amplitude detuning. Paragraph 5.6.2 discusses the studies of the resonance driving terms. Paragraph 5.6.3 discusses the results of the chromatic measurements.

5.6.1 Amplitude detuning

Non-linear magnetic fields (i.e. from sextupoles onward) are the source of amplitude detuning. Sextupoles and octupoles introduce a linear dependence of the tunes in the action [14]:

$$Q_z = Q_z^0 + \frac{\partial Q_z}{\partial \epsilon_x} 2J_x + \frac{\partial Q_z}{\partial \epsilon_y} 2J_y. \tag{5.1}$$

where z stands either for the horizontal (x) or vertical plane (y). Q_z represents the perturbed tune and Q_z^0 the unperturbed tune. $J_{x,y}$ is the action. $\epsilon_{x,y}$ is the single particle emittance and relates to the action as $\epsilon_{x,y} = 2J_{x,y}$.

During machine studies in 2011 an experiment was conducted to measure and correct the linear and non-linear chromaticity for Beam 2. For this study a knob was calculated to correct the linear and non-linear chromaticity [96]. Non-linear chromaticity was corrected using octupolar and decapolar correctors installed around the ring on one side of the dipole magnets. Correcting the non-linear chromaticity also had an effect on the amplitude detuning, as discussed above. Measurements were conducted to measure the amplitude detuning. In figure 5.57 the amplitude detuning is shown. The amplitude detuning values are calculated using a linear fit and are listed in Table 5.19 . The tune derivatives $\frac{\partial Q}{\partial \epsilon}$ before and after correction are listed. The terms are obtained by a linear fit from the data presented in figure 5.57. A significant reduction of the amplitude detuning is achieved. The two main sources for decoherence are chromaticity and amplitude detuning [20]. In figure 5.58 turn-by-turn data is shown before and after correction. A clear improvement in the decoherence is observed. More turns could be analyzed, hence improving the measurement resolution of the optics functions.

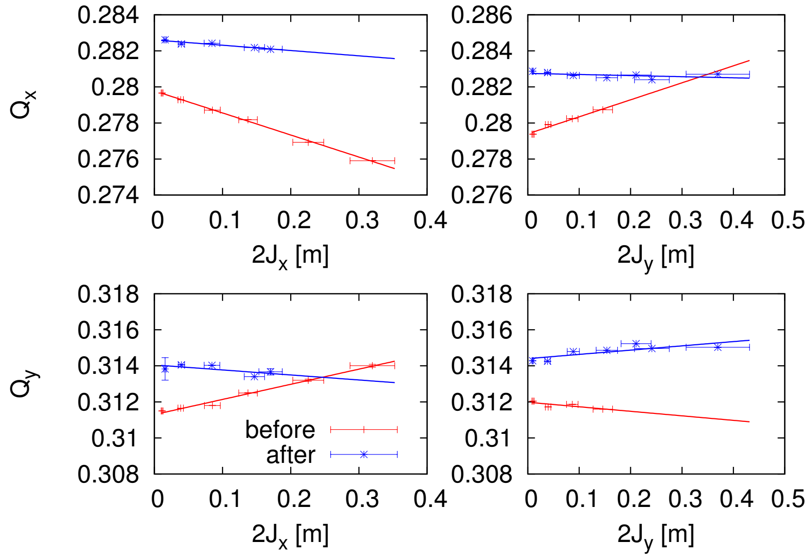

Figure 5.57: Amplitude detuning before any corrections (red) and after (blue). Horizontal plane (top) and vertical plane (bottom) are shown.

function	Before [10^6 m rad]	After [10^6 m rad]
$\frac{\partial q_x}{\partial \epsilon_x}$	-0.0122 $\pm$ 0.0002	-0.0029 $\pm$ 0.0006
$\frac{\partial q_x}{\partial \epsilon_y}$	0.0094 $\pm$ 0.0013	0.0006 $\pm$ 0.0005
$\frac{\partial q_y}{\partial \epsilon_x}$	0.0084 $\pm$ 0.0005	-0.0027 $\pm$ 0.0017
$\frac{\partial q_y}{\partial \epsilon_y}$	-0.0025 $\pm$ 0.0015	0.0023 $\pm$ 0.0008

Table 5.19: Amplitude detuning before and after correction, cross terms are included.

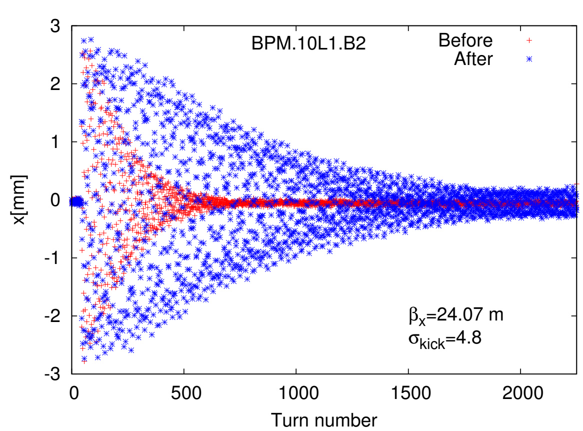

Figure 5.58: Turn-by-turn data before (red) and after (blue) correction of the non-linear chromaticity.

5.6.2 Measurement of resonance driving terms

Measurements of resonance driving terms were conducted during one experiment in 2011 [97]. The collimators were opened allowing an aperture of 12σ, some collimators were limited to 8σ. For this experiment the aperture kicker was limited to 5σ, due to operational and hardware reasons. Only measurements for Beam 2 were conducted. Kicks were applied in different combinations. First the horizontal plane only was excited in steps, later both planes were excited in steps.

BPM spectrum

From the turn-by-turn data about 1500 turns were acquired. The turn-by-turn data was then analyzed using an interpolated FFT, such as SUSSIX. The amplitude and phase of the main betatron tune line and the secondary lines were identified for every BPM. Figure 5.59 shows the horizontal plane of BPM.12L1 for beam 2, this for the case were only a 4.6σ was applied in the horizontal plane. Only two lines could be identified, the horizontal main betatron tune line (Q_x) and the sextupolar line ($2Q_x$).

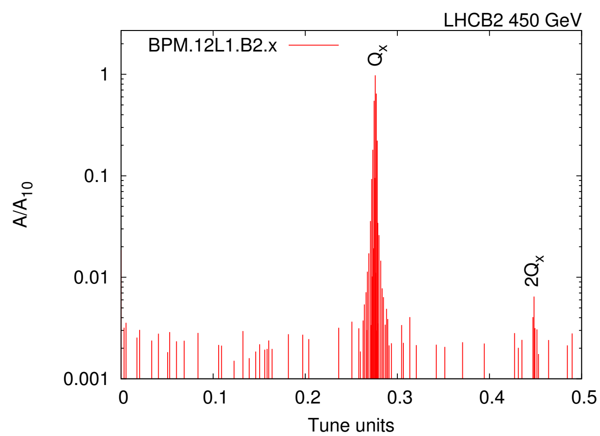

Figure 5.59: Horizontal tune spectrum for BPM BPM.12L1.B2.

Figure 5.60 shows the normalized sextupolar ($2Q_x$) line and octupolar ($3Q_x$) line around the ring together with the noise for beam 2. The signal to noise ratio is about 3 for the $2Q_x$ line and about 2 for the $3Q_x$ line. For some BPMs the $3Q_x$ line is below the noise threshold, meaning the signal acquired is noise. In sector 6-7 points are missing because of a crate of BPMs which was not acquiring data.

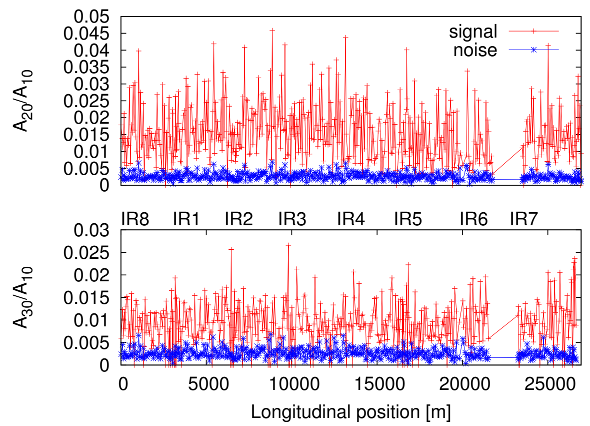

Figure 5.60: Sextupolar ($2Q_x$) line (top) and octupolar ($3Q_x$) line around the ring for beam 2. Normalized signal in red and the noise in blue.

First LHC measurement of the f_{3000} resonance driving term

A first attempt to measure non-linearities has been mode. In figure 5.61 the absolute value of the f_{3000} resonance driving term is shown. f_{3000} is the resonance driving term coming from normal sextupolar terms and is identified in the frequency spectrum by the $-2Q_x$ line. The effect of decoherence is taken into account for the measured data. Measurement and model [98], in the arcs, are in relatively good agreement. However, around the IP a large discrepancy is observed. Measurement is significantly larger. This discrepancy between measurement and model could be explained by several factors [99], such as noise, phase advance between the BPMs in the IP or by the non-linearity of the BPMs. A plausible explanation is that the observed f_{3000} around the IPs is dominated by the non-linearity of the BPMs.

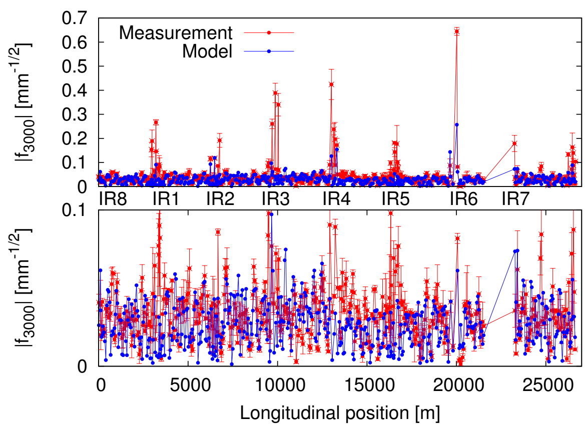

Figure 5.61: The absolute value of the f_{3000} resonance driving term is shown. Top plot includes large values around the IPs. The bottom plot zooms in on the arcs. The gap in the data is due to some missing BPMs.

5.6.3 Chromatic measurements

During the course of the commissioning several measurements for the chromatic measurements were conducted for squeezed optics. Measurements for the chromatic function were also conducted during injection, but because of a too large off-momentum trim the error bars are large.

Measurements at all IPs β^* value of 3.5 m

First measurements for the chromatic β were conducted in the second half of 2010 when all IPs were squeezed to a β^* value of 3.5 m. Frequency trims in the order of ± 50 Hz,± 100 Hz corresponding to a $\frac{\delta p}{p}$ value of $\mp 0.4 \times 10^{-4}$,$\mp 0.8 \times 10^{-4}$ respectively were applied.

Figure 5.62 shows the Montague amplitude function for beam 1 (left) and beam 2 (right). A discrepancy for the vertical plane between IR8 to IR2 was observed.

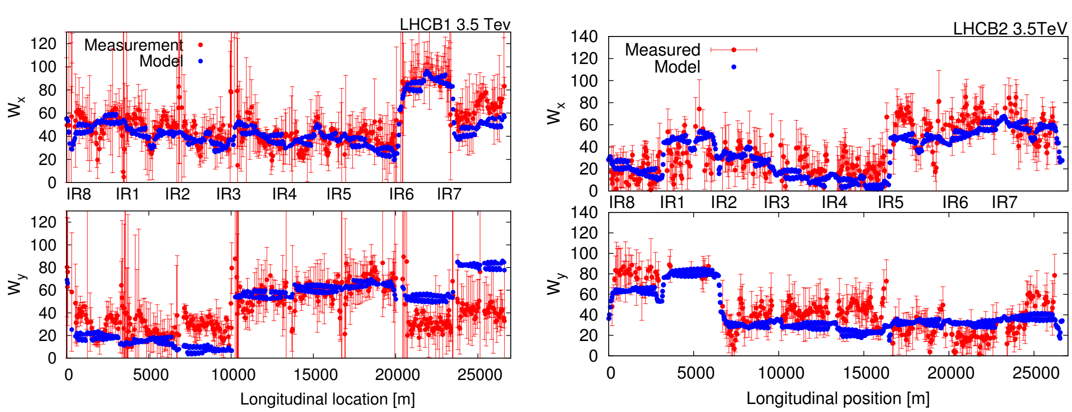

Figure 5.62: The amplitude of the Montague function is shown before correction of all IPs at a β^* value of 3.5 m for beam 1 (left) and beam 2 (right). The model is shown in blue and the measurements in red.

New measurements were conducted after local corrections, for beam 1 and beam 2, and global correction, for beam 2, were applied in September 2010. The error on the measurement was larger, but the observed discrepancy for the vertical plane of beam 1 was reduced. This means that correcting the β-beat has a positive effect on the chromatic functions.

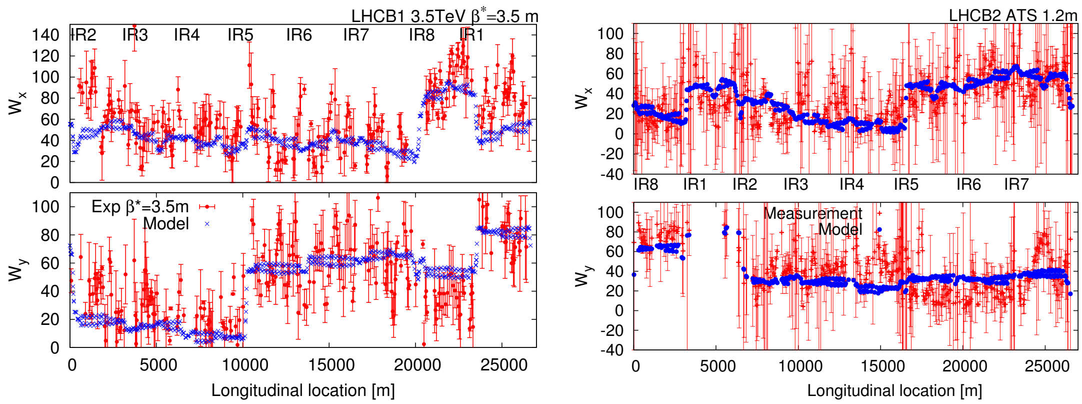

Figure 5.63: The amplitude of the Montague function is shown after correction of all IPs at a β^* value of 3.5 m for beam 1 (left) and beam 2 (right). The model is shown in blue and the measurements in red.

Measurements at β^* value of 1 m for all IPs

In 2011, during the commissioning of β^* value of 1.0 m for the high luminosity experiments, IP1 and IP5, measurements were conducted for the chromatic functions. Frequency trims were applied of the order of ± 50 Hz, corresponding to a $\frac{\delta p}{p}$ value of $\mp 0.8 \times 10^{-4}$. Small discrepancies were observed for the vertical plane of beam 1, sector 8-1, same sector as for β^* 3.5 m. The discrepancy for 1 m is smaller than for 3.5 m, this could be explained by the fact that the β-beat for 3.5 m is about 15% and for 1 m about 10%.

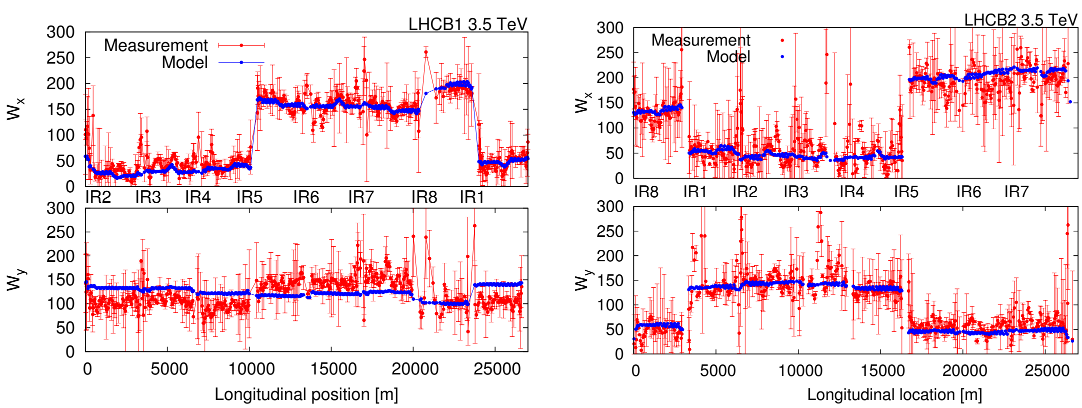

Figure 5.64: The amplitude of the Montague function is shown for IP1 and IP5 at a β^* value of 1.0 m, 10 m for IP2 and 3 m for IP8 m for beam 1 (left) and beam 2 (right). The model is shown in blue and the measurements in red.

5.7 Observations

In this section observations made during the commissioning will be discussed. These observations allow for a better understanding of the optics and the LHC in general. Observations during injection and flattop are discussed in section 5.7.1. Section 5.7.2 highlights observations made during the measurements with squeezed optics. The performance of the beam position monitors is discussed in section 5.7.3. The error bars measured for different optics functions at different time steps are presented in section 5.7.4.

5.7.1 Observations at injection and flattop

In this section some special observations made during the measurement at injection will be presented.

The importance of precycle

The importance of precycling the machine is shown in figure 5.65. The red dots represent the first measurements conducted for beam 1, the blue dots shows measurements conducted 5 days later. The latter was conducted without precycling the machine, and it showed a difference in the beta-beat of up to 20%.

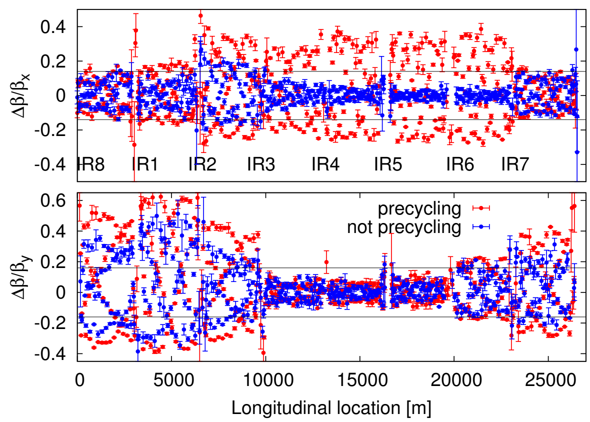

Figure 5.65: Beam 2 measurement are shown for the horizontal (top) and vertical (bottom) β-beat. Two cases are shown, the first case for precycling the LHC (red) and the second for not precycling the LHC (blue).

Stability of the optics

Stability of the optics and in general stability of the magnets are of great importance for the safe operation of the machine. Large fluctuations have a large impact on machine operations. Therefore it was of great importance to regularly check the stability of the optics. Measurements at injection were conducted during several instances during the commissioning. In 2010 two measurements were conducted over a period of 3 months. A difference of up to 8%, which exceeded the measurement resolution, was observed. On the other hand, two measurements conducted over a period of 8 months in 2011 showed no indication of drift in the optics stability of the machine. A histogram with the relative difference is shown in figure 5.66.

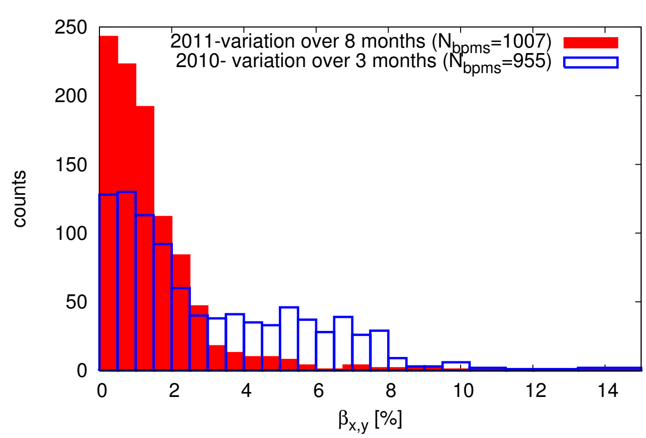

Figure 5.66: Histogram shows the relative variation in the β-beat over a period of 8 months (red) and 3 months (blue).

Ramp rate

The ramp rate was initially set to 2 A/s, and was later changed to 10 A/s. In figure 5.67 the two ramps are plotted. By implementing the 10 A/s ramp, a large amount of time – about 30 min per fill– was saved. The gain in time was about 3, instead of 5. This was because the beginning of the ramp for the 10 A/s ramp is not linear. Increasing the ramp rate reduced the turn around time between physics fill, hence the amount of time allocated for physics was increased.

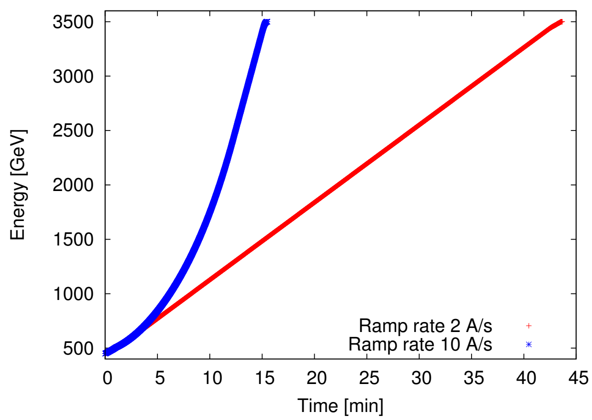

Figure 5.67: The time needed for ramping up the LHC from an energy of 450 GeV to 3.5 TeV, for a ramp rate of 2 A/s (red) and 10 A/s (blue).

An investigation whether the change in ramp rate could have an effect on the optics was conducted. Figure 5.68 shows the beta-beat for the two ramps of beam 1 (left) and beam 2 (right). The change is within the error bars, meaning that the faster ramp had no significant effect on the optics.

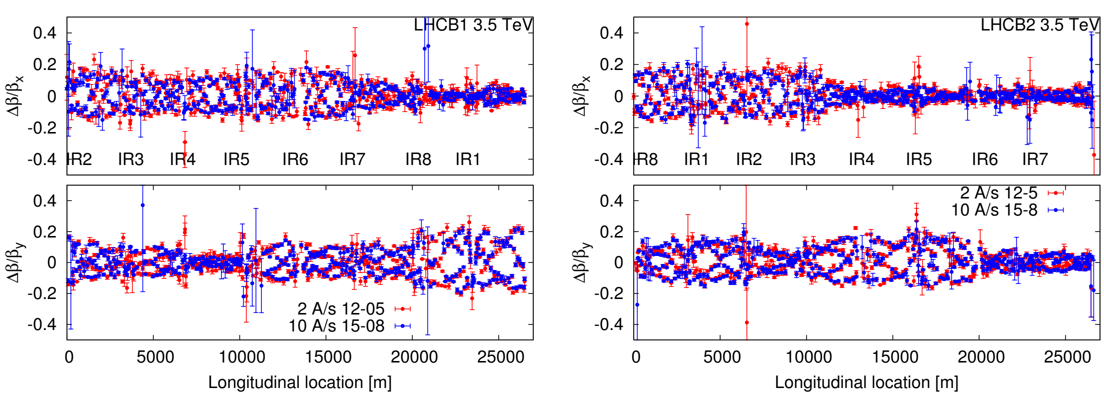

Figure 5.68: β-beat for the horizontal plane (top) and the vertical plane (bottom), for beam 1 (left) and beam 2 (right). Ramp rate of 2 A/s is shown in red and of 10 A/s in blue.

5.7.2 Observations with squeezed beams

In this section some special observations made during the measurement at squeezed optics will be presented.

Stability of the optics

Figure 5.69 shows the stability of the optics for a β^* value of 3.5 m over a 3 month period. Both measurements were conducted right after the squeeze. The main distribution of the variation for the optics is up to 5%, about the same value as the measurement resolution. Therefore it was concluded that the optics of the LHC is reproducible for squeezed optics.

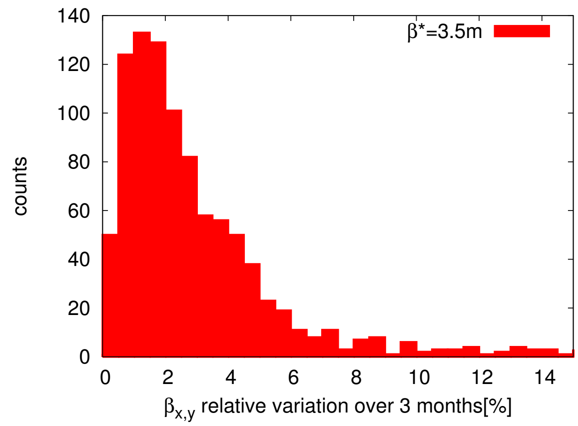

Figure 5.69: Stability of the optics for $\beta^* = 3.5$ m.

End-of-fill measurements

End-of-fill studies were performed for $\beta^* = 2$ m. No measurements were conducted right before the fill, but the data was compared with a previous measurement from a prior fill. The time lapse between the beginning and the end of the fill was about 30 hours. Figure 5.70 shows the difference in β-beat for beam 1. The plot shows a peak difference in the β-beat of around 10%, larget than the value of the measurement resolution. Both in the horizontal and vertical plane abrupt jumps at IP_1, IP_2 and IP_8 are observed. A possible explanation is the decay of the quadrupolar errors in IR superconducting magnets along the fill. Such a decay was observed in magnetic measurements with the 7 TeV settings [100] but there is no data available for the settings at 3.5 TeV. More statistics are needed to better understand the level of reproducibility and the possible dynamic error sources.

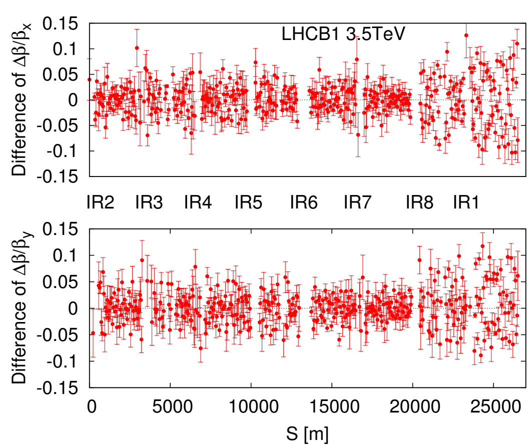

Figure 5.70: β-beat for end of fill study.

5.7.3 Beam position monitors

An optimal performance of the LHC BPM system is crucial for the optics measurement. Figure 5.71 shows the failing rate for the BPMs for beam 1 and figure 5.72 for beam 2 in 2010. For this analysis about 383 and 351 files, respectively for beam 1 and beam 2, were analyzed. Figure 5.73 shows the failure rate for the BPMs for beam 1 and figure 5.74 for beam 2 for 2011. For this analysis about 258 and 313 files, respectively for beam 1 and beam 2, were analyzed. For the analysis performed, no difference was made between BPMs failing at injection or squeezed optics. Missing crates, meaning missing sections of BPMs, was also disregarded. For beam 1 the maximum number of BPMs failing decreased by about 38% in 2011 with respect to 2010. For beam 2, on the other hand, the maximum number of failing BPMs increased by about 47% in 2011 compared to 2010. But the LHC BPMs have been performing excellently, with a maximum failing rate of about 10%.

Most common causes for the BPMs being filtered out are:

- BPM did not acquire any signal (returning 0).

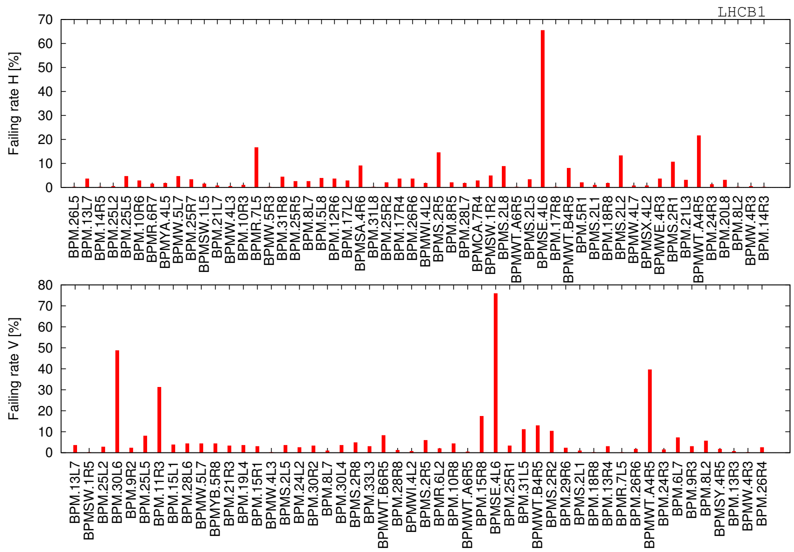

Figure 5.71: Failing rate for the BPMs of beam 1 (left) and beam 2 (right) for 2010.

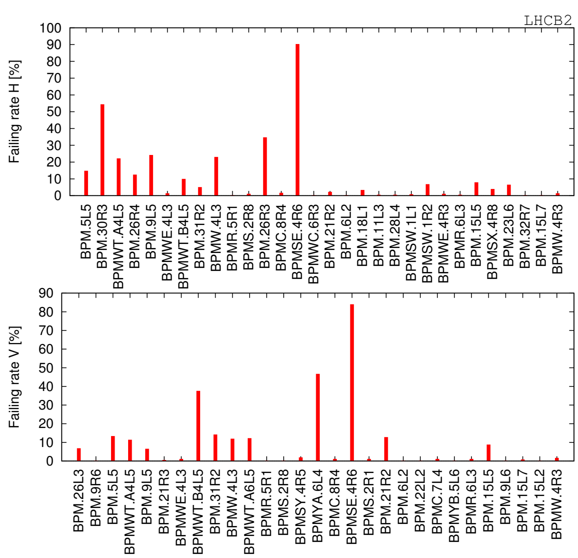

Figure 5.72: Failing rate for the BPMs of beam 1 (left) and beam 2 (right) for 2010.

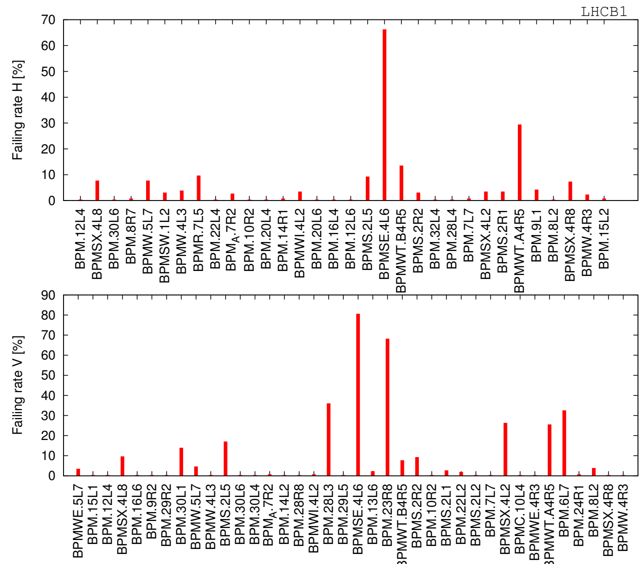

Figure 5.73: Failing rate for the BPMs of beam 1 (left) and beam 2 (right) for 2011.

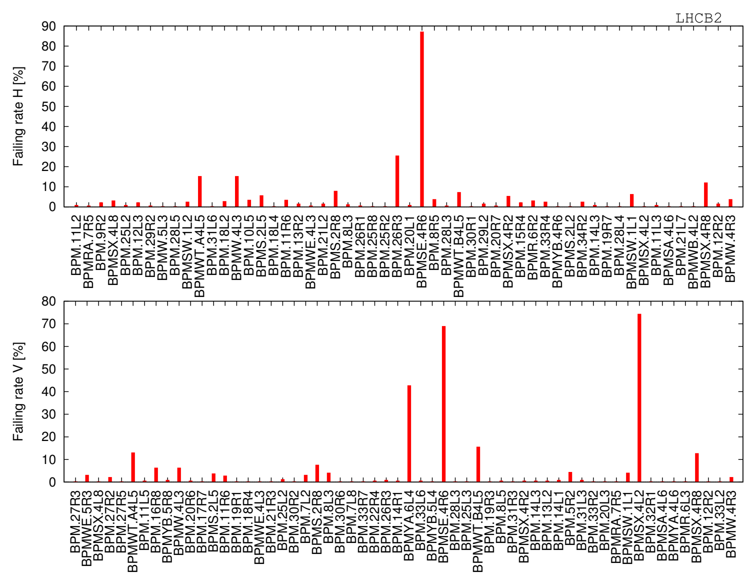

Figure 5.74: Failing rate for the BPMs of beam 1 (left) and beam 2 (right) for 2011.

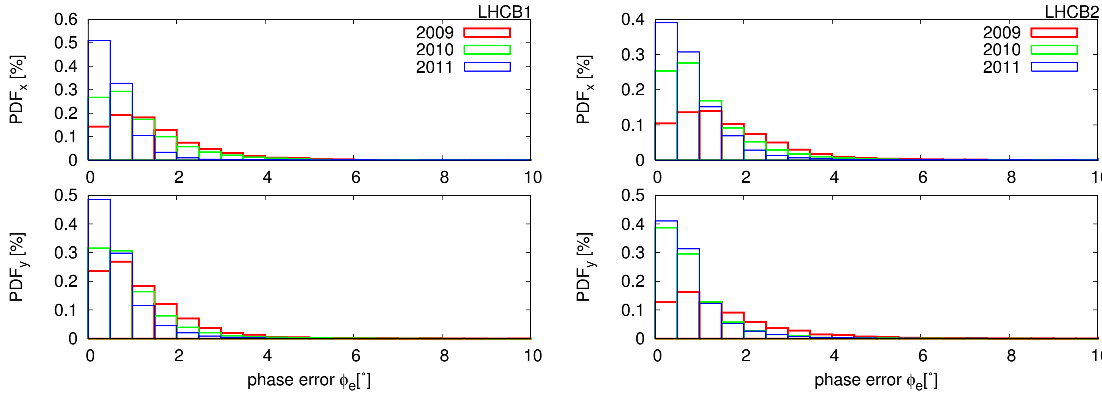

Figure 5.75: Probability density function for the statistical phase error for beam 1 (left) and beam 2 (right) separated by year. Horizontal plane is shown on the top and the vertical plane on the bottom.

- Only noise was acquired.
- The data being corrupted for some turns in the BPM signal .

5.7.4 Statistics on the measurement errors of the optics functions

Statistics on the measurement errors of the optics functions were gathered during December 2009 to December 2011, The statistics were only gathered for measurements conducted during the optics measurements. No difference was made between measurements with tune kicker or AC-dipole [101]. The statistics from the three years are presented separately. In 2009 no dispersion measurements were conducted. In total about 979 files were analyzed.

Statistics of the ϕ and β error

The statistical phase error is shown in figure 5.75. This error is computed as the standard deviation between a number of files. In most cases 3 datasets were acquired and analyzed. Figure 5.76 shows the total error from the β-function from phase, derived using the 3-BPM technique. The total error is computed as $\Delta\beta_{tot} = \sqrt{\Delta\beta^2_{phase} + \Delta\beta^2_{std}}$. β_{phase} being the error coming from calculating the β using the three BPM method and β_{std} being the statistical error. A clear improvement was observed between 2009 and 2010. This is because in 2009 injection oscillation and tune kicker were used, and the acquired number of turns was lower than in 2010 and 2011. In 2010 and 2011 between 1500 and 2000 turns were acquired. The improvement between 2010 and 2011 is attributed to the updated algorithm.

Figure 5.77 shows the statistical error from the β from amplitude of the main betatron tune line. The error in 2010 was slightly lower than in 2011. This could be explained by the performance of the BPMs which was slightly worse in 2011 for beam 2, as was observed in section 5.7.3. A clear improvement was observed between 2009 and 2010.

Statistics of the coupling error

The statistical error is calculated for the difference resonance driving term, f_{1001} and the sum resonance driving term, f_{1010}. This error is calculated from the standard deviation for several files. In most cases three datasets were acquired. A clear improvement was observed from 2009 and 2010 to 2011. This is because less turns were acquired in 2009 than in 2010 and 2011. The main motivation was that the AC-dipole was commissioned and this allowed the analysis of more turns. The difference between 2010 and 2011 was due to two reasons. Firstly the coupling algorithm was updated. In this update the phase was properly taken into account. For example in the past 0.05 (2π) and 0.95 (2π) return a standard deviation of 0.45. This was changed such that the phase correctly returns 0.0. Secondly, a new algorithm was implemented to cancel the effect of the AC-dipole [102]. The data for canceling the effect is processed in a different way, returning a different standard deviation.

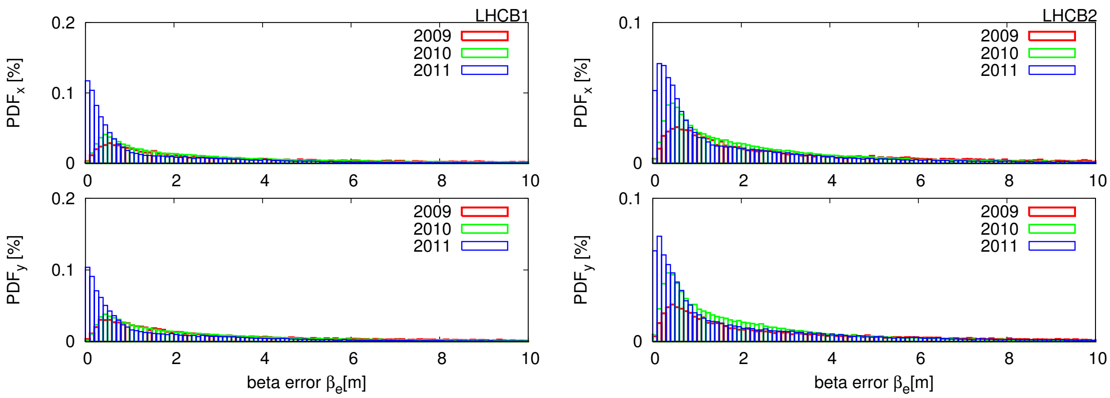

Figure 5.76: Probability density function for the total β error from phase for beam 1 (left) and beam 2 (right) separated by year. Horizontal plane is shown on the top and the vertical plane on the bottom.

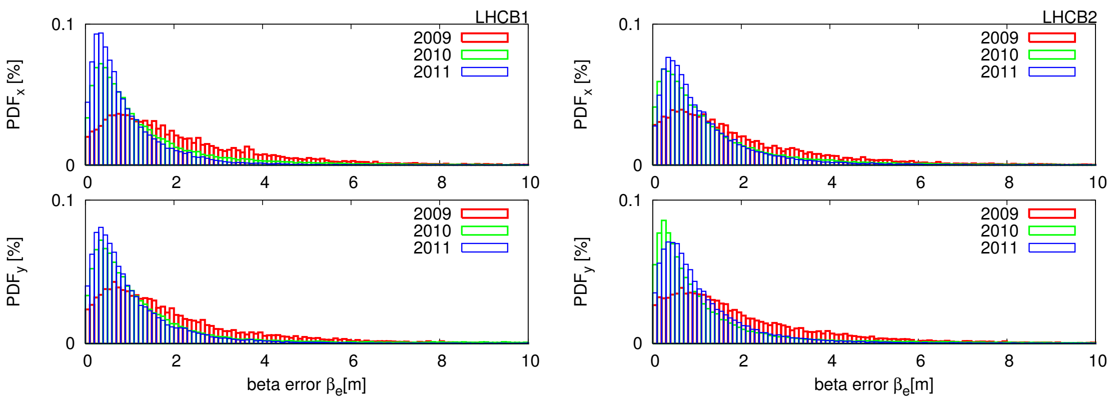

Figure 5.77: Probability density function for the statistical β error from amplitude for beam 1 (left) and beam 2 (right) separated by year. Horizontal plane is shown on the top and the vertical plane on the bottom.

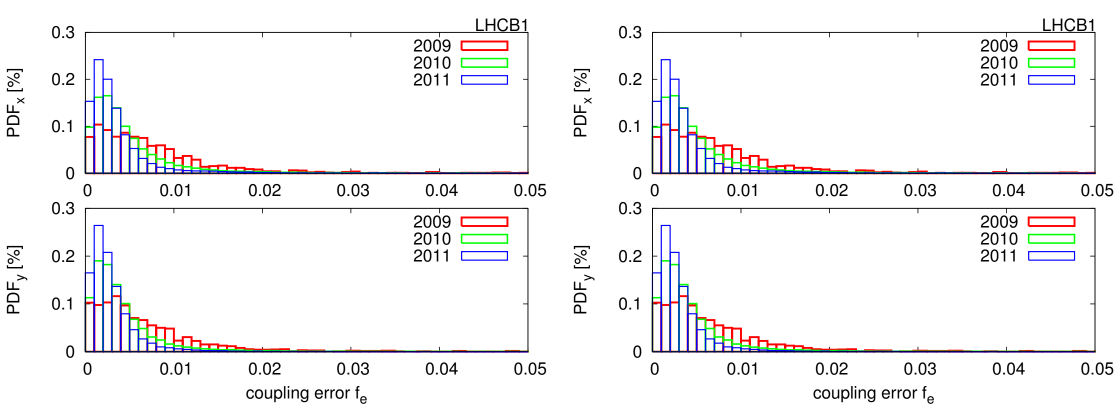

Figure 5.78: Probability density function for the statistical coupling error. The error for the difference resonance driving term, f_{1001}, is shown on top and the sum resonance driving term on the bottom. Beam 1 is shown at the left and beam 2 on the right. The data is separated by year.

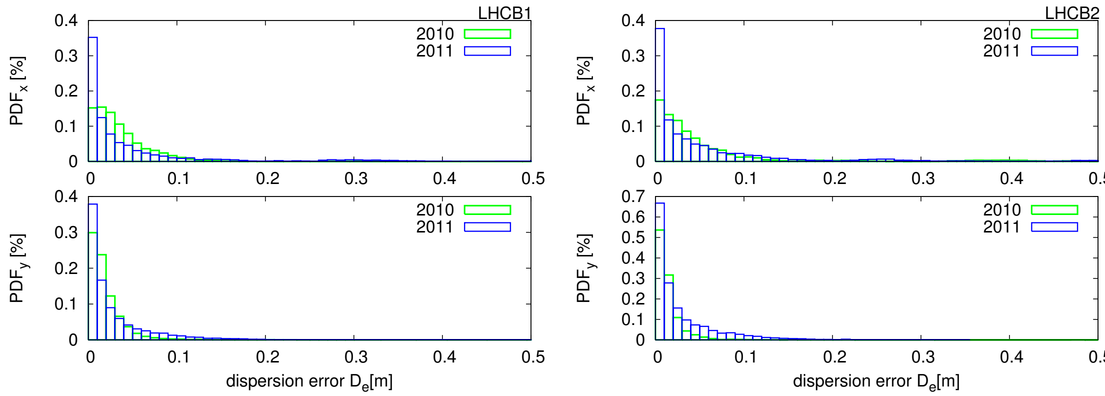

Figure 5.79: Statistical dispersion error for beam 1 (left) and beam 2 (right). The horizontal dispersion is shown on the top and the vertical dispersion on the bottom. The data is presented separated by year.

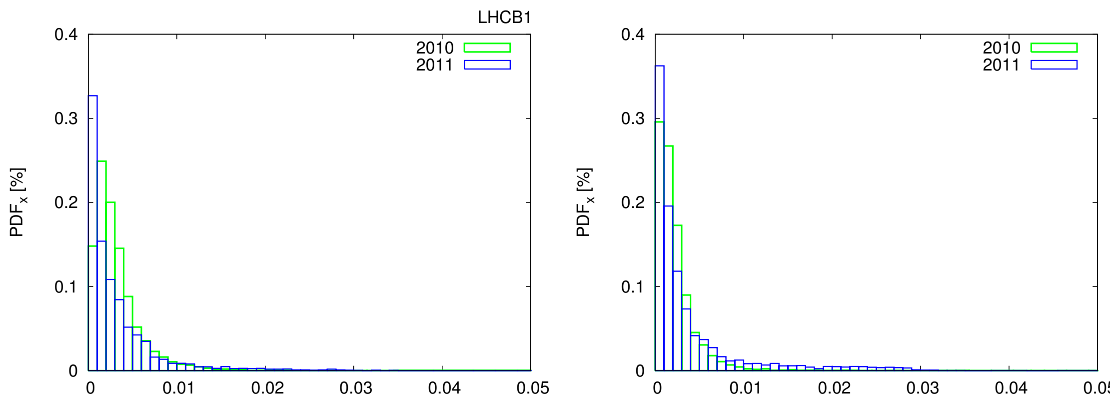

Figure 5.80: Statistical normalized dispersion error for beam 1 (left) and beam 2 (right). The data is presented separated by year.

Statistics of the dispersion error

In 2009 no dispersion measurements were conducted. In 2010 about 59 files were analyzed and in 2011 about 23 . For squeezed optics the frequency trims were about $\pm 50Hz$, $\pm 100Hz$ in some measurements, these correspond to a $\frac{\delta p}{p}$ value of 0.4×10^{-4}, 0.8×10^{-4} respectively. Figure 5.79 shows the horizontal and vertical dispersion, figure 5.80 shows the normalized horizontal dispersion. For both the horizontal and normalized horizontal dispersion, an improvement is observed between 2010 and 2011. For the vertical dispersion, however, the error seems to have increased between 2010 and 2011.

5.8 Outlook for the β-beating

The LHC has been operating during 2010 and 2011 at an intermediate energy of 3.5 TeV. An extrapolation of the errors for β-beat was done for the ultimate energy of 7 TeV. Figure 5.81 shows the extrapolation of the β-beat to a lower β^*. For this extrapolation only the local errors were included, not the global corrections. The measurements (dots) conducted at different β^* are shown. The different lines show the extrapolation of the β-beat for the implemented local corrections at different β^*. From the figure it is clear that the challenge remains for a β^* value of 0.55 m. Dedicated local and global corrections will be needed to correct the optics to a satisfactory level.

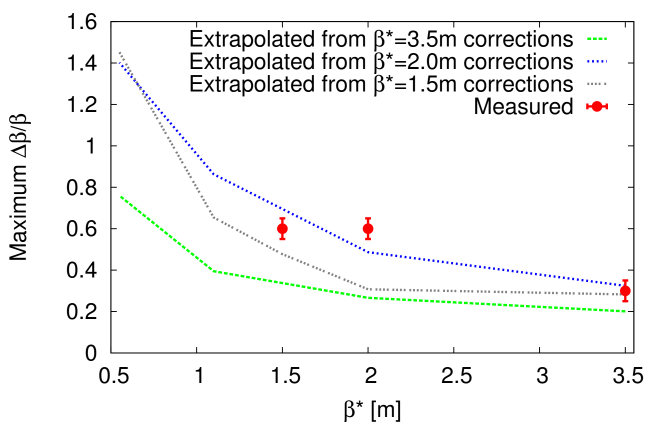

Figure 5.81: Extrapolated errors to a lower β^* are shown. Only the observed local errors at different β^* settings are included in the extrapolation. Red dots show the measured peak β-beat at the different β^* settings. Lines represents extrapolation for different settings. For $\beta^* = 1.5$m only IP_1, IP_5 and $IP_8 = 3$ m are squeezed. For the operational settings of 2010, all IPs were squeezed to a β^* value of 2 m and later 3.5 m.

Chapter 6

LHC special optics studies

During the 2011 run, dedicated time was allocated for machine development studies. These studies covered a large range of different topics [103]. For two of these studies, optics measurements were conducted during several sessions in 2011. The topics were unsqueezing IP1 and IP5 to a β^* value of 90 m and the achromatic telescopic squeeze (ATS). Unsqueezing IP1 and IP5 is discussed in section 6.1. In this section the measurements as well as the motivation for conducting these measurements will be discussed. The achromatic telescopic squeeze, a scenario studied for a possible upgrade of the LHC, is discussed in section 6.2.

6.1 High β^* optics

The precise measurement of the total cross section at LHC requires the observation of elastically scattered particles at extremely small angles [104]. The ATLAS-ALFA [105] and TOTEM [106] collaborations are the two experiments that perform these measurements. The precise measurements are done using specially designed equipment at the LHC to measure the total cross section, called the roman pot [107]. The observed displacement of the beam, z_{rp}, at the roman pot is expressed as:

$$z_{rp} = \sqrt{\beta_{rp}\beta^*}\theta_z^*. \tag{6.1}$$

Where θ_z^* is the horizontal or vertical scattering angle. z_{rp} being the displacement of the beam at the roman pot, β_{rp} and β^* the β-function at respectively the roman pot and the IP. Equation 6.1 is obtained from the matrix elements m_{11} and m_{12} in equation 1.24.The dispersion is irrelevant for elastic scattering [105]. The high-β optics was optimized in such a way that the phase advance between the roman pot and the IP was close to $\frac{\pi}{2}$, α^* is negligible at the IP.

To reach the smallest possible scattering angle, the distance between the roman pots and the center of the beam should be as small as possible (z_{rp}):

$$\theta_z^* = \frac{z_{rp}}{\sqrt{\beta_{rp}\beta^*}}. \tag{6.2}$$

With $\sigma_z = \sqrt{\epsilon\beta_z}$, z_{rp} can be rewritten as follows:

$$z_{rp} = n_{rp}\sqrt{\epsilon\beta^*}. \tag{6.3}$$

Where n_{rp} is the smallest possible distance to the beam center expressed as a multiple of the beam spot size. Equation 6.4 can then be rewritten as:

$$\theta_z^* = n_{rp}\sqrt{\frac{\epsilon}{\beta^*}}. \tag{6.4}$$

The closest distance of the roman pot to the center of the beam (n_d) and the emittance (ϵ) are almost constant. In order to be able to further decrease the scattering angle, the β^* should be further increased. For this reason high-β^* optics of up to 2600 m was developed [108]. The 90 m β^* optics was developed [109] to investigate the feasibility and the procedures needed for such optics. The goal is to achieve very high-β^* optics of above 1 km.

6.1.1 Introduction to the 90 m optics

In normal operations the beams are squeezed down to a β^* value as low as possible. For high-β optics the β^* is increased, thereby decreasing the currents. From the optics point of view this changes the perspective from the errors emerging from the triplets. The high-β squeeze together with the normal squeeze allow to better understand the optics.

This optics was implemented and tested during several machine development studies [110]. Figure 6.1 shows a zoom around IR1. In this plot the horizontal β-function is shown. During normal operation the β in the triplet increases, and decreases for the high-β optics.

In order to increase the β^* the current in the triplets has to be reduced, as shown in figure 6.2. When the high-β optics will reach higher β^*, the current in the triplets will decrease close to zero Ampere.

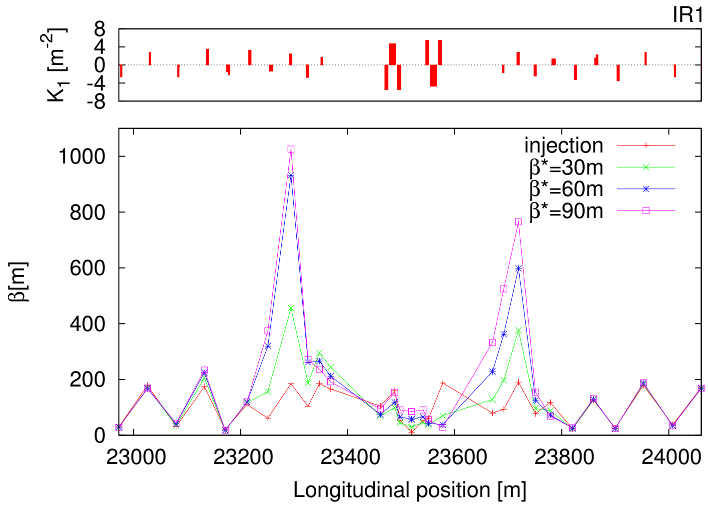

Figure 6.1: Evolution of the β during the unsqueeze.

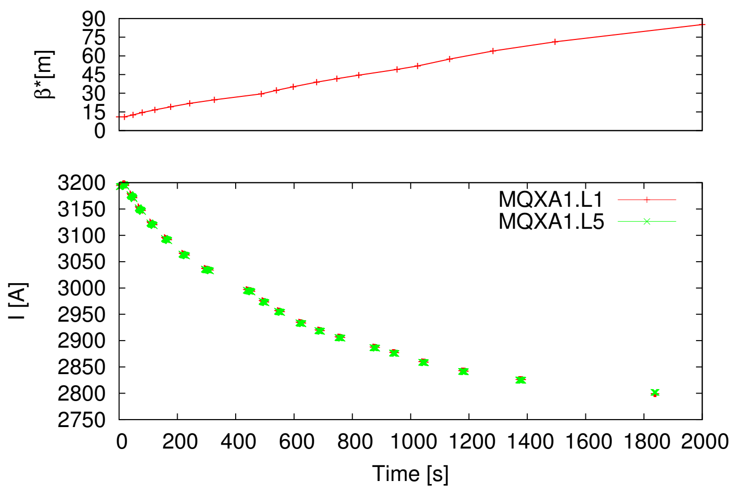

Figure 6.2: Top plot shows β^* versus time. Bottom plot shows the current in the triplet magnets of IR1 versus time.

6.1.2 Measurements

The measurements conducted for the β-beat, coupling, dispersion and β^* will be discussed in this section.

Beta-beat

The beta-beat was measured at β^* values of 11 m, 30 m and 90 m in IP1 and IP5. Evolution of the beta-beat for beam 2 is shown in figure 6.3. From this plot it can be concluded that the change in beta-beat during the unsqueeze is negligible. The beta-beat at β^* value of 90 m is shown in figure 6.4. The peak beta-beat for beam 1 is $\sim$ 25% in the horizontal plane and $\sim$ 20% in vertical plane. The peak beta-beat for beam 2 is slightly larger than for beam 1 with a beta-beat of $\sim$ 30% in both planes. The measurement of the β-beat for beam 2 in sector 2-3 was of poor quality because of malfunctioning BPMs.

Coupling

A local coupling correction was applied at flattop. Local corrections were applied in IR1, IR2, IR5 and IR8. A summary of the correction strengths is shown in table 6.1. In figure 6.5 an example of the

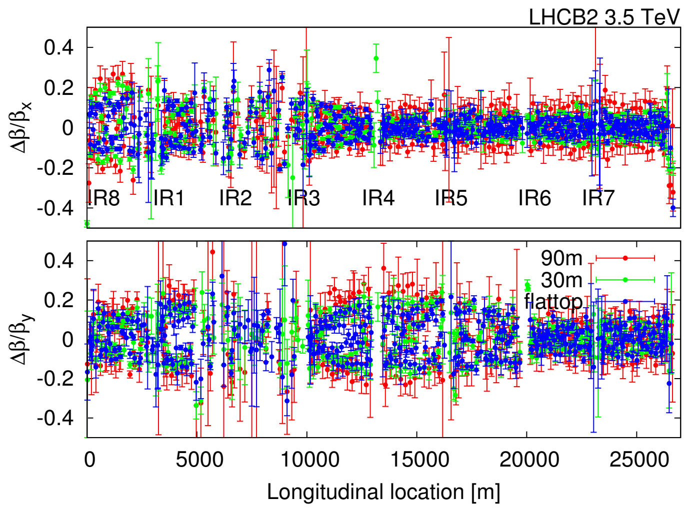

Figure 6.3: Evolution of the beta-beat during the unsqueeze for beam 2. Three measurements are shown for a β^* value of 11 m (blue), 30 m (green) and 90 m (red) in IP1 and IP5.

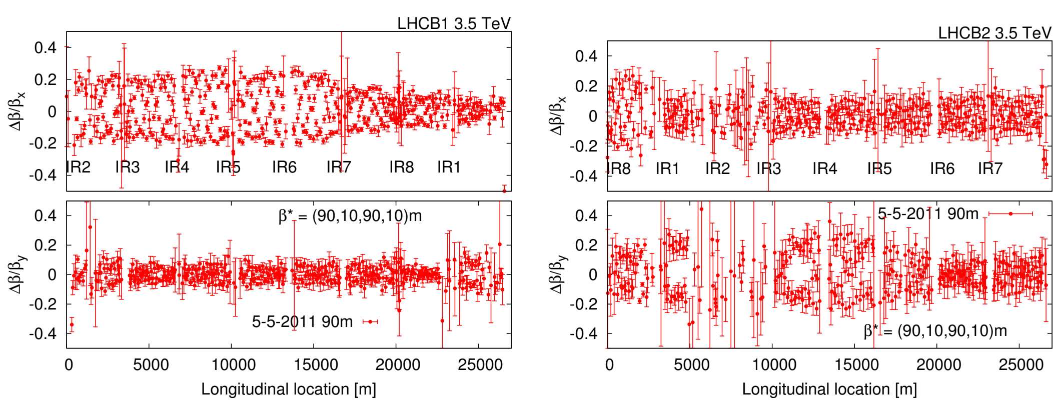

Figure 6.4: Beta-beat at a β^* value of 90 m in IP1 and IP5 for beam 1 (left) and beam 2 (right).

correction is shown for IR2, beam 1. The figure on the left shows measurements before the correction was applied and on the right after. The local jump which was observed at IR2 is corrected. This was achieved by powering the two skew quads in the triplet, left and right of the IP. A suitable correction was needed for the coupling in both beams as the correctors are located in the common beam pipe. The knob was applied with a constant value of 1 during the unsqueeze. A compensation knob was applied to minimize the impact of the local knob on C^-.

Corrector	Strength [m^{-2}]	Corrector	Strength [m^{-2}]
kqsx3.l1	0.0008	kqsx3.l5	0.0006
kqsx3.r1	0.0008	kqsx3.r5	0.0006
kqsx3.l2	-0.0009	kqsx3.l8	-0.0007
kqsx3.r2	-0.0009	kqsx3.r8	-0.0007

Table 6.1: Summary of local corrections applied. Corrections were applied in IR1, IR2, IR5 and IR8. The correctors used are common for both beams, changing the coupling in both beams.

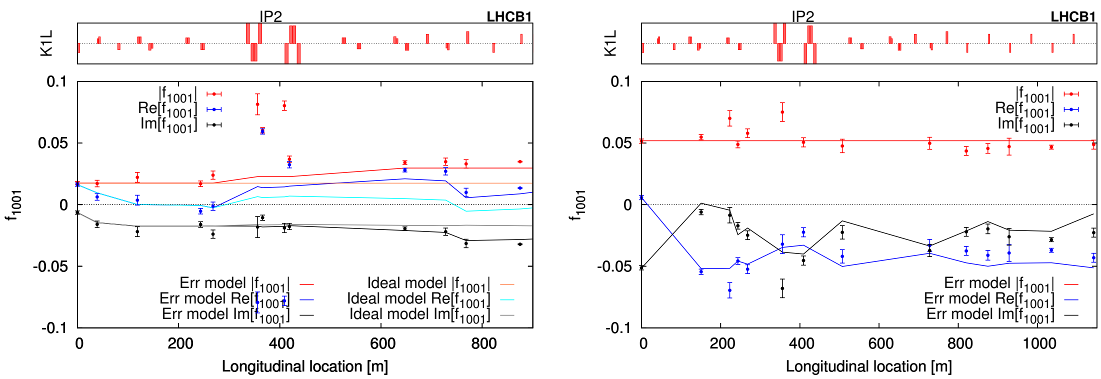

Figure 6.5: Example of local correction at IR2. Only beam 1 is shown, before corrections (left) and after (right) correction. Red line indicates the amplitude of the difference resonance term, blue line real part and black line imaginary part.

In figure 6.6 the measured coupling at a β^* value of 90 m in IP1 and IP5 is shown. The local jumps which were observed at flattop before are still corrected. Small coupling source at IR6 for beam 1 (left), and for IR1, beam 2 (right) is observed.

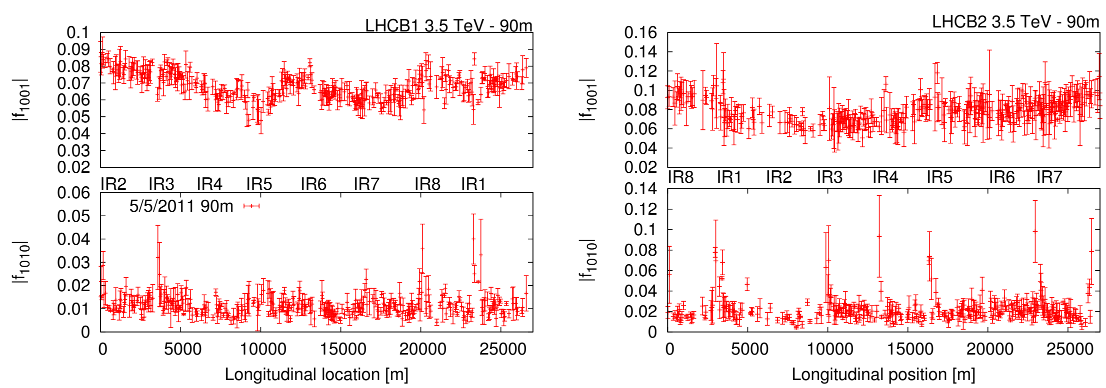

Figure 6.6: Measured coupling for beam 1 and beam 2 at a β^* value of 90 m in IP1 and IP5.

Dispersion

Turn-by-turn data with an energy offset, $\frac{dp}{p} = -0.408$ for beam 1 and $\frac{dp}{p} = -0.394$ for beam 2, was acquired to measure the dispersion function. Figure 6.7 shows the difference between the measured and model normalized horizontal dispersion function, $\frac{D_x}{\sqrt{\beta}}$, for both beams. Figure 6.8 shows the difference between the measured and model vertical dispersion function for both beams. For the vertical dispersion of beam 2 a local jump left from IR1 is observed.

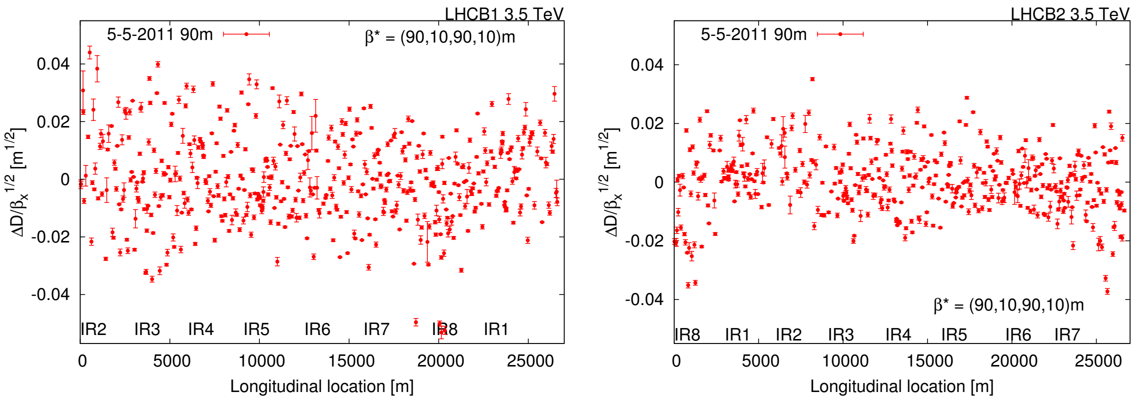

Figure 6.7: Difference between measured and model normalized horizontal dispersion function is shown for both beams. Beam 1 is shown on the left and beam 2 on the right.

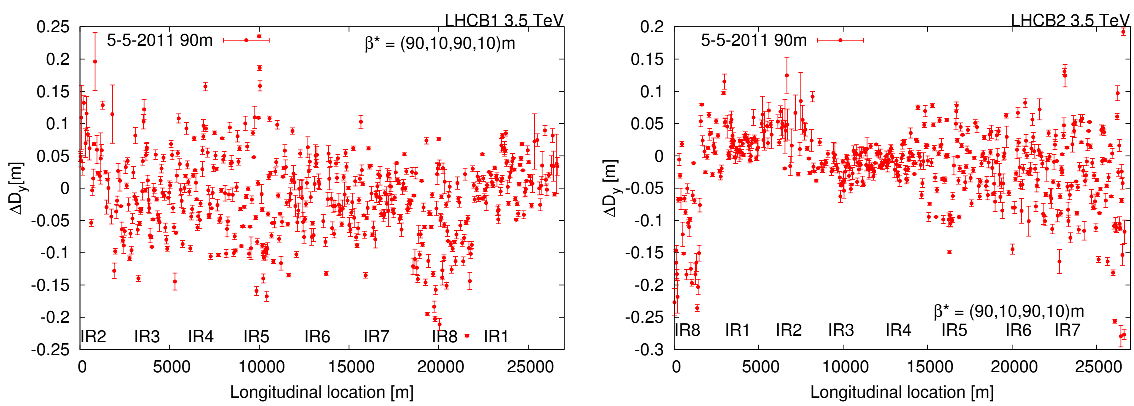

Figure 6.8: The difference between measured and model vertical dispersion function is shown for both beams. Beam 1 is shown on the left and beam 2 on the right.

IP	Beam	Model β_x^*	β_x^*	error	Model β_y^*	β_y^*	error
IP1	1	85.17	80.15	2.82	90.20	87.19	6.06
IP5	1	91.31	82.52	10.25	90.04	92.73	4.72
IP1	2	92.94	97.11	11.39	89.63	98.61	1.62
IP5	2	90.51	90.66	2.74	92.37	76.21	5.93

Table 6.2: β^* measurements at IP1 and IP5 at a β^* value of 90 m.

β^* measurements for IP1 and IP5

β^* measurements for IP1 and IP5 at a β^* value of 90 m were conducted. The values are listed in table 6.2. The β^* for IP1 and IP5 is not exactly 90 m by design. The error bars listed in the table are large. The largest asymmetry between the two beams, about 18%, was observed for the vertical plane of IP5 and the horizontal plane of IP1.

6.2 ATS optics

During the machine development studies dedicated to the ATS optics, optics measurements were conducted. The motivation behind these measurements was the emergence of new requirements for the available tools and algorithms:

- A strict limit on the phase advances between BPM.14/15 left and right of the IP to the BPM nearest to the IP.
- Detailed measurements were required for the chromatic functions.
- β-beat should be as small as possible to allow maximum available aperture in the arcs and triplets. As a result [111], dedicated corrections should be applied to obtain the smallest possible β-beat.

6.2.1 Introduction to the ATS optics

At top energy (7 TeV) the β^* will have a nominal value of 55 cm at IP1 and IP5. For the upgrade project the minimum β^* should be reduced. It is limited by the strength of the sextupoles [112] and aperture limitations in the IR. A new optics [113, 114] was developed to cope with the limitations mentioned above.

Figure 6.9 shows the ATS optics a β^* value of 1 m and 10 cm. To cope with the limitations of the sextupole strengths the beta function in the arcs is increased when β^* is decreased below a value of 1 m. The β-function in the arcs, left and right from IP1 and IP5, is increased by a factor of about 4 between a β^* value of 1 m and 10 cm. For this optics the tunes are changed from 64, 59 to 62, 60 in the horizontal and vertical plane respectively.

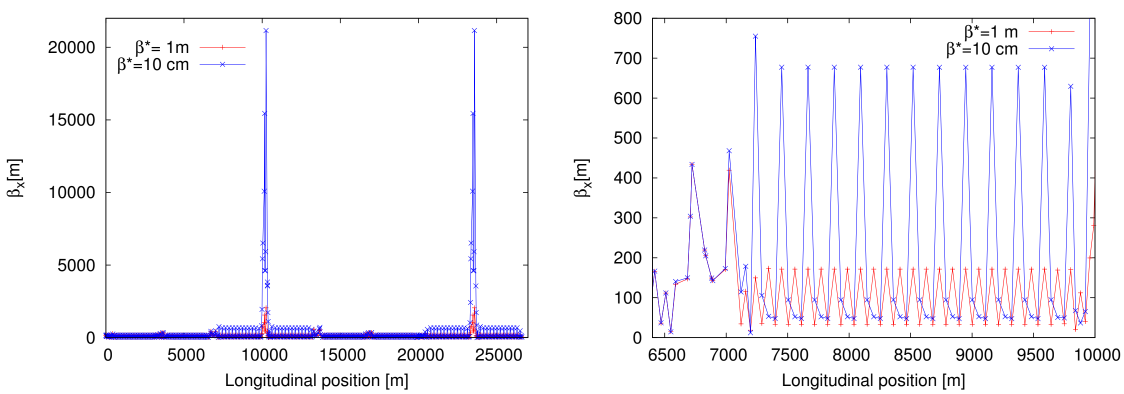

Figure 6.9: β-function (left) around the ring, zoomed in (right) around the arc left from IR1 is shown during the ATS squeeze.

Figure 6.10 shows β^* versus time (top) and the sextupoles strengths versus time along the squeeze (bottom). When squeezing the β^* below 4 m the sextupole strengths are increasing. For β^* lower than 40 cm the strengths in the sextupoles remain constant, as the β in the arcs is increased.

This scheme is called ATS (Achromatic Telescopic Squeezing) and was tested during several machine development studies [115], [116] and [111]. During these studies several optics measurements were conducted. The next sections will discuss these measurements.

6.2.2 Measurement at injection

Measurements, both at injection and flattop, were conducted to check the new ATS optics. Beta-beat, coupling and dispersion were measured. Measurements at injection energy were conducted as the ATS optics features different integer tunes than the nominal optics.

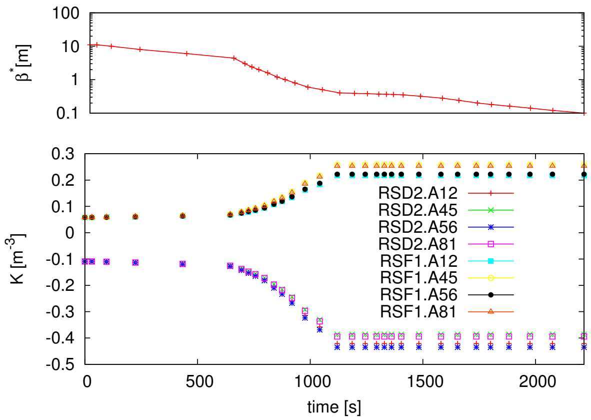

Figure 6.10: Top plot shows the β^* versus time. Bottom plot the strength in the sextupoles around the adjacent arcs.

Beta-beat

In figure 6.11 the beta-beat at injection is shown for beam 1 (left) and beam 2 (right). The measured peak beta-beat at injection is about 25% for beam 1 and about 30% for beam 2. In both figures some abrupt local jumps were observed at the IRs, indicating that some local error sources were present. For a peak beta-beat in the $20\% - 30\%$ range local corrections will be hard to identify.

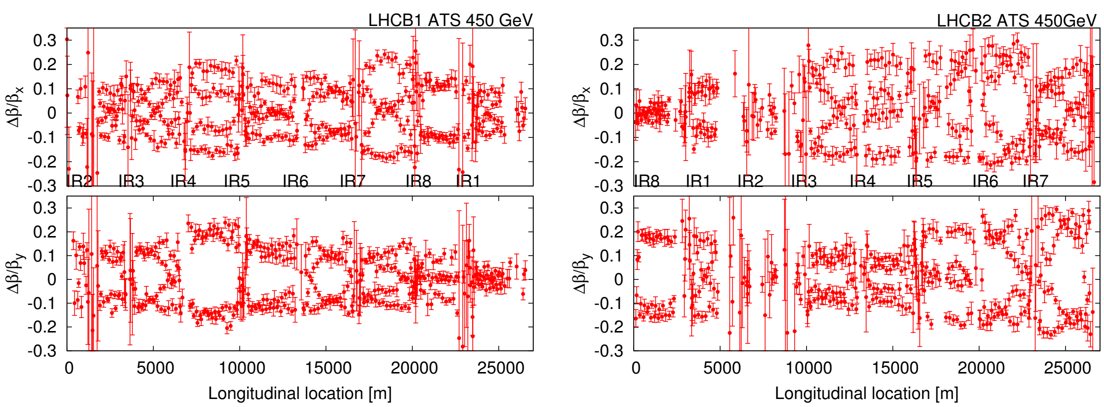

Figure 6.11: The beta-beat at injection is shown for beam 1 (left) and beam 2 (right).

In figure 6.12 the beta-beat at flattop is shown for beam 1 (left) and beam 2 (right). The peak measured beta-beat at flattop is about 15% for beam 1 and about 15% and 10% for beam 2, for the horizontal and vertical plane respectively. The beta-beat observed at flattop was decreased by approximately a factor of 2 in comparison to injection. The large error bars for beam 1 in sectors 1-3 were due to the fact that only 50 turns were acquired for these sectors. When re-injecting, the number of turns acquired was reset to 50 turns in the injection region to acquire injection oscillations. The large error bars in beam 2 sector 2-3 ares due to malfunctioning BPMs.

Checking the dipole b_2 correction

The systematic quadrupolar component of the LHC dipoles has been determined from magnetic measurements [82] and [83]. The total phase advance error, which is the difference between the measured and model phase advance, is shown for injection in figure 6.13 and for flattop in figure 6.14. Only beam 2 at flattop is shown, since due to BPM issues, no measurements were conducted for beam 1. The residual phase-beating is smaller at flattop than at injection. The saw-tooth pattern is due to the dipole b_2 and the MQT correction.

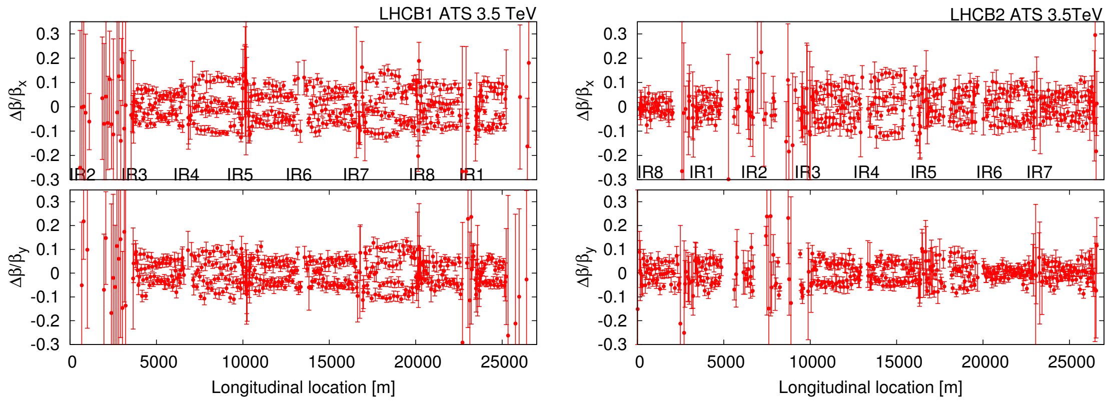

Figure 6.12: The beta-beat at flattop is shown for beam 1 (left) and beam 2 (right).

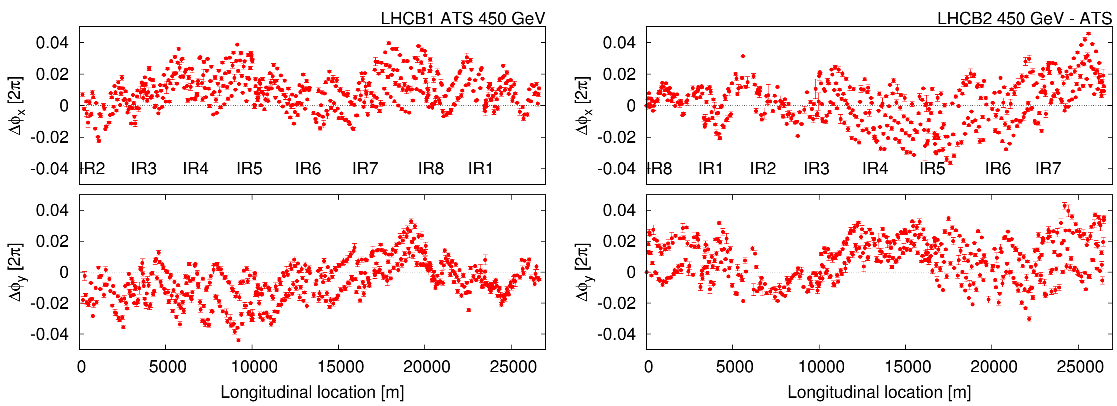

Figure 6.13: The total phase advance is shown at injection for beam 1 (left) and beam 2 (right).

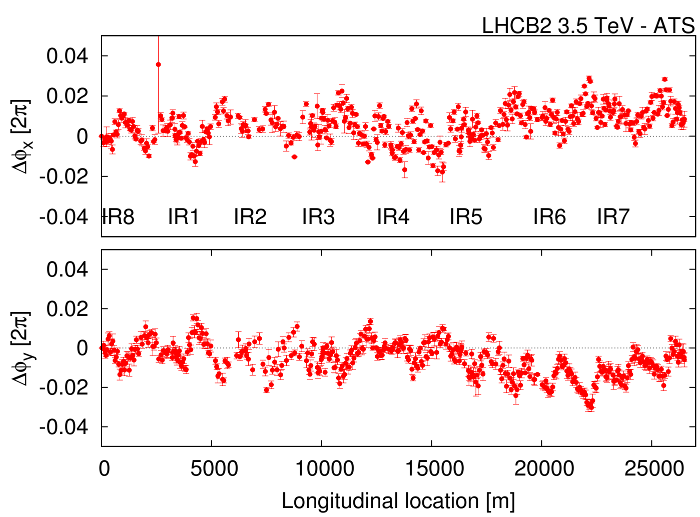

Figure 6.14: The total phase advance, which is the difference between the measured and model phase advance, is shown at flattop, 3.5 TeV, for beam 2. Due to BPM issues, no measurements were conducted for beam 1

Coupling

In figure 6.15 the coupling, before and after local corrections, is shown at injection for beam 1 and beam 2. This knob was calculated from the nominal injection optics and tested during the 90 m MD [110]. Local correction were applied in IR1, IR2, IR5 and IR8. A summary of the correction strengths is shown in table 6.3. The correctors used were common for both beams, resulting in a coupling change for both beams. Local jumps at these locations were reduced, as can be seen in figure 6.15. For beam 2 a jump at IR7 is observed in the real (middle plot) and imaginary part (bottom plot). The appearance of the jump is explained by the change in the phases after the corrections were applied. A detailed analysis for beam 2 IR7 is shown in figure 6.16. A jump in the real (blue) and imaginary part (red) is also observed. But the propagated model is in good agreement with the measurements, thus indicating that the jump in the real and imaginary parts is not an error. A jump is also observed in IR6 for beam 1.

Corrector	Strength $[m^{-2}]$	Corrector	Strength $[m^{-2}]$
kqsx3.l1	0.0008	kqsx3.l5	0.0006
kqsx3.r1	0.0008	kqsx3.r5	0.0006
kqsx3.l2	-0.0009	kqsx3.l8	-0.0007
kqsx3.r2	-0.0009	kqsx3.r8	-0.0007

Table 6.3: Summary of local corrections applied. Corrections were applied in IR1, IR2, IR5 and IR8.

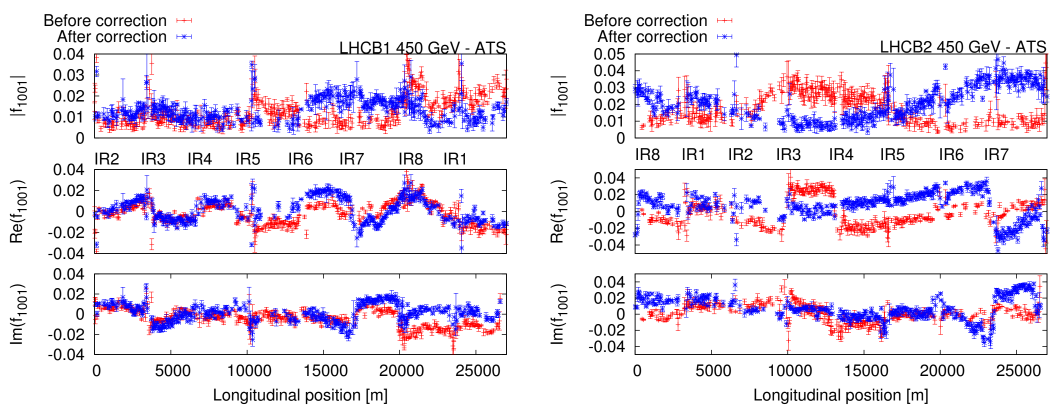

Figure 6.15: The coupling is shown at injection for beam 1 (left) and beam 2 (right), before (red) and after local (blue) corrections were applied.

In figure 6.17 the coupling is shown at flattop (3.5 TeV) for beam 1 and beam 2. The local variations in IR4 were not completely corrected, indicating that the coupling source in IR4 was changing during the ramp. An iteration on the local coupling correction would correct this. BPMs were not plotted for beam 1 sectors 1-3, this was because of the filtering in the coupling algorithm and the 50 turn acquisition.

Dispersion

In figure 6.18 the dispersion is shown at flattop (3.5 TeV) for beam 1 (left) and beam 2 (right). In this figure the top plot shows the normalized horizontal dispersion, $\frac{D_x}{\sqrt{\beta_x}}$, and the bottom plot the vertical dispersion function. For this dispersion, measurement of the on and off-momentum data, $(\frac{dp}{p})_{B1} = -0.428 \times 10^{-3}$ and $(\frac{dp}{p})_{B2} = -0.423 \times 10^{-3}$, were acquired. The normalized horizontal dispersion function in beam 2 is larger than beam 1 by a factor of 2. Vertical dispersion for both beams is similar. For beam 1 the measured dispersion in sectors 1-3 should be ignored, because only 50 turns were acquired for these BPMs.

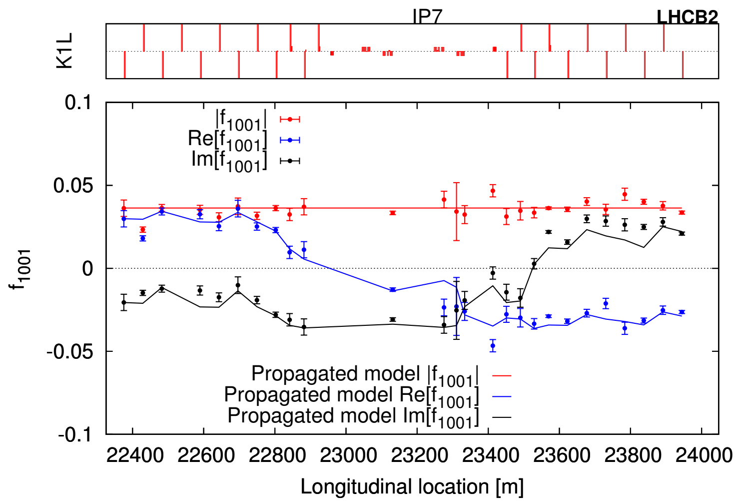

Figure 6.16: Coupling around IR7 calculated from segment-by-segment technique. Amplitude (red), imaginary part (blue) and real part (black).

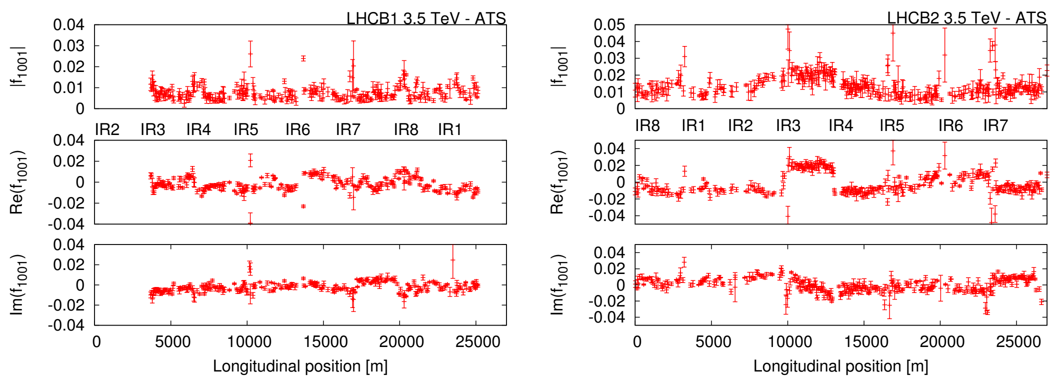

Figure 6.17: Coupling shown at flattop (3.5 TeV) for beam 1 (left) and beam 2 (right)

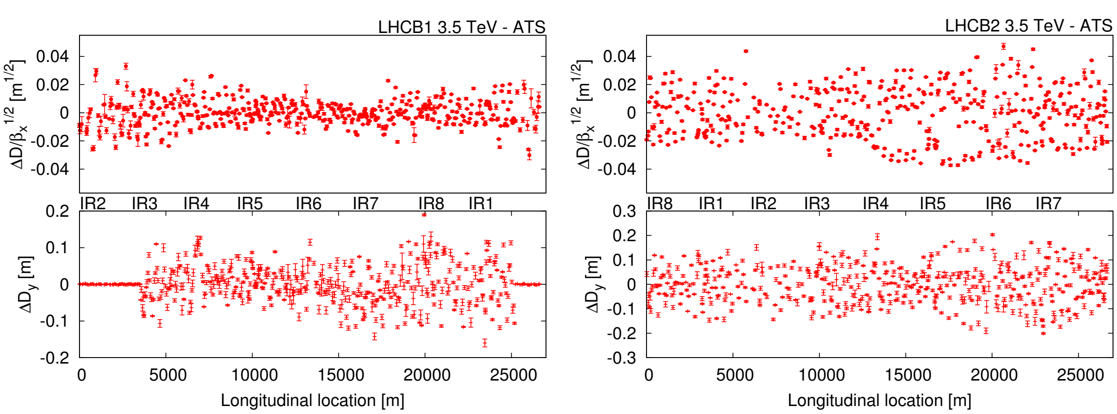

Figure 6.18: The dispersion is shown at flattop (3.5 TeV) for beam 1 (left) and beam 2 (right). In this figure the top plot shows the horizontal dispersion and the bottom plot the vertical dispersion.

Phase measurements

For the ATS MD it was important that certain constraints for phase advances were maintained during the squeeze. For beam 1 the largest deviation is about 3% in the horizontal plane and for beam 2 about 7% in the vertical plane.

$\beta^*[m]$ setting	BPM	$\Delta\phi_x^{me}$	$\Delta\phi_x^{mo}$	$\Delta\phi_y^{me}$	$\Delta\phi_y^{mo}$
$IP_{1,5}$ =1.2m	BPM.14L1 BPMSW.1L1	-0.0322 (0.0001)	-0.0289	-0.3790 (0.0031)	-0.3852
	BPMSW.1R1 BPM.14R1	-0.3505 (0.0007)	-0.3542	-0.0271 (0.0023)	-0.0198
	BPM.15L1 BPMSW.1L1	-0.1547 (0.0017)	-0.1645	-0.4936 (0.0029)	-0.4991
	BPMSW.1R1 BPM.15R1	-0.4840 (0.0006)	-0.4904	-0.1365 (0.0023)	-0.1337
IP_1 =0.54m	BPM.14L1 BPMSW.1L1	-0.0145 (0.0006)	-0.0128	-0.4286 (0.0042)	-0.4377
	BPMSW.1R1 BPM.14R1	-0.3999 (0.0018)	-0.4112	-0.0123 (0.0030)	-0.0089
IP_5 =1.2m	BPM.15L1 BPMSW.1L1	-0.0935 (0.0011)	-0.0977	-0.4967 (0.0033)	-0.4996
	BPMSW.1R1 BPM.15R1	-0.4939 (0.0017)	-0.4956	-0.0757 (0.0030)	-0.0711
IP_1 =0.3m	BPM.14L1 BPMSW.1L1	-0.0085 (0.0012)	-0.0071	-0.4562 (0.0040)	-0.4639
	BPMSW.1R1 BPM.14R1	-0.4342 (0.0014)	-0.4464	-0.0067 (0.0041)	-0.0050
IP_5 =1.2m	BPM.15L1 BPMSW.1L1	-0.0591 (0.0014)	-0.0588	-0.4986 (0.0040)	-0.4998
	BPMSW.1R1 BPM.15R1	-0.4953 (0.0011)	-0.4975	-0.0454 (0.0038)	-0.0411

Table 6.4: Phase advance measurement for beam 1. First column shows β^* setting, third measured horizontal phase advance with error, fourth model horizontal phase advance, fifth measured vertical phase advance with error, sixth model vertical phase advance.

$\beta^*[m]$ setting	BPM	$\Delta\phi_x^{me}$	$\Delta\phi_x^{mo}$	$\Delta\phi_y^{me}$	$\Delta\phi_y^{mo}$
$IP_{1,5}$ =1.2m	BPM.14L1 BPMSW.1L1	-0.3797(0.0010)	-0.3847	-0.0345 (0.0053)	-0.0291
	BPMSW.1R1 BPM.14R1	-0.0229 (0.0004)	-0.0202	-0.3350 (0.0038)	-0.3536
	BPM.15L1 BPMSW.1L1	-0.4953 (0.0009)	-0.4985	-0.1675 (0.0057)	-0.1653
	BPMSW.1R1 BPM.15R1	-0.1302 (0.0005)	-0.1341	-0.4819 (0.0050)	-0.4898
IP_1 =0.54m	BPM.14L1 BPMSW.1L1	-0.4302 (0.0029)	-0.4373	-0.0150 (0.0012)	-0.0132
	BPMSW.1R1 BPM.14R1	-0.0106 (0.0028)	-0.0091	-0.3836 (0.0013)	-0.4106
IP_5 =1.2m	BPM.15L1 BPMSW.1L1	-0.4983 (0.0026)	-0.4993	-0.1060 (0.0012)	-0.0985
	BPMSW.1R1 BPM.15R1	-0.0708 (0.0021)	-0.0714	-0.4923 (0.0012)	-0.4954
IP_1 =0.3m	BPM.14L1 BPMSW.1L1	-0.4591 (0.0019)	-0.4636	-0.0086 (0.0026)	-0.0073
	BPMSW.1R1 BPM.14R1	-0.0056 (0.0009)	-0.0050	-0.4252 (0.0029)	-0.4459
IP_5 =1.2m	BPM.15L1 BPMSW.1L1	-0.4983 (0.0014)	-0.4996	-0.0647 (0.0026)	-0.0593
	BPMSW.1R1 BPM.15R1	-0.0402 (0.0016)	-0.0412	-0.4955 (0.0028)	-0.4974

Table 6.5: Phase advance measurement for beam 2. First column shows β^* setting, third measured horizontal phase advance with error, fourth model horizontal phase advance, fifth measured vertical phase advance with error, sixth model vertical phase advance.

6.2.3 Measurement during the squeeze at IR1

Measurements during several sessions during the squeeze of IR1 down to a value of 30 cm were conducted for β-beat, coupling, dispersion and the chromatic function. For both beams measurements were conducted for IR1 at a β^* value of 1.2 m, 0.54 m. For beam 2 an additional measurement was conducted at 4.4 m.

Beta-beating

Measurements were conducted at a β^*, as shown in figure 6.19, value of 1.2 m, 0.45 m and 0.3 m. Additional measurements for beam 2 at β^* value of 4.4 m were conducted. It was impossible to measure beam 1 at $\beta^* = 4.4$ m, due to problems which occurred with the crate settings for the BPM acquisition.

The initial measurement at 1.2 m revealed a peak beta-beat of 20% for the horizontal plane of beam 1 and 15% for the vertical plane of beam 2.

The β-beat was increased to 40% for the horizontal plane for beam 1 and to 45% for the vertical plane for beam 2 at a β^* value of 0.3 m. The peak beta-beat for the vertical plane for beam 1 and horizontal plane for beam 2 remained constant at 20% and 15% respectively.

The observed gaps in beam 1 are due to the BPM filtering when calculating β. The gap in beam 2 is due to the fact that no data was acquired for that sector.

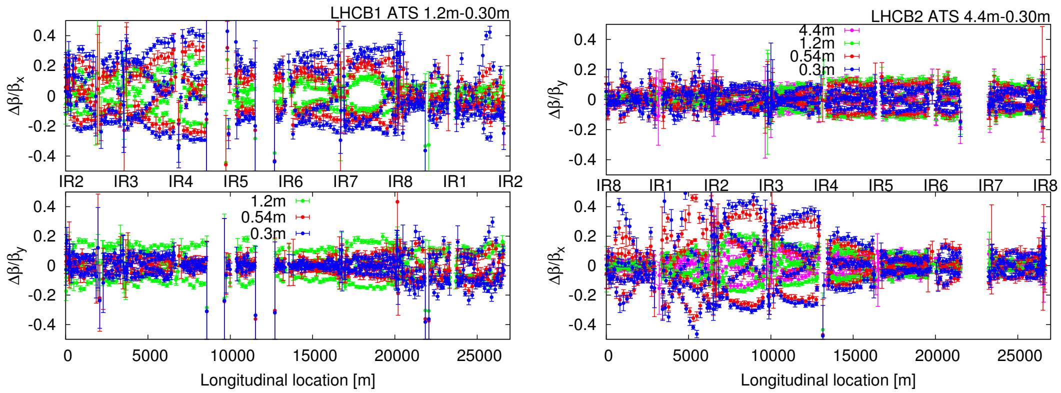

Figure 6.19: β-beat for different β^* for beam 1 (left) and beam 2 (right).

Coupling

The coupling observed during the squeeze is shown in figure 6.20. Global online corrections using the orthogonal knobs were carried out for a β^* value of up to 1.2 m. Due to time limitations, global corrections were not carried out for β^* below 1.2 m. This explains the growth in the amplitude of the coupling for β^* lower than 1.2 m. Local jumps in IR5 and for both beams are observed. A local jump is also observed in ARC 8-1 for beam 1.

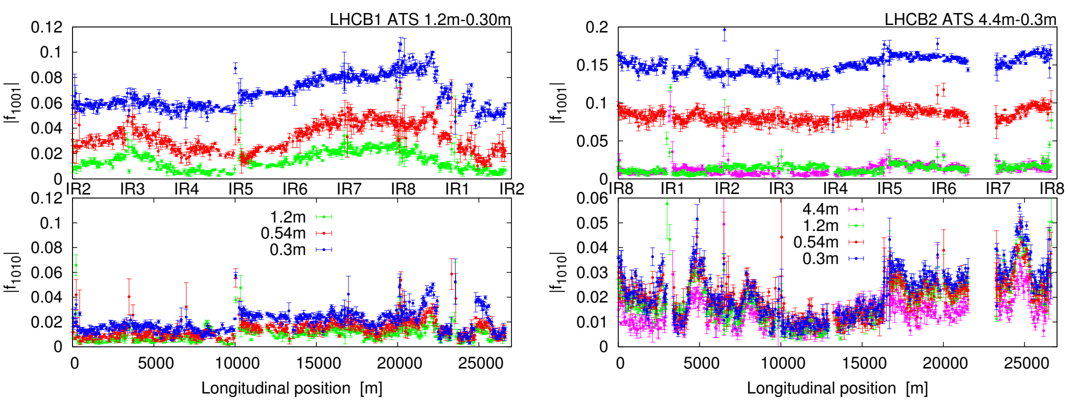

Figure 6.20: Coupling observed during the squeeze is shown in figure 6.20, for beam 1 (left) and beam 2 (right). Difference resonance is shown on the top plots and sum resonance on the bottom.

Off-momentum measurements

Off-momentum measurements were conducted at $\beta^* = 1.2$ m. Radial trims were applied in the order of 120 Hz, 60 Hz, -60 Hz and 120 Hz. 60 Hz corresponds to a $\frac{dp}{p}$ of 0.485. In the following sections the results will be discussed.

Dispersion The normalized dispersion is shown in figure 6.21. For both normalized horizontal and vertical dispersion the dispersion for beam 2 is two times larger than for beam 1. The same was observed at injection. The error bars for beam 1 are substantially larger between IR2 and IR5. The same was observed for beam 2 between IR2 and IR6.

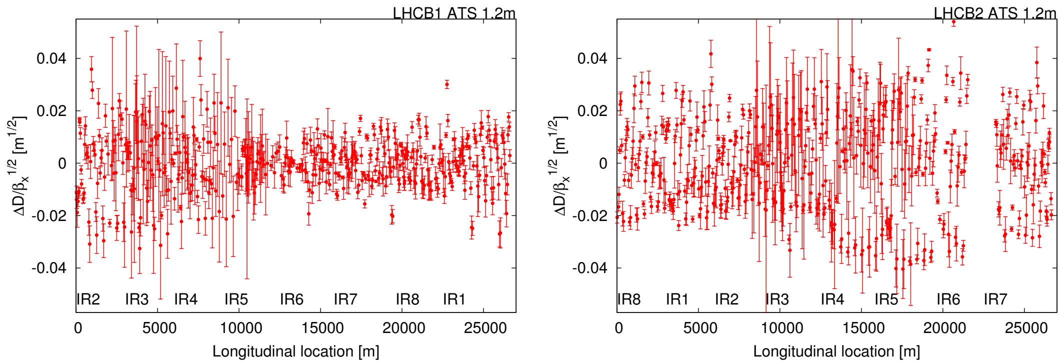

Figure 6.21: Normalized horizontal dispersion for beam 1 (left) and beam 2 (right) for IR1 at a β^* value of 1.2 m.

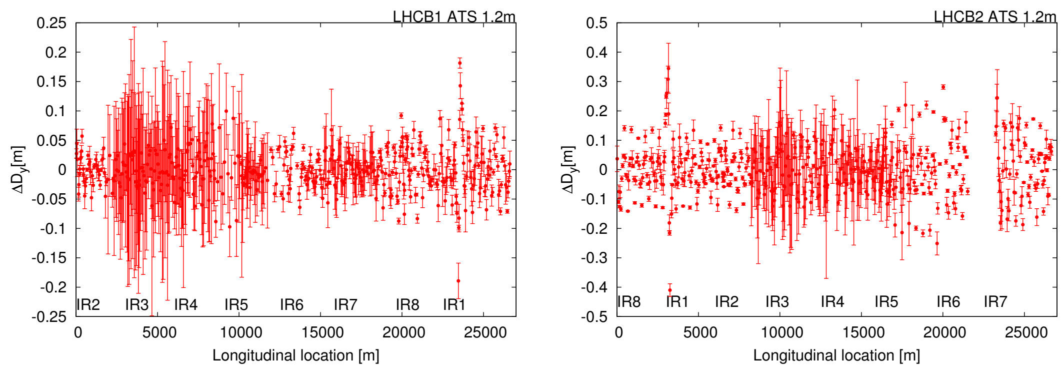

Figure 6.22: Vertical dispersion for beam 1 (left) and beam 2 (right) for IR1 at a β^* value of 1.2 m.

Chromatic functions The chromatic functions are calculated for both beams. The model and measurements are in good agreement, as shown in figure 6.23. The error bar in beam 2 is significantly larger than in beam 1. BPMs in sector 6-7 were not acquired. No large discrepancies between model and measurement were observed.

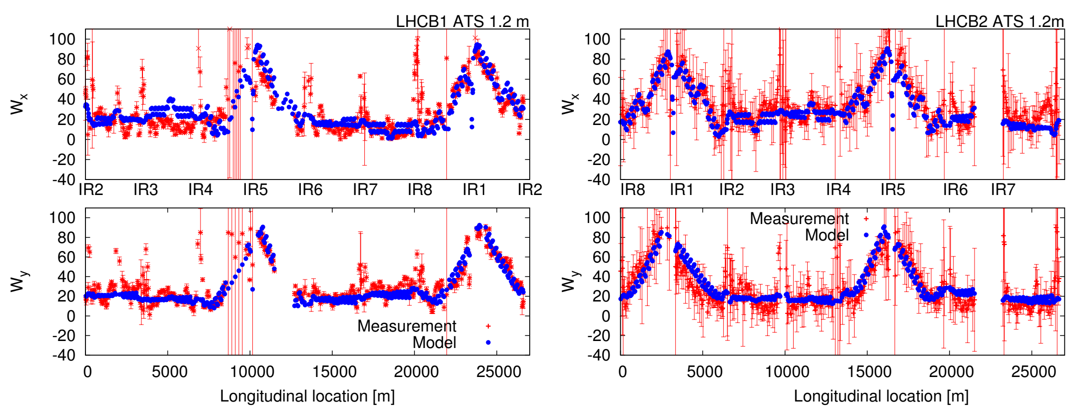

Figure 6.23: Chromatic functions for beam 1 (left) and beam 2 (right). Model and measurement are in good agreement for both beams.

Comparing the chromatic measurement for the ATS optics, see figure 6.23, to the nominal optics for IP1 and IP5 at a β^* value of 1 m, see figure 6.24, the amplitude of the Montague function is decreased by a factor of about 2.

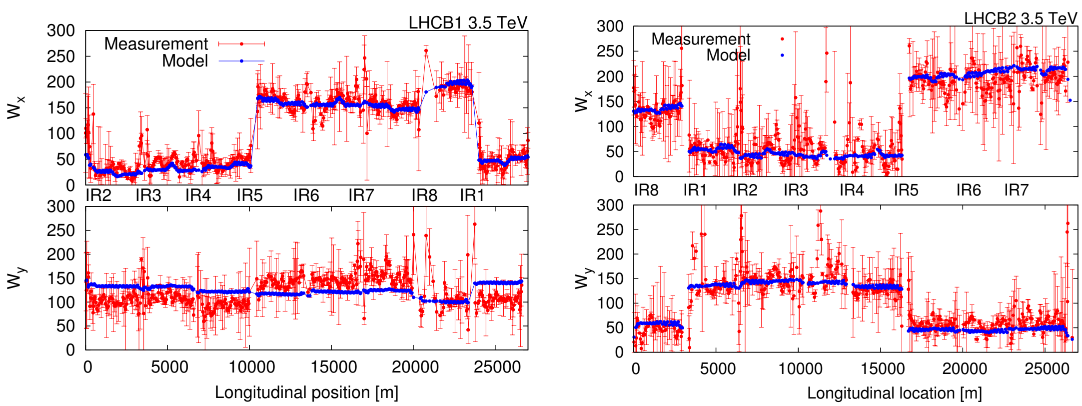

Figure 6.24: The amplitude of the Montague function for nominal optics is shown for IP1 and IP5 at a β^* value of 1.0 m, 10 m for IP2 and 3 m for IP8 m for beam 1 (left) and beam 2 (right). Model is shown in blue and measurement in red.

Chapter 7

Implementation of the Segment-by-Segment technique at RHIC.

The segment-by-segment technique was successfully demonstrated in the LHC operation for reducing the beta-beat [79]. It was decided to develop and apply the same technique to RHIC during the polarized proton operation in 2011. Few limitations had to be taken into account during the development of the segment-by-segment technique for RHIC. First limitation is that double plane BPMs are installed only around the IPs, elsewhere single plane BPMs are available. Second limitation is that small numbers of independent power converters are available, meaning that the available number of correctors is limited. The RHIC lattice and optics are discussed in section 7.1. The measurements are discussed in section 7.2. The first corrections calculated and implemented during operations are presented in section 7.3. Optics stability, presented in section 7.4, is important for safe operations. Measurements were conducted between two fills separated by 1.5 months. A summary is given in section 7.5.

7.1 Introduction to the relativistic heavy ion collider

RHIC consists of two six-fold symmetric superconducting rings with a circumference of 3.833 km. The two rings (blue and yellow in figure 7.1) are made up of six arcs intersecting at six interaction regions (IRs) and provide collisions for 2 or 4 experiments. The names of the four experiments are PHOBOS, BRAHMS, PHENIX and STAR. An overview of the accelerator complex is shown in figure 7.1. The main goal of RHIC is to provide collisions at energies of up to 100 GeV/u per beam for heavy ions. The accelerator is also designed for colliding lighter ions all the way down to protons (250 GeV), including polarized protons [117], [118].

7.1.1 RHIC optics layout

The optics layout for the blue ring is shown in figure 7.3. As opposed to the LHC, RHIC is not equipped with double plane BPMs everywhere. Single plane BPMs are installed in the arcs, where double plane BPMs were installed in the insertion regions. Due to this limitation the segment-by-segment algorithm had to be adjusted. The adjustment that had to be made for this is that the BPM data had to be filtered separately per plane. A second limitation is that the number of independent power supplies around the IPs is limited, this significantly reduced the number of available variables.

Table 7.1 shows the main optics parameters for the blue ring of RHIC during proton operation.

7.2 Optics measurements

Optics measurements were conducted at several instances during the 2011 polarized proton run. The measurements described in this thesis are for the blue ring at 250 GeV. Figure 7.4 shows a comparison between the two methods, i.e, the fit and phase methods, which are used to measure the linear optics. The fit method [119] consists of fitting the amplitude of the betatron oscillations. The phase method

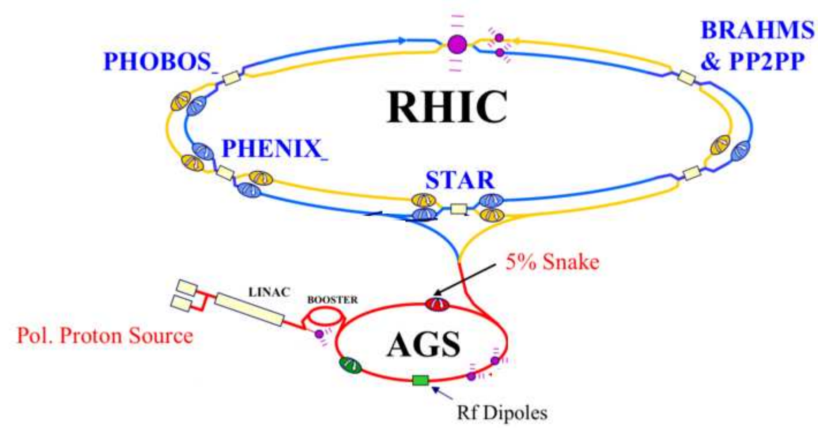

Figure 7.1: Overview of the RHIC complex.

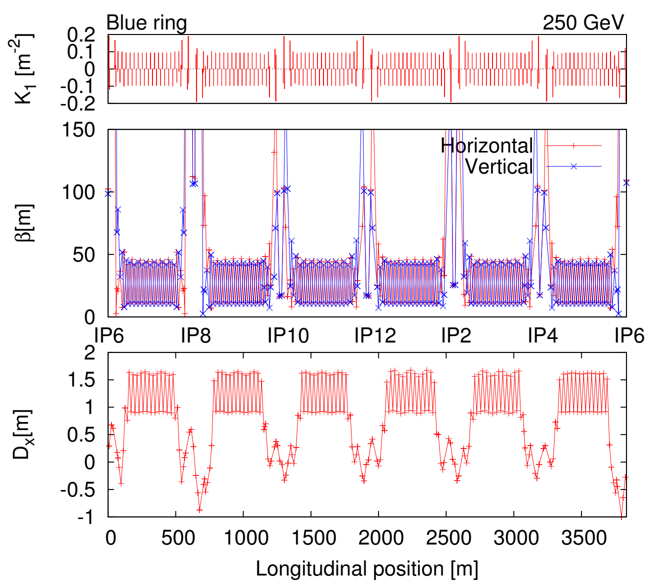

Figure 7.2: Optics layout for the blue ring of RHIC. Quadrupole strengths are shown on top. β-functions in the middle, for horizontal plane (red) and vertical plane (blue). The horizontal dispersion is shown on the bottom. This is for RHIC at top energy, 250 GeV. IP6 and IP8 are squeezed down to 0.62 m and IP2 to 3 m.

Parameter	Value
Store energy [GeV]	250
Circumference [m]	3833
Horizontal tune	28.69
Vertical tune	29.68
Horizontal natural chromaticity	-58.62
Vertical natural chromaticity	-57.36
γ at store	14.498
Normalized emittance [μm]	$\sim$ 1.3
β^*_{2011} at IP6,IP8 [m]	0.62
beam size at IP6,IP8 [μm]	81.25

Table 7.1: Main parameters for the blue ring of RHIC at store during proton operation.

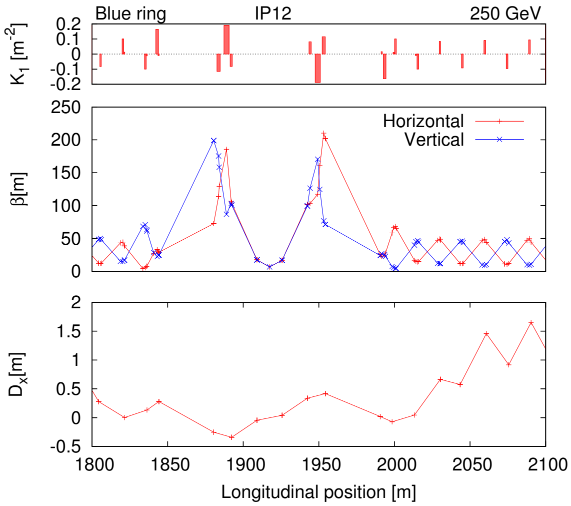

Figure 7.3: Optics layout for IP12. Quadrupole strengths are shown on top. β-functions in the middle, for horizontal plane (red) and vertical plane (blue). The horizontal dispersion is shown on the bottom. This is for RHIC at top energy, 250 GeV.

uses the phase of the main betatron line and the model. The β-beat, i.e being the normalized difference between measurement and model, is shown. A good agreement between the two methods is observed.

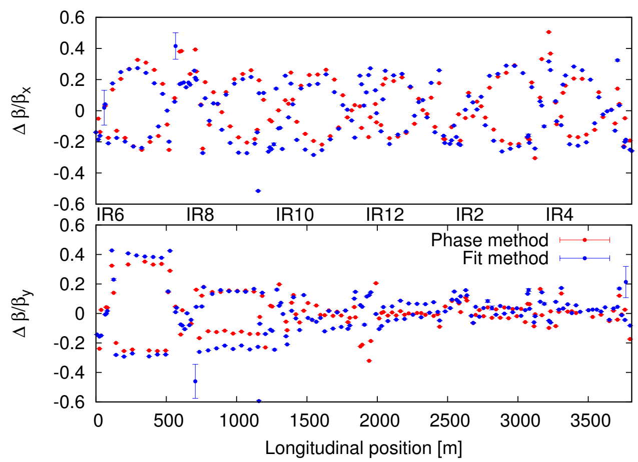

Figure 7.4: A comparison between the two different methods used to measure the optics at RHIC, for the horizontal plane (above) and vertical plane (below). Abrupt jumps are observed in the vertical plane for IR6, IR8 and IR10.

A peak beta-beat of $\sim 30\%, 40\%$, in the horizontal and vertical plane respectively is observed. Abrupt jumps in the β-beat indicate strong local errors. Large local jumps are observed in IR6, IR8 and IR10.

7.3 Optics corrections

In this section the analysis and correction of IR6 and IR12 will be discussed. The observable used is the phase error, i.e. the difference between the measured and model phase advance. Figure 7.5 shows the phase error observed for IR6, the largest error is observed in the vertical plane. A suitable correction was found, but due to technical limitations, an alternative correction had to be found. The result is presented in the figure, showing measurements with correction (blue), before any corrections (red) and after applying 80% of the correction strength (green). The local error originates from the right of the IP, indicating that the main error source is the triplet. Applying 100% of the correction had a negative impact on the optics. A list of the correctors used for IR6 is shown in table 7.2.

Corrector	$\Delta K[10^{-4}\mathrm{m}^{-2}]$	rel values[%]
Q7I6	0.84	1
Q5IT6	-0.53	2
Q1I6	-0.05	-0.1
Q2O6	0.05	0.1
Q5OT6	1.97	7

Table 7.2: List of local correctors used for IR6 correction.

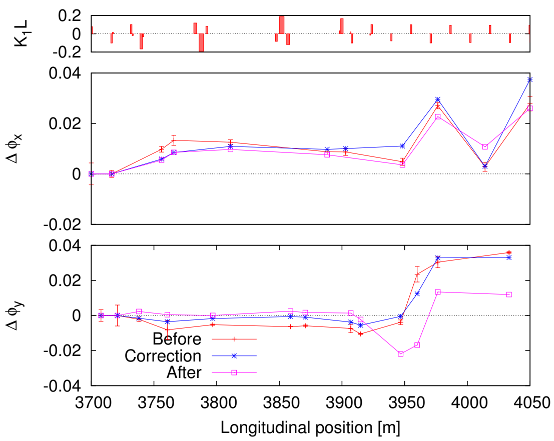

Figure 7.5: Local correction for IR6. The top plot shows the location and strengths of the quadrupoles in the segment. The middle plot shows measurements in the horizontal plane and the bottom plot refers to the vertical plane. Measurements before correction are shown in red, fitted model in blue and measured after correction in green. The largest deviation is observed in the vertical plane.

Figure 7.6 shows the phase error observed for IR12. A suitable correction was found using the correctors listed in table 7.3. A large number of correctors was used to achieve the correction shown. The calculated correction (blue) agrees well with the measurement (red). A correction of only 20% was applied. Measurements after correction (green) indicate a change in the observed phase error.

Corrector	$\Delta K[10^{-4}m^{-2}]$	rel values[%]
Q6O12	8.9	0.1
Q5O12	-17.9	2
Q2I12	-2.2	0.4
Q3I12	2.7	0.5
Q4I12	18.0	-2.0
Q5I12	26.9	3.0
Q6I12	-44.9	5.0

Table 7.3: List of local correctors used for IR12 correction.

β-beat for several steps in the correction process is shown in figure 7.7. The top plot shows the horizontal plane and bottom plot the vertical plane. The beta-beat is $\sim 30\%, 40\%$ around the ring for the baseline measurement (red), some outer layers are at 60%. After the correction in IR6 was applied (green) the peak beta-beat in the horizontal plane remained the same. In the vertical plane the large local jump at IR6 is corrected. The peak beta-beat is reduced to a 20% level. After applying IR6 and IR12 correction (blue) simultaneously, a difference is observed in both planes. The peak beta-beat in the horizontal plane was reduced to a 20% level around the ring. In the vertical plane, however, the peak beta-beat was not further reduced.

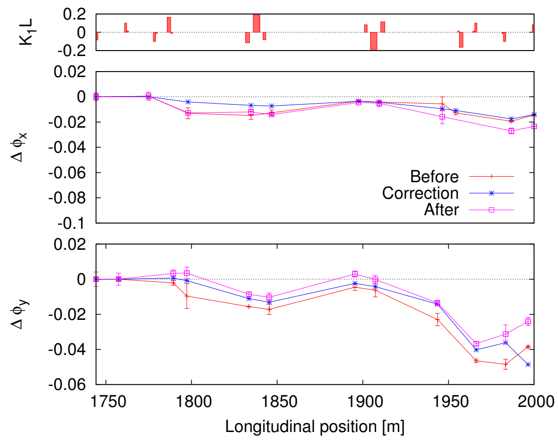

Figure 7.6: Local correction for IR12. The top plot shows the location and strengths of the quadrupoles in that segment. The middle plot shows the measurements in the horizontal plane and bottom in the vertical plane. Measurements before correction are shown in red, fitted model in blue and measurement after correction in green. Largest error is observed in the vertical plane.

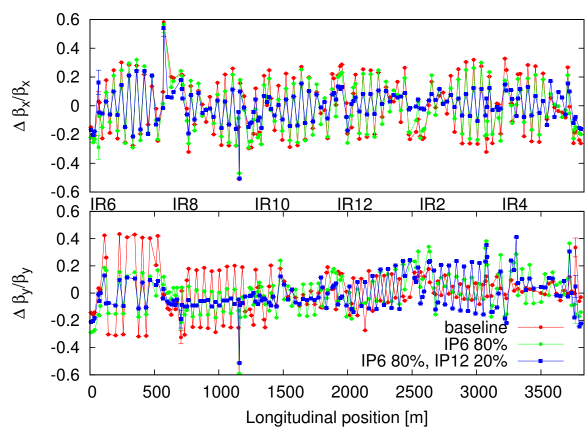

Figure 7.7: β-beat for several steps in the correction process. After the correction in IR6 was applied (green) the peak beta-beat in the horizontal plane remained the same. In the vertical plane the large local jump at IP_6 is corrected. The peak beta-beat is reduced to a 20% level. Applying IR6 and IR12 correction simultaneously a difference is observed in both planes (blue). Peak beta-beat, in the horizontal plane was reduced to a 20% level. In the vertical plane however, the peak beta-beat was not further reduced and remained at a 20% level.

7.4 Optics stability

Optics stability is important for safe operation. Measurements were conducted to investigate the variation of the β-beat over a period of time. Baseline measurements were conducted separated by 1.5 months. In figure 7.8 a histogram of the difference in the β-beat is shown. The main distribution is below 10%.

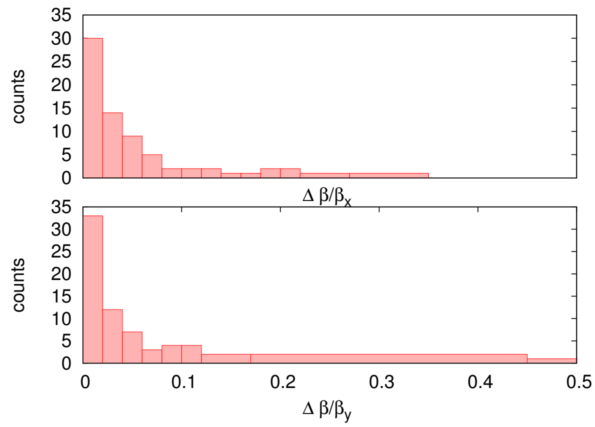

Figure 7.8: Histogram of the difference in the β-beat. Results for the horizontal plane are shown on the top plot and for the vertical plane on the bottom plot. Horizontal axis shows the difference in the β-beat between two fills separated by 6 weeks.

Figure 7.9 shows the phase error for the horizontal plane (top) and vertical plane (bottom) spread over 6 weeks and using different BPMs. The observed error is very similar for both fills.

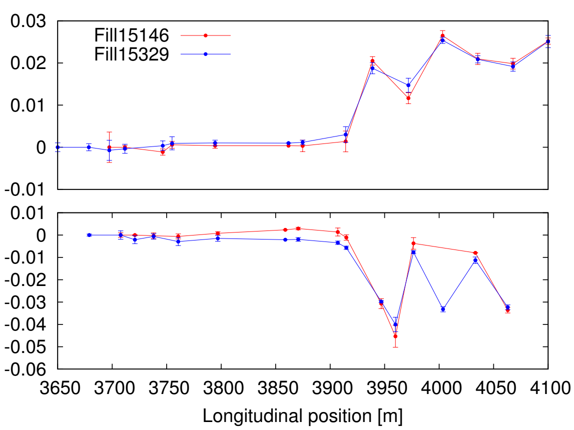

Figure 7.9: Measurement for the phase error in IR6 is shown. The horizontal plane, top and vertical plane, bottom. Different starting BPMs were used and measurements were separated by 6 weeks. In the vertical plane there is one missing BPM for fill15329, compared to fill 15220.

7.5 Summary

First measurements and corrections using the segment-by-segment technique show promising results. Corrections for IR6 and IR12 have been implemented and a reduction in the $\beta-$beat has been achieved. The $\beta-$beat around in the ring in both planes was reduced from 30%, 40%, respectively in the horizontal and vertical plane, to a $\sim 20\%$ level. Corrections were applied in the order of $20\%, 80\%$ of the calculated corrections. Further investigation should be carried out to find out why the full calculated corrections were successful. A plausible explanation could be the spurious effects from the AC-dipole on the β measurement. $\beta-$beat has been shown to be stable at the $\sim 10\%$ level over a 6 week period.

The observed local errors are reproducible from fill to fill and are not dependent on the starting BPM chosen. Scans of IR4, IR2 and IR8 corrections were also performed during the polarized proton run in 2011. Local errors at IR4 have been identified and a suitable correction was found. A first correction campaign for IR4 showed promising results. Detailed analysis and comparisons are in progress.

More detailed measurements and systematic scans of all IPs should be performed. The effect of the AC-dipole on the linear optics should be taken into account. When all local errors are corrected to a satisfactory level, a global correction should be calculated to correct small distributed errors. The same measurements and corrections will be repeated for the yellow ring. When the $\beta-$beat in both rings is corrected the segment-by-segment technique should be extended to measure and correct locally the coupling, dispersion and chromatic β.

Chapter 8

CLIC

Scientist and engineers around the globe are looking into future linear colliders. Two of the future designs of linear colliders are the International Linear Collider (ILC) [120] and the Compact LInear Collider (CLIC) [121]. This chapter will discuss the simulations conducted for the coupling and vertical dispersion for the CLIC Damping Ring (DR) using the algorithms developed for the LHC. Section 8.1 will give a general overview of CLIC. Section 8.2 introduces the damping ring in more detail. The results for the simulations are discussed in section 8.2.1. The first tests of the developed tools at an electron machine are discussed in section 8.4.

8.1 Introduction to the Compact Linear Collider

The Compact LInear Collider (CLIC) is a potential new high energy physics collider for the post-LHC era [121]. CLIC is based on the Two-Beam Acceleration (TBA) method in which the RF power for sections of the main linear accelerator is extracted from a secondary, low energy, high intensity electron beam running parallel to the main linear accelerator [122]. The power is extracted from the beam by special Power Extraction and Transfer Structures (PETS).

An overview of the CLIC complex is sketched in figure 8.1. In the current design two interaction points are foreseen. For a center of mass of 3 TeV, an accelerating gradient of 100 $\frac{MV}{m}$, and allowing ~ 10 km for the Beam Delivery (BD) area, CLIC would cover a total length of approximately 48 km.

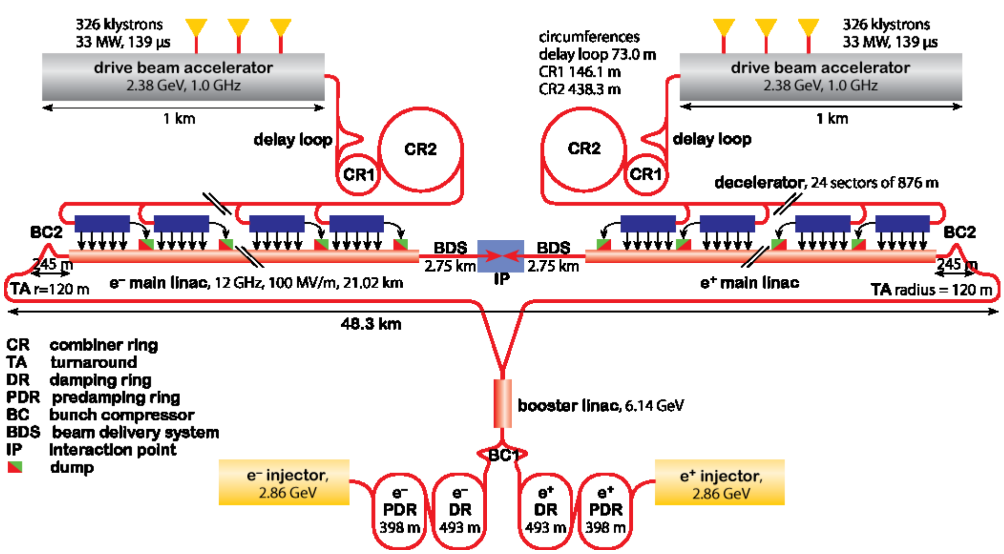

Figure 8.1: Overview of the CLIC complex

8.2 CLIC Damping rings

Studies were conducted for the correction of coupling and vertical dispersion for the damping rings of CLIC. The damping rings of CLIC play a crucial role in reaching the design ultra-low emittance at the interaction point. The term damping refers to damping by radiation. When an electron is accelerated it emits radiation, causing it to lose energy. This results in a reduction of the oscillation around its reference orbit and a shrinking of the beam. The importance of achieving ultra-low vertical emittance is twofold:

- Reduction of the magnetic gap of insertion devices, this allows to reach higher magnetic fields, resulting in a higher photon flux.
- The vertical emittance will induce higher luminosity.

In figure 8.1 the position of the damping ring in the CLIC complex is shown. Before the electrons and positrons are injected into the main linac the beam is damped in the damping rings. An overview of the main parameters is shown in table 8.1, the full list of parameters can be found in table [123].

Parameter	Value
Energy [GeV]	2.86
Circumference [m]	427.5
Number of dipoles	100
Dipole field [T]	1.0
Horizontal tune	48.35
Vertical tune	10.39
Horizontal natural chromaticity	-115
Vertical natural chromaticity	-85
Horizontal normalized emittance (ϵ_{norm})[nm.rad] (2/1Ghz)	472/456
Vertical normalized emittance (ϵ_{norm})[nm.rad](2/1Ghz)	4.8/4.8
Number of wigglers	52
Wiggler peak field [T]	2.5

Table 8.1: Main parameters for the CLIC damping ring.

8.2.1 Optics of the damping ring

A plot of the optics for half of the ring is shown in figure 8.2. The plot on the left shows the beta-function, for the horizontal (middle), the vertical plane (bottom) and the quadrupole strength (top). The plot on the right shows the dispersion. The horizontal dispersion is shown on the right.

Sextupoles and skew quadrupoles are installed along with the normal quadrupoles and dipoles in the arcs. From 0 to 80 m the long straight section is shown. This long straight section is equipped with normal quadrupoles and wigglers, used for damping. Figure 8.3 shows one fourth of the arc. In this figure the horizontal and vertical β-function, horizontal dispersion and horizontal and vertical phase-advances between the skew quadrupoles are plotted. Only one of the two arcs is shown, the long straight section is not equipped with any skew quads or sextupoles. In total 198 skew quadrupoles are installed, with 2 skew quadrupoles per cell. The vertical β function at the skew quadrupoles is about a factor of two larger in the focusing plane. The vertical phase-advance is much smaller than the horizontal one, resulting in the lower betatron tune.

8.3 Simulations for the CLIC Damping Ring

Simulations for the misalignments and rotations in the damping ring have been performed for the first time in [124]. The main contributors to an increase in the vertical emittance are the coupling and the vertical dispersion. Coupling and vertical dispersion are induced by the following errors:

- Tilt errors in the main dipole or orbit correctors.
- Vertical orbit bumps in the quadrupoles.

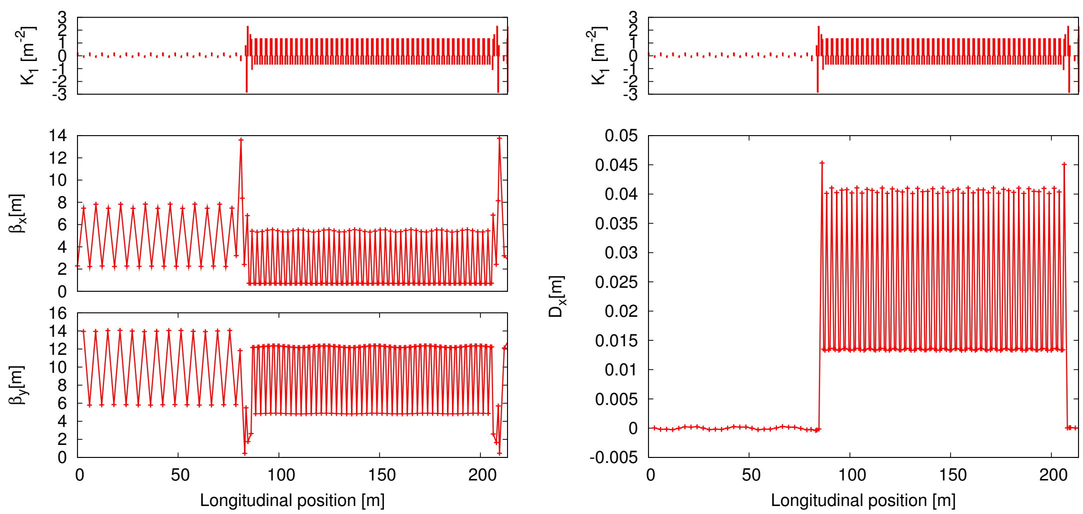

Figure 8.2: Half of the circumference of the damping ring is shown for the β-function (left) and horizontal dispersion (right). The top plot shows the strength and location of the quadrupoles.

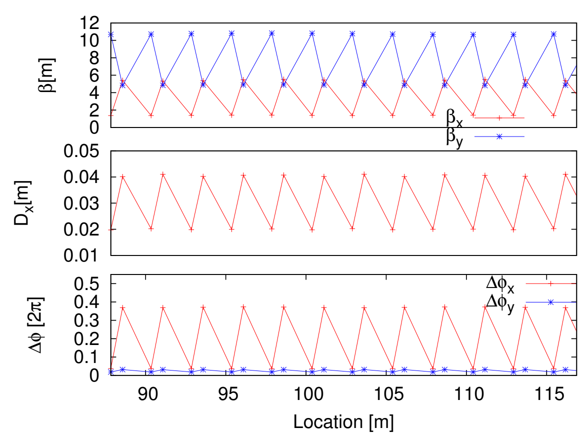

Figure 8.3: One fourth of an arc cell is shown. The optical functions at the skew quadrupoles are shown. Top plot shows the β-functions, middle plot the horizontal dispersion and bottom plot the phase advances.

- Vertical sextupole misalignment.
- Vertical orbit bumps in the sextupoles.
- Tilt in the quadrupoles.

Several simulations with random error assignment to the dipoles and quadrupoles have been conducted. Horizontal and vertical misalignments at the sextupoles were ignored. A list of the specified tolerances in [124] are listed in table 8.2

Imperfections	Symbol	1 RMS
Quadrupole misalignment	$< \Delta Y_{quad} >$,$< \Delta X_{quad} >$	$90\mu m$
Quadrupole rotation	$< \Delta\Theta_{quad} >$	100μrad
Dipole rotation	$< \Delta\Theta_{dipole} >$	100μrad

Table 8.2: Random alignment errors assigned to the CLIC damping rings.

In order to see how the corrections change for a range of assigned errors, the simulations were conducted for a range of errors.

8.3.1 Corrections

Several cases were studied. No noise was applied to the BPMs. In the following paragraphs the results are discussed. Random errors with increasing amplitude were applied. After the random errors, an orbit correction for the horizontal and vertical plane respectively, chromaticity correction using the sextupoles in the arcs and a tune correction using the quadrupoles in the long straight section were applied. After these corrections a correction was calculated for the coupling and vertical dispersion using the skew quadrupoles. This was followed again by an orbit correction in the horizontal and vertical plane respectively, and a chromaticity and tune correction. This was to correct the orbit, chromaticity or tune that was generated from the correction using the skew quadrupoles. There is an initial horizontal orbit, which was implemented to reach the required emittance. This initial horizontal orbit was set as a target correction for the orbit in the horizontal plane. The vertical orbit was corrected down to the zero orbit.

The linear optics functions are calculated at the following instances during the correction process:

- after random errors were applied and after the orbit, chromaticity and tune were corrected.
- after skew quadrupole corrections were applied.
- after skew quadrupole corrections were applied and after the orbit, chromaticity and tune are corrected.

Assumptions For the conducted simulations it was assumed that the skew quadruples do not have any field errors and that they were perfectly aligned. Furthermore it was also assumed that the beam position monitors are double plane BPMs. If single plane BPMs would be installed in the future, additional work should be done to implement the technique called pseudo double plane BPMs. The effect on the correction accuracy should be investigated.

Skew quad families In total 198 skew quadrupoles are installed in the arcs. No skew quadrupoles are installed in the long straight section. In the design lattice only 2 skew quadrupole families are implemented. This means that only 2 variables are available for correcting the coupling and vertical dispersion. Two skew quadrupoles are installed per cell, the first skew quadrupole is powered by the first family and the second by the second family of power supplies. The decision on the number of independent variables is mainly driven by economical reasons. The more families needed, the more independent power supplies need to be installed, which in turn increases the overall cost. A first simulation was conducted using all 198 skew quadrupoles independently and this was compared with using only 99 skew quadrupole families. For the 99 families, the skew quadrupoles in the same cell are one family. From the simulation it was observed that reducing the number of families by two had no clear effect on the coupling and vertical dispersion. For this reason it was decided to conduct the measurements with the 2 skew quadrupoles families as is stated in the design, and 99 independent skew quadrupole families.

Motivation of the weights A small study was conducted to investigate the effect of applying different weights. For the algorithm which corrects coupling and vertical dispersion, 5 weights could be allocated. The first two are the real and imaginary part of the difference resonance driving term. The two following weights are to correct the sum resonance driving term. The last one is to correct the vertical dispersion.

Two cases were studied. Both studies were conducted using the 99 skew quadrupole families. In the first case, shown in figure 8.4, the effect of applying weights on the sum resonance was investigated, this was done for when rotations were applied in the quadrupoles. From the difference and sum resonance plot it was obvious that even when weights were placed on the sum resonance it was impossible to correct this resonance, and the correction had a large effect on the correction of the leading difference coupling resonance. The difference resonance was corrected 50% less when the weight was placed on the sum resonance. Furthermore the correction of the sum resonance had a negative effect on the vertical dispersion , the vertical dispersion was increased by a factor of two.

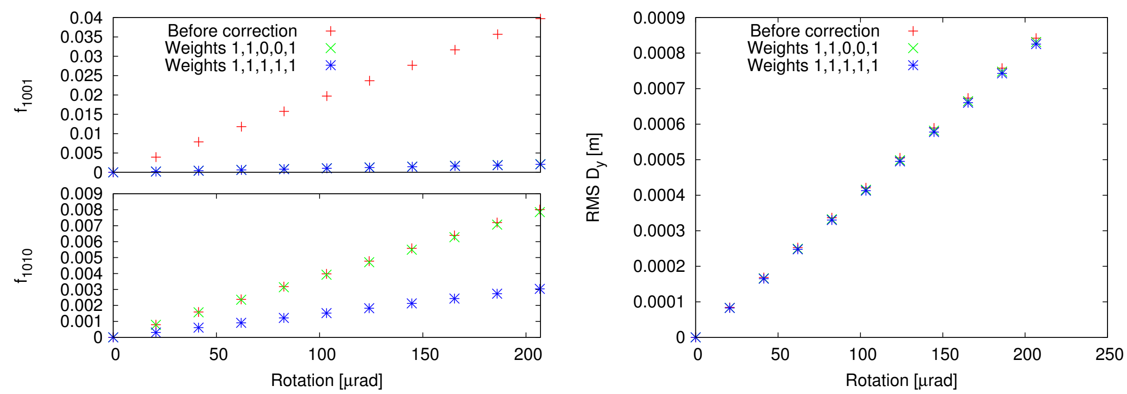

Figure 8.4: The f_{1001} (top) and f_{1010} (bottom) coupling resonance term is shown for the case that quadrupole rotations were applied. Correction is shown for using 99 skew quadrupole families. Three cases are shown: before correction (red), after correction using skew quadrupoles, but before orbit, chromaticity and tune corrections were applied (green) and after correction (blue).

For the second study the effect of placing weights on the correction of the vertical dispersion was investigated. It was discovered that placing the weight for the correction of the vertical dispersion did not correct the vertical dispersion, it remained constant. Also no effect could be observed for the difference and sum resonances, as it had no negative effect on the difference coupling resonance.

It was decided not to place weights for the correction of the sum resonance, as this has a negative effect on both the vertical dispersion and the difference resonance. The weight for the correction of the vertical dispersion was enabled.

Dipole rotation

Dipole rotations were applied to 81 wigglers and 196 dipoles. The error was randomly applied in a range from 0 to 230 μrad. Figure 8.6 shows the horizontal and vertical orbit. For the 2 and 99 families the orbit was well corrected before and after applying the corrections. This was expected, as the same number of skew quadrupoles was used. The effect of not correcting the orbit is large, especially in the vertical orbit. This was expected, as rotating the dipoles introduces a vertical orbit.

Figure 8.7 shows the difference (top) and sum coupling resonance (bottom). The generated difference resonance (f_{1001}) is larger than the sum resonance (f_{1010}). This was expected as the tunes are 0.35 and 0.39, for the horizontal and vertical tune respectively, as the tunes are closer to the integer

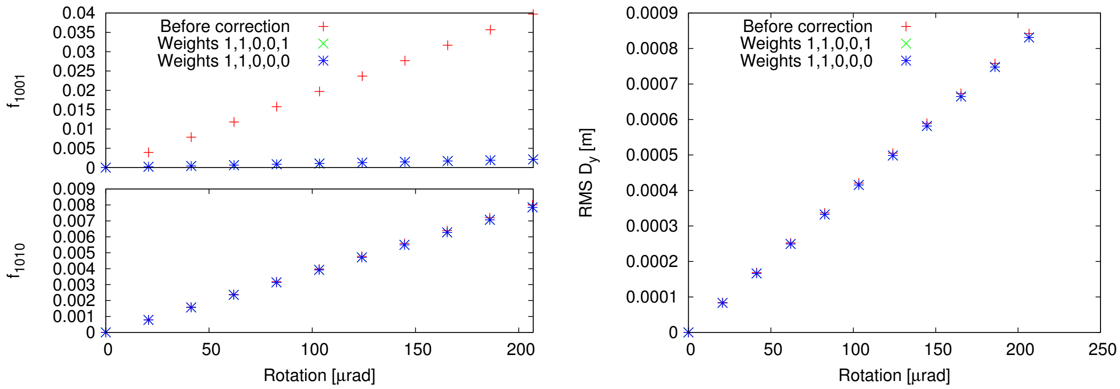

Figure 8.5: The f_{1001} (top) and f_{1010} (bottom) coupling resonance term is shown for quadrupole rotations. Correction is shown for using 99 skew quadrupole families. Three cases are shown: before correction (red), after correction using skew quadrupoles, but before orbit (green) and after correction using skew quadrupoles and orbit correctors (blue).

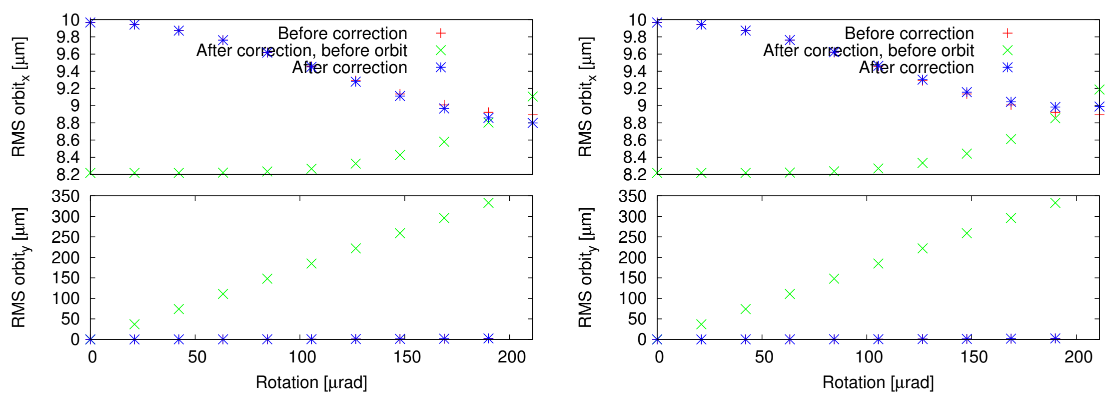

Figure 8.6: Horizontal (top) and vertical (bottom) orbit is shown when dipole rotations were applied. Left plot shows the correction using 2 skew quadrupole families and right plot using 99 skew quadrupole families. Three cases are shown: before correction (red). After correction using skew quadrupoles, before orbit, chromaticity and tune corrections were applied (green) and after correction (blue).

for the difference resonance (0.35-0.39) than for the sum resonance (0.35+0.39). The importance of correcting the orbit to a satisfactory level is apparent. As the effect of the coupling before and after the skew quadrupole correction was not visible a plot leaving out the orbit, chromaticity and tune correction was made.

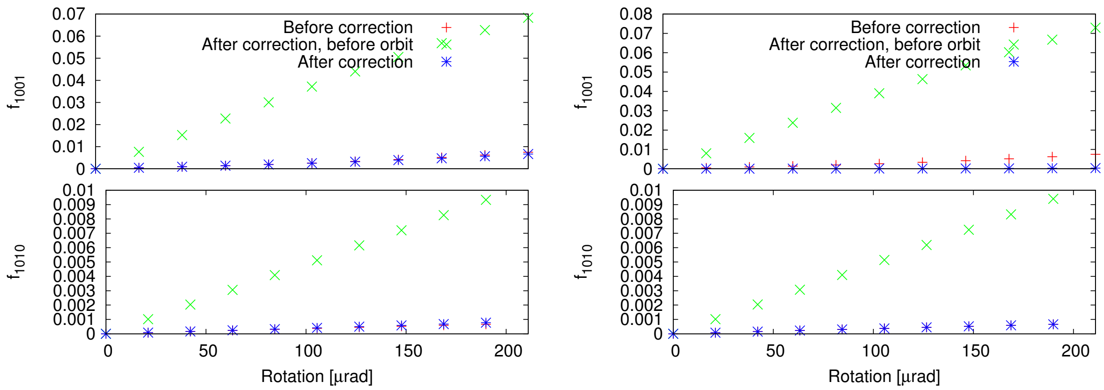

Figure 8.7: The f_{1001} (top) and f_{1010} (bottom) coupling resonance term is shown for when dipole rotations were applied. Left plot shows the correction using 2 skew quadrupole families and right plot using 99 skew quadrupole families. Three cases are shown: before correction (red), after correction using skew quadrupoles, but before orbit, chromaticity and tune correction was applied (green) and after correction (blue).

Figure 8.8 shows the difference (top) and sum coupling resonance (bottom) only after the orbit correction was applied. Using only the 2 skew quadrupole families foreseen in the design it is clear that it is not possible to sufficiently correct the difference or sum resonance. The difference resonance is slightly corrected, but the sum resonance increased slightly. Using the 99 skew quadrupole families the correction of the difference resonance was more effective. The difference resonance was corrected by a factor of about 7. The sum was slightly corrected, even though no weight was placed on the correction.

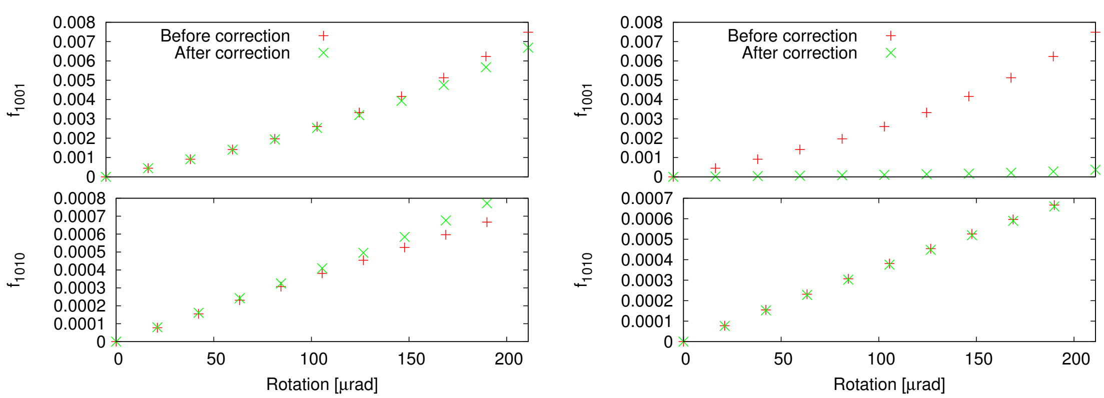

Figure 8.8: The f_{1001} (top) and f_{1010} (bottom) coupling resonance term is shown for when dipole rotations were applied. Left plot shows the correction using 2 skew quadrupole families and right plot using 99 skew quadrupole families. Two cases are shown, before (red) and after correction(green).

Figure 8.9 shows the vertical dispersion. Without correcting the orbit, chromaticity and tune the vertical dispersion increases to a peak value of 8 mm. Figure 8.10 shows the vertical dispersion before and after corrections were applied. By using only 2 families it was not possible to correct the vertical dispersion, the vertical dispersion even increased by a factor of about 4. When using the 99 families it was possible to keep the vertical dispersion constant.

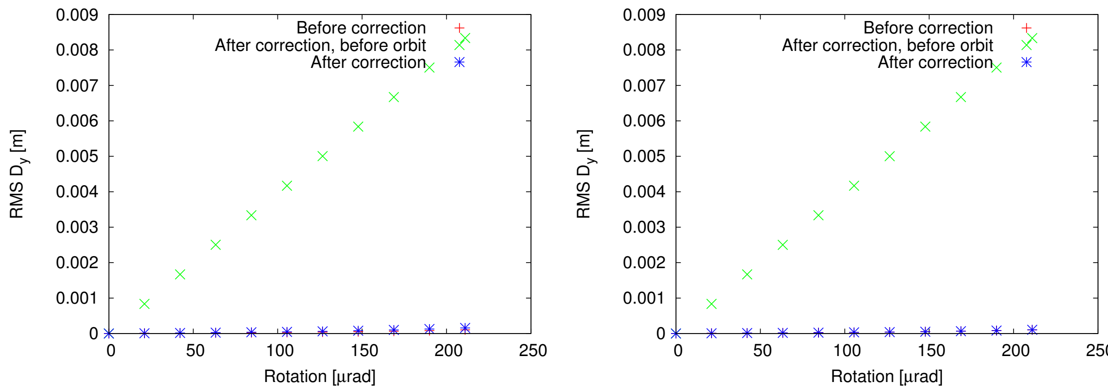

Figure 8.9: Vertical dispersion is shown for when dipole rotations were applied. Left plot shows the correction using 2 skew quadrupole families and right plot using 99 skew quadrupole families. Three cases are shown before correction (red), after correction using skew quadrupoles, but before orbit, chromaticity and tune (green) and after correction(blue).

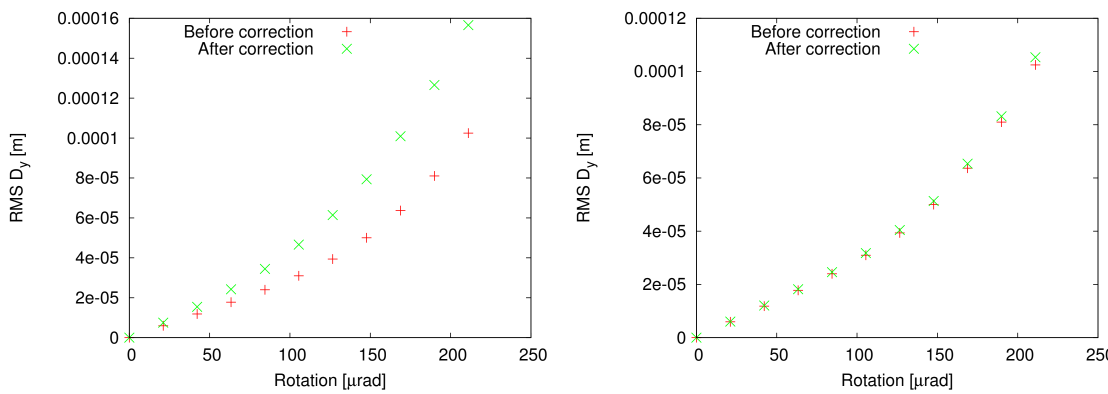

Figure 8.10: Vertical dispersion is shown for when dipole rotations were applied. Left plot shows the correction using 2 skew quadrupole families and right plot using 99 skew quadrupole families. Two cases are shown, before (red) and after correction (green).

Figure 8.11 shows the emittance before and after correcting the orbit, chromaticity and tune. It was observed for the vertical dispersion, when the orbit, chromaticity and tune was not corrected, that the imbalance between the horizontal and vertical emittance is large for both cases.

For a closer look at the emittance imbalance after the orbit, chromaticity and tune was corrected, see figure 8.12. For the case of the 2 families the emittance imbalance increases significantly by a factor of about 13. For the 99 families the correction was more successful. The emittance imbalance was reduced significantly by a factor of about 5. It was observed, from figure 8.10, that the vertical dispersion could not be corrected, but the difference resonance was corrected to a satisfactory level. This shows that the main contributor for the case of the dipole rotation to the emittance imbalance comes mainly from the difference resonance.

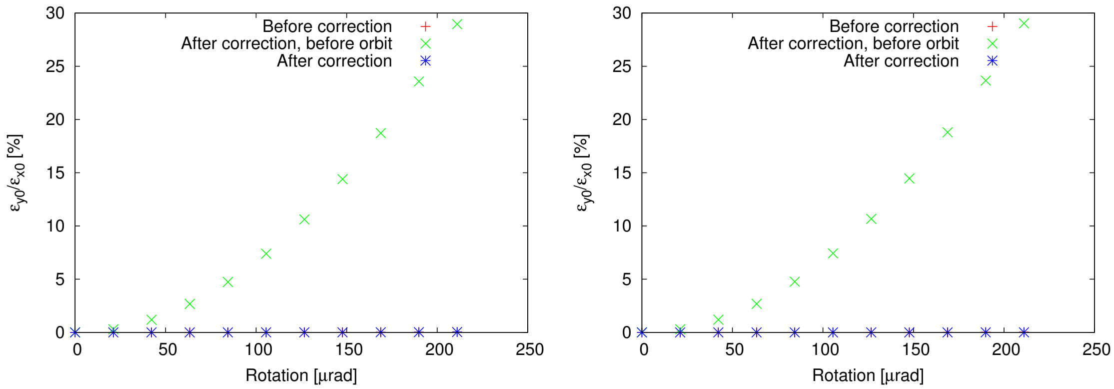

Figure 8.11: Emittance imbalance is shown for when dipole rotations were applied. Left plot shows the correction using 2 skew quadrupole families and right plot using 99 skew quadrupole families. Three cases are shown before correction (red): after correction using skew quadrupoles, but before orbit, chromaticity and tune (green) and after correction (blue).

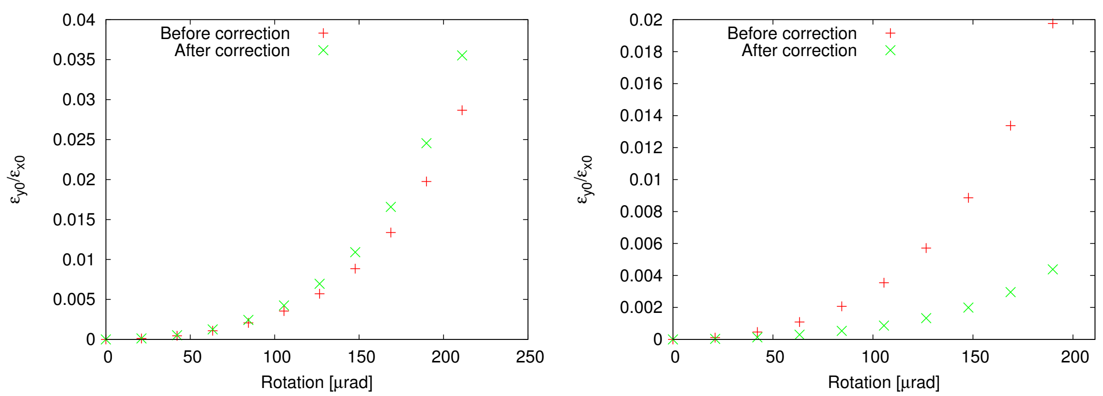

Figure 8.12: Emittance imbalance is shown for dipole rotations. Left plot shows the correction using 2 skew quadrupole families and right plot using 99 skew quadrupole families. Three cases are shown before correction (red). After correction using skew quadrupoles, before orbit (green) and after correction using skew quadrupoles and orbit correctors (blue).

Quadrupole rotation

Quadrupole rotations were randomly applied to 384 normal quadrupoles. The quadrupole rotations were applied in a range from 0 to 230 μrad. As expected it was observed that the orbit after applying the skew quadrupole correction has a smaller effect than with the dipole rotation, see figure 8.13. For the 2 family case the vertical orbit was increased after the correction. For the 99 family case the vertical orbit was not perfectly corrected, but as they are so small the effect is negligible.

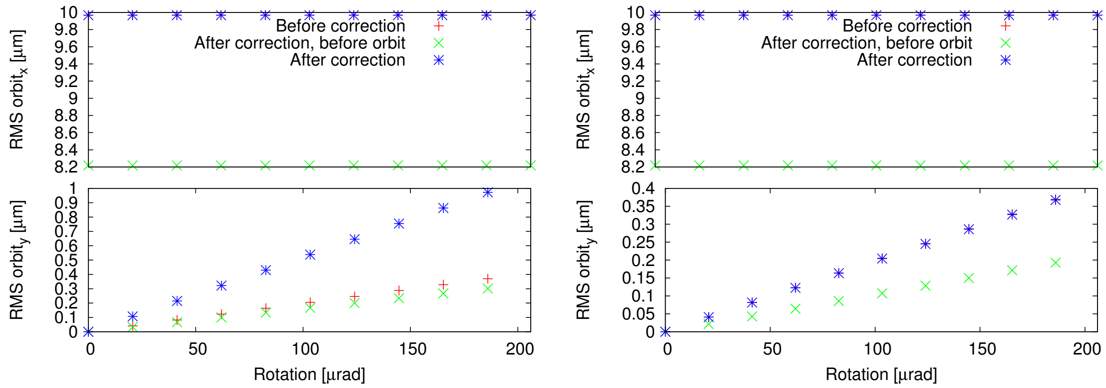

Figure 8.13: Horizontal (top) and vertical (bottom) orbit is shown for when quadrupole rotations were applied. Left plot shows the correction using 2 skew quadrupole families and right plot using 99 skew quadrupole families. Three cases are shown before correction (red): after correction using skew quadrupoles, but before orbit, chromaticity and tune corrections were applied (green) and after correction (blue).

Figure 8.14 shows the difference and sum resonance driving term. For the case of 2 families the correction has a positive effect on both the difference and sum resonance. The difference resonance was corrected by about 30%. The sum was corrected less, by about 25%. When looking at the case for 99 families the difference resonance was corrected by a factor of 8. However, in the case of the 99 families the sum resonance was not corrected, but remained constant.

The orbit correction had little or no effect on the difference or sum driving terms, whereas in the case of the dipole rotation the effect was larger.

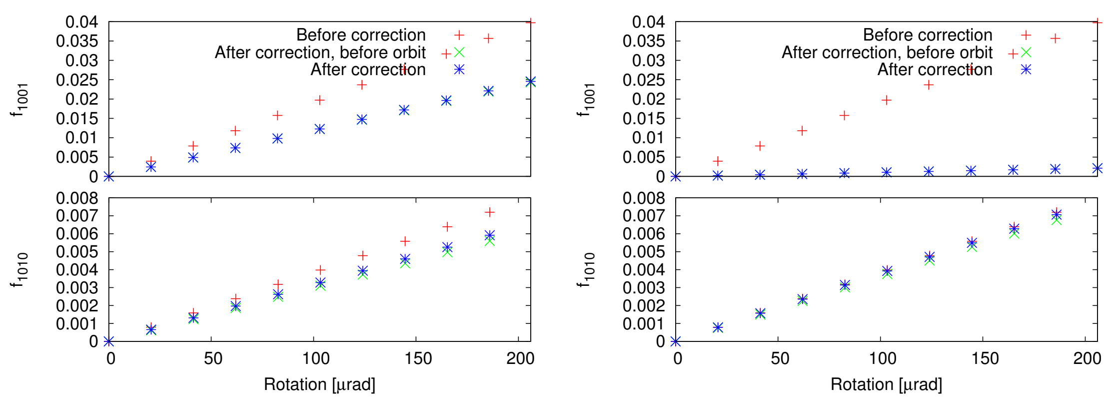

Figure 8.14: The f_{1001} (top) and f_{1010} (bottom) coupling resonance term is shown for when quadrupole rotations were applied. Left plot shows the correction using 2 skew quadrupole families and right plot using 99 skew quadrupole families. Three cases are shown before correction (red): after correction using skew quadrupoles, but before orbit, chromaticity and tune correction were applied (green) and after correction (blue).

The impact of the skew quadrupole rotations on the vertical dispersion is shown in figure 8.15. For the 2 family case the vertical dispersion was increased by 14%. For the case of the 99 families the vertical dispersion was kept constant.

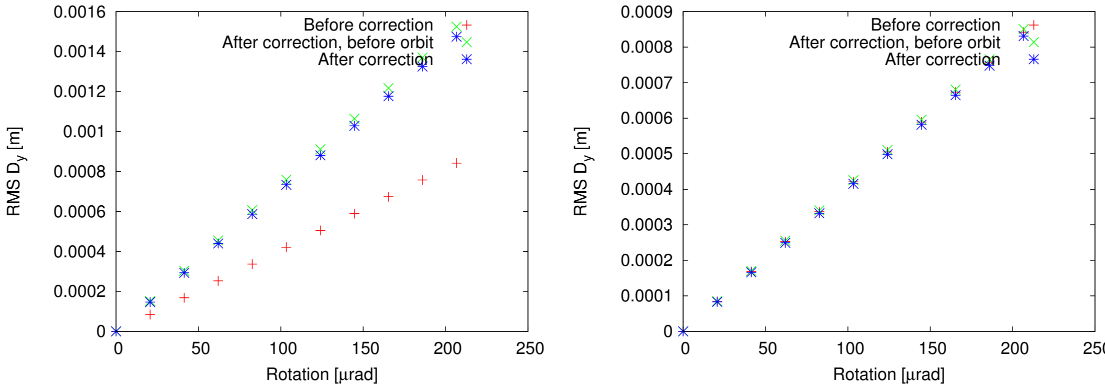

Figure 8.15: Vertical dispersion is shown for when quadrupole rotations were applied. Left plot shows the correction using 2 skew quadrupole families and right plot using 99 skew quadrupole families. Three cases are shown before correction (red): after correction using skew quadrupoles, but before orbit, chromaticity and tune corrections were applied (green) and after correction (blue).

Figure 8.16 shows the emittance imbalance. The emittance imbalance deteriorates for the 2 family case. For the 99 families the emittance imbalance was corrected by a factor 3, for the 2 family case the imbalance was increased by 30%.

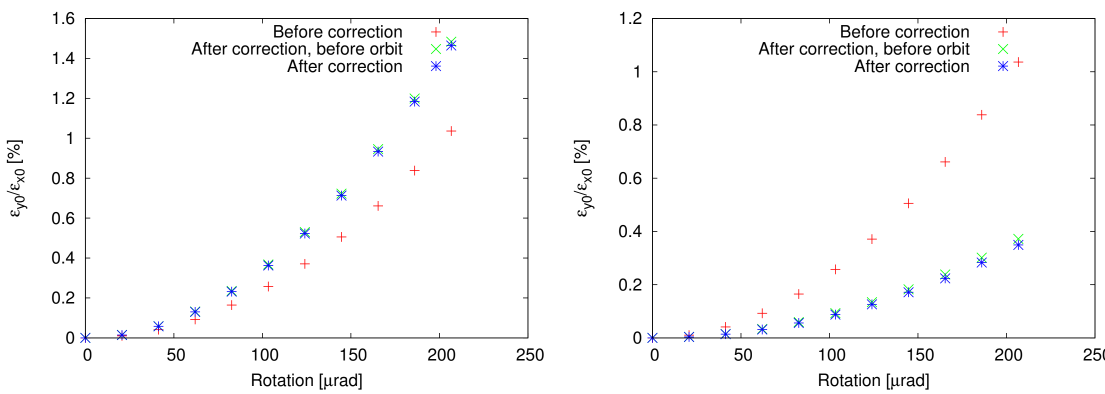

Figure 8.16: Emittance imbalance is shown for when quadrupole rotations were applied. Left plot shows the correction using 2 skew quadrupole families and right plot using 99 skew quadrupole families. Three cases are shown before correction (red): after correction using skew quadrupoles, but before orbit, tune and chromaticity corrections were applied (green) and after correction using skew quadrupoles and orbit correctors (blue).

Quadrupole misalignments

Quadrupole misalignments were randomly applied to 384 normal quadrupoles. Misalignments were applied for both the horizontal and vertical plane of a range from 0 to 10 μm. Figure 8.17 shows the horizontal and vertical rms orbit. For both cases the orbit increases significantly after implementing the errors.

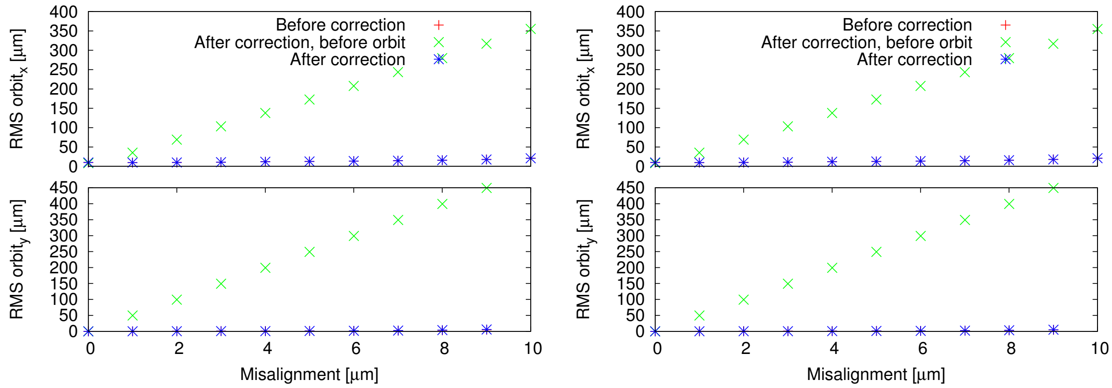

Figure 8.17: Horizontal (top) and vertical (bottom) orbit is shown for when quadrupole misalignments were applied in both directions. Left plot shows the correction using 2 skew quadrupole families and right plot using 99 skew quadrupole families. Three cases are shown before correction (red): after correction using skew quadrupoles, but before orbit, chromaticity and tune corrections were applied(green) and after correction (blue).

Figure 8.18 shows the difference and sum coupling resonance. As can be observed from the figure the coupling that is generated by the misalignments in the quadrupole is large, when the orbit is not corrected. Figure 8.18 shows the difference and sum coupling resonance before and after the corrections. For the 2 family case both the sum and difference resonances were corrected, but for the 99 families case the difference resonance was corrected more than for the 2 family cases. However it is interesting to observe that the sum resonance was corrected more than the difference resonance.

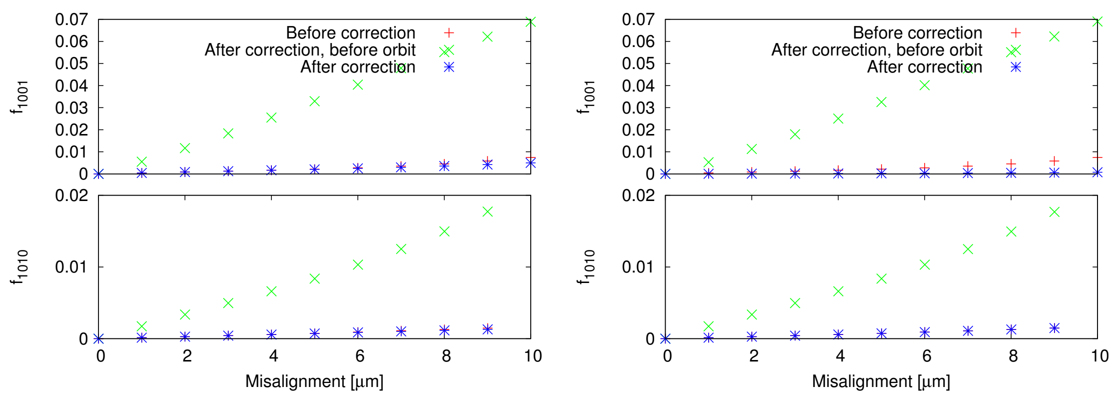

Figure 8.18: The f_{1001} (top) and f_{1010} (bottom) coupling resonance term for when quadrupole misalignments were applied in both directions. Left plot shows the correction using 2 skew quadrupole families and right plot using 99 skew quadrupole families. Three cases are shown before correction (red): after correction using skew quadrupoles, but before orbit, chromaticity and tune corrections were applied (green) and after correction (blue).

Figure 8.20 shows the vertical dispersion for the two cases. For the 99 family case the vertical dispersion remained constant. For the 2 family cases the vertical dispersion was increased by a factor of 2.

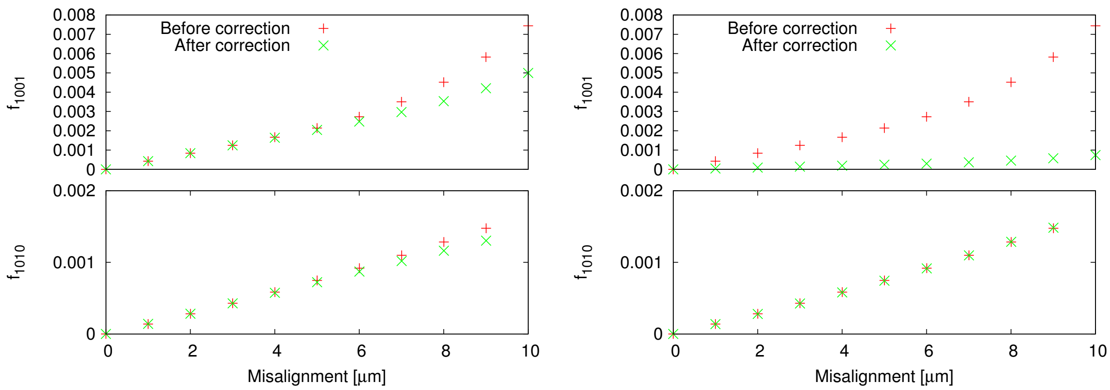

Figure 8.19: The f_{1001} (top) and f_{1010} (bottom) coupling resonance term for when quadrupole misalignments were applied in both directions. Left plot shows the correction using 2 skew quadrupole families and right plot using 99 skew quadrupole families. Two cases are shown, before (red) and after correction (green).

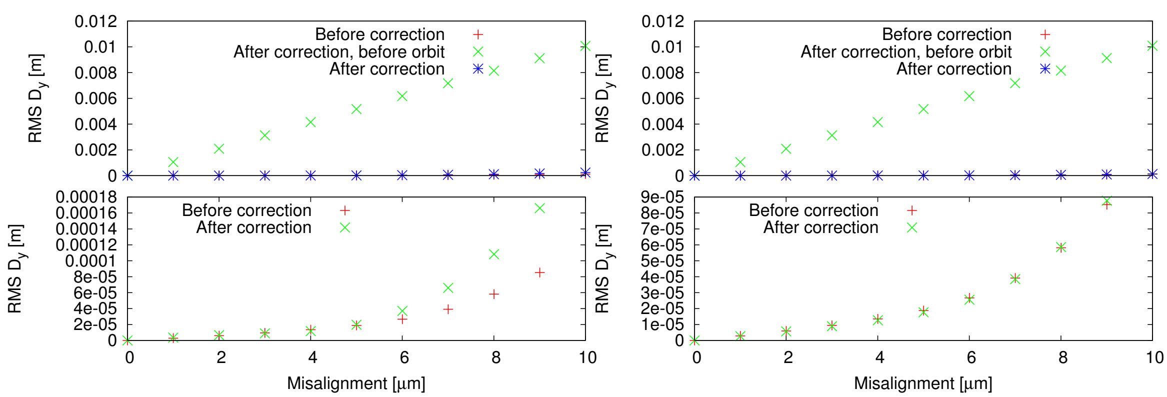

Figure 8.20: Vertical dispersion is shown for when quadrupole misalignments were applied in both directions. Left plot shows the correction using 2 skew quadrupole families and right plot using 99 skew quadrupole families. Top plot shows three cases: before correction (red), after correction using skew quadrupoles, but before orbit, chromaticity and tune corrections were applied (green) and after correction (blue). Bottom plot shows only before (red) and after (green) correction.

The emittance imbalances are shown for the two cases in figure 8.21. It is clear that when the orbit is not corrected the emittance imbalance is large. When looking closer to before and after corrections it is clear that for the 2 family case the imbalance was corrected by about a factor of 6.

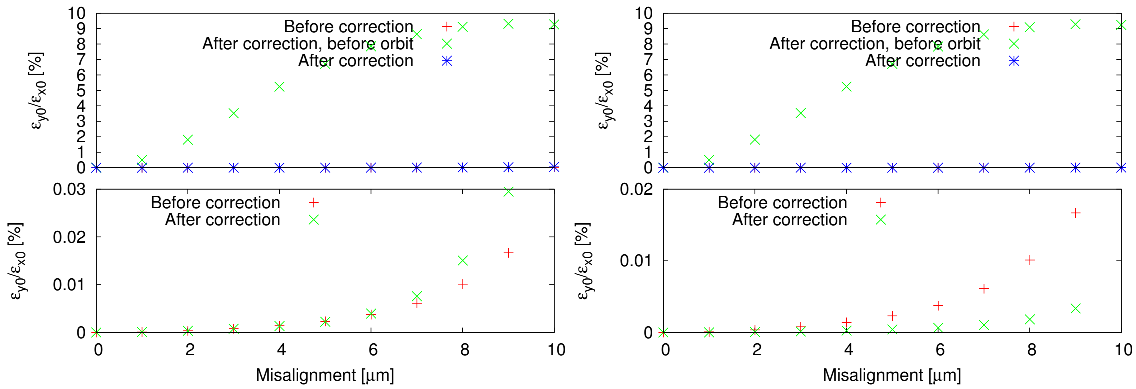

Figure 8.21: Emittance imbalance is shown for when quadrupole misalignments were applied in both directions. Left plot shows the correction using 2 skew quadrupole families and right plot using 99 skew quadrupole families. Top plot shows three cases: before correction (red), after correction using skew quadrupoles, but before orbit, chromaticity and tune corrections were applied (green) and after correction (blue). Bottom plot shows only before (red) and after (green) correction.

Summary for the CLIC damping ring studies

Figure 8.3 shows the calculated emittance imbalances before and after correction for the three cases studied. It is clear that for the three cases the emittance imbalances can be corrected by a factor of 3-5, depending on the case studied. It is shown that the developed algorithm for the correction of the coupling and vertical dispersion could be applied to the CLIC damping ring. The correction of the emittance imbalance is shown for the specifications which are listed in table 8.2, except for the quadrupole misalignments. For these quadrupole misalignments it was impossible to introduce an error which was larger then $10\mu m$. This was due a failure to match the tune, chromaticity and orbit for large errors.

A possible solution for this would be to apply the error in small steps and correct during every step the tune, chromaticity and orbit.

Correction	$\epsilon_{y0}/\epsilon_{x0}$ for dipole rotation [%]	$\epsilon_{y0}/\epsilon_{x0}$ for quadrupole rotation[%]	$\epsilon_{y0}/\epsilon_{x0}$ for quadrupole misalignments [%]
Before	0.0057	0.3710	0.027
After	0.0013	0.1256	0.005

Table 8.3: Emittance imbalances before and after corrections.

The results in table 8.3 are encouraging. They show that it would be possible to use the developed algorithms to correct the coupling and vertical dispersion to a satisfactory level.

From the simulations it follows that it is impossible to correct the vertical dispersion, but in the case of the 99 families it is possible to keep it constant. The decision on the number of families will be based on a balance between budget and the allowable emittance imbalance. An optimization routine could be written to find the optimal number of families.

The installation of skew quadrupoles in the long straight sections should be considered, as this would increase the number of variables available. Another advantage would be that the correction will be spread around the ring and not only in the arcs. A good orbit correction will be very important. Without a good orbit correction it will be nearly impossible to correct the emittance imbalances to a satisfactory level.

8.4 First test of the algorithms in SOLEIL

The motivation for conducting measurements at the SOLEIL was to explore the possibility of applying the developed algorithms and tools for the LHC to an electron machine. The main difference between a hadron machine and an electron machine is that a electron machine has flat beams, vertical emittance is smaller than horizontal emittance. The emittance is much smaller in electron machine than in a hadron machine, resulting in an optics stability and resolution which is more robust than in hadron machines. In an electron machine beam stability is easier thanks to the synchrotron radiation. Electron machines have been using LOCO [125] as the preferred tool for the measurement and correction of the linear optics [126].

8.4.1 SOLEIL

SOLEIL is a third generation light source [127]. This type of light sources are characterized by the emittance of synchrotron light all along the circumference of the storage ring. This is achieved in the bending magnets and also in the straight sections which are equipped with the wigglers and undulators [128].

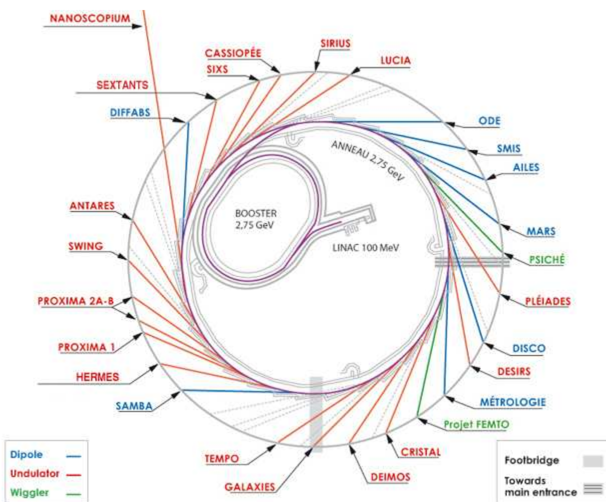

Figure 8.22: Layout of the SOLEIL light source.

Figure 8.22 shows a layout of the light source complex at SOLEIL. In total 27 beam lines are installed. These beam lines can be classified in several categories according to the beam spot size, energy range and analyzing method [129]. Electrons are injected into the LINAC, called HELIOS [130] at an energy of 90 KeV. In the LINAC the beam is accelerated to an energy of 100 MeV. From there the beam goes into the BOOSTER [131], which has a circumference of 156.620 m and will further accelerate the beam to an energy of 2.75 GeV. The beam is extracted into the main storage ring. The main parameters of the storage ring are listed in table 8.4.

8.4.2 Measurements at SOLEIL

During the experiments several linear and non-linear measurements were conducted. In the following paragraphs the linear optics, third and fourth order resonances and the effect of the undulator will be discussed.

Linear optics

Linear optics is measured by the phase advance between adjacent BPMs. The phase-beat, which is the difference between the measured and model value, is shown in Fig. 8.23. In both planes the phase-beat is relatively small ($\Delta\phi_{x,rms} = 0.32°, \Delta\phi_{y,rms} = 0.44°$). The vertical phase-beat shows some periodic high peaks at the low beta regions.

The beta function is calculated from the phase-advances between three BPMs, as was done in LEP [35]. The measured and model beta functions for both planes are shown in Fig. 8.24. Both planes

Parameter	Value
Nominal energy [GeV]	2.75
Circumference [m]	354.097
Horizontal betatron tune [-]	18.2
Vertical betatron tune [-]	10.3
Horizontal natural chromaticity [-]	-53
Vertical natural chromaticity [-]	-23
Maximum horizontal dispersion [m]	0.28
Horizontal emittance [nm.rad]	3.74
Revolution period [ns]	1181.40
Revolution frequency [MHz]	0.84664
Bunch length [ps]	13.8
Number of cells	16
Number of superperiods	4

Table 8.4: Main parameters of SOLEIL

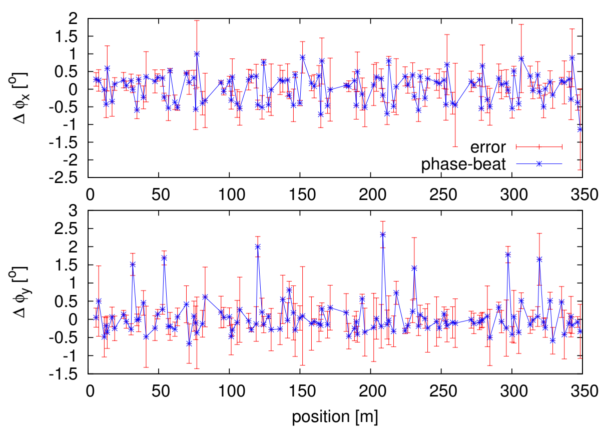

Figure 8.23: Phase beat for horizontal (top) and vertical (bottom).

show a good agreement with the model, but in the horizontal plane the error bars are larger than in the vertical plane. The beta-beat, which is the relative difference between the measurement and the model, is shown in Fig. 8.25. A maximum beta-beat of $\sim 6\%$ and $\sim 20\%$, in the vertical and horizontal plane respectively, are measured. The beta-beat is large and differs from the experience at SOLEIL, where the LOCO [134] algorithm is used. The error bar is rather large for the phase-based method.

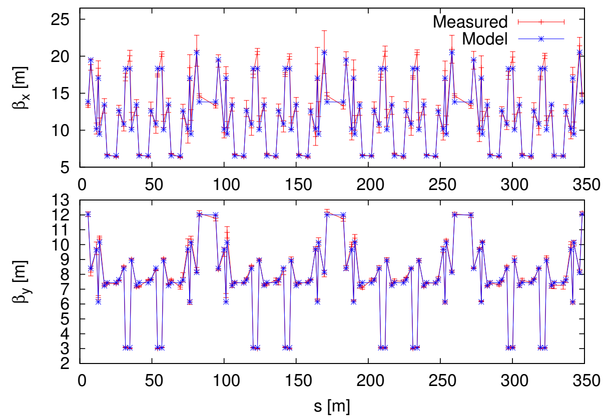

Figure 8.24: Measured and model betatron function for horizontal (top) and vertical (bottom) planes. The super periodicity of the ring is four.

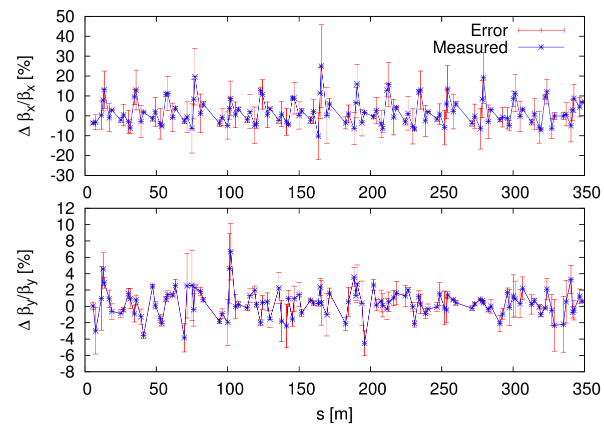

Figure 8.25: Beta-beat for horizontal (top) and vertical direction (bottom). A maximum beta-beat of $\sim 6\%$ and $\sim 20\%$, in the vertical and horizontal planes respectively is measured.

Figure 8.26 shows histograms of the relative measurement error of the beta functions. The maximum error on the vertical plane is 4.0%.

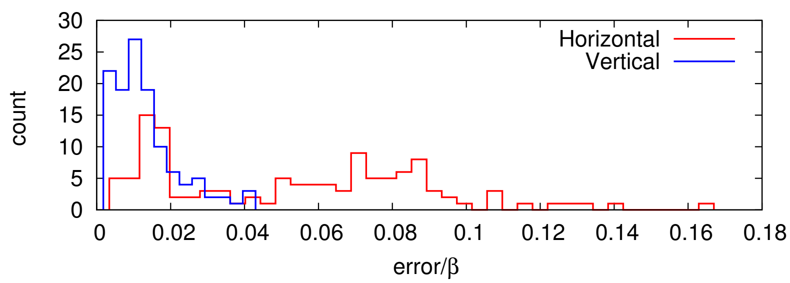

Figure 8.26: Histogram of the beta function error bar normalized to the beta.

Third order resonance

The horizontal spectral line with a frequency of $2Q_x$ was used to probe the beam dynamics of sextupolar order. Figure 8.27 shows a plot of Amp_{20} versus the longitudinal location, for two working points $Q_x = 18.21, 18.273$. Amp_{20} is defined as the height of the spectral line at the frequency $2Q_x$. The measurement is scaled with a factor of three to fit the simulation. The three reasons for the scale difference were the decoherence factors [14], possible kicker calibration error and synchrotron radiation damping. The decoherence factor, however, should be around two for the $2Q_x$ line. The local variations of the $2Q_x$ line around the ring show a qualitative agreement with the model. The sources for local discrepancy could be due to BPM non-linearities [135] and real errors such as optical and sextupolar errors. Before attempting nonlinear corrections it should be verified that the effect of BPM nonlinearities operating with this new filter in turn-by-turn mode are negligible.

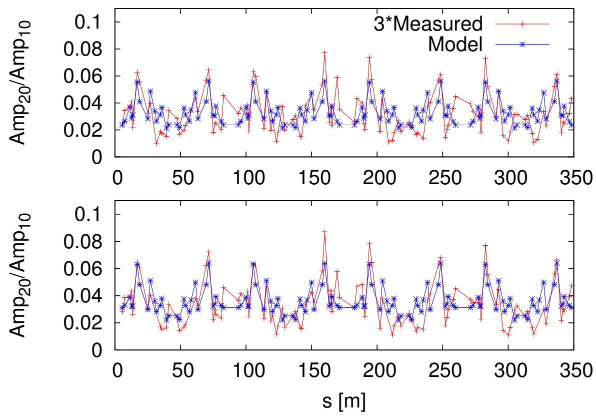

Figure 8.27: Normalized Amp_{20} for $Q_x = 0.21$ (top) and $Q_x = 0.273$ (bottom).

Fourth order resonance

Amp_{30} is defined as the height of the spectral line at the frequency $3Q_x$. The horizontal spectral line with a frequency of $3Q_x$ was used to prove the beam dynamics of octupolar order. An increase in Amp_{30} is typically observed when approaching the fourth order resonance. Figure 8.28 shows the spectrum of the motion for measured and simulated data, for three working points $Q_x = 18.21, 18.241, 18.245$. The simulation consists of a single particle tracked for 2000 turns, therefore the zero tune spread in the spectrum. The observed coupling in the measurement (Q_y) seems to come from electrical coupling. In Fig. 8.29 the normalized Amp_{30} versus the longitudinal location for the tunes is shown. Measurement and simulation show different longitudinal variation. In both figures and both for measurement and simulation, the variation of the octupolar lines when approaching the fourth order resonance (18.25) was negligible. Phase_{m0} corresponds to the phase of the spectral line at the frequency of mQ_x. Phase_{10} and phase_{30} are evaluated, shown in figure 8.30 for both measurement and simulation. For both data sets phase_{10} was multiplied by three. It can be seen that $\mathrm{phase}_{30} = 3\mathrm{phase}_{10}$ from the measurement. Figure 8.30 indicates that the octupolar line was dominated by the third order response of the BPMs.

Undulators SOLEIL is equipped with three in-vacuum (located at 121.67, 210.11 and 232.43 m) and one long undulator (located at 88.52 m). These two different types of undulators were examined separately. Figure 8.31 shows the difference of the $2Q_x$ spectral line between the lattices, with and without undulators. In both cases a small effect can be observed in the sextupolar line ($2Q_x$), indicating that the undulator could have sextupolar errors. However, the striking similarity between the two cases was not yet fully understood.

Summary

The phase-beat measurement shows a good result. However, the beat-beat measurement seems to be too large compared to the experience at SOLEIL. This could be due to the quality of the BPM data or to the technique used. The measurement of the sextupolar line ($2Q_x$) is showing promising results. The measurement of the octupolar line ($3Q_x$) seems to be dominated by BPM non-linearities. When looking at the undulators an effect on the $2Q_x$ spectral line was observed, but further analysis is necessary.

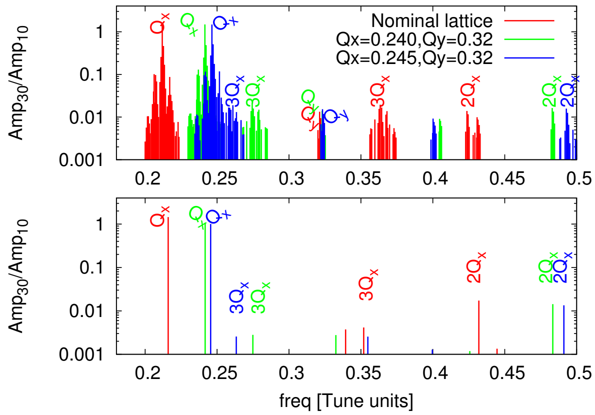

Figure 8.28: Frequency spectrum for horizontal tune approaching 4^{th} order resonance. For measured (top) and simulation taking into account the decoherence (bottom).

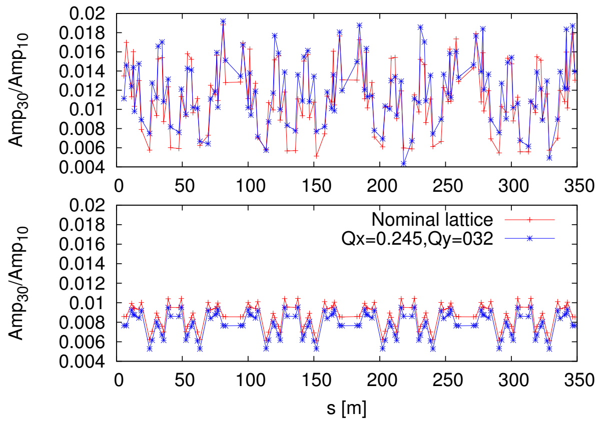

Figure 8.29: Normalized Amp_{30} for measured (top) and simulation (bottom) approaching 4^{th} order resonance.

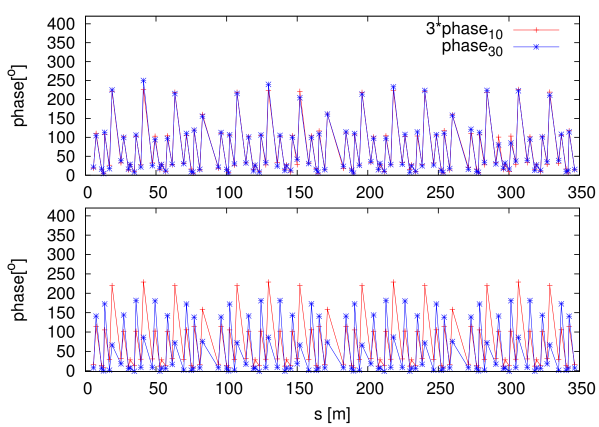

Figure 8.30: Phase_{10} and phase_{30} plotted versus longitudinal location for both measured (top) and simulation (bottom) for $Q_x = 0.21$.

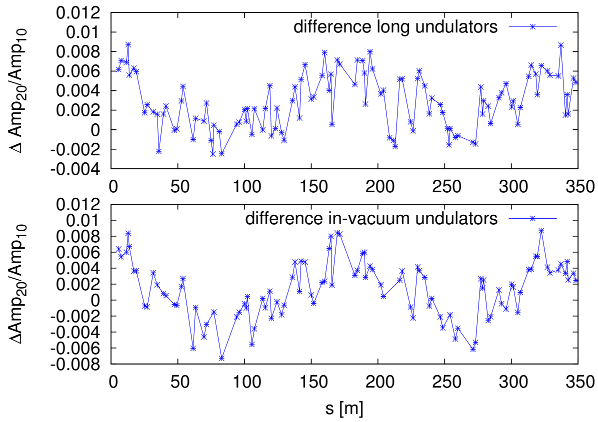

Figure 8.31: Plot showing the effect of the undulators on the Amp_{20}. Long undulator (top) and in-vacuum undulators (bottom).

The new BPM turn-by-turn filter still needs further tuning in order to improve its calibration and reproducibility. Moreover the flat chamber of the storage ring is the source of strong non-linearities and saturation of the BPM, and BPM electronic induces 5% crosstalk. The implication for the CLIC damping ring is that the BPM non-linearity should be well compensated.

Chapter 9

Software package

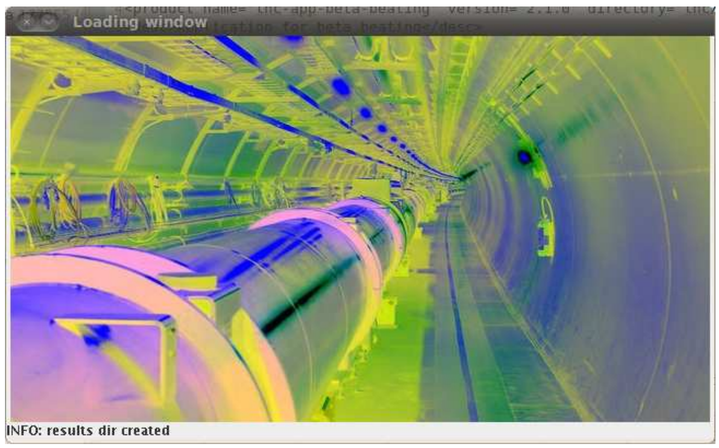

A software package was developed [137] to ease and minimize the user input for the measurement and corrections of the optics functions. The software package was developed in such a way that the different modules could be run separately and are easily adaptable to different accelerators. A general introduction of the software package is discussed in section 9.1. The different panels of the Graphical User Interface (GUI) are discussed in section 9.2, including a short discussion of the usage and functionality. Some functionalities of the LHC Software Architecture (LSA) [139] are implemented in the software package, and this is briefly discussed in section 9.3. Performance is crucial for every software package. In section 9.4 an overview of the performance is given. Lastly, a list of possible improvements is given and discussed in section 9.5.

9.1 Overview

A schematic overview of the software package is shown in figure 9.1. This schematic shows the steps that are followed during operation. The steps are followed from top to bottom, it starts by importing the turn-by-turn data.

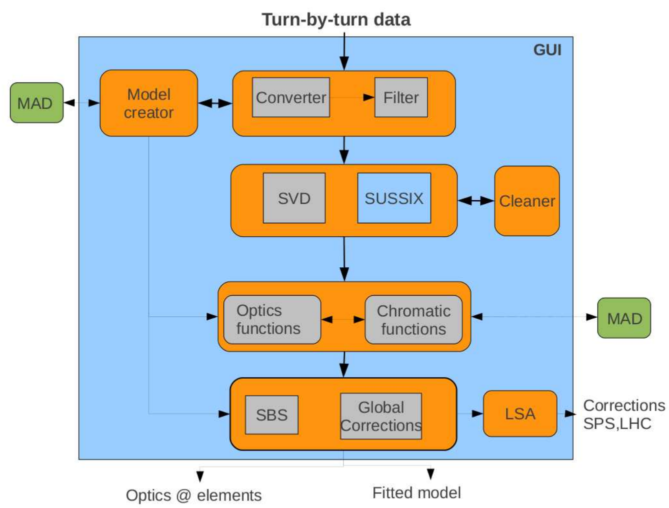

Figure 9.1: Flow diagram showing the steps done in the Graphical User Interface during normal operations.

Explanation of the different colors in the flow diagram:

- The orange blocks are the different panels implemented in the GUI. These panels will be explained in section 9.2.
- The gray blocks are external programs that are developed in python.
- The blue blocks is an external program that is developed in C and Fortran.
- The green blocks represents external programs that are developed in MAD.

Figure 9.2 shows the data structure used for storing the data generated by the different algorithms. This data structure is created automatically by the beta-beat application.

The names in italic/bold are the names that are created, the others are replaced by the specific file names. The 'date', 'name' and 'time' directories are automatically created by the GUI. The 'accel/beam' and 'model name' are created after manual selection and input from the user. The blue boxes are directories and the orange boxes are the files inside the specific directory. The different files that are generated:

- *.sdds; output after converting and filtering the turn-by-turn data.
- *.lin*; output files of sussix. Two files, one per plane, containing the amplitude and phase of the main and secondary betatron tune lines.
- *.svd*; output files for the singular value decomposition.
- *.bad; output of the filtering. In this file the faulty BPMs are listed.
- *.out; output that contains optics functions. The list of output files:
  - getCO*; files containing the closed orbit, one file per plane.
  - getIP*; files containing the β^*, phase advance.
  - getampbeta*; files containing the beta from amplitude, one file per plane (in case of AC-dipole free and driven data is computed).

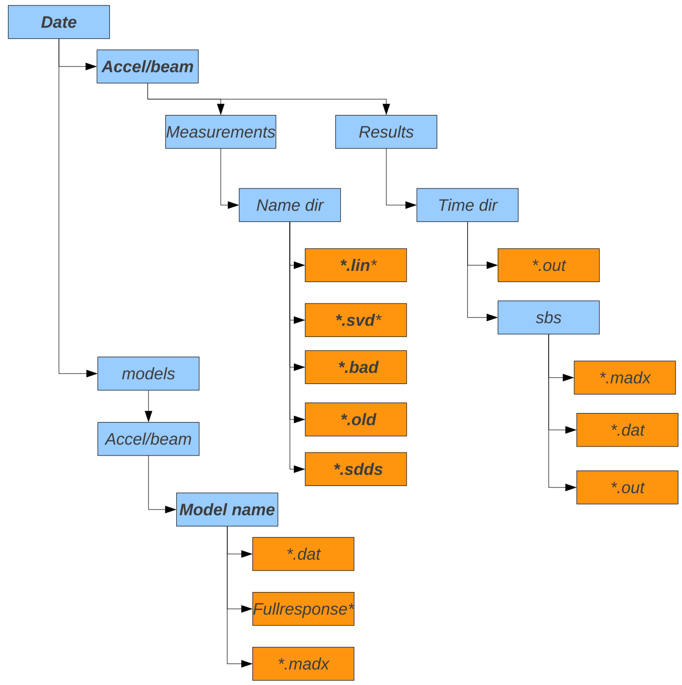

Figure 9.2: Flow diagram showing the data structure

  – getbeta*; files containing the beta from phase, one file per plane (in case of AC-dipole free and driven data is computed).
  – getchi*; files containing the χ terms.
  – getcouple*; files containing the coupling (in case of AC-dipole free and driven data is computed).
  – getsex/oct*; files containing the resonance driving terms.
  – getphase*; files containing the phase-advances, one file per plane (in case of AC-dipole free and driven data is computed).
  – getphasetot*; files containing the total phase-advances, one file per plane (in case of AC-dipole free and driven data is computed).
  – getkick*; files containing the kick amplitudes.
  – getD*; files containing the dispersion, one per plane (if off-momentum data is acquired).
  – getNDx*; files containing the normalized horizontal dispersion (if off-momentum data is acquired).

- *.madx; madx scripts for model and full response generation.
- *.dat; output of the madx scripts containing optics functions.
- Fullresonse*; fullresponse for beta, phase and horizontal dispersion and fullresponse.couple for coupling and vertical dispersion. The fullresponses are a response matrix calculated using the ideal optics functions used to calculate the corrections.

The *.lin*, *.svd*, *.bad, *.out, *.dat are in the so called Table File System (TFS) format. The idea behind them is that of a Self-Describing Data Set, invented for data in the LEP Control System in the late 1980s [138]. An example of a TFS format:

@ DESCRIPTION %f VALUE
** NAME1 ... NAMEN*
$ %s ... %le

VALUE1 ... VALUEN

Further explanation of the data format:

- If '@' is the first character of a line in the data, a single variable with value can be added (%f can be either %s, string or %le, double).
- If '*' is the first character of a line in the data, the column names can be found after.
- If '$' is the first character of a line in the data, the format of the column names can be found after (%s, string; %le, double).
- The lines with no symbol as the first character is the data corresponding to the column.

Figure 9.3 shows the organization structure for were the main programs and model files are stored. For experiments that are conducted at CERN, this directory is located at /afs/cern.ch/eng/sl/lintrack/Beta-Beat.src/. This directory contains the main codes. The color code has the following meaning:

- Blue squares represent the directories which contain the different codes or sub-directories.
- Orange squares represent the programs or files in the directory that are used in the GUI.
- Green squares represent directories that are chosen by the user when the GUI is started. The green squares contain default models for different accelerators.

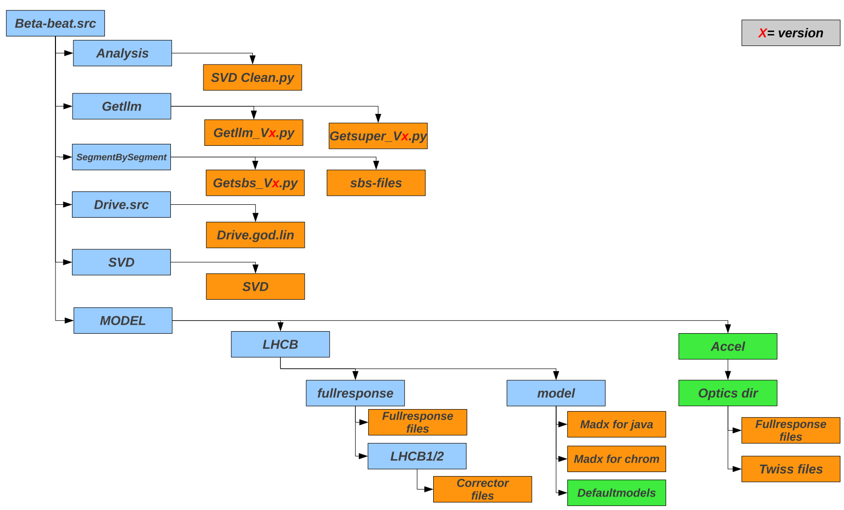

Figure 9.3: Flow diagram showing organization structure for were the main programs and model files are stored. The blue squares represent the directories which contain the different codes or sub-directories, orange represent the programs or files in the directory that are used in the GUI. Green squares represent directories that are chosen by the user when the GUI is started.

The analysis directory contains SVD clean, the algorithm which is responsible for removing noise and bad BPMs. In the Getllm directory the algorithms are stored which calculate the optics functions. Getllm calculates the optics functions at the BPM, Segment-by-Segment calculates the optical functions using a propagated model in a segment or at machine elements. The sbs-files contain the files for generating the madx and gnuplot scripts. Getsuper is the program that with the help of Getllm the chromatic functions calculate.

The Drive.src contains the drive.god.lin code which uses SUSSIX the calculate main betatron and higher order frequency, phase and amplitudes at the BPMs. The SVD directory has an alternative code which could be used the calculated the phase and amplitudes of the main signal. The model directory contains several sub-directories depending on the usage and accelerator. For accelerators other than the LHC the user will be redirected to the optics dir of choice containing the model Twiss files and the fullresponses for the correction.

For the LHC the process of generating a model and fullresponse was more automated. The user can create his own model in the GUI, which will use the madx scripts and full response script which are stored in the directory model.

9.2 Detailed description

In the next paragraphs the mains panels and functions will be shown and discussed.

BPMpanel A print screen of the BPMpanel in BPM viewer mode is shown in figure 9.4. The turn-by-turn data is acquired using the multiturn application [31] and the file is imported by the user. The data format is automatically recognized and the corresponding converter is used to convert the data into the internal data format. An example of data the format:

Plane BPM S Turn1 Turn2 Turn3.... Turn N.

Further explanation of the data format:

- Plane (fist column): 0 for horizontal plane and 1 for vertical plane.
- BPM (second column): Name of the BPM.
- S (third column): Position of the BPM in the accelerator.
- Turn1 ... TurnN (fourth until Nth column): Position of the beam in the specified plane for turn N.

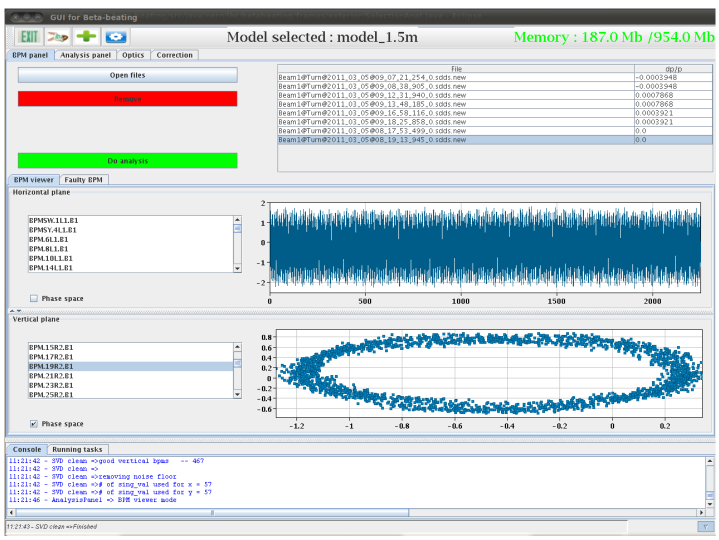

Figure 9.4: First window of the BPM panel showing the turn-by-turn data.

The table in the top right corner of figure 9.4 shows the filenames and the δp values (which are added manually) of the datafiles imported. The lower panel of figure 9.4 can either display the beam position versus turn, or the phase-space. This is done by taking the data from two BPMs that are separated by $\pi/2$.

The BPMpanel can also be used in faulty BPM mode, shown in figure 9.5. This allows the user to identify the faulty BPMs (which is read from *.bad file) according to the longitudinal position.

AnalysisPanel In the analysis panel the data that was calculated using SUSSIX or an SVD is visualized. Figure 9.6 shows the selection frame. This frame is used to specify some inputs for SUSSIX and SVD. In the selection frame the following input parameters should be specified/selected:

- The algorithm to be used, SUSSIX or SVD.
- Option for parallel computing. This option allows the data to be computed in parallel for SUSSIX.
- An initial guess for the horizontal and vertical tunes.

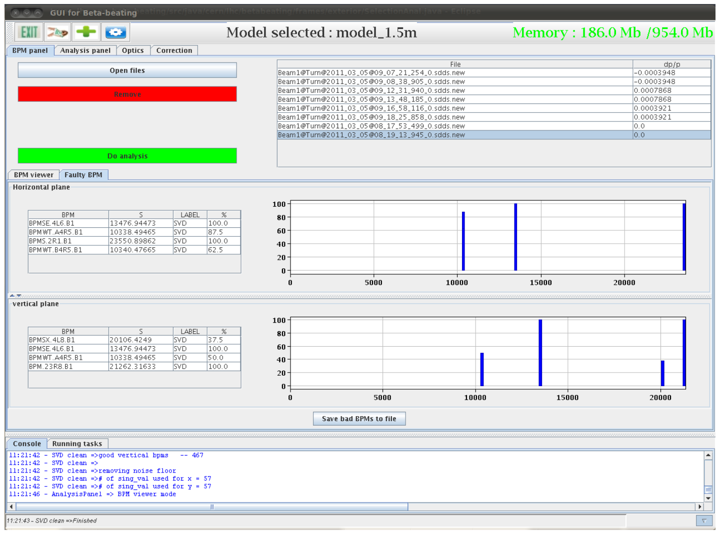

Figure 9.5: Second window of the BPM panel showing the bad BPMs which were filtered.

- The range of BPMs to be analyzed.
- Specification of the turn number where the kick starts. This can be computed automatically. In case of using the tune/aperture kicker it is important to start analyzing the data after the kick occurred.
- Window a1, a2, b1 and b2, for the computation of the noise. The two windows $(a_1, a_2; b_1, b_2)$ specify a tune range where the data is analyzed to determine the noise.
- Number of turns to be analyzed.

An output of the SUSSIX algorithm for several files is shown in figure 9.7. The files shown are for different δp settings. A manual cleaner is available that can be used to remove the bad points. This is done by placing a window around the tune versus the longitudinal position. The data points outside the window will be removed.

OpticsPanel The optics panel displays the optics functions calculated at the BPMs and allows the user to calculate the optic functions at the elements. Figure 9.8 shows an output of the optics functions at the BPMs for the phase. Different sub panels are available to display the calculated optics functions.

With the current algorithm it is possible to calculate:

- Linear optics:
  - phase advance
  - beta from phase
  - beta from amplitude
  - linear betatron coupling, output as the difference and sum resonance.
- off-momentum optics:
  - horizontal and vertical dispersion
  - normalized horizontal dispersion
  - chromatic functions
  - tune vs dpp
- higher order optics:
  - f3000, f2100 resonance driving term. Related to the sextupolar term.
  - tune vs kick

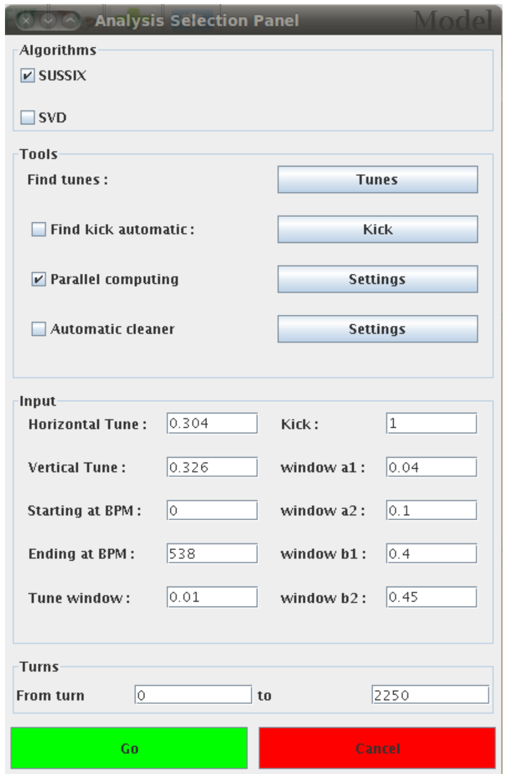

Figure 9.6: The selection analysis panel which allows the user to specify input parameters for SVD and SUSSIX.

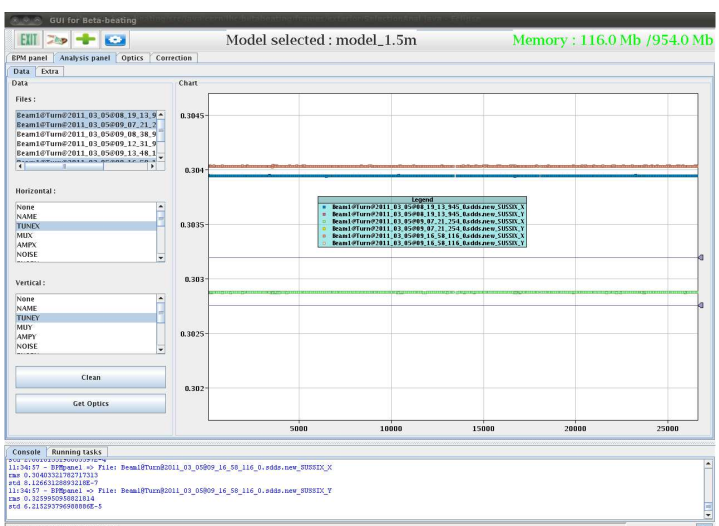

Figure 9.7: AnalysisPanel showing the horizontal and vertical tunes for several files.

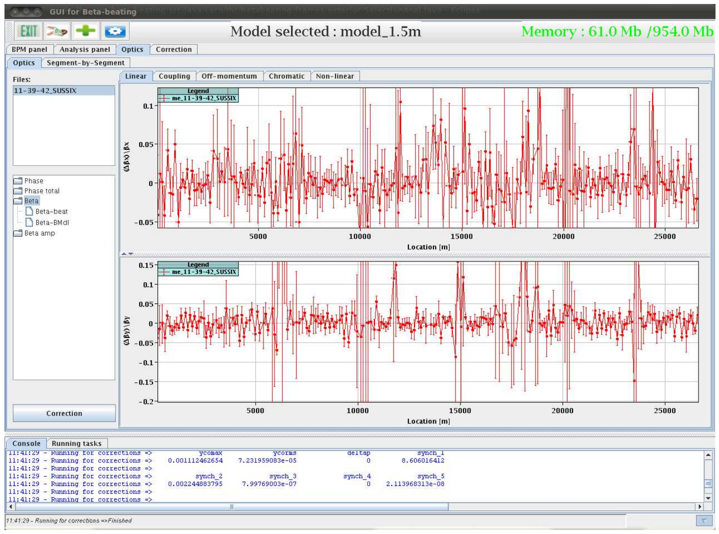

Figure 9.8: OpticsPanel showing the first window with the measured optics functions.

For the linear optics the results are shown in the window. The second window contains the tables for the segment-by-segment technique, element mode. In this panel either, the optics functions at elements, such as the wire scanner can be calculated, or the accelerator can be divided into segments for the calculation of local errors. The outcome of some beam instrumentation depends on the optics function, such as the β. In the cases the calculated β is used to calibrate the instruments.

CorrectionPanel The correction panel is the main panel used to calculate corrections for the beta-beat, coupling and horizontal and vertical dispersion.

For the correction of the linear optics different algorithms are available:

- Local correction technique for most linear optics.
- Correction for 1 beam for phase, beta and horizontal dispersion.
- Iterative correction, 2 beams for phase, beta and horizontal dispersion.
- Correction for 1 beam for coupling and vertical dispersion.

The correctors are grouped into different lists. The selection of the list depends on the correction. The different categories of the lists are:

- The common correctors in the IPs.
- The correctors in the insertion region, except the common correctors.
- Trim correctors around the ring, except the ones in the common region.

9.3 LSA

The LHC Software Architecture (LSA) [139] project provides homogeneous application software to operate the Super Proton Synchrotron (SPS) accelerator, its transfer lines, and the Large Hadron Collider (LHC). The system is entirely written in Java and it is using the Spring framework, an open-source lightweight container for Java platform, taking advantage of dependency injection (DI), aspect oriented programming (AOP) and provided services like transactions or remote access. Some of the functionalities have been implemented in the beta-beat applications. The main functionality that has been implemented is the generation of the knobs. With the knobbuilder functionality it is possible to generate a knob, a knob is list containing the correctors and its delta values, for different optics.

9.4 Time consumption

During the course of the commissioning of the LHC, several important improvements were made in order to reduce the time between measurement and analysis. SUSSIX has been evolving during the course of the commissioning. Figure 9.9 shows a plot of the evolution of the computing time of SUSSIX. In this example the data was analyzed for 538 dual plane BPMs for 2000 turns.

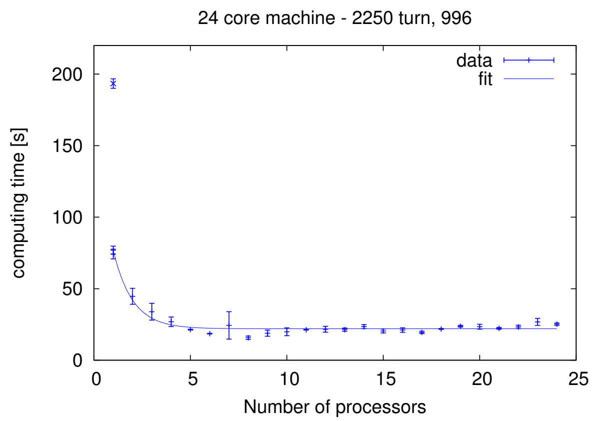

Figure 9.9: Flow diagram showing the data structure

As observed from figure 9.9 major step in the computing time has been achieved. The following changes were implemented:

- First improvement: usage of a different compiler [142].
- Second improvement: parallelization of SUSSIX [140]. This has been achieved, using the OpenMP API [141] to parallelize with respect to the independent analysis of BPMs.

9.5 Improvements

Some improvement of the GUI is foreseen for the future. First of all, the graphical design of the panels could be improved. Also, the correction algorithm should be improved such that it allows the placement of cuts separately on the horizontal and vertical plane. The correction panel should be updated such that it allows to select independently the variables, for the moment their are divided in lists. To save time for the computation of the full responses it would be recommended to compute the full responses in parallel.

Appendix A

Equations of motion

The most commonly used coordinate system in accelerator physics is the Frenet-Serret coordinate system. This system is convenient as it follows the particles along the reference path. Figure A.1 shows the trajectories of particles in deflecting systems.

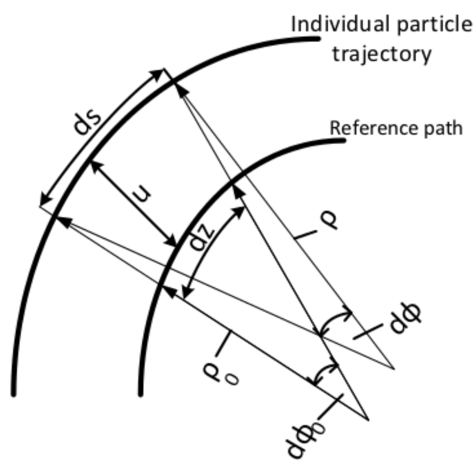

Figure A.1: The trajectories of particles in deflecting systems.

The deflection angle of the ideal path is $d\phi_0 = k_0 dz$, where k_0 ($\frac{1}{\rho_0}$) is the curvature of the ideal path. The deflection angle for an arbitrary trajectory is $d\phi = kds$. The ideal curvature k_0 is evaluated along the reference trajectory (u=0) for a particle with the ideal momentum. In linear approximation the path length element with respect to the coordinates for an arbitrary trajectory is:

$$ds = (1 + k_0 u)dz + O(2). \tag{A.1}$$

Since u is the deviation of a particle from the ideal path, the equation of motion can be written as:

$$u'' = -(1 + k_0 u)k + k_0. \tag{A.2}$$

The equation of motion for charged particles in electromagnetic fields can be derived from equation (A.2) and (1.1). The horizontal (x) and the vertical (y) deflection can be expressed using the general field expansion (appendix B) as follows:

$$\begin{aligned} \kappa_x &= \frac{e}{p}B_y = \frac{e}{p}[k_{0x} + kx + \frac{1}{2}mx^2 + O(3)], \\ \kappa_y &= \frac{e}{p}B_x = \frac{e}{p}[k_{0y} - ky - mxy - O(3)], \end{aligned} \tag{A.3}$$

k_{0z}, k, m are the strength parameters (m^{-n+1}) independent of the energy. No skew components were considered for the moment. The potentials and magnetic fields until the 2^{th} order are given, the sextupoles. In appendix B the magnetic field expansion is explained in more detail. As a real particle beam is never monochromatic, effects due to small momentum are included. The particle momentum close to the ideal momentum can be expanded to:

$$\frac{1}{p} = \frac{1}{p_0(1+\delta)} \approx \frac{1}{p_0}(1-\delta+...), \tag{A.4}$$

$$\begin{aligned} x'' + (k+k_{0x}^2)x = \quad & k_{0x}(\delta-\delta^2) + (k+k_{0x})x\delta, \\ & -\tfrac{1}{2}mx^2 - kk_0x^2 + O(3) \end{aligned} \tag{A.5}$$

$$\begin{aligned} y'' - (k-k_{0y}^2)y = \quad & k_{0y}\delta - (k-k_{0y}^2)y\delta. \\ & +mxy + k_{0y}ky^2 + O(3)) \end{aligned} \tag{A.6}$$

For the horizontal plane the $(k+k_{0x}^2)x$ term describes the focusing effects from quadrupoles and a pure geometrical focusing from bending in a sector magnet. A dispersive effect arises from $k_{0x}(\delta-\delta^2)$ which reflects the varying deflection angle for particles which do not have the ideal design energy. Focusing is also energy dependent and the term $(k+k_{0x})x\delta$ gives rise to chromatic aberrations describing focusing errors due to energy deviation. The term $-kk_0x^2$ must only be included if focusing and bending are present in the same magnet, for example in a synchrotron magnet. The last term $-\frac{1}{2}mx^2$ is the sextupole term, which introduces both chromatic and geometric aberration. The chromatic aberration from sextupoles can be used to cancel some of the chromatic aberration from quadrupoles, but in doing so a quadratic effect which leads to geometric aberrations is introduced.

Appendix B

Potentials and magnetic fields

The magnetic potential in Cartesian coordinates is written as:

$$-\frac{e}{p}V_n(x,y) = \sum_{n=0}^{\inf} \frac{1}{n+1!} k_n (x+iy)^{n+1}. \tag{B.1}$$

The magnetic fields of a multipole of order n is written by:

$$\begin{aligned} B_x &= -\frac{\partial V_n}{\partial x}, \\ B_y &= -\frac{\partial V_n}{\partial y}. \end{aligned} \tag{B.2}$$

Table B.1 shows the magnetic multipole potentials up to the 2^{th} order, the sextupole. k_0, k, m are

Name	Order	Magnetic potential (-$\frac{e}{p}V$)
Dipole	0	$-k_0 x + k_0 y$
Quadrupole	1	$-\frac{1}{2}\bar{k}(x^2 - y^2) + kxy$
Sextupole	2	$-\frac{1}{6}\bar{m}(x^3 - 3xy^2) + \frac{1}{6}m(3x^2y - y^3)$

Table B.1: The magnetic multipole potentials up to the 2^{th} order.

the strength parameters (m^{-n+1}) independent of the energy and the parameters with the hat above are their equivalent skew parameters.

Table B.3 shows the upright magnetic fields up to the 2^{th} order.

Name	Order	Horizontal magnetic field ($\frac{e}{p}B_x$)	Vertical magnetic field ($\frac{e}{p}B_y$)
Dipole	0	0	k_0
Quadrupole	1	gy	g x
Sextupole	2	mxy	$\frac{1}{2}m(x^2 - y^2)$

Table B.2: Upright magnetic fields up to the 2^{th} order.

Table B.3 shows the skew magnetic fields up to the 2^{th} order. In the last column the rotation angle with respect to the upright magnetic field is given. The angle is determined by $(90°/n)$, with n being the order.

Name	Order	Horizontal magnetic field ($\frac{e}{p}B_x$	Vertical magnetic field ($\frac{e}{p}B_y$)	Tilt (°)
Dipole	0	-k_{0s}	0	90
Quadrupole	1	-$\bar{k}$ x	$\bar{k}$ y	45
Sextupole	2	-$\frac{1}{2}\bar{m}(x^2 - y^2)$	$\bar{m}xy$	30

Table B.3: Skew magnetic fields up to the 2^{th} order.

Appendix C

Derivation of resonance driving terms

In case the motion is regular it can be decomposed into a series of spectral lines [143] the frequencies of which are the fundamental tunes υ_x and υ_y and their linear combinations, e.g for the linearly normalized horizontal plane after N turns:

$$\hat{z}(N) - i\hat{p}_x = \sum_{j=1}^{inf} a_j e^{i[2\pi(m_j\upsilon_x + n_j\upsilon_y)N + \phi_j]} \qquad m_j, n_j \in \mathbf{Z}. \tag{C.1}$$

Where a_j and ϕ_j are the amplitude and phase of the corresponding spectral line.

C.1 Generating function

The idea of using a generating function is to reduce the initial map to a simpler map. In this case the Cartesian coordinates are transformed to action-angle variables.

In the lowest order, the linear case, the action angle variables $(J_x, \phi_x, J_y, \phi_y)$ are related to the Courant-Snyder variables (section 1.2.1) $(\hat{x}, \hat{p}_x, \hat{y}, \hat{p}_y)$ by the formula:

$$\begin{aligned} \hat{z} &= \sqrt{2J_z}\cos(\phi_z + \phi_{zo}), \\ \hat{p_z} &= -\sqrt{2J_z}\sin(\phi_z + \phi_{zo}), \end{aligned} \tag{C.2}$$

where ϕ_{z0} is the initial phase. It is convenient to express the linearly normalized variables in the so called resonance basis $\mathbf{h}$=$(h_x^+, h_x^-, h_y^+, h_y^-)$ defined by the relations:

$$h_z^\pm = \hat{z} \pm i\hat{p}_z = \sqrt{2J_z}e^{\mp i(\phi_z + \phi_{z0})}. \tag{C.3}$$

The transformation to the new set of canonical coordinates $\zeta = (\zeta_x^+, \zeta_x^-, \zeta_y^+, \zeta_y^-)$ which brings the map into the Normal form is expressed as a lie series:

$$\zeta = e^{-:F_r:}\mathbf{h}, \tag{C.4}$$

where

$$\zeta_z^\pm = \sqrt{2I_z}e^{\mp i(\phi_z + \phi_{z0})}. \tag{C.5}$$

And $(I_x, \phi_x, I_y, \phi y)$ are the nonlinear action angle variables. In the resonance basis , F_r can be written as a sum pf homogeneous polynomials variables ζ as

$$F_r = \sum_{jklm} f_{jklm}\zeta_x^{+j}, \zeta_x^{-k}, \zeta_y^{+l}, \zeta_y^{-m}. \tag{C.6}$$

Introducing $\zeta_z^\pm$:

$$F_r = \sum_{jklm} (2I_x)^{\frac{j+k}{2}} (2I_y)^{\frac{l+m}{2}} e^{-i[(j-k)(\phi_x + \phi_{x0}) + (l-m)(\phi_y + \phi_{y0})]}. \tag{C.7}$$

The transformation from the new action-angle variables to the linearly normalized variables is given by:

$$\mathbf{h} = e^{:F_r:}\zeta = \zeta + [F_r, \zeta] + [F_r, [F_r, [F_r, \zeta]]] + ..., \tag{C.8}$$

where $[F_r, \zeta]$ denotes the Poisson bracket of F_r and ζ. To the first order transformation to the h_x^- reads:

$$h_x^- \approx \zeta_x^- + [F_r, \zeta_x^-] = \zeta_x^- - 2i \sum_{jklm} j f_{jklm} \zeta_x^{+j-1}, \zeta_x^{-k}, \zeta_y^{+l}, \zeta_y^{-m}. \tag{C.9}$$

The evolution of the variable in Normal Form after N turns is given by:

$$\zeta_x^-(N) = \sqrt{2I_x} e^{2\pi \upsilon_x N + \phi_{x0}}. \tag{C.10}$$

The evolution of the linearly normalized horizontal variable:

$$\begin{aligned} h_x^-(N) = & \sqrt{2I_x} e^{i(2\pi \upsilon_x N + \phi_{x0})} \\ & -2i \sum_{jklm} j f_{jklm} (2I_x)^{\frac{j+k-1}{2}} (2I_y)^{\frac{l+m}{2}} e^{i[(1-j+k)(2\pi\upsilon_x N + \phi_{x0}) + (m-l)(2\pi \upsilon_y N + \phi_{y0})]}, \end{aligned} \tag{C.11}$$

and the vertical horizontal variable:

$$\begin{aligned} h_y^-(N) = & \sqrt{2I_y} e^{i(2\pi \upsilon_y N + \phi_{y0})} \\ & -2i \sum_{jklm} l f_{jklm} (2I_x)^{\frac{j+k}{2}} (2I_y)^{\frac{l+m-1}{2}} e^{i[(k-j)(2\pi\upsilon_x N + \phi_{x0}) + (1-l+m)(2\pi \upsilon_y N + \phi_{y0})]}. \end{aligned} \tag{C.12}$$

Bibliography

[1] H. Wiedemann, “Particle accelerator physics”, Birkhauser,2003.

[2] S. Y. Lee, “Accelerator physics”, 2^{nd} edition, World Scientific Publishing, 2004.

[3] A. Franchi, E. Métral, R. Tomás, “Emittance sharing and exchange driven by linear betatron coupling in circular accelerators”, Phys. Rev. Spec. Top. Accel. Beams 10 (2007) 064003.

[4] K. Schindl and P. van der Stok, CERN/PS/BR 76-19, 1976.

[5] G. Guignard, CERN ISR-BOM/77-43, 1977.

[6] D. Edwards and L. C. Teng, IEEE Trans. Nucl. Sci. 20, 885 (1973).

[7] E. D. Courant and H. S. Snyder, “Theory of the alternating gradient synchrotron”, Annals of Physics, 3:1-48, 1958.

[8] D. Sagan and D. Rubin, “Linear analysis of coupled lattices”, Wilson Laboratory, Cornell University, Ithaca, New York 14853.

[9] D. A. Edwards and L. C. Teng, “Parametrization of linear coupled motion in periodic systems”. IEEE Trans. Nucl. Sci. 20 (1973) 885.

[10] R. Calaga, R. Tomás and A. Franchi, “Betatron coupling: Merging Hamiltonian and matrix approaches”, Phys. Rev. ST Accel. Beams 8, 034001 (2005) [10 pages].

[11] F. Willeke and G. Ripken, “Methods of beam optics”, Desy 88-114, 1988

[12] V. A. Lebedev and S. A. Bogacz, “betatron motion with coupling of horizontal and vertical degrees of freedom”, Thomas Jefferson National Accelerator Facility 2010.

[13] Y. Luo, P. Cameron, A. Della Penna, J. Laster, A. Marusic, F. Pilat, T. Roser, and D. Trbojevic , “Fast and robust global decoupling with angle modulation”, PRSTAB 8, 074002 (2005).

[14] R. Tomás, “Direct Measurement of Resonance Driving Terms in the Super Proton Synchrotron (SPS) of CERN using Beam Position Monitors”, PhD thesis, University of Valencia ,2003.

[15] A. Franchi, R. Tomás, G. Vanbavinckhove, “Computation of the Coupling Resonance Driving term f_{1001} and the coupling coefficient C from turn-by-turn single-BPM”, to be published.

[16] B. Dehning, G. Ferioli, W. Friesenbichler, E. Gschwendtner and J. Koopman, “LHC Beam Loss Monitor System Design”, Beam Instrumentation Workshop 2002.

[17] A. S. Fisher, A. Goldblatt, T. Lefévre, “The LHC Synchrotron-Light Monitors”, Beam Diagnostics and Instrumentation for Particle Accelerators, Basel, Switzerland, 25 - 27 May 2009.

[18] M. Gasior, A. Boccardi, R. Jones, R. J. Steinhagen, “An overview of the LHC transverse diagnostics systems”, 13th Beam Instrumentation Workshop, Tahoe City, CA, USA, 04 - 08 May 2008, pp.409-414.

[19] O. R. Jones, “performance of and first experiences with the LHC beam diagnostics”, Proceedings of DIPAC09, Basel, Switzerland MOOA02.

[20] R.E Meller, A. W. Chao, J. M. Peterson, S. G. Peggs, and M. Furman, “Decoherence of kicked beams”, SSC-N-360, 1987.

[21] J. Serrano and M. Cattin, “The LHC AC Dipole system: an introduction”, CERN BE Note 2010-14-CO, 2010.

[22] S. Peggs and C. Tang, Brookhaven National Laboratory Report No. RHIC/AP/159, 1998.

[23] R. Tomás, “Normal form of particle motion under the influence of an ac dipole”, PRSTAB 5, 054001 (2002).

[24] S. D. Fartoukh, “Determination of betatron tunes, Twiss parameters and sum and difference coupling coefficients with an AC dipole”, CERN-SL-2002-059-AP. - 2002. - 34 p.

[25] M. Bai,“RHIC vertical AC-DIPOLE commissioning”, Paris, France, June 2-7, 2002.

[26] R. Miyamoto, “Diagnostics of the Fermilab Tevatron using an AC-Dipole”, PhD thesis, 2008.

[27] S. Fartoukh, “Determination of betatron tunes, Twiss parameters and sum and difference coupling coefficients with an AC dipole”, CERN-SL-2002-059-AP. - 2002. - 34 p.

[28] R. Myamoto, R. Calaga, R. Tomás and G. Vanbavinckhove, “Accuracy of the LHC optics measurement based on AC-dipoles”. IPAC 2011.

[29] R. Myamoto, R. Calaga, R. Tomás and G. Vanbavinckhove, “Measurement of coupling resonance driving terms in the LHC with AC Dipoles”. IPAC 2011.

[30] R. Bartolini and F. Schmidt, “A Computer Code for Frequency Analysis of Non-Linear Betatron Motion” SL-Note-98-017-AP.

[31] V. Kain, Responsible for the multi-turn aqcuisition code in the SPS.

[32] R. Calaga and R. Tomás, “Statistical analysis of RHIC beam position monitors performance”, PHYSICAL REVIEW SPECIAL TOPICS - ACCELERATORS AND BEAMS, VOLUME 7, 042801 (2004).

[33] R. Calaga, “Linear Beam Dynamics and Ampere Class Superconducting RF Cavities at RHIC”, PhD thesis, Stony Brook University, 2006.

[34] A. Petrenko, “Model-Independent Analysis of Turn-by-Turn BPM Measurements in Storage Rings”, OMCM workshop 2010.

[35] P. Castro, “Luminosity and beta function measurement at the electron-positron collider ring LEP”, PhD thesis, University of Valencia ,1996.

[36] A. Lagner, R. Calaga, R. Myamoto, R. Tomás and G. Vanbavinckhove, “Optics measurement in the LHC close to the half integer tune resonance”, CERN-ATS-Note-2011-095 TECH

[37] R . Calaga, A. Langner, E . Maclean, T. Persson, M. Pojer, P. Skowronski, R. Steinhagen, R. Tomas, G. Vanbavinckhove, S. White, “Optics measurement and correction close to the half integer resonance”, CERN-ATS-Note-2011-124 MD.

[38] R. Calaga, R. Tomás, F. Zimmermann, “BPM calibration independent LHC optics correction”, PAC07, Albuquerque, New Mexico, USA.

[39] B. W. Montague, “Linear Optics for Improved Chromaticity Correction”, LEP Note 165, CERN, 1979.

[40] M. Aiba, R. Calaga, S. Fartoukh, A. Franchi, M. Giovannozzi, V. Kain, M. Lamont, A. Morita, R. Tomás, G. Vanbavinckhove, J. Wenninger, and F. Zimmermann, “First β-beating measurement and optics analysis for the CERN Large Hadron Collider”, PRSTAB 12, 2009.

[41] R. Tomas, M. Aiba, C. Alabau, R. Calaga, J. Cardona, O. Dominguez, S. Fartoukh, M. Giovannozzi, V. Kain, M. Lamont, E. Mcintosh, R. Miyamoto, G. Mueller, S. Redaelli, F. Schmidt, G. Vanbavinckhove, J. Wenninger, S. White, F. Zimmermann, "LHC optics model, measurements and corrections", Evian 2010 Workshop on LHC Commissioning, Evian-les-Bains, France, 19 - 20 Jan 2010, pp.29-36

[42] R. Tomás, O. S. Brüning, R. Calaga, S. Fartoukh, A. Franchi, M. Giovannozzi, Y. Papaphilippou, S. Peggs, F. Zimmermann, "Procedures and accuracy estimates for beta-beat correction in the LHC", 10th European Particle Accelerator Conference, Edinburgh, UK, 26 - 30 Jun 2006, pp.2023

[43] R. Tomas, O. S. Brüning, M. Aiba, R. Calaga, M. Giovannozzi, P. Hagen, M. Lamont, R. Miyamoto, F. Schmidt, G. Vanbavinckhove, "CERN Large Hadron Collider optics model, measurements and corrections", PRSTAB 13, 121004 (2010).

[44] A. Morita, H. Koiso, Y. Ohnishi and K. Oide, "Measurement and correction of on- and off-momentum beta functions at KEKB", Phys. Rev. ST Accel. Beams **10**, 072801 (2007).

[45] K. Fuchsberger, "Novel Concepts for Optimization of the CERN Large Hadron Collider Injection Lines.", CERN-THESIS-2011-075.

[46] D. Einfeld, "Optics codes", OMCM workshop 2010.

[47] MAD-X Home Page, http://mad.web.cern.ch/mad/.

[48] E. Forest, F. Schmidt, E. McIntosh, "Introduction to the Polymorphic Tracking Code", CERNSL2002044 (AP).

[49] C. Alabau Pons, E. Maclean, F. Schmidt and R. Tomás, "β-beating in the effective model of the lhc using PTC", Proceedings of IPAC2011, San Sebastin, Spain.

[50] http://user.web.cern.ch/public/en/Research/PS-en.html.

[51] "The 300 GeV Programme",CERN-1050-E, Geneva, CERN, 1972.

[52] C. Boccard, "Performance of the new SPS beam position orbit system (MOPOS)",CERN-SL-99-048-BI,1999.

[53] E. Shaposhnikova, "Lesson from SPS studies in 2010", Proceedings of Chamonix 2011 workshop on LHC performance, 2011.

[54] B. Salvant, "Transverse mode-coupling instability in the CERN SPS", Proceedings of EPAC08, Genoa, Italy.

[55] H.G. Hereward, "Landau damping", CAS - CERN Accelerator School : Accelerator Physics, Oxford, UK, 16 - 27 Sep 1985, pp.255-263

[56] G. Arduini, "Test of a low gamma transition optics", SL-Note-98-001-MD,1998

[57] H. Bartosik, G. Arduini, Y. Papaphilippou, "Optics considerations for lowering transition energy in the SPS", 2nd International Particle Accelerator Conference, San Sebastian, Spain, 4 to 9 September, 2011, MOPS012.

[58] Y. Papaphilippou, "Possible reduction of transition energy in the SPS", CERN-NOTE, to be published.

[59] G. Brianti, "The large hadron collider (LHC) in the LEP tunnel", LHC Working Group, Part. Accel. 26 (1990) pp.141-150.

[60] "LHC Design Report Volume I: The LHC Main Ring", chapter 4: Optics and Single Particle Dynamics, CERN-2004-003-V-1, 2004.

[61] A.P. Verweij, "Consolidation of the 13 kA Interconnects in the LHC for Operation at 7 TeV", IEEE Trans. Appl. Supercond. 21 (2011) 2376-2379.

[62] ATLAS collaboration, “ATLAS Detector and physics performance”, ATLAS TDR 14, CERN-LHCC 99-14, 1999.

[63] CMS collaboration, “CMS Physics Technical Design Report Volume I: Detector Performance and Software”, CERN/LHCC 2006-001, CMS TDR 8.1.

[64] O. Bruning, “Optics Solutions in IR1 and IR5 for Ring-1 and Ring-2 of the LHC Version 6.0”, 5LHC Project Note 187, April 1999.

[65] ALICE collaboration, “ALICE Technical Design Report”, CERN /LHCC 2001-021, 2001.

[66] O. Brunfing, “Optics Solutions in IR2 for Ring-1 and Ring-2 of the LHC Version 6.0”, LHC Project Note 188, April-1999.

[67] P. R. Sala, S. Praire, “Conceptual Optimisation of the TDI and TCDD Protections for LHC Injection Lines”, AB-Note-2003-059-ATB, 14 Aug 2003.

[68] “LHC Design Report Volume I: The LHC Main Ring”, chapter 13: Beam instrumentation, CERN-2004-003-V-1, 2004.

[69] “LHC Design Report Volume I: The LHC Main Ring”, chapter 17: Beam dump system, CERN-2004-003-V-1, 2004.

[70] LHCB collaboration, “LHCB experiment A Large Hadron Collider Beauty Experiment for Precision Measurements of CP-Violation and Rare Decays”, CERN/LHCC 98-4, 1998.

[71] O. Bruning, “Optics Solutions in IR8 for Ring-1 and Ring-2 of the LHC Version 6.0”, LHC Project Note 193, June-1998.

[72] S. Fartoukh, O. Bruning, “Field Quality Specification for the LHC Main Dipole Magnets”, LHC Project Report 501, CERN.

[73] “LHC design report volume 6: The RF systems and beam feedback”, CERN-2004-003-V-1, 2004.

[74] “Coupling and Vertical Dispersion Correction in the SPS”, M. Aiba, R. Calaga, A. Franchi, R. Tomás, G. Vanbavinckhove, 1st International Particle Accelerator Conference, Kyoto, Japan, 23 - 28 May 2010, pp.THPE024.

[75] G. Vanbavinckhove, M. Aiba, R. Calaga, A. Franchi, R. Tomás, “Coupling and vertical dispersion correction studies for the LHC using skew quadrupoles and vertical orbit bumps”, 1st International Particle Accelerator Conference, Kyoto, Japan, 23 - 28 May 2010, pp.THPE025

[76] O. Brüning, “Linear coupling compensation for the LHC version 6.1”, CERN, Geneva, Switzerland.

[77] T. Taylor, “Incident at the CERN LHC : The event, the repair and lessons to drawn”, TEION KOGAKU 45 (2010) 344-351.

[78] J. Wenninger,“YASP: Yet Another Steering Program”.

[79] R. Tomás, M. Aiba, C. Alabau, O. Brüning, R. Calaga, M. Giovannozzi, V. Kain, P. Hagen, M. Lamont, R. Miyamoto, F. Schmidt, M. Strzelczyk, G. Vanbavinckhove, “The LHC optics in practice”, 2nd Evian 2010 Workshop on LHC Beam Operation, Evian-les-bains, France, 7 - 9 Dec 2010, pp.211-223.

[80] B. Goddard and J. Uythoven, private communication.

[81] P. Hagen, “The correction of the MQW transfer functions based upon extra magnetic measurements”, to be published.

[82] P. Hagen, M. Giovannozzi, J. P. Koutchouk, T. Risselada, S. Sanfilippo, E. Todesco, E. Wildner. “WISE: An Adaptative Simulation of the LHC Optics”, in Proceedings of Tenth European Particle Accelerator Conference, ed. by J. Poole and C. Petit-Jean-Genaz, Institute of Physics UK London, p. 2248 (2006).

[83] P. Hagen, M. Giovannozzi, J. P. Koutchouk, T. Risselada, F Schmidt, E. Todesco, E. Wildner, “WISE : A Simulation of the LHC Optics including Magnet Geometrical Data”, 11th European Particle Accelerator Conference, Genoa, Italy, 23 - 27 Jun 2008, pp.TUPP091 in Proceedings of Eleventh European Particle Accelerator Conference, ed. by C. Petit-Jean-Genaz, Institute of Physics UK London, p. 1744 (2008).

[84] R. Calaga, A. Langner, R. Miyamoto, R. Tomas, G. Vanbavinckhove, S. White, “Alternative Working Point(s) for the LHC”, CERN-ATS-2011-148. - 2011. - 3 p.

[85] R. Tomas, “LHC optical model and necessary corrections”, Evian 2010 Workshop on LHC Commissioning, Evian-les-Bains, France, 19 - 20 Jan 2010, pp.29-36.

[86] M. Gasior, A. Boccardi, S. Jackson, O.R. Jones, R. J. Steinhagen, “LHC Beam Stability and Performance of the Q/Q’ Diagnostic Instrumentation”, CERN-BE-2010-008. - 2010. - 5 p.

[87] LHC Machine Committee, minutes of 58th LMC Meeting held on 3 June 2010.

[88] Massimo Giovannozzi, private communication.

[89] M. Strzelczyk, private communication.

[90] M. Lamont, private communication.

[91] R. Bruce, R. Assmann, “How low can we go? Getting below 3.5 m β^*”, Evian-les-bains, France, 7 - 9 Dec 2010, pp.133-142.

[92] C. Alabau Pons, “IR1 and IR5 aperture at 3.5 TeV”, CERN-ATS-Note-2011-110 MD. - 2011.

[93] R. Assmann, R. Bruce, M. Giovannozzi, M. Lamont, E. Maclean, R. Miyamoto, G. Mueller, G. Papotti, L. Ponce, S. Redaelli, R. Tomas, G. Vanbavinckhove, J. Wenninger, “Commissioning of the betatron squeeze to 1 m in IR1 and IR5”,CERN-ATS-Note-2012-005 MD. - 2011.

[94] J. M. Jowett, “First run of the LHC as a heavy-ion collider”, CERN-ATS-2011-143. - 2011. - 3 p.

[95] J. M. Jowett, private communication.

[96] E. Hamish Maclean, F. Schmidt, R. Tomás, R. Bartolini, E. Todesco, R. Steinhagen, G. Vanbavinckhove, M. Giovannozzi, “Non-linear Chromaticity Study of the LHC at Injection, IPAC 2011, Saint-Sebastian, Spain.

[97] M. Albert, G. Crockford, S. Fartoukh, M. Giovannozzi, E. Maclean, A. MacPherson, R. Miyamoto, L. Ponce, S. Radaelli, F. Roncarolo, F. Schmidt, R. Steinhagen, E. Todesco, R.Tomás, G. Vanbavinckhove, W. Venturini Delsolaro, “Non-linear beam dynamics tests in the LHC”, CERN-ATS-Note-2011-052 MD.

[98] E. Maclean,An Effective Model of the LHC to Understand the Measured Beta-beating, IPAC 2011, Saint-Sebastian, Spain.

[99] R. Jones, private communication.

[100] W. Venturini, private communication.

[101] R. Miyamoto, R. Calaga,R. Tomas, G. Vanbavinckhove, ”Accuracy of the LHC optics measurement based on AC Dipoles”, IPAC 2011, San Sebastian, Spain, 4 - 9 Sep 2011.

[102] R. Miyamoto, R. Calaga, M. Aiba, R. Tomas, G. Vanbavinckhove, ”Measurement of coupling resonance driving terms in the LHC with AC Dipoles”, San Sebastian, IPAC 2011,Spain, 4 - 9 Sep 2011.

[103] F. Zimmermann, “First thoughts on MD priorities for 2012”, LHC Beam Operation workshop - Evian 2011, to be published.

[104] A. Faus-Golfe, M. Haguenauer, J. Velasco, “Precise measurement of the total cross section and the Coulomb scattering at the LHC”, 7th European Particle Accelerator Conference, Vienna, Austria, 26 - 30 Jun 2000, pp.e-proc. 352.

[105] ATLAS collaboration, “ATLAS Dectectors for Measurement of Elastic Scattering and Luminosity”, ATLAS-TDR-018, CERN-LHCC-2008-004, 2008.

[106] TOTEM Collaboration, “The TOTEM experiment at the CERN Large Hadron Collider”, JINST 3 (2008) S08007.

[107] M. Oriunno, M. Deile, K. Eggert, J. M. Lacroix, S. J. Mathot, E. P. Noschis, R. Perret, E. Radermacher, G. Ruggiero, “The roman pot for the LHC“, Proceedings of EPAC 2006, Edinburgh, Scotland.

[108] H. Burkhardt, S. White, “High-β^* Optics for the LHC”, LHC Project Note 431May 25, 2010.

[109] H. Burkhardt, “High-β optics”, LHC Lumi Days: LHC Workshop on LHC Luminosity Calibration, CERN, Geneva, Switzerland, 13 - 14 Jan 2011, pp.109.

[110] H. Burkhardt et al, “Un-squeeze to 90 m”,CERN-ATS-Note-2011-032 MD. - 2011. - 10 p.

[111] S. Fartoukh et al, “The Achromatic Telescopic Squeezing (ATS) MD part III”, CERN-ATS-Note-2011-132 MD. - 2011. - 8 p.

[112] S. Fartoukh, “Optics Challenges and Solutions for the LHC Insertion Upgrade Phase I”, Chamonix 2010 Workshop on LHC Performance, Chamonix, France, 25 - 29 Jan 2010, pp.262-290

[113] S. Fartoukh, “Towards the LHC Upgrade using the LHC well-characterized technology”, sLHC-PROJECT-Report-0049,20 Oct 2010. - 26 p.

[114] S. Fartoukh, “Breaching the Phase I optics limitations for the HL-LHC”, Chamonix 2011 Workshop on LHC Performance, Chamonix, France, 24 - 28 Jan 2011, pp.280-294

[115] S. Fartoukh et al, “The Achromatic Telescopic Squeezing (ATS) MD part I”, CERN-ATS-Note-2011-033 MD. - 2011. - 17 p.

[116] S. Fartoukh et al, “The Achromatic Telescopic Squeezing (ATS) MD part II”, CERN-ATS-Note-2011-060 MD. - 2011. - 26 p.

[117] M. Harrison, S. peggs, and T. roser, “The RHIC Accelerator”, Annual revision nuclear particle science 2002. 52:425 69 (2002).

[118] H. Hahn RHIC design manual, October 2000, available at http://www.agsrhichome.bnl.gov/NT-share/rhicdm/00 tocli.htm.

[119] M. Bai,S. Peggs, T. Roser, T. Satogata, D. Trbojevic, Proceedings of the 2003 PAC, 2003.

[120] N. Phinney, N. Toge and N. Walker, “International Linear Collider Reference Design Report: Volume 3: Accelelator” August 2007.

[121] J. Ellis, E. Keil and G. Rolandi, ”Options for future colliders at CERN”, CERN-EP/9803, CERN-SL 98004(AP) and CERN-TH/9833 (1998).

[122] R.W. Assmann, et al,“A 3 TeV e^+e^- Linear Collider Based on CLIC Technology”, CERN-2000-008, 2009.

[123] https://twiki.cern.ch/twiki/bin/view/CLIC/DampingRings

[124] M. Korostelev, PhD thesis, Geneva Switzerland, 2006

[125] L. S. Nadolski, “Use of LOCO at synchrotron SOLEIL”, Proceedings of EPAC08, Genoa, Italy.

[126] M. Aiba, M. Bge, J. Chrin, N. Milas, T. Schilcher, A. Streun, “Comparison of Linear Optics Correction Means at the SLS”, Second international particle accelerator conference, San Sebastian , 2011.

[127] W. Namkung, “Review of Third Generation Light Sources”, First international particle accelerator conference, Kyoto Japan, 2010.

[128] A. Chao, H. O. Moser and Z. Zhao, Overseas Chinese Physics Association, “Accelerator physics, technology and applications”, pg 489.

[129] http://www.synchrotron-soleil.fr/Recherche/LignesLumiere

[130] http://www.synchrotron-soleil.fr/portal/page/portal/SourceAccelerateur/Accelerateurs/ParametresLINAC

[131] http://www.synchrotron-soleil.fr/portal/page/portal/SourceAccelerateur/Accelerateurs/ParametresBooster

[132] J-M. Filhol et al., “Operation and Performance of the SOLEIL Storage Ring”, Proceedings of EPAC08, Genoa, Italy.

[133] L. Nadolski et al., “First Frequency Maps for Probing the Non-linear Dynamics of SOLEIL”, EPAC’08 Proceedings, Genoa, Italy, pp. 3128–3130 .

[134] L. Nadolski, “Use of LOCO at Synchrotron SOLEIL”, EPAC’08 Proceedings, Genoa, Italy, pp. 3131–3133.

[135] L. Nadolski et al., SOU-PM-NT-1595, 2004

[136] A. Franchi, “Studies and measurements of linear coupling and nonlinearities in hadron circular accelerators” , PhD thesis, GSI DISS 2006-07 (2006).

[137] G. Vanbavinckhove, M. Aiba, R. Calaga, R. Tomas, “Software Package for Optics Measurement and Correction in the LHC”, 1st International Particle Accelerator Conference, Kyoto, Japan, 23 - 28 May 2010, pp.THPE026.

[138] http://proj-lhc-optics-web.web.cern.ch/proj-lhc-optics-web/Documentation/TableFormats.html

[139] G. Kruk, S. Deghaye, M. Lamont, M. Misiowiec, W. Sliwinski. “LHC software architecture [LSA] evolution toward LHC beam commissioning.”

[140] M. Albert, G. Crockford, S. Fartoukh, M. Giovannozzi, E. Maclean, A. MacPherson, R. Miyamoto, L. Ponce, S. Redaelli, H. Renshall, F. Roncarolo, F. Schmidt, R. Steinhagen, E. Todesco, R. Tomás, G. Vanbavinckhove, W. Venturini Delsolaro, “Non-linear beam dynamics tests in the LHC”, CERN-ATS-Note-2011-052 MD, July 2011.

[141] www.openmp.org/wp/

[142] E. Mcintosh, R. Tomás, private communication.

[143] R. Bartolini and F. Schmidt, Normal Form via Tracking or Beam Data, Part. Accel., in press and CERN LHC Project Report 132, (1997).

Summary

The goal of this PhD is the development of tools and techniques for the measurement and correction of the linear optics in colliders and other storage rings. The modus operandi used for measuring and correcting the optics are described in great detail. Turn-by-turn data acquired at the beam position monitors was used to measure the optics parameters.

A new algorithm, called the Segment-by-Segment technique, was further developed to identify strong local sources. This technique allowed for the identification of strong local sources for the main optics parameters. The Segment-by-Segment technique has been proven to be extremely useful during the commissioning of the LHC. Although it has been an important and effective tool there is still room for improvements. This technique could be improved by implementing an automated way for identifying the local sources, by using a matching script or local response matrix.

The CERN SPS was used to test the algorithms before the LHC started. During the first experiment the measurements and corrections for the phase of the betatron oscillations and horizontal dispersion were tested. The ϕ-beat (difference between model and measured phase advance) was used as an observable, as the β-beat (section 1.4.2) could not be used due to the 90° phase advance in the SPS lattice. For the first time horizontal orbit correctors at the sextupoles were used to correct the ϕ-beat in the SPS, as only three quadrupole families are available. The ϕ-beat was reduced by a factor of two. A second experiment was dedicated to the correction of coupling and vertical dispersion. This correction scheme uses vertical orbit bumps at the sextupoles, as only one skew quadrupole family is available in the SPS. The outcome of this study is that it was possible to correct the leading coupling resonance and the vertical dispersion simultaneously. They were both reduced by a factor of two. The sum resonance was also corrected even though no weight was put on this resonance. Lastly, studies were conducted for the low γ_t optics. For this optics the phase advance is changed from 90° in the nominal optics to 67° for the low γ_t optics and this gave the opportunity to measure the β-function in the SPS. These experiments at the SPS were important and proved that the algorithms developed for measuring and globally correcting the optics were performing well.

During the commissioning of the LHC several optics measurements and corrections were conducted. The experience with the LHC has revealed a number of important lessons concerning optics correction. First of all it is important to identify and correct the dominant local sources. When the local sources are corrected to a level where no further corrections are possible anymore, a global correction can be applied, which tries to make a global fit using all available correctors. An attempt was made to use only the correctors around IR2 to do a global correction (during the ion commissioning), as it was expected that the errors would arise only from the squeeze of IP2. This attempt was successful in correcting the optics globally, but the correction had a negative effect on the optics locally. The correction was changing the local phase advance significantly. The leading quadrupole and skew-quadrupole error sources were identified in the inner triplets and the values for the correction used were constant during the squeeze. The β-beating was successfully corrected at injection (450 GeV) to a 30% level. It was decided that this level, though above tolerances, was acceptable for the existing aperture margins, due to lower than expected RMS orbit. For the squeezed optics several measurements and corrections sessions were conducted at different β^* (section 1.2.1) values. For a β^* value of 1.5 m the β^* error was corrected from a 60% to about a 15% level. Table C.1 shows a summary of the achieved results during the course of the commissioning.

A successful collaboration was started with the Relativistic Heavy Ion Collider (RHIC) at BNL, New York. The goal of this collaboration was to implement the Segment-by-Segment technique (de-

Run	E (GeV)	β^* $(IP_1, IP_2, IP_5, IP_8$	Peak $\frac{\Delta\beta}{\beta}_{before}$ [%]	Peak $\frac{\Delta\beta}{\beta}_{after}$ [%]
2009-2010	450	(11,10,11,10)	~ 50	~ 30
2009-2010	3500	(2,2,2,2)	~ 60	~ 25
2009-2010	3500	(3.5,3.5,3.5,3.5)	~ 35	~ 15
2011	3500	(1.5,10,1.5,10)	~ 60	~ 15
2011	3500	(1,10,1,10)	-	~ 10

Table C.1: Summary of the corrections achieved during the course of the commissioning.

veloped for the LHC) at RHIC. This implementation faced some challenges. The first challenge was that RHIC only has double plane BPMs around the IRs, and outside of the IR only single plane BPMs are available. The second challenge was that only a limited number of independent quadrupoles are available around the IRs, limiting the correction. Despite these limitations, first results from the segment-by-segment technique are promising. The $\beta-$beat around the ring in both planes was reduced from 30% and 40%, respectively in the horizontal and vertical plane, to a $\sim$ 20% level. Nevertheless, some issues will need to be clarified. For instance the effect of the AC-dipole at RHIC has to be investigated and algorithms need to be implemented to filter the bad BPMs.

The same algorithms that were developed for the global correction of coupling and vertical dispersion in the LHC have been applied to the CLIC damping ring in simulations. Errors were randomly applied. Three different cases were studied. Rotations were applied to the dipoles and quadrupoles, and misalignments were applied to the quadrupoles. The main contribution to the emittance H-V ratio comes from the difference coupling resonance (section 2.4.3). The case with the largest emittance H-V ratio was the skew quadrupole rotation. However, simulations with quadrupole misalignments could not be carried out for an RMS error higher than 10 μm. The correction algorithm for the coupling and vertical dispersion shows good results. The emittance H-V ratios are reduced by a factor of 3-5. Better correction could be achieved by applying an iterative correction process. The first results for the CLIC damping ring are promising and show that the same algorithms that were developed for the SPS and LHC could be applied to an electron machine. However, further study will be needed to investigate the effect of sextupole misalignments. Investigations about the number of skew-quadrupoles and the number of different families of skew-quadrupoles should also be conducted. These explorations will not only depend on the results of the beam optics studies but also on the available budget. Measurements were also conducted at SOLEIL, a lightsource, to test whether the measurement techniques developed for hadron machines could be experimentally applied to lepton machines. First experiments showed that the measurement techniques could be applied to measure the linear optics and non-linear terms, but a more detailed study would be needed to investigate the BPM non-linearities and the discrepancy between the standard LOCO (section 2.6) analyses and the techniques discussed here.

Samenvatting

Het doel van dit proefschrift is de ontwikkeling van methodes en technieken voor de meting en correctie van de lineaire optica in versnellers en andere opslagringen. De modus operandi gebruikt voor het meten en corrigeren van de optiek worden in detail beschreven. De 'turn-by-turn data' verkregen in de 'beam position monitors' (BPMs, monitoren die de positie van de bundel waarnemen) werden gebruikt om de optische parameters te meten.

Een nieuw algoritme, genaamd de 'Segment-by-segment' techniek, werd verder ontwikkeld om sterke lokale fouten te identificeren. Deze techniek kon sterke lokale foutenbronnen voor de belangrijkste optische parameters identificeren. De 'Segment-by-segment' techniek heeft bewezen zeer nuttig te zijn tijdens de ingebruikname van de LHC. Hoewel het een belangrijke en effectieve techniek is, is er nog ruimte voor verbetering. Deze techniek kan worden verbeterd door een meer geautomatiseerde manier voor het identificeren van lokale fouten, bijvoorbeeld door gebruik te maken van een lokaal 'matching' script of lokale respons matrix.

De CERN SPS werd gebruikt om de algoritmen te testen voor de LHC werd opgestart. In het eerste experiment werden de metingen en correcties voor de fase van de betatron oscillaties en horizontale dispersie getest. De 'ϕ-beat' (het verschil tussen de gemeten en gemodeleerde fase verschuiving tussen twee BPMs) werd gebruikt. De reden hiervoor is dat de 'β-beat' (sectie 1.4.2) niet kon worden gebruikt vanwege het 90° faseverschil tussen twee monitoren in het SPS-lattice. Voor de eerste keer werden horizontale baancorrectoren in de sextupoles gebruikt om de 'ϕ-beat' in de SPS te corrigeren, dit omdat slechts drie quadrupoolfamilies beschikbaar zijn. Het resultaat was dat de 'ϕ-beat' verminderd werd met een factor twee. Een tweede experiment was gewijd aan de correctie van de koppeling en verticale dispersie. Dit correctieschema maakt gebruik van verticale baancorrectoren aan de sextupoles, omdat er slechts één 'skew'-quadrupool (normale quadrupool 45° gedraaid in het transversale vlak) familie beschikbaar is in de SPS-lattice. Het resultaat van dit onderzoek was dat het mogelijk is de dominante koppelingresonantie en de verticale dispersie tegelijk te corrigeren. Beiden werden verminderd met een factor twee. De som resonantie werd ook gecorrigeerd, hoewel er geen gewicht werd geplaatst op deze resonantie. Tenslotte werden studies uitgevoerd voor de lage γ_t optica (sectie 3.3). Voor deze optica werd het faseverschil tussen twee monitoren gewijzigd van 90° in de nominale optica naar 67 ° voor de lage γ_t optica en dit gaf de mogelijkheid om de β-functie te meten in de SPS. Deze experimenten in de SPS waren belangrijk en bewezen dat de algoritmen ontwikkeld voor het meten en globaal corrigeren van de optiek uitstekende prestaties leverden.

Tijdens de ingebruikname van de LHC werden meerdere optica metingen en correcties uitgevoerd. Een aantal belangrijke lessen konden geleerd worden over opticacorrectie in de LHC. In de eerste plaats is het belangrijk om de dominante lokale fouten te identificeren en te corrigeren. Wanneer de lokale fouten gecorrigeerd worden tot een niveau waarbij geen verdere lokale correcties meer mogelijk zijn, kan een globale correctie toegepast worden, die probeert een globale 'fit' met alle beschikbare correctoren te vinden. Er is geprobeerd om alleen de correctoren rond IR2 te gebruiken om een globale correctie (tijdens de periode dat de LHC ionen versnelde) uit te voeren, omdat verwacht werd dat de fouten alleen zouden ontstaan uit de 'squeeze' rond IP2. Deze poging was succesvol bij het corrigeren van de globale optische functies, maar de correctie had een negatief effect op de lokale optische functies. Deze correctie veranderde het lokale faseverschil aanzienlijk. De dominante quadrupool en 'skew'-quadrupoolfouten zijn waargenomen in de triplet magneten en de waarden voor de gebruikte correctie zijn constant tijdens de 'squeeze' ('squeeze' is de techniek waarin de β^* word verlaagt in de IPs). De 'β-beating' werd met succes gecorrigeerd tijdens injectie (450 GeV) tot ongeveer 30%. Er werd besloten dat deze correctie, net boven de toleranties, aanvaardbaar was, als gevolg van lagere dan verwachte 'RMS' spreiding van de baan. Meerdere meet- en correctiesessies werden gehouden voor verschillende β^* (sectie 1.2.1) waarden. Voor een β^* waarde van 1,5 m werd de fout gecorrigeerd van 60 % tot ongeveer 15 %. Tabel C.2 geeft een overzicht van de behaalde resultaten in de loop van de ingebruikname van de LHC.

Run	E (GeV)	β^* $(IP_1, IP_2, IP_5, IP_8$	Peak $\frac{\Delta\beta}{\beta}_{voor}$ [%]	Peak $\frac{\Delta\beta}{\beta}_{na}$ [%]
2009-2010	450	(11,10,11,10)	~ 50	~ 30
2009-2010	3500	(2,2,2,2)	~ 60	~ 25
2009-2010	3500	(3.5,3.5,3.5,3.5)	~ 35	~ 15
2011	3500	(1.5,10,1.5,10)	~ 60	~ 15
2011	3500	(1,10,1,10)	-	~ 10

Table C.2: Samenvatting van de bereikte correcties in de loop van de ingebruikname van de LHC.

Een succesvolle samenwerking werd gestart met de Relativistic Heavy Ion Collider (RHIC) van het BNL laboratorium, New York. Het doel van deze samenwerking was om de 'Segment-by-segment' techniek (ontwikkeld voor de LHC) te implementeren in RHIC. Deze implementatie kende een aantal uitdagingen. De eerste uitdaging was dat in RHIC alleen 'dual plane' BPMs (BPMs die de positie van de straal in beide vlakken waarnemen) geïnstalleerd zijn rond de 'Interaction regions' (IRs), en buiten de IR slechts 'single plane' BPMs (zijn BPMs die de positie van de straal oftwel in het horizontale of vertical vlak waarnemen) beschikbaar zijn. De tweede uitdaging was dat slechts een beperkt aantal onafhankelijke quadrupolen beschikbaar zijn rond de IRs, dit vormt een beperking voor mogelijke correcties. Ondanks deze beperkingen, zijn de eerste resultaten van de segment-by-segment techniek veelbelovend. De '$\beta-$beat' in de ring is voor beide vlakken teruggebracht van 30 %, 40 %, respectievelijk voor het horizontale en verticale vlak, tot een niveau van $\sim$ 20%. Toch zal een aantal zaken verduidelijkt moeten worden in de toekomst. Bijvoorbeeld het effect van de AC-dipool in RHIC zal onderzocht moet worden en algoritmen zullen moeten worden ontwikkeld om de slechte BPMs te filteren.

Dezelfde algoritmes die zijn ontwikkeld voor de globale correctie van de koppeling en de verticale dispersie in de LHC zijn toegepast voor simulaties van de CLIC 'damping ring'. Drie verschillende gevallen werden bestudeerd. Rotaties werden toegepast op de dipolen en quadrupolen en verplaatsingen op de quadrupolen. De belangrijkste bijdrage aan de 'emittance' verhouding tussen het horizontale en verticale vlak komt van de 'verschil koppelingresonantie' (sectie 2.4.3). Het geval met de grootste 'emittance' HV-verhouding was voor de de 'skew'-quadrupool rotatie. Simulaties met quadrupool verplaatsingen konden niet worden uitgevoerd voor een 'RMS' spreiding hoger dan 10 μm. Het correctiealgoritme voor de koppeling en verticale dispersie toont goede resultaten. De emittance HV-verhoudingen werden verminderd met een factor 3-5. Betere correctie kan worden bereikt door een iteratief correctieproces. De eerste resultaten voor de CLIC 'damping ring' zijn veelbelovend en tonen aan dat de dezelfde algoritmen die zijn ontwikkeld voor de SPS en de LHC zouden kunnen worden toegepast op een elektronmachine. Echter verder onderzoek zal nodig zijn om het effect van verplaatsingen van de sextupolen te onderzoeken. Onderzoeken over het aantal 'skew'-quadrupolen en het aantal verschillende families van skew-quadrupolen moeten in meer detail worden uitgevoerd. Dit zal niet alleen afhangen van de resultaten van de optische studies, maar ook het beschikbare budget. Metingen werden ook uitgevoerd bij SOLEIL, een lichtbron, om te testen of de ontwikkelde meettechnieken voor hadronmachines kunnen worden toegepast op leptonmachines. Eerste experimenten toonden aan dat de meting zou kunnen worden toegepast op de lineaire optica en niet-lineaire termen, maar een meer gedetailleerde studie is nodig om de niet-lineariteiten van een BPM te onderzoeken en de discrepantie tussen de standaard LOCO analyses (sectie 2.6) en de technieken die hier werden besproken.

Acknowledgements

The final, and probably the hardest part that I have to write for my thesis, is the acknowledgements. But here we go.

This thesis would not have been possible without the help of many people. First of all I would like express my gratitude to my daily supervisor Rogelio Tomás Garcia, for all his help and support during my PhD. I was probably not always the easiest person to work with, but without his help this PhD would never have been possible.

I would also like to thank my supervisors, Jos Engelen and Lyn Evans, for their precious advice and guidance during the course of my PhD. I especially would like to thank Jos Engelen for his patience in reading my thesis over and over again and giving me very much appreciated feedback. A special thanks also goes to Stan Bentvelsen and Frank Linde for accepting me as a PhD student at NIKHEF.

I also would like to express my gratitude to Masamitsu Aiba, Rama Calaga and Ryoichi Miyamoto for the many fruitful discussions and their company during the long nights spent in the CERN control room. These guys made the long hours bearable. I also want to thank my colleagues in the Accelerator Beam Physics group and the operations group at CERN. A special thanks also to the engineers in charge of the LHC who tolerated my occasional impatience and various requests. I am also grateful towards all the women and men who worked hard to make the LHC possible. Without them this marvelous machine and consequently my PhD would not have been possible.

During the course of my PhD I have had the opportunity to contribute to RHIC, and for this I would like to thank Mei Bai and Wolfgang Fischer for their support and generosity. I would especially like to thank Mei for the continuous help and stimulating discussions, whether physics related or not. I would also like to thank Laurent Nadolski for the opportunity to conduct measurements at the SOLEIL light-source.

On a personal note, I would like to thank my parents, Ingrid and Ludo, and my little brother, Niels, for all their support and their listening ear when the goings were tough. A special thanks also to my close friends from the University of Delft. Especially to Mattias GenBrugge, Kristof Byttebier, Stijn Meysen and Bram De Vogeleer for the memorable time spent together. I hold fond memories of our nightly discussions, long hours in the library and the dinner-table conversations during our university days.

I would also like to thank Yngve Levinsen, Jochem Snuverink, Simon White, Daniel Wollmann and my many office mates for the great moments spent in and outside of CERN. I also want to thank Reina Camacho and Anne Gentil-Beccot for the nice lunches together. A very special thanks to Stef Janssens and Arnaud Vande Craen, for the many meaningful discussions, their steadfast friendship and for being my best men on my wedding. This brings me to the last, but certainly not least person I would like to thank. That person is my sweetie π Yi Ling Hwong. Thank you for being a huge support to me, proofreading my thesis, and especially for tolerating my sleepless nights during the final couple of months of my PhD.